# Internal tides around New Caledonia : dynamics, eddy-internal tide interactions, and SWOT observability

Arne Bendinger

## To cite this version:

Arne Bendinger. Internal tides around New Caledonia : dynamics, eddy-internal tide interactions, and SWOT observability. Ocean, Atmosphere. Université Paul Sabatier - Toulouse III, 2023. English. NNT : 2023TOU30336 . tel-04618408

HAL Id: tel-04618408
https://theses.hal.science/tel-04618408

Submitted on 20 Jun 2024

**HAL** is a multi-disciplinary open access archive for the deposit and dissemination of scientific research documents, whether they are published or not. The documents may come from teaching and research institutions in France or abroad, or from public or private research centers.

L'archive ouverte pluridisciplinaire **HAL**, est destinée au dépôt et à la diffusion de documents scientifiques de niveau recherche, publiés ou non, émanant des établissements d'enseignement et de recherche français ou étrangers, des laboratoires publics ou privés.

# THÈSE

**En vue de l'obtention du**

## DOCTORAT DE L'UNIVERSITÉ DE TOULOUSE

**Délivré par :** *l'Université Toulouse 3 Paul Sabatier (UT3 Paul Sabatier)*

---

**Présentée et soutenue le** *12/12/2023* **par :**

Arne BENDINGER

# Marées internes autour de la Nouvelle-Calédonie: dynamique, interactions tourbillon-marée interne et challenge pour le satellite SWOT

## Internal tides around New Caledonia: dynamics, eddy-internal tide interactions, and SWOT observability

---

### JURY

| | | |
|---|---|---|
| Rosemary MORROW | Physicienne CNAP<br>(LEGOS) | Présidente du Jury |
| Emmanuel COSME | Maître de conférences<br>(Université Grenoble Alpes) | Rapporteur |
| Edward D. ZARON | Senior researcher<br>(Oregon State University) | Rapporteur |
| Aurélien PONTE | Chercheur<br>(IFREMER) | Examinateur |
| Jérôme CHANUT | Ingénieur<br>(MERCATOR Ocean) | Examinateur |
| Pascale BOURUET-AUBERTOT | Professeure d'Université<br>(Sorbonne Université) | Examinatrice |

**École doctorale et spécialité :**

*SDU2E : Océan, Atmosphère, Climat*

**Unité de Recherche :**

*Laboratoire d'études en géophysique et océanographie spatiales, LEGOS (UMR 5566)*

**Directeur(s) de Thèse :**

*Lionel GOURDEAU* et *Sophie CRAVATTE*

**Rapporteurs :**

*Emmanuel COSME* et *Edward D. ZARON*

## Abstract —

The oceanic energy cascade and the associated redistribution of energy from planetary scales to microscales are crucial to achieve climate equilibrium, yet they remain to be fully understood and quantified. Among the submesoscale flow regime which is characterized by equal contributions from rotational (balanced) and non-rotational (unbalanced) effects, it is internal tides (internal gravity waves at tidal frequency) which have been shown to represent a major energy transfer toward dissipative scales. The Surface Water Ocean Topography (SWOT) satellite mission will push forward global sea surface height (SSH) observations of fine-scale physics of combined balanced and unbalanced motions, and their interactions. Our understanding of these processes will ultimately depend on our ability to disentangle these two different dynamical flow regimes. This thesis aims to tackle SWOT SSH observability of balanced and unbalanced motions around New Caledonia, an area with pronounced internal tide activity alongside elevated level of mesoscale to submesocale eddy variability located beneath two swaths of SWOT's fast-sampling phase, during which SWOT orbited on a 1-day repeat cycle to collect high-frequency measurements. As an initial step, this thesis provides the first comprehensive description of internal-tide dynamics around New Caledonia, an internal generation hot spot in the southwestern tropical Pacific that has not yet been explored in the literature, based on a tailored regional high-resolution (1/60°) numerical modeling effort. Internal tide generation around New Caledonia is associated with the main bathymetric structures, i.e. continental slope, shelf breaks, small- and large-scale ridges, and seamounts, strongly dominated by the semidiurnal tide and low-vertical modes, with a strong signature in SSH. It is found to be a major source of tidal energy propagation toward the open ocean despite enhanced energy dissipation rates close to the generation sites. Mesoscale eddy variability is shown to be a potential source of the loss of tidal coherence (or tidal incoherence) due to eddy-internal tide interactions, either through the refraction of tidal beam energy propagation by mesoscale currents toward the open ocean or by mesoscale-eddy-induced variations of barotropic-to-baroclinic energy conversion. Important insight is provided by in-situ observations of autonomous underwater gliders. They reveal the numerical model's realism of internal-tide dynamics while proving to be a suitable in-situ platform to infer internal tides, including SSH signature. SWOT SSH observability of balanced and unbalanced motions represents a challenge around New Caledonia because the internal tide dominates SSH variance at wavelengths similar to those of balanced motion at scales less than 200 km wavelength. Particular emphasis is given to the incoherent tide, which manifests in SSH at scales less than 100 km, while limiting the observability of mesoscale and submesoscale motions. An outlook is given on the impact of internal tides on the mesoscale to submesoscale circulation with promising routes for future work on cross-scale energy exchanges and the closure of the oceanic energy budget. Finally, the comprehensive description of internal-tide dynamics conducted in this thesis has important implications for the New Caledonia marine ecosystem, with the hope of paving the way for the island's efforts in the conservation of marine protected areas.

**Keywords:** Internal tides, eddy-internal tide interactions, SWOT SSH observability

---

**Résumé —**

L'équilibre énergétique de l'océan traduit des échanges d'énergie entre les termes sources aux échelles planétaires et la dissipation aux micro-échelles. Cette cascade d'énergie, cruciale dans la compréhension du systéme océanique, demande à être mieux comprise et quantifiée. La plus grande part de l'énergie dans l'océan est associée à la dynamique mésoéchelle. Les échelles spatiales correspondantes sont aussi celles des marées internes et dans les régimes océaniques où l'énergie des ondes internes est suffisamment forte celles-ci représentent un transfert d'énergie majeur vers les échelles dissipatives. La nouvelle mission satellite SWOT (Surface Water Ocean Topography) permettra d'observer globalement pour la première fois ces processus de fines échelles. Une motivation de cette thèse est l'observabilité du niveau de la mer SWOT avec le challenge de comprendre la part respective de la dynamique méso et sous-mésoéchelle et des ondes internes. La région d'étude se situe autour de la Nouvelle Calédonie dans le Pacifique sud-ouest et plus particulièrement dans la région sud survolée par une fauchée SWOT lors de la phase de cal-val du satellite caractérisée par une orbite à 1 jour. La thèse s'appuie sur une simulation régionale dédiée à haute résolution (1/60°) forcée ou pas par la marée barotrope en plus des forçages « classiques ». Pour la première fois la dynamique des marées internes autour de la Nouvelle-Calédonie est décrite. Cette région s'avère être un hot spot de génération de marées internes associé aux principales structures bathymétriques,. La marée interne est principalement semi diurne. Elle se caractérise par un premier mode barocline très important et une forte signature dans la SSH (>6 cm). Cette énergie de marée interne se propage dans l'océan ouvert à partir de deux zones localisées au nord et au sud de la Nouvelle Calédonie malgré des taux de dissipation d'énergie élevés à proximité des zones de génération. Cette propagation est majoritairement associée à de la marée interne cohérente mais l'activité méso-échelle s'avère être une source potentielle de perte de cohérence de la marée interne (marée incohérente). Cette marée interne incohérente est associée aux interactions avec les tourbillons océaniques soit par la réfraction de la propagation de l'énergie du faisceau de marée par les courants à méso-échelle lors de la propagation de l'énergie de marée, soit par les variations de la conversion de l'énergie barotrope en énergie barocline dues aux changements de stratification induits par les tourbillons à méso-échelle. Des observations in situ obtenues par des planeurs sous-marins autonomes révèlent le réalisme du modèle numérique quant à la simulation des marées internes tout en s'avérant être une plateforme in-situ appropriée pour documenter les marées internes, y compris leur signature de la SSH. Dans les régions de forte marée interne, celle-ci domine la variance de la SSH pour des longueurs d'onde jusqu'à 200 km correspondant. Une attention particulière est accordée à la marée incohérente, qui se manifeste dans la SSH à des échelles inférieures à 100 km. Cette thèse initie également l'étude de l'impact des marées internes sur la circulation à méso-échelle et sous-méso-échelle, avec des voies prometteuses pour les travaux futurs sur les échanges d'énergie entre les échelles et la fermeture du bilan énergétique océanique. Ces travaux participeront à la valorisation des données SWOT dans le cadre de SWOT-AdAC avec la campagne SWOTALIS. Enfin, ils sont une première initiative dans l'implication des marées internes en lien avec l'écosystème marin de la Nouvelle-Calédonie associée à un objectif de mise en place d'aires marines protégées au sein du parc naturel de la mer de Corail.

**Mots clés:** Marées internes, interactions tourbillon-marée interne, SWOT SSH observabilité

---

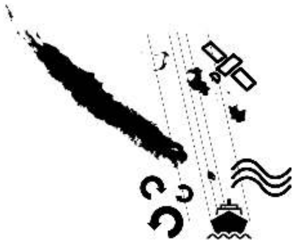

# General introduction

Oceanic motion features a wide spectrum of spatial and temporal scales, ranging from planetary-scale phenomena driven by climate forcing, such as the thermohaline and gyre circulation down to microscales characterized by irreversible three-dimensional turbulence. Climate equilibrium is only achieved when the large-scale potential energy input is balanced by kinetic energy dissipation, which in a viscous ocean can only occur at very small scales. The exact route of kinetic energy is not fully understood and explored yet due to the complex nature of non-linear interactions and a lack of observations of fine-scale motion on global scales. Conventional satellite altimetry has given us insight into the large-scale circulation and mesoscale dynamics at scales $O$(100-1000 km). And, even though mesoscale dynamics, i.e. mesoscale eddies, contain an overwhelmingly large part of the global kinetic energy, they do not provide a route to energy dissipation.

A route to energy dissipation may be provided by what we call the submesoscale flow regime which acts at scales $O$(1-10 km) and internal gravity waves which represent the broad spectrum of kinetic energy at frequencies higher than the local Coriolis frequency. Three major types of internal gravity waves exist depending on their forcing: internal lee waves, near-inertial waves, and internal tides. These internal gravity waves represent a large reservoir of high-frequency motions from the surface, down to mid-depths and the ocean bottom.

Next to submesoscale motion, internal gravity waves are believed to play a crucial role in the energy transfer toward dissipative scales through direct wave breaking or non-linear interaction with the mesoscale and submesoscale circulation. This thesis is dedicated to internal tides which are internal waves at tidal frequency. Internal tides form when the barotropic tide interacts with ocean bathymetry causing vertical displacements of isopycnal surfaces while radiating internal waves into the stably stratified water column. They have received increasing attention in the last two decades as they are considered an important energy source for diapycnal mixing in the deep ocean away from lateral boundaries while maintaining the abyssal stratification and contributing to the closure of the oceanic energy budget.

Global observations encompassing both mesoscale and submesoscale geostrophic dynamics (balanced) and both ageostrophic dynamics (unbalanced) from submesoscale motions and internal gravity waves will be soon provided by sea surface height (SSH) measurements of the wide-swath Surface Water Ocean Topography (SWOT) satellite mission, launched in December 2022, aiming to give revolutionary insight into fine-scale surface dynamics at unprecedented scales down to 15 km wavelength. The primary objective of SWOT from an oceanographic point of view is to provide fine-scale observations of mesoscale to submesoscale dynamics. These observations aim to understand the associated redistribution of energy, momentum, and the vertical transport of physical and biogeochemical tracers between the atmosphere-ocean, the mixed layer, and the ocean interior, with significant implications for climate on a large scale.

The fact that balanced and unbalanced motions coexist in the ocean has been recognized for a long time, first confirmed by historic space photographs from numerous Space Shuttle operations and exemplarily shown for the Sea of Japan revealing small-scale spirals and internal waves at spatial scales $O(1\text{-}10\ \text{km})$ in Fig. 1. On the one hand, SWOT's combined SSH measurements of balanced and unbalanced motions could be seen as unique opportunity to study non-linear scale interactions and cross-scale energy exchanges and to improve our understanding of how kinetic energy is transferred toward dissipative scales. On the other hand, internal tides pose a significant challenge to SWOT's SSH observability of the mesoscale and submesoscale flow regimes, given that internal tides can exhibit similar wavelengths and contribute equally to SSH variance. This complicates the distinction between these two different dynamical regimes and their exact imprint in SSH.

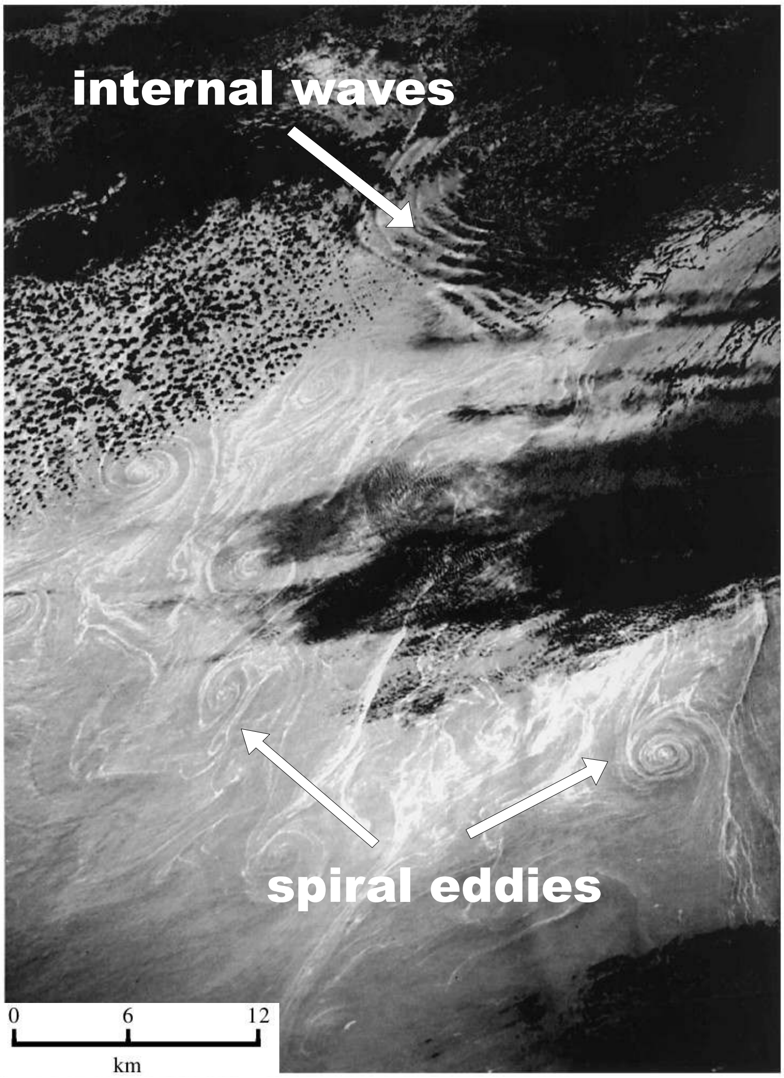

**Figure 1:** Adapted from Munk et al. (2000). Space photograph (16 September 1982) exploiting sunglitter on the sea surface reveals submesoscale dynamics expressed by spiral eddies in the Sea of Japan. The surface signature of internal (solitary) waves is also visible in the upper part of the image. Black splotches are cumulus clouds.

An accurate disentangling of balanced and unbalanced motion will be required for better interpretation of SWOT's SSH. A distinct fraction of the internal tide is predictable, i.e. the coherent internal tide which is characterized by tidal stationarity (constant amplitude and phase), and thus rather straightforward to correct for. The other part of the tidal signal is incoherent or non-stationary. The incoherent internal tide is characterized by its unpredictable nature due to temporal variations of stratification or eddy-internal tide interactions. Tidal incoherence poses, thus, a more challenging task for SWOT observability.

This thesis aims to understand SWOT's SSH observability in an area of high mesoscale eddy variability and pronounced internal tides. Pronounced internal-tide activity can be found near prominent bathymetric features such as the Hawaiian Ridge or the Luzon Strait in the Pacific Ocean. For these regions, internal tides have been extensively studied using numerical modeling and in-situ observations. Here, the focus is on the internal tide field around New Caledonia - an archipelago in the southwestern tropical Pacific at the entrance of the Coral Sea - which has not been explored yet despite being recognized as an internal tide generation hot spot from conventional satellite altimetry.

New Caledonia represents an unique study site for three major reasons: **(1)** It is characterized by a complex regional circulation encompassing western boundary currents, zonal jets, and enhanced **mesoscale eddy activity**. **(2)** It is an **internal tide generation hot spot** due to complex bathymetry such as continental slopes, shelf breaks, oceanic ridges, and seamounts. **(3)** Potentially being subject to **eddy-internal tide interactions**, the study region is located just beneath two swaths of **SWOT's fast sampling phase** during which the satellite orbited in a 1-day repeat cycle, providing high-frequency measurements of the governing dynamics at play. In the framework of the SWOT Adopt-A-Crossover (AdAC) consortium, a dedicated in-situ experiment was carried out south of New Caledonia during the fast-sampling phase. The collected high-frequency in-situ observations beneath two SWOT swaths will help interpret SWOT's SSH measurements (see Fig. 2).

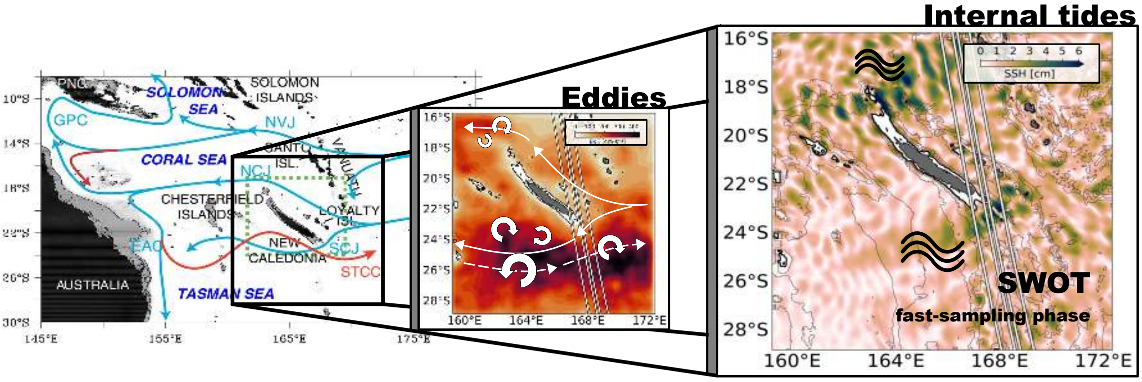

**Figure 2:** New Caledonia represents a unique study site in the context of SWOT SSH observability. **(left)** The southwestern tropical Pacific exhibits a complex regional circulation (adapted from Cravatte et al., 2015), **(middle)** giving rise to enhanced mesoscale eddy variability **(middle)**. **(right)** New Caledonia represents an internal tide generation hot spot due to complex bathymetry with strong SSH amplitudes. Further, the study region is located beneath two swaths of SWOT's fast sampling phase during which SWOT orbited in a 1-day repeat cycle.

A state-of-the-art and tailored high-resolution regional modeling effort has been initiated in the framework of this thesis, complemented by valuable in-situ observations from autonomous underwater gliders. **The objectives of this thesis** are a **first comprehensive description of the internal tide field including SSH signature around New Caledonia**, the identification of **potential sources of tidal incoherence**, and a complementary **validation with in-situ observations**. Further, preliminary insight will be given on the **impact of internal tides on energy cascades**.

This work is presented as follows: Chapter I provides the scientific background, presenting the current state of our knowledge and remaining questions on energy cascade, internal tides, and SWOT. Chapter II introduces the numerical modeling effort, glider observations, and the applied methodologies. Chapter III presents the results acquired during this thesis, divided into the coherent (III.1) and incoherent internal tide characteristics (III.2) based on regional numerical modeling, the in-situ glider approach (III.3), and the impact of internal tides on cross-scale energy exchanges (III.4). Finally, this work presents the main thesis results before providing perspectives for potential routes of future work in the Conclusion and Perspectives.

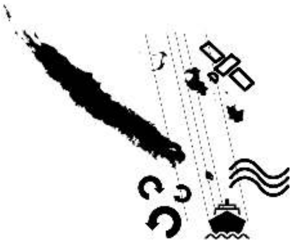

# Introduction générale

Les mouvements océaniques présentent un large spectre d'échelles spatiales et temporelles, allant des échelles planétaires induits par le forçage climatique, tels que la circulation thermohaline et la circulation des gyres subtropicales, jusqu'aux micro-échelles caractérisées par une turbulence tridimensionnelle irréversible. L'océan est en équilibre lorsque l'apport d'énergie potentielle à grande échelle est équilibré par la dissipation de l'énergie cinétique, ce qui, dans un océan visqueux, ne peut se produire qu'à de très petites échelles. Les transferts d'énergie cinétique entre les grandes et petites échelles ne sont pas encore entièrement compris en raison de la nature complexe des interactions d'échelle non linéaires et du peu d'observations caractérisant les fines échelles océaniques. Si la dynamique méso-échelle $O$(100-1000 km), telle qu'observée par l'altimétrie satellitaire, contient une grande partie de l'énergie cinétique globale, elle ne permet pas d'accéder aux plus fines échelles importantes pour comprendre comment cette énergie dissipe.

Celles-ci font appel à la dynamique turbulente sous mésoéchelle $O$(1-10 km) et aux ondes de gravité internes qui représentent le large spectre de l'énergie cinétique pour les fréquences supérieures à la fréquence locale de Coriolis. Les ondes de gravité internes sont censées jouer un rôle crucial dans le transfert d'énergie vers les échelles dissipatives en interagissant de manière non linéaire entre elles ou avec la circulation à méso-échelle et à sous-méso-échelle.

Ces ondes de gravité internes représentent un ensemble de mouvements à haute fréquence affectant toute la colonne d'eau de la surface, jusqu'au fond de l'océan. Il existe trois grands types d'ondes de gravité internes en fonction de leur forçage: les ondes de Lee générées par un écoulement sur un fond rugueux, les ondes quasi-inertielles forcées en surface par le vent haute fréquence et les ondes internes de marée ou marées internes générées par les interactions entre la marée barotrope et la bathymétrie. Les marées internes ont fait l'objet d'une attention croissante au cours des deux dernières décennies car elles sont considérées comme une source d'énergie importante pour le mélange diapycnal dans l'océan intérieur et contribuent à la fermeture du bilan énergétique océanique. Dans cette thèse, je vais m'intéresser particulièrement à ces ondes internes de marée.

Ces fines échelles océaniques englobant à la fois la dynamique géostrophique méso-échelle et sous-méso-échelle et les dynamiques agéostrophiques sous méso-échelle et des ondes de gravité internes ont été observées depuis longtemps par des photographies spatiales à haute résolution comme celle prise en mer du Japon (Fig. 3) qui révèle des tourbillons, des filaments et des ondes internes à des échelles spatiales $O$(1-10 km). Aujourd'hui, elles sont en mesure d'être observées par les mesures de la hauteur de la surface de la mer (SSH) de la nouvelle mission satellitaire SWOT (Surface Water Ocean Topography) lancée en décembre 2022.

Basé sur le concept d'interférométrie SWOT se distingue des autres missions altimétriques par des mesures 2D sous une fauchée du satellite et une résolution de l’ordre de 15 km de longueur d’onde. L’objectif principal de SWOT pour l’observation de l’océan est d’améliorer la compréhension de ces fines échelles dans les transferts d’énergie vers les échelles dissipatives, d’observer la dynamique sous méso-échelle et instruire les vitesses verticales associées importantes à la fois pour la dynamique de la couche mélangée et les transports verticaux de flux biogéochimiques et de quantité de mouvement.

Un défi important porte sur l’observabilité de la SSH SWOT afin de distinguer les dynamiques meso et sous méso-échelle des ondes internes de marée étant donné que ces processus ont des longueurs d’onde similaires et peuvent contribuer à niveau égal à la variance de la SSH. Faire la part entre les signatures méso et sous méso-échelle et celles de la marée interne est essentiel pour interpréter correctement la mesure de SSH SWOT. La marée interne se décompose en une partie cohérente caractérisée par

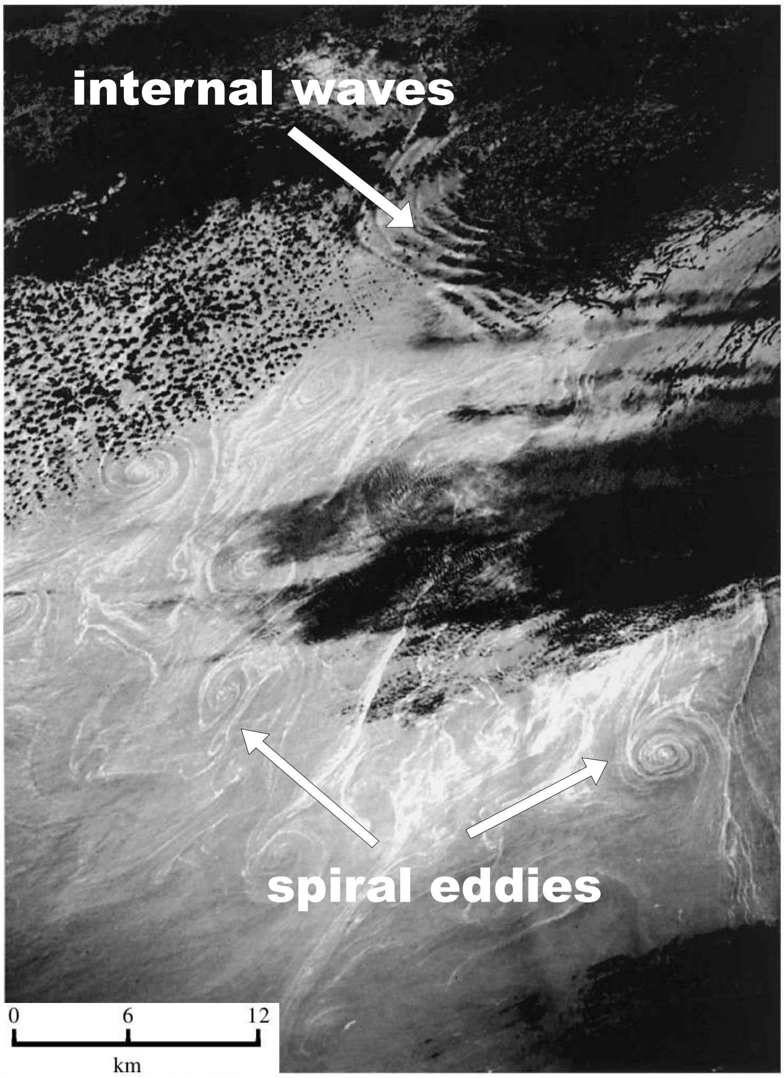

**Figure 3:** Adapté de Munk et al. (2000). Une photographie spatiale (16 septembre 1982) exploitant les paillettes du soleil à la surface de la mer révèle une dynamique à méso-échelle exprimée par des tourbillons en spirale dans la mer du Japon. La signature superficielle des ondes internes (solitaires) est également visible dans la partie supérieure de l’image. Les taches noires sont des cumulus.

des amplitude et phase constantes et une partie incohérente caractérisée par sa nature imprévisible due aux variations temporelles de la stratification ou aux interactions avec les tourbillons. Si la partie cohérente est prédictible et donc assez simple à estimer l'incohérence de la marée représente un défi plus important pour l'observabilité SWOT.

Des fortes signatures de marées internes sont localisées dans des régions spécifiques comme Hawaï ou Luzon strait dans le Pacifique et ont été largement étudiées à l'aide de modèles numériques et d'observations in situ. Un des objectifs de cette thèse vise à appréhender l'observabilité de la SSH SWOT dans une région, la Nouvelle Calédonie, où l'activité tourbillonnaire et celle des marées internes ont des niveaux d'énergie équivalent. La Nouvelle-Calédonie est située dans le sud-ouest du Pacifique tropical à l'entrée de la mer de Corail. Elle est le siège d'importantes marées internes comme le montre l'altimétrie satellitaire sans avoir fait jusqu'à aujourd'hui l'objet d'études particulières.

La Nouvelle-Calédonie représente un site d'étude unique dans le cadre de cette thèse pour trois raisons principales: **(1)** Une circulation régionale complexe avec des courants de bord, des jets zonaux générant une forte **activité tourbillonnaire**. **(2)** Une bathymétrie complexe avec des pentes continentales, des plateaux, des rifts, des monts sous-marins **source de génération de marée interne**. **(3)** Le survol d'une fauchée SWOT lors des premiers 6 mois de la mission **SWOT** au cours de laquelle le satellite a une orbite à un jour (**fast sampling phase**) idéale pour observer une dynamique à haute fréquence. Dans le cadre du consortium du SWOT Adopt-A-Crossover, une campagne à la mer, SWOTALIS, était effectuée au sud de la Nouvelle-Calédonie sous la fauchée SWOT lors de la fast-sampling phase ayant pour but l'interprétation des mesures de SSH SWOT. La Nouvelle Calédonie apparait donc comme un endroit idéal pour étudier les **interactions entre la marée interne et la dynamique tourbillonnaire** dans le cadre de la mission SWOT (Fig. 4).

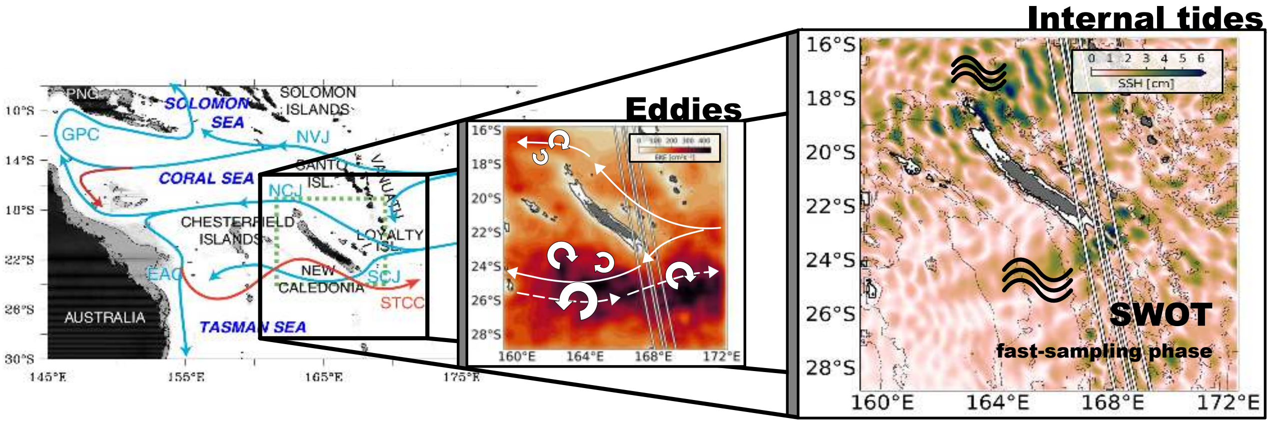

**Figure 4:** La Nouvelle-Calédonie représente un site d'étude unique dans le contexte de l'observabilité SWOT SSH. **(left)** Le sud-ouest du Pacifique tropical présente une circulation régionale complexe (adaptée de Cravatte et al., 2015), **(middle)** donnant lieu à une variabilité accrue des tourbillons à méso-échelle **(middle)**. **(right)** La Nouvelle-Calédonie représente une zone importante de génération de marée interne en raison d'une bathymétrie complexe avec de fortes amplitudes de SSH. De plus, la région étudiée est située sous deux fauchées de la phase d'échantillonnage rapide de SWOT pendant laquelle SWOT a orbité dans un cycle de répétition d'un jour.

Cette thèse se base sur le développement et l'analyse d'une simulation régionale à haute résolution mais également sur l'analyse des rares observations in-situ disponibles à partir de planeurs sous-marins dans cette région et capables de documenter la marée interne. **Les objectifs de la thèse** visent à **documenter le champ de marée interne autour de la Nouvelle Calédonie** avec ses **composantes cohérentes et incohérentes**, et **identifier les sources potentielles d'incohérence de la marée** en lien avec l'activité mésoéchelle à partir de la simulation numérique mais également à partir des observations in-situ. En outre, un aperçu préliminaire illustre le rôle des marées internes dans les cascades d'énergie à partir des simulations numériques avec et sans forçage de marée.

Le plan de la thèse se décline avec le Chapitre I qui présente le contexte scientifique, l'état de l'art de nos connaissances et les questions en suspens. Le Chapitre II présente l'effort de modélisation numérique, les observations des planeurs sous-marins et les méthodologies d'analyse utilisées. Le Chapitre III présente les résultats qui concernent les caractéristiques de la marée interne cohérente (III.1) et incohérentes (III.2) basées sur la modélisation numérique régionale, l'analyse des observations in situ (III.3), et l'impact des marées internes sur les cascades d'énergie (III.4). Enfin, ce travail présente les principaux résultats de la thèse avant d'offrir des perspectives pour des travaux futurs potentiels dans les Conclusion et Perspectives.

# Scientific activity and collaborations

## Field work

| | |
|---|---|
| March-April 2023 | **Research cruise SWOTALIS aboard RV Antéa (Nouméa, New Caledonia)**<br>Scientific cruise member involved in CTD (Conductivity-Temperature-Depth) and VMP (Vertical microstructure profiler) data acquisition and sampling of oxygen, chlorophyll, nutrients, and ammonium |

## International collaborations

| | |
|---|---|
| March-May 2022 | **Visiting scholar at the University of Michigan, Ann Arbor, USA at the Department of Earth and Environmental Studies (Brian Arbic)**<br>Kinetic energy spectra and spectral kinetic energy flux calculations using high-resolution numerical modeling output |
| October-November 2022 | **Visiting scholar at the University of Washington, Seattle, USA at the Applied Physics Laboratory (Kyla Drushka, Luc Rainville)**<br>Analysis of Observing System Simulation Experiments in the context of SWOT-AdAC |

## Conferences and workshops

| | |
|---|---|
| February 2022 | **Ocean Sciences Meeting, Honolulu, Hawaii, USA (online)**<br>Fine-scale dynamics and internal tides around New Caledonia using in-situ observations and modeling (poster presentation) |
| June 2022 | **SWOT Science Team Meeting, Toulouse, France**<br>High-resolution regional modeling effort around New Caledonia (lightning talk) |
| August 2022 | **SWOT-AdAC and CLIVAR-OMDP FilaChange workshop, Paris, France**<br>Eddy-internal tide interactions around New Caledonia (presentation) |
| February 2023 | **Eddy-wave Meeting, Hamburg, 2023 (online)**<br>Eddy-internal tide interactions around New Caledonia (presentation) |
| September 2023 | **SWOT Science Team Meeting, Toulouse, France**<br>SWOT in the Tropics: Regional modeling of internal tide dynamics around New Caledonia (poster) |

## Scholarships

| | |
|---|---|
| February 2021 | **Toulouse Graduate School of Earth and Space Science (TESS) BOOSTER award in the amount of 10.000 €** |

# Acknowledgments

This thesis represents an important chapter in my journey over the past ten years, and it would not have been possible without the help and support of many people along the way, from my beginnings in Kiel, Germany to Toulouse, France.

To begin with, I thank Sophie and Lionel for their incredible support throughout my thesis, from the moment I arrived in Toulouse to the final days before thesis submission. Both professionally and personally, Sophie and Lionel were always available and supported me with full passion. I especially appreciate their efforts in encouraging me in all the scientific activities I was able to undertake during my thesis, including numerous conferences, research visits in the US, and my stay in New Caledonia. These opportunities allowed me to broaden my scientific network within the French and American oceanographic community. Sophie and Lionel played a special role in this regard through their interest and self-conception in scientific exchanges with colleagues on a national and international level. I especially thank Sophie for her hospitality in New Caledonia and Lionel for his mental support whenever needed.

A special thank you goes to Brian Arbic, Kyla Drushka, and Luc Rainville for having me as part of their research group at the University of Michigan and the University of Washington. These research visits were a unique opportunity for me to share my science with international colleagues and establish collaborations. I also want to thank Clément Vic for his support and availability for scientific discussions. The same applies to Aurélie Albert and Laurent Brodeau, who played a key role at the beginning of my thesis by introducing me to the high-performance CINES platform. Finally, I thank Michel for being available at any time to answer my questions.

A huge thank you goes to all the people I met on the way in Toulouse. To start with, I thank the colleagues and friends at LEGOS which supported me especially in the last weeks and months of my thesis: Elisa and Adrien, the greatest office mates I could imagine that made everyday life in the lab a bit sweeter, may it be through philosophical discussions or just the appreciation of good coffee. I am truly thankful for the support from Juliette, Amélie, and Adrien who were highly present and supported me in any possible way - not only in the final weeks of my manuscript submission but all the way to the day of my PhD defense. You gave me the necessary energy for the final steps, which I will always appreciate. I also want to thank Audrey, Pierre, Adélaide, Gabriela, Manon, Simon, Julia, and Wassim for their warm welcome when I arrived at LEGOS and for being part of this journey.

I am very grateful to have met Johanna, Alida, Juliette, Manu, and not to be forgotten, Chachou. Without you, my arrival and stay in Toulouse would not have been the same, and I highly appreciate your support throughout. Not only have you had a profound impact on my experience in France, but I am sure we have made friends for a lifetime. Thank you for being there, all the conversations and discussions we had in both good and bad times, the culinary side of our friendship, and finally your patience you had with me upon my arrival, especially when it came to my French language skills. Une

petite partie de moi quitte Toulouse en tant que Français.
I also want to express my deepest appreciation to Laura, Agustina, Myriam, and Isaias for their constant support and openness in recent months. You are one of the reasons I have held out for the last few months while making it difficult to leave Toulouse.

There are special people to thank who I met in Kiel, Germany during my Bachelor's and Master's studies and who motivated me to pursue a PhD. A big thank you to Thomas, Johann, Tamara, Camille, Wolfgang, Mareike, Marie, Nora, Jonathan, Philip, Gabriel, Tobias, Ilmar, Jöran, Joan, Goratz, and many more, who were all part of this adventure. A special thanks goes to Johannes, who supported me throughout my studies, giving me the opportunity to participate in various research cruises in the Labrador Sea and the EUREC4A cruise. The scientific experiences that I gained during these field campaigns as well as the associated work back at the GEOMAR were a huge motivation for me to pursue a PhD. I have always felt appreciated by Johannes and that is certainly a reason why I decided to stay in science.

There are some other people I would like to thank. Léa and Louis who I met during my Erasmus exchange in Svalbard. Not only did they make my stay in Svalbard more pleasant, but they also welcomed me in France, whether for an overnight stay in Paris or a weekend in the Bretagne. I also want to thank Valentina, Andréa, and Hassan, who I met during my visit at the University of Michigan. They made this experience really special. Also, I want to thank Nico, who supported me, especially in the final months of the thesis, providing helpful advice and motivation. Thank you for this friendship which represents a very important part of my life in France.

I also thank my family for being there, making this journey possible while letting me freely choose my path. The last three years were not the easiest, and the distance certainly did not help, but in the end, we have held together.

Finally, I thank Jessie - the most important part of this journey. Thank you for your support, any sacrifices you may have made, and the amazing time we had in Toulouse and southwestern France. I will never forget this experience with you, despite the physical distance it may have caused from time to time. The adventures we have had together during this time are unforgettable for me, whether it was our time in New Caledonia or simply the weekends in and around Toulouse, in the Pyrenees mountains, along the Mediterranean coast or in the Basque country. I am not sure I would have gone the same way without you.

# Contents

## Chapter I

# Scientific background

---

## Contents

# I

# Scientific Background

This thesis begins with a comprehensive review of our current knowledge on fine-scale motions with a focus on internal tides and their role in the oceanic energy cascade. Subsequently, it dives into the theoretical foundations, observations, and numerical modeling of internal tides before exploring both the opportunities and challenges inherent in the wide-swath SWOT satellite mission. Finally, the New Caledonia study site will be presented, followed by a detailed description of this thesis' research objectives.

## I.1 Oceanic energy cascade

At planetary scales, oceanic motion is governed by geostrophic flow. This flow describes the isobaric flow that develops due to the exact balance between the horizontal pressure gradient and the Coriolis force, creating large-scale currents (e.g. the Antarctic Circumpolar Current or western boundary currents such as the Gulf Stream, the Kuroshio, and the Agulhas Current). Those currents are subject to barotropic and/or baroclinic instabilities due to the horizontally and/or vertically sheared system associated with the shedding of mesoscale eddies in geostrophic balance at spatial scales $O$(10-100 km). Today, it is commonly acknowledged that roughly 80 % of the oceanic

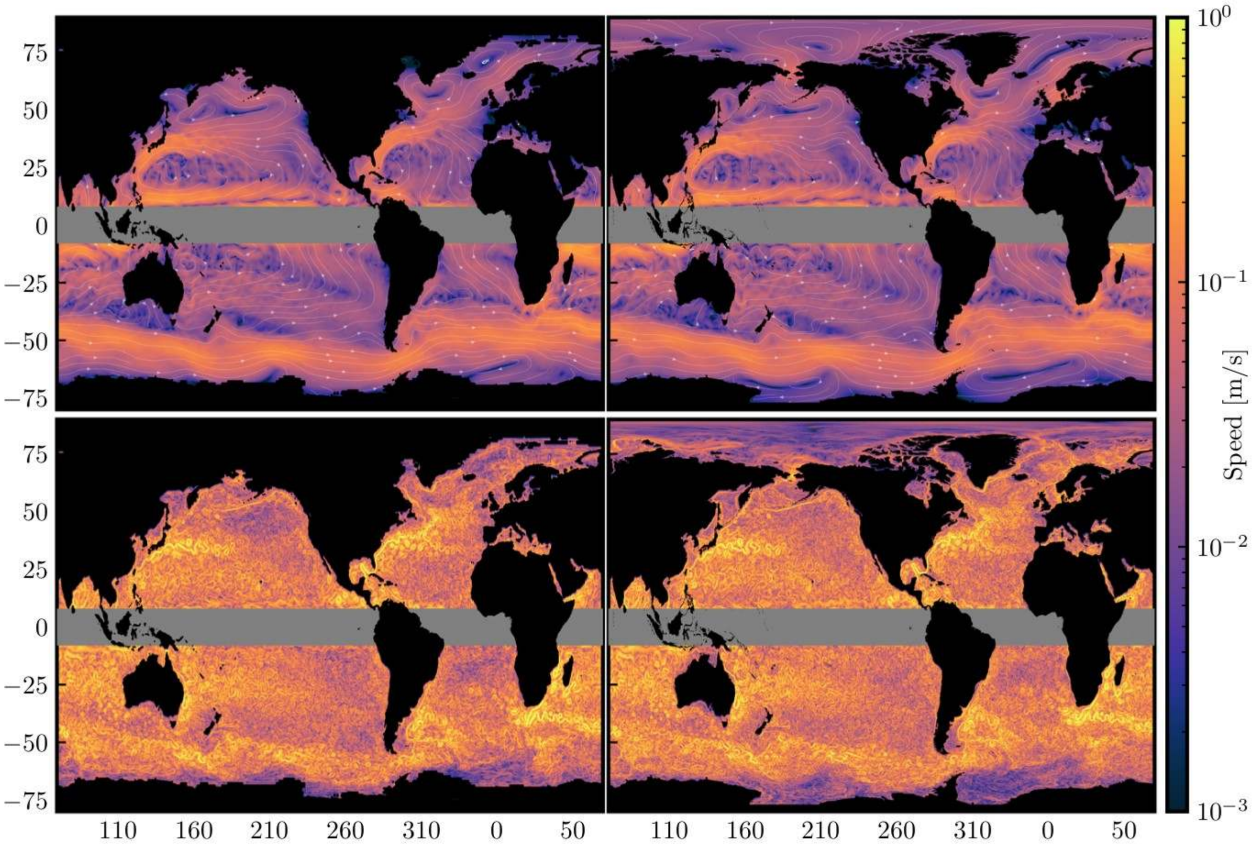

**Figure I.1:** From Storer et al. (2022). Snapshot of surface geostrophic velocity magnitudes (upper panels) representative for motion $O(1000\,\mathrm{km})$ and (lower panels) representative for motion $O(100\,\mathrm{km})$ from the gridded 1/4° AVISO/CMEMS dataset (left panels) and the 1/12° NEMO model reanalysis dataset (GLORYS). Streamlines for motion $O(1000\,\mathrm{km})$ in the upper panels are also given.

kinetic energy is contained in the geostrophic eddy field (Ferrari and Wunsch, 2009; Sasaki et al., 2014; Torres et al., 2018; Klein et al., 2019).

Figure I.1 demonstrates the spatial extent and corresponding magnitude of the large-scale circulation (for scales >1000 km) and the geostrophic eddy field (for scales <1000 km) shown for the gridded 1/4° AVISO/CMEMS dataset and the 1/12° NEMO model reanalysis dataset (GLORYS). For scales >1000 km, the basin-wide gyre circulation and the large-scale currents are clearly evident (flow direction highlighted by streamlines). For scales <1000 km, the flow is dominated by geostrophic eddies associated with the swirling features with strong velocity magnitudes. They are ubiquitous in the global ocean, but stand out in magnitude along the Antarctic Circumpolar Current and the western boundary currents.

Mesoscale eddies exhibit distinctive characteristics that set them apart from linear waves. One key feature is their non-linearity, evident when the ratio between relative vorticity advection and planetary vorticity advection exceeds unity (Early et al., 2011). Thus, they can be understood as mesoscale rotating structures or large-scale vortices that maintain some kind of coherence, i.e. they conserve their temporal and spatial features during their life cycle (Chelton et al., 2011). Mesoscale eddies are associated with two important dimensionless quantities: the Rossby number ($Ro$) and the Richardson number ($Ri$) (Gill, 1982).
$Ro$ assesses the balance between fluid inertia and the Coriolis force, and it is calculated as $Ro = U/(fL)$, where $U$ is the velocity scale, $f$ is the local Coriolis frequency, and $L$ is the horizontal length scale. A small $Ro$ ($Ro << 1$) indicates that geostrophic balance dominates. $Ri$ describes the ratio between buoyancy and flow shear, and is defined as $Ri = N^2H^2/U^2$, with $N$ representing the buoyancy frequency and $H$ the vertical length scale. A large $Ri$ ($Ri >> 1$) signifies stable stratification, where the stabilizing effect of density stratification suppresses turbulent mixing.

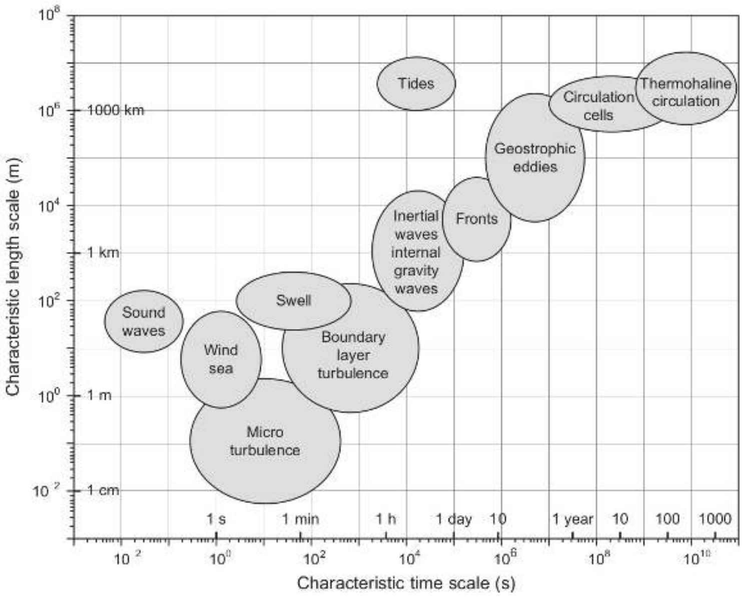

**Figure I.2:** From Cushman-Roisin and Beckers (2011). Characteristics length and time scales for oceanic processes and structures.

In fact, the global ocean features motions among all spatial and temporal scales. It ranges from the large-scale oceanic circulation (e.g. thermohaline and gyre circulation) acting on ocean basin scales $O(1000\text{ km})$ and decadal time scales down to microscale turbulence where viscous dissipation acts (Fig. I.2). Oceanic motion as we know it up to this day is the result of non-linear scale interactions and the redistribution of kinetic energy toward dissipation. One of key questions in the oceanographic community lies in understanding how energy is transferred from large to small scales and, consequently, how a climate equilibrium is achieved. In the following, the basic concept of the oceanic energy cascade is presented while focusing on the governing dynamics and processes that provide a direct route to energy dissipation.

### I.1.1 Cross-scale energy exchanges

Climate equilibrium requires a dynamical route from the large-scale energy input to energy dissipation, i.e. from the rotational and balanced regime to the non-rotational and unbalanced regime, as shown in the schematic in Fig. I.3. Barotropic and/or baroclinic instabilities due to the horizontally and/or vertically sheared current systems of the large-scale circulation. Since the upper ocean is highly stratified, baroclinic instabilities play a crucial role in the development of quasi-geostrophic turbulence. They gain their energy from the potential energy of the mean flow which is then con-

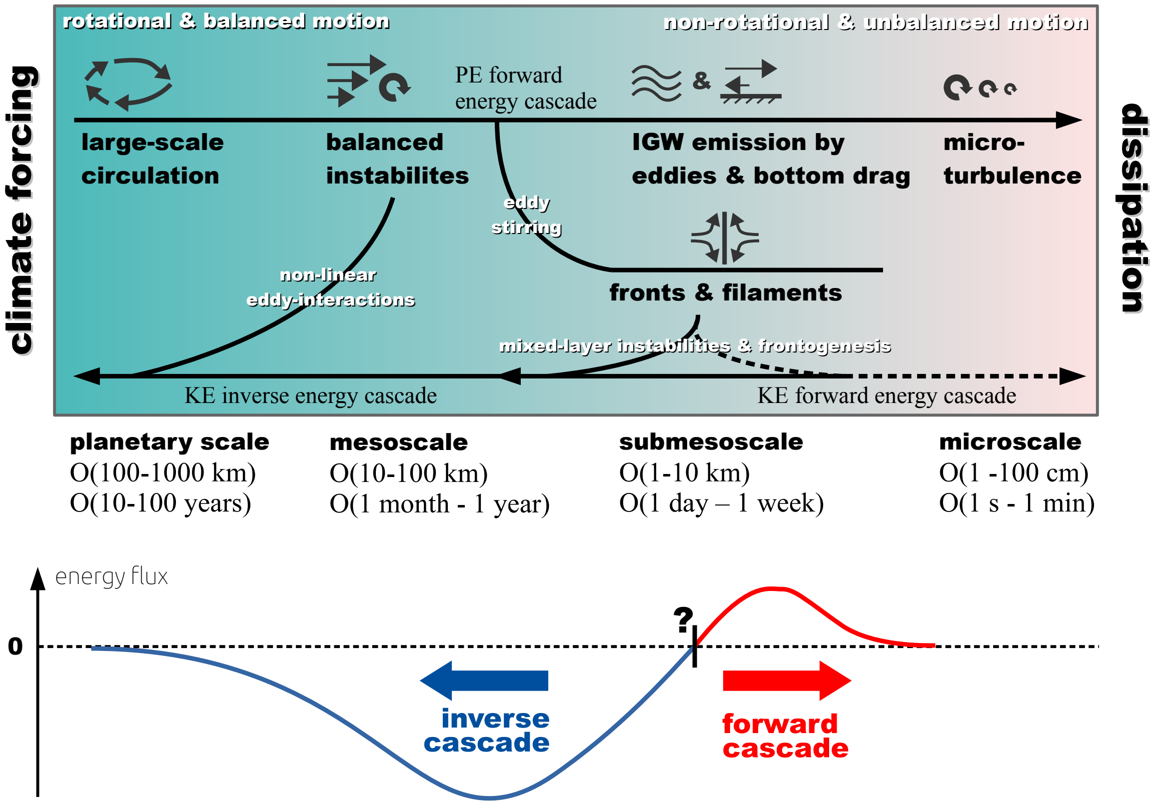

**Figure I.3:** Inspired from McWilliams (2016) and Klein et al. (2019). Schematic of the cross-scale energy transfer among planetary scales, mesoscales, submesoscales, down to microscales. It illustrates the transformation of potential energy to kinetic energy exhibiting both the forward and inverse energy cascade. A schematic of the characteristic spectral kinetic energy flux is also given. Note that the transition scale between the inverse and forward cascade remains an open question.

verted into kinetic energy. The associated two-dimensional oceanic turbulence plays an important role in cross-scale energy exchanges by predicting an upscale kinetic energy flux, i.e. an inverse energy cascade that transfers energy from smaller to larger scales, and a barotropization of the flow. This inverse energy cascade is concomitant with non-linear eddy interactions such as the merging of coherent vortices resulting in increasing kinetic energy at larger scales (Vallis, 2017). This was confirmed by spectral flux calculations applied on satellite altimetry observations revealing a net inverse energy cascade at low wavenumbers, i.e at mesoscales (sco, 2005).

Potential sources of energy dissipation linear drag/boundary friction or internal gravity emission by mesoscale eddies. However, these processes compensate only a minor fraction of the kinetic energy input (Wunsch and Ferrari, 2004; McWilliams, 2016; Vallis, 2017). Another energy sink must necessarily exist, i.e. a mechanism that describes the energy transfer from large to small scales through a forward cascade, a process not accounted for by quasi-geostrophic theory. Further, it remains unclear at what length scales the inverse cascade transitions into a forward cascade. In quasi-geostrophic theory, this length scale is given by the Rossby radius of deformation $R_d$ (sco, 2005; Scott and Arbic, 2007), which represents the length scale at which rotation effects become as important as buoyancy effects Gill (1982). $R_d$ is defined for a baroclinic ocean as $R_d = c_n/|f|$, where $c_n$ is the $n$-th eigenspeed value from the Sturm-Liouville problem. It can be approximated by $c_n \approx \frac{NH}{n\pi}$, where $H$ is the scale height (e-folding scale).

As our understanding of smaller-scale dynamics has grown through recent numerical modeling efforts (Capet et al., 2008), it has been demonstrated that the transition scale between the inverse and forward cascade may be found much smaller than $R_d$. Further,this transition scale is known to exhibit strong dependence on the region and season (Mensa et al., 2013; Qiu et al., 2014; Sasaki et al., 2014; Rocha et al., 2016a,b). The submesoscale flow regime is assumed to play a key role in the energy transfer from large to small scales serving as an energy conduit towards three-dimensional turbulence and dissipation at microscales. This is presented in more detail in the following section.

### I.1.2 The submesoscale flow regime

The submesoscale flow regime is assumed to play a key role in the energy transfer from large to small scales serving as an energy conduit between rotational and balanced dynamics and non-rotational and unbalanced dynamics acting on scales $O$(1-10 km) (McWilliams, 2016). It has only received major attention since the new millennium related to the progress of submesoscale permitting or resolving numerical modeling, computing power, as well as high-resolution satellite-based images of the ocean surface.

Acting on spatial scales $O$(1-10 km) and temporal scales in the order of hours to days, submesoscale motion distinguishes from mesoscale motion by equally strong contributions from planetary vorticity, lateral, and vertical shears accompanied by $O(1)$ $Ro$ and $Ri$ (Thomas et al., 2008; McWilliams, 2016). Further, it features vertical velocities that are usually an order of magnitude larger than the divergence induced vertical velocities at mesoscales, reaching up to 100 m day$^{-1}$ (Thomas et al., 2008). For this particular reason, submesoscale turbulence is assumed to play a key role in the vertical transport of physical and biogeochemical tracers between the atmosphere-ocean interface, mixed layer, and ocean interior (Capet et al., 2008; Thomas et al., 2008; Klein and Lapeyre, 2009). It is believed that submesoscale dynamics provide a direct route to energy dissipation by breaking the rotation and stratification constraints (McWilliams, 2016). There are two predominant processes that drive motion at submesoscale, presented in the following: mesoscale-driven frontogenesis and mixed layer instabilities.

### I.1.2.1 Mesoscale-driven frontogenesis

Mesoscale-driven frontogenesis is a crucial process for the energy transfer at submesoscales (Lapeyre et al., 2006; Capet et al., 2008; McWilliams, 2016), illustrated and summarized in Fig. I.4. It represents an intensification of pre-existing surface horizontal buoyancy gradients driven by the mesoscale strain field, i.e. eddy stirring. The intensification of a lateral buoyancy gradient is associated with a disruption of the geostrophic balance, which is counteracted by secondary (ageostrophic) circulation. The secondary circulation that develops in the cross-front plane expresses by an overturning circulation in the cross-front plane and acts to restore the geostrophic balance. This is achieved by advectively tilting isopycnals toward the horizontal with upward (downward) vertical velocities on the light (dense) side (Fig. I.4). In the upper layer, these vertical velocities add to the vertical vorticity $\zeta$ (apart from the geostrophic component) by vertical vortex stretching: $\partial_t\zeta \approx (f+\zeta)\partial_z w + ...$ with negative (anticyclonic) vorticity $\partial_z w < 0$ on the light side and positive (cyclonic) vorticity on the dense side $\partial_z w > 0$. Since cyclonic vorticity on the dense side is favored (due to the finite-$Ro$ asymmetry, McWilliams et al., 2015; Srinivasan et al., 2017), the secondary circulation promotes restratification and, thus, counteracts the formation

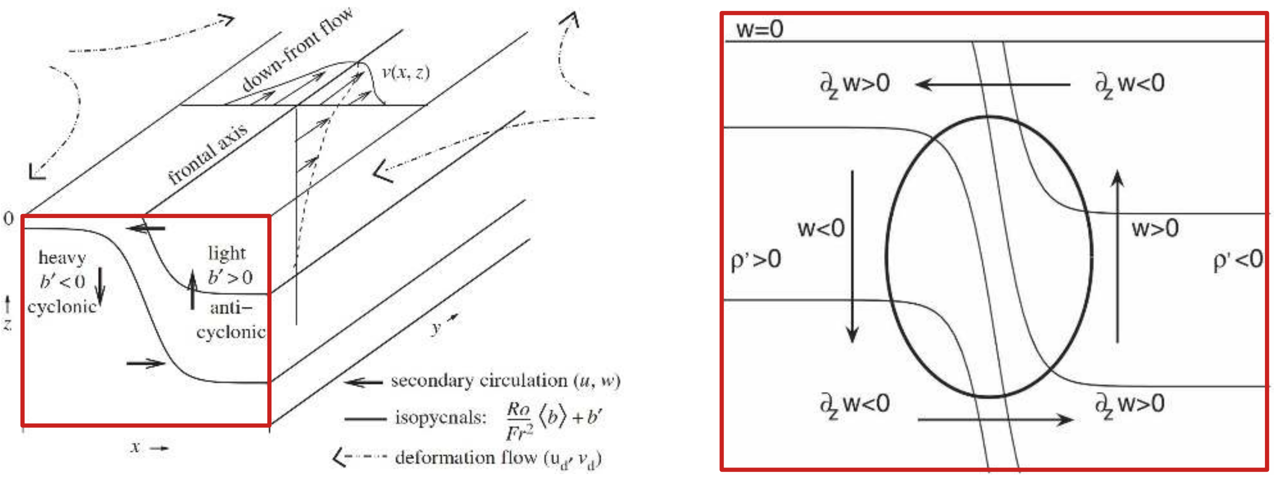

**Figure I.4:** Adapted from **(left)** McWilliams (2016) and **(right)** Lapeyre et al. (2006). Schematic illustrating the mesoscale-driven frontogenesis which acts to intensify pre-existing surface horizontal buoyancy gradient induced by the mesoscale strain field. In response to departure from geostrophy, a secondary (ageostrophic) overturning circulation develops in the cross-front plane expressed by upward (downward) vertical velocities on the light (dense) side. Since downwelling on the dense side favored, the secondary circulation promotes restratification.

of strong horizontal buoyancy gradients and the departure from geostrophy, initially induced by background straining. Following Lapeyre et al. (2006), the evolution of frontal dynamics, i.e. a horizontal density gradient $\nabla_H \rho$, can be described by the following equation:

$$\frac{D(\boldsymbol{\nabla}_H \rho)}{Dt} = -(\boldsymbol{\nabla}_H \mathbf{u})^T \boldsymbol{\nabla}_H \rho - \frac{\partial \rho}{\partial z} \boldsymbol{\nabla}_H w \tag{I.1}$$

where $\boldsymbol{\nabla}_H = (\frac{\partial}{\partial x}, \frac{\partial}{\partial y})$ is the horizontal gradient operator. Note that $\frac{D}{Dt} = \frac{\partial}{\partial t} + \vec{u} \cdot \boldsymbol{\nabla}$ is the material derivative. The first term on the right hand side is representative of the straining of the density field by the velocity gradient tensor $(\nabla_H \mathbf{u})^T$. In particular, the velocity gradient tensor is defined as:

$$\mathbf{A} = \frac{1}{2} \begin{pmatrix} \sigma_n & \sigma_s + \zeta \\ \sigma_s - \zeta & -\sigma_n \end{pmatrix}$$

with $\sigma_n = \frac{\partial u}{\partial x} - \frac{\partial v}{\partial y}$ the normal strain, $\sigma_s = \frac{\partial v}{\partial x} + \frac{\partial u}{\partial y}$ the shear strain, and $\zeta = \frac{\partial v}{\partial x} - \frac{\partial u}{\partial y}$ the relative vorticity. The second term on the right hand side represents the flattening of isopycnals by vertical velocity $w$, i.e. the secondary (ageostrophic) circulation that develops to restore geostrophic balance.

The overall role of frontogenesis in cross-scale energy exchanges is presented in Fig. I.3. On the one hand, frontogenesis provides a route to dissipation via the forward energy cascade. In particular, potential energy is transferred to smaller scales through mesoscale stirring and stretching that lead to the production of surface density anomalies such as submesoscale fronts or filaments. This is especially true near the surface where the vertical velocities vanish and, hence, the vertical gradient $\frac{\partial w}{\partial z}$ becomes strong. This is accompanied by increasing horizontal divergence, a further growth of the frontogenetic rate, and eventually small-scale density gradients with large amplitudes (Lapeyre et al., 2006; Capet et al., 2008; McWilliams, 2016). On the other hand, frontogenesis establishes an inverse energy cascade, i.e. a transfer of potential energy to kinetic energy through the developing secondary circulation and the associated vertical fluxes of density (Klein et al., 2019).

#### I.1.2.2 Mixed layer instabilities

Another important source for submesoscale energy are mixed layer instabilities (Boccaletti et al., 2007; Callies et al., 2016). This process is representative for baroclinic instability of a weakly stratified layer (i.e. mixed layer) in the presence of a lateral buoyancy gradient. Mixed layers are mainly formed by atmospheric forcing leaving behind a homogenized, well-mixed upper ocean layer that is clearly separated from the stratified interior (thermocline) below. This is most specifically the case after the passage of a storm which acts to vanish vertical gradients near the surface, whereas a buoyancy gradient remains in the horizontal associated with the stratified interior (thermocline; Ferrari and Rudnick, 2000). The lateral buoyancy gradient is not affected by the localized atmospheric forcing but rather it is governed by spatial variations of atmospheric fluxes or mesoscale stirring at scales well above the local deformation radius.

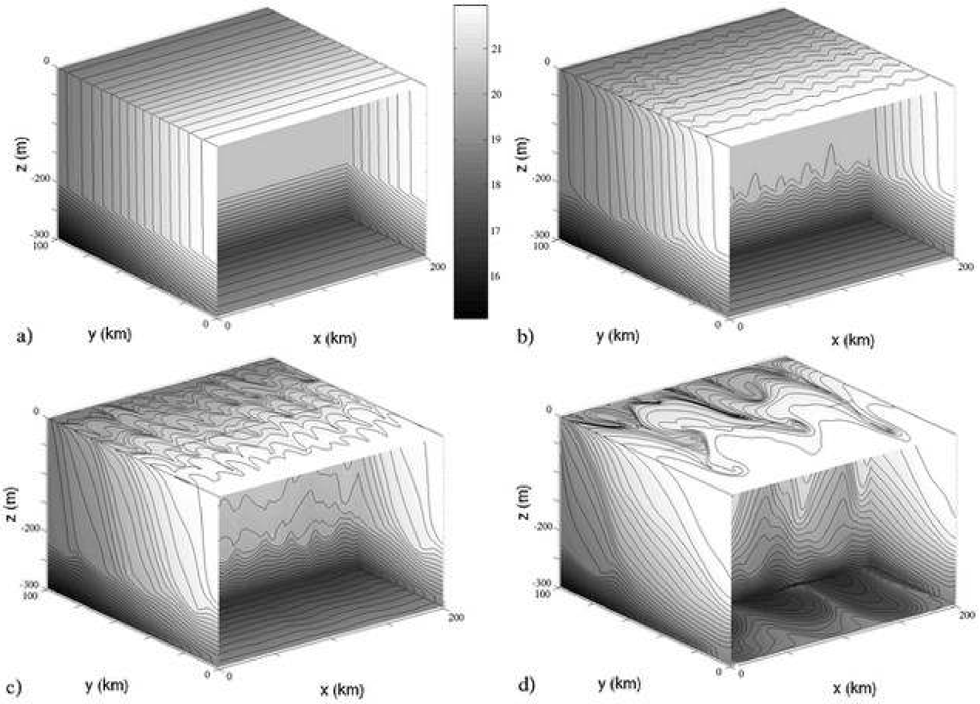

**Figure I.5:** From Boccaletti et al. (2007). Numerical simulation in a channel configuration showing the development of mixed layer instabilities. **(a)** The initial configuration consists of a homogenized, well-mixed surface layer sitting above a stable density stratification. **(b)** Gravitational slumping of vertical isopycnals sets in after 10 days creating wavelike disturbances. **(c)** Fast-growing instabilities develop that act to further restratify the mixed layer after 12 days. **(d)** After 17 days, the instabilities have evolved into mixed-layer eddies and frontogenesis. The shading represents temperature.

The development of mixed layer instabilities is shown by a idealized numerical simulation configuration in Fig. I.5. Mixed layer instabilities extract their energy from the lateral buoyancy gradient that represents a reservoir of potential energy which is released by gravitational slumping of vertical isopycnals down the buoyancy gradient (Fig. I.5a, Ou, 1984; Tandon and Garrett, 1995; Haine and Marshall, 1998). Constrained by geostrophic adjustment, the gravitational slumping is subject to fast-growing ageostrophic baroclinic instabilities at submesoscales which allow for the onward restratification of the mixed layer by tilting the isopycnals toward the horizontal (Fig. I.5b-c, Boccaletti et al., 2007). Mixed layer instabilities differ from mesoscale baroclinic instabilities in the ocean interior by the actions of spatial and temporal scales in the order of $O$(1-10 km) and $O$(1 day), respectively. This is linked to the weakly stratified surface layer and its vertical extent such that instability generated fluctuations are associated with the submesoscale range (McWilliams, 2016). The developing instabilities express by wavelike disturbances and break the geostrophic adjustment of the slumping isopycnals (Fig. I.5d). Implications of mixed layer instabilities for cross-scale energy transfer are as follow. On the one hand, mixed layer instabilities can evolve in submesoscale mixed-layer eddies, which in turn flux energy upscale while strengthening mesoscale eddies (Schubert et al., 2020). On the other hand, mixed layer instabilities facilitate frontogenesis and, hence, flux energy downscale to smaller scales as described in Sect. I.1.2.1 (Boccaletti et al., 2007; Schubert et al., 2020).

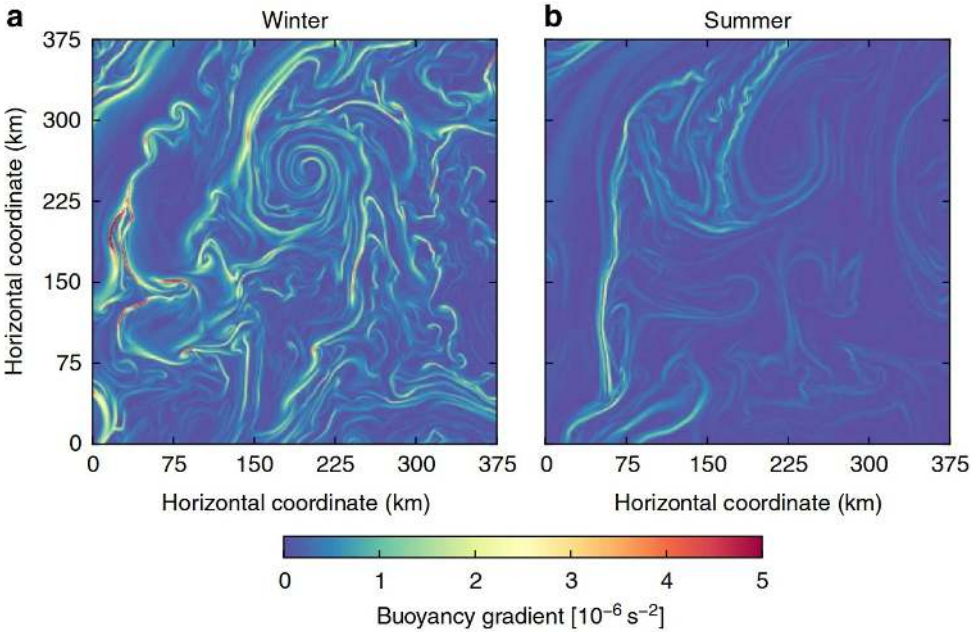

**Figure I.6:** From Callies et al. (2015). Magnitude of the surface buoyancy gradient for **(a)** winter and **(b)** summer extracted from a numerical simulation in the Gulf Stream region. The surface buoyancy gradient and frontal dynamics are more pronounced in winter time linked to increased mixed layer instabilities.

Mixed layer instabilities are a key mechanism responsible for the seasonal variability of submesoscale kinetic energy (Mensa et al., 2013; Sasaki et al., 2014; Callies et al., 2015). Submesoscale turbulence exhibits pronounced seasonal variations, as illustrated by the intensification of surface buoyancy gradients during winter (Fig. I.6). For a given lateral buoyancy gradient, this increase in buoyancy gradients is usually linked to increasing available potential energy due to the deepening of the mixed layer. In contrast, mesoscale-driven frontogenesis does not exhibit a strong seasonal cycle, as it relies on the background strain field induced by the mesoscale eddy field. The mesoscale eddy field itself experiences only minor seasonal variations. However, recent research has demonstrated that the absorption of submesoscale mixed-layer eddies by the mesoscale eddy field may enhance the seasonal cycle at mesoscales (Schubert et al., 2020).

Next to mesoscale and submesoscale motions, a broad spectrum of high-frequency internal gravity waves coexists in the global ocean. The role of internal gravity waves for the oceanic energy budget and their potential in transferring energy to dissipative scales will be addressed in the following.

### I.1.3 The role of internal gravity waves

Internal gravity waves represent a considerable source of kinetic energy in a broad spectrum at frequencies higher than $f$ (Garrett and Munk, 1975; Cairns and Williams, 1976; Garrett and Munk, 1979). Globally, they play an important role in the redistribution of energy toward smaller scales through wave breaking and diapycnal mixing with implications for the global circulation and climate (Whalen et al., 2020). Three major mechanisms of internal wave generation exist: 1) Internal lee waves that form when the geostrophic flow interacts with the ocean topography (0.15-0.75 TW; Nikurashin and Ferrari, 2011; Melet et al., 2014). 2) Near-inertial waves through high-frequency wind stress forcing (0.3-1.4 TW; D'Asaro, 1985; D'Asaro et al., 1995; Jiang et al., 2005; Furuichi et al., 2008; Rimac et al., 2013; Alford, 2020). 3) Internal tides that form when barotropic tidal currents interact with the ocean bathymetry (0.7-1.3 TW; Munk, 1966; Munk and Wunsch, 1998; Egbert and Ray, 2001; Nycander, 2005; Garrett and Kunze, 2007). An illustrative chart is given in Fig. I.7 showing the energy input by currents, wind, and tides that drive internal wave motion in the ocean and fill the internal wave continuum through non-linear wave-wave, wave-topography, or wave-mean flow interactions.

Even though near-inertial waves contribute significantly to oceanic energy dissipation, they are mostly confined to the upper ocean, i.e. the mixed layer and the boundary layer. Internal lee waves represent an energy source in the deep ocean. However, their contribution to energy dissipation is rather low and remains uncertain. The consideration of internal tides as an important contribution to energy dissipation dates back to the 20th century when trying to link large-scale convective motions (i.e. the meridional overturning circulation) with deep ocean mixing processes. Munk and Wunsch (1998) concluded from the Sandström's theorem (Sandström, 1908):

> "*Without deep mixing, the ocean would turn, within a few thousand years, into a stagnant pool of cold salty water with equilibrium maintained locally by near-surface mixing and with very weak convectively driven surface-intensified circulation.*"

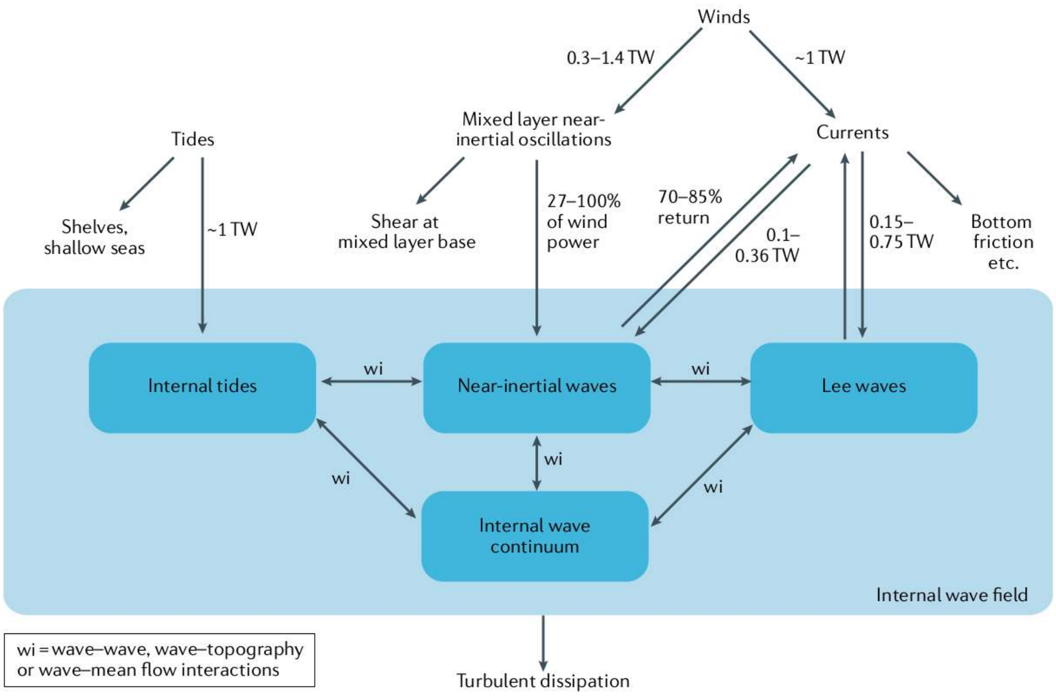

**Figure I.7:** From Whalen et al. (2020). Simplified schematic showing the energy input by currents, wind, and tides which drive internal wave motion in the ocean. Non-linear wave-wave, wave-topography, or wave-mean flow interactions fill the internal wave continuum at frequencies higher than $f$. At these scale, there is an irreversible cascade of energy toward three-dimensional turbulent dissipation.

Using a climatology database, Munk and Wunsch (1998) estimated that approximately 2 TW of energy is required in the deep ocean to maintain the abyssal stratification. The potential of tidal energy dissipation has been discussed as early as in Taylor (1920) and Jeffreys (1921). Even though, 3.5 TW was estimated to be available through the tidal energy input, dissipation associated with tidal motion was only linked to shallow and marginal seas. In the search for potential energy sources in the deep ocean, Munk and Wunsch (1998) and Egbert and Ray (2001) came to the conclusion that a fraction of 1 TW of the tidal energy input is available for mixing in the abyssal ocean in the form of internal tides accounting for approximately half of the estimated 2 TW needed for abyssal mixing. Thus, internal tides are an important source for diapycnal mixing away from lateral boundaries and the surface and play a key role in the closure of the global oceanic energy budget and the meridional overturning circulation (Melet et al., 2013; Kunze, 2017a,b).

The exact role of internal gravity waves, and specifically internal tides, in modulating energy pathways is far from being fully explored. Recent numerical experiments suggest that internal gravity waves can induce a geostrophic forward cascade given that wave energy is high relative to balanced energy (Fig. I.8, Thomas and Daniel, 2021). If wave energy is not significantly higher than balanced energy, energy pathway remain unchanged, i.e. balanced motion exhibits an inverse energy cascade (Fig. I.8a). However, in regions where wave motion is dominant, wave-balance energy exchanges can promote a forward flux of balanced energy by extracting energy from the geostrophically constrained flow making geostrophic energy available for dissipation (Fig. I.8b). A realistic high-resolution numerical model study using a twin configuration with and without tidal forcing is in partial agreement with the above findings (Ajayi, 2020). In the tidal run, the authors find an enhanced forward energy cascade, which is restricted to the summer months.

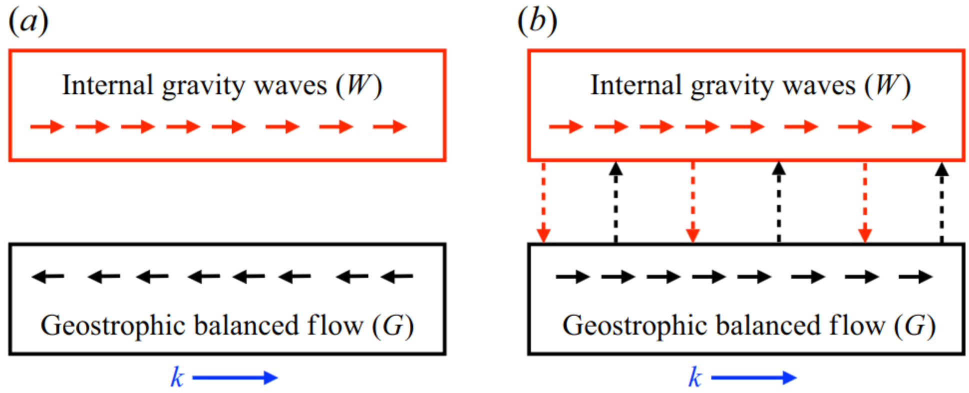

**Figure I.8:** From Thomas and Daniel (2021). Schematic showing turbulent energy flow pathway may be modulated by internal wave energy. The red and black boxes represent internal gravity wave and geostrophic flow, respectively. Wavenumber $k$ increases to the right (blue arrow). The inverse (forward) cascade shows in direction of decreasing (increasing) wavenumbers. **(a)** Energy pathways are unaltered, when wave energy is comparable with balanced energy, i.e. a forward cascade for internal gravity waves and an inverse cascade for the geostrophic flow. **(b)** Wave-balance energy (dashed arrows) reverse the direction of the geostrophic energy flux, i.e. from the inverse to a forward cascade enhancing geostrophic energy dissipation.

### I.1.4 Open questions

In conclusion, the oceanic energy cascade represents the interplay of numerous processes at different spatial and temporal scales while underlying different dynamics and constraints. To understand how climate equilibrium can be achieved in such a complex system, the role of the individual components on non-linear interactions and cross-scale energy exchanges have been presented. Even though we have a rather comprehensive view on the large-scale and balanced flow, many open questions remain for processes at higher wavenumbers, which are difficult to observe or model. Key questions include:

**Open questions**

**1**) How and to what extent do internal tides break the balanced flow constraints to promote a forward flux of energy to dissipative scales?

**2**) How do internal tides modify the length scale at which the inverse energy cascade transitions into a forward energy cascade? How does the transition scale vary regionally and seasonally?

## I.2 Internal tides

Internal tides as introduced in Sect. I.1.3 are internal gravity waves at tidal frequency. They are generated when the lunisolar barotropic or surface tide (of which the major five tidal constituents are the semidiurnal M2, S2, N2 and diurnal K1, O1) encounters and interacts with ocean bathymetric features such as oceanic ridges, continental slopes, shelf breaks, seamounts, etc., causing vertical displacements of density surfaces while radiating internal waves into the stably stratified water column (see Fig. I.9, Bell Jr, 1975; Baines, 1982). In the ocean interior, these vertical isoypcnal displacements $\eta$ are in the order of 10-100 m. At the surface, they are typically just a few centimeters.

As pointed out in the previous section, internal tides represent a crucial source for vertical mixing processes in the deep ocean both close the generation site (near-field) and toward the open ocean (far-field). The study of the internal tide life cycle, which encompasses their generation, dissipation, and propagation constitutes an active field of research. A comprehensive understanding of these processes, including their spatial and temporal variability, is essential for determining the extent to which internal tides and the associated irreversible turbulent mixing can influence the large-scale circulation and climate.

Observation efforts, such as the Hawaii Ocean Mixing Experiment (HOME, Fig. I.10) have largely contributed to the understanding of the tides-to-turbulence cascade (Rudnick et al., 2003; Klymak et al., 2006; Lee et al., 2006; Alford et al., 2007; Zhao et al., 2010). Particularly, it confirmed the energy conversion from the barotropic to the baroclinic tide. Early microstructure measurements and mooring observations have linked increased dissipation near rough topography with internal waves which in turn

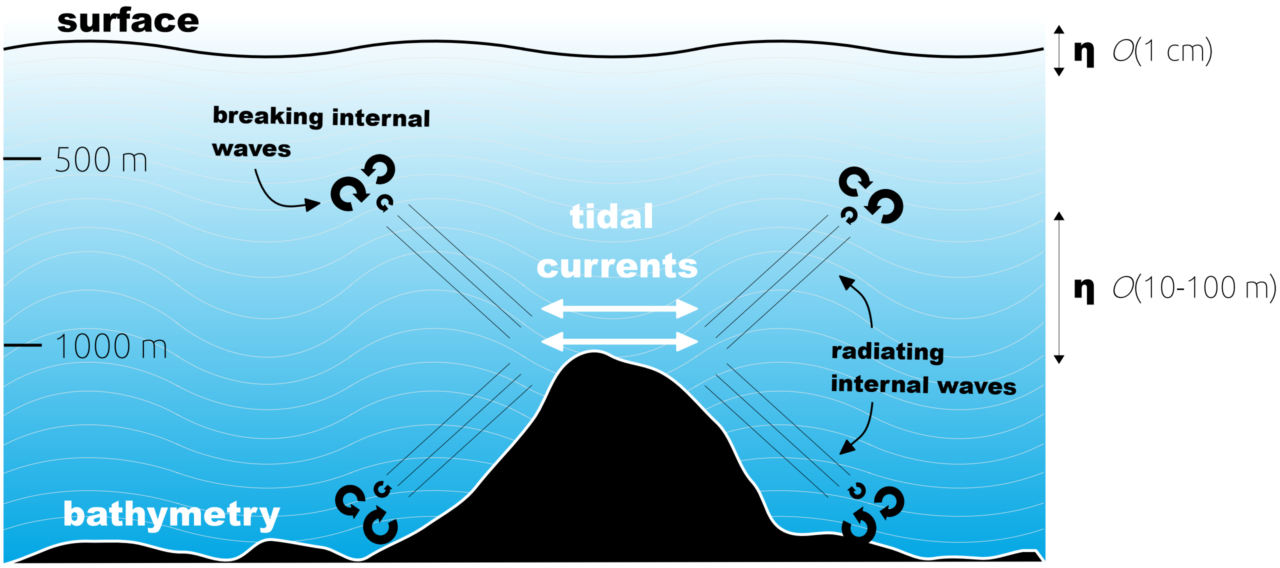

**Figure I.9:** Schematic of the periodically reversing barotropic tidal currents over bathymetry (e.g. oceanic ridge or seamount) while radiating internal waves (at tidal frequency) into the initially stably stratified ocean. Internal wave breaking occurs in the interior and deep parts of the ocean, particularly, away from any kind of boundaries. In the ocean interior, the internal tides can express in vertical isopycnal displacements $\eta$ of more than 100 m. At the surface, they express by not more than a few centimeters.

have their origin in the dissipation of the barotropic tide prominent bathymetric structures, e.g. oceanic ridges and seamounts (Lueck and Mudge, 1997; Polzin et al., 1997).

Over the years, in-situ platforms such as moorings have provided valuable information on generation, dissipation, and the overall life cycle of internal tides (Zilberman et al., 2011; Pickering et al., 2015; Ansong et al., 2017; Vic et al., 2018; Löb et al., 2020). They mostly provide excellent temporal resolution along with a sufficient resolution in vertical direction to resolve the wave's vertical structure. However, the scattered in-situ observations do not provide a global view. This is linked to the challenges in operational oceanography (e.g. operational costs and spatial coverage of field work). Even at regional scales, internal tide characteristics may strongly vary in space. More comprehensive measurements have been provided using autonomous underwater gliders, which were exploited in some studies to infer the spatio-temporal variability of internal-tide dynamics in dedicated areas (Rainville et al., 2013; Johnston et al., 2013, 2015; Johnston and Rudnick, 2015).

Internal tide characteristics, or more generally those of internal gravity waves can be deduced from the linearized equations of motion in a rotational framework and for a continuously stratified, incompressible, inviscid fluid allowing for small perturbations from the equilibrium state. The theory is recalled in the following before presenting recent efforts and challenges in observations and modeling.

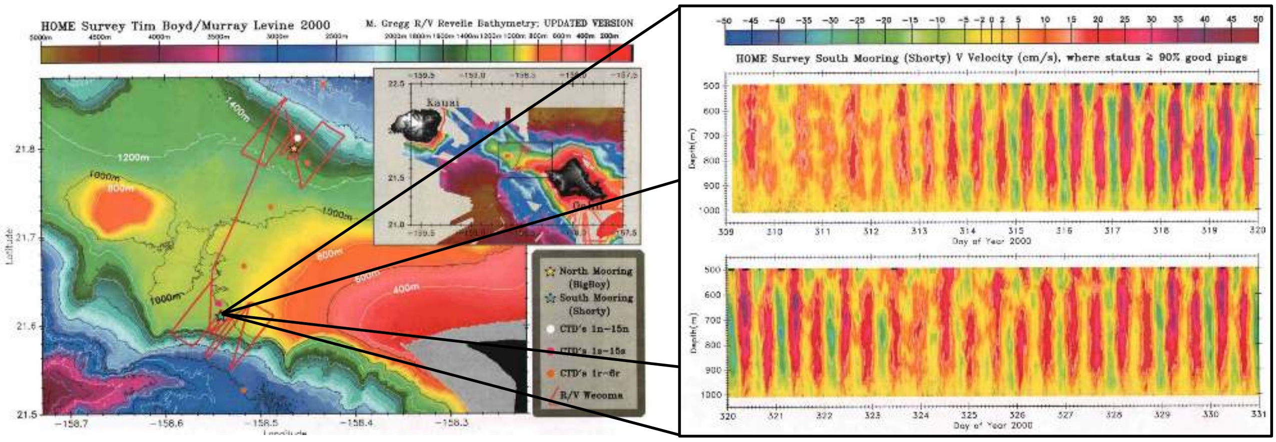

**Figure I.10:** Adapted from Boyd et al. (2002). The study/survey site for the Hawaii Ocean Mixing Experiment between Kauai and Oahu showing the bathymetry and the location of two moorings (North Mooring: yellow star; South Mooring: green star). The inset shows the time series of the northward velocity component as obtained from the South Mooring for a month of duration. Note the strong modulations at semidiurnal frequency.

## I.2.1 Internal tides as an internal gravity wave

### I.2.1.1 Dispersion relation

The linearized equations of motion for a rotating, continuously stratified, incompressible, and inviscid fluid, which allow for small perturbations from the equilibrium state are given below. They are composed of the continuity equation (I.2), the horizontal momentum equations (I.3), (I.4), the vertical momentum equation (I.5), and the density equation (I.6):

$$\frac{\partial u}{\partial x} + \frac{\partial v}{\partial y} + \frac{\partial w}{\partial z} = 0 \tag{I.2}$$

$$\frac{\partial u}{\partial t} - fv = -\frac{1}{\rho_0}\frac{\partial p'}{\partial x} \tag{I.3}$$

$$\frac{\partial v}{\partial t} - fu = -\frac{1}{\rho_0}\frac{\partial p'}{\partial y} \tag{I.4}$$

$$\frac{\partial w}{\partial t} = -\frac{1}{\rho_0}\frac{\partial p'}{\partial z} - \frac{1}{\rho_0}\rho' g \tag{I.5}$$

$$\frac{\partial \rho'}{\partial t} - \frac{\rho_0}{g}N^2 w = 0 \tag{I.6}$$

where $N^2 = -\frac{g}{\rho_0}\frac{d\rho_0}{dz}$ is the buoyancy frequency and $p'$, $\rho'$ are the perturbation pressure and density relative to a state of rest or mean state $\overline{p}$, $\overline{\rho}$, i.e. $p' = p - \overline{p}$, $\rho' = \rho - \overline{\rho}$. Note that $f$ is assumed to be constant. Combining the horizontal momentum equations $\frac{\partial}{\partial x}$(I.3), $\frac{\partial}{\partial y}$(I.4) with the continuity equation $\frac{\partial}{\partial t}$(I.2) yields:

$$\frac{\partial^2 w}{\partial z \partial t} + f\zeta = \frac{1}{\rho_0}\nabla_h^2 p' \tag{I.7}$$

where $\zeta = \frac{\partial v}{\partial x} - \frac{\partial u}{\partial y}$ is the vertical vorticity and $\nabla_h^2 = \frac{\partial^2}{\partial x} + \frac{\partial^2}{\partial y}$ the second-order horizontal gradient operator. Equation (I.7) describes the relation between horizontal divergence and the perturbation pressures.

Taking the curl of the horizontal momentum equations $\frac{\partial}{\partial y}$(I.3) and $\frac{\partial}{\partial x}$(I.4), together with Equation I.2 gives:

$$\frac{\partial \zeta}{\partial t} - f\frac{\partial w}{\partial z} = 0 \tag{I.8}$$

Combining I.8 with I.7 gives us the relation between vertical vorticity and pressure perturbation:

$$\frac{\partial^2 \zeta}{\partial t^2} + f^2\zeta = \frac{f}{\rho_0}\nabla_h^2 p' \tag{I.9}$$

Together with Equation I.8, this can be rewritten to:

$$(\frac{\partial^2}{\partial t^2} + f^2)\frac{\partial w}{\partial z} = \frac{1}{\rho_0}\frac{\partial}{\partial t}\nabla_h^2 p' \tag{I.10}$$

For the following, we need another equation that relates vertical velocity $w$ with the perturbation pressure $p'$. It is achieved by eliminating the perturbation density $\rho'$, i.e. combining $\frac{\partial}{\partial t}$(I.5) with (I.6):

$$\frac{\partial^2 w}{\partial t^2} + N^2 w = -\frac{1}{\rho_0}\frac{\partial^2 p'}{\partial z \partial t} \tag{I.11}$$

This equation represents the relation between vertical motion and the perturbation pressure $p'$. Eliminate the perturbation pressure $p'$ between (I.10) and (I.11) to come up with an equation for the vertical velocity alone:

$$\frac{\partial^2}{\partial t^2}(\nabla_h^2 w + \frac{\partial^2 w}{\partial z^2}) + f^2\frac{\partial^2 w}{\partial z^2} + N^2\nabla_h^2 w = 0 \tag{I.12}$$

Note, that the Boussinesq approximation is applied, i.e. $\frac{1}{\rho_0}\frac{\partial}{\partial z}(\rho_0\frac{\partial}{\partial z})w = \frac{\partial^2 w}{\partial z^2}$. Solve (I.12) using the Ansatz $w = w_0 \exp\{i(kx + ly + mz - \omega t)\}$. Assuming uniform buoyancy, we obtain the dispersion relation for internal gravity waves in a rotating fluid:

$$\omega^2 = \frac{f^2m^2 + N^2(k^2 + l^2)}{k^2 + l^2 + m^2} \tag{I.13}$$

where $w$ is the wave frequency and $k$, $l$, $m$ are the zonal, meridional, and vertical wavenumber that make up the wavenumber vector $\vec{k}$. In polar coordinates, (I.13) expresses by:

$$\omega^2 = f^2 \sin^2\varphi + N^2\cos^2\varphi, \tag{I.14}$$

where $\varphi$ is the phase angle, which describes the orientation of the wavefront with respect to the horizontal plane. We learn the following from this: 1) The wave frequency $\omega$ is only a function of $\varphi$, i.e. it is independent of the magnitude of the wavenumber vector. 2) The wave frequency $w$ is bounded by the Coriolis frequency $f$ and the buoyancy frequency $N$.

An important feature of internal gravity waves (including internal tides) is the vertical propagation of energy as shown by the tank experiment applying shadowgraphs (or Schlieren techniques) in Fig. I.11. Created by density perturbations, small amplitude waves are visible from the constant lines of phase, i.e. the wave crest (or wave front). Energy propagation happens to be radially upward, i.e. in the direction of the group velocity. Particularly, energy propagation is perpendicular to the wavenumber vector

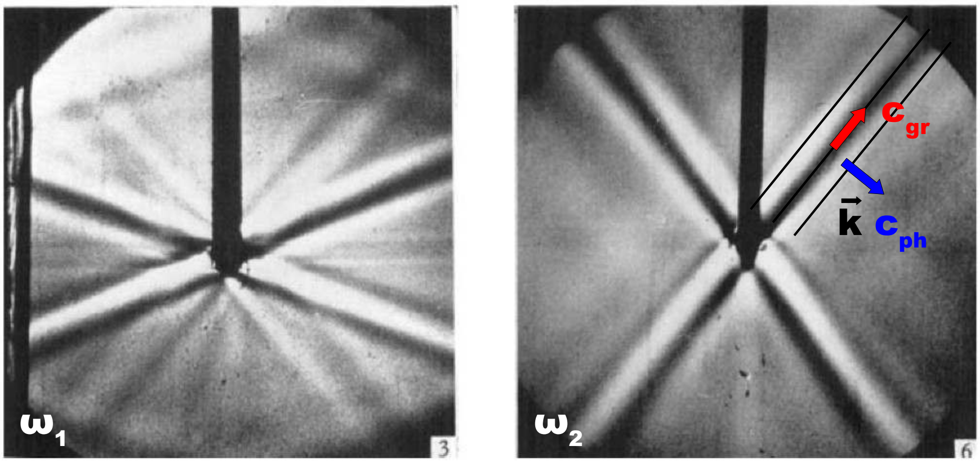

**Figure I.11:** Adapted from Mowbray and Rarity (1967). Tank experiment applying shadowgraphs (or Schlieren techniques) that reveal internal wave patterns away from a vibrating cylinder for two different frequencies ($\omega_1$ and $\omega_2$). The internal waves propagate outward (dark lines) creating a wave crest (or wave front). The direction of energy propgation (group velocity $c_{gr}$) and phase propagation (phase speed, $c_{ph}$) including the wavenumber vector $\vec{k}$ are given. In particular, phase propagation is perpendicular to group velocity.

$\vec{k}$ and the phase propagation. The angle of the energy beam depends only on the frequency, i.e. the fixed frequency of the vibrating cylinder which is the point source of the outward propagating waves.

#### I.2.1.2 Vertical eigenmodes

The vertical structure and dynamical behaviour of internal gravity waves are often described using vertical eigenmodes. The idea of vertical eigenmodes underlies the fact that the vertical structure of the ocean can be expressed by a sum of normal modes, i.e. barotropic and baroclinic modes, assuming a separation of variables in the form of:

$$[u(x,y,z,t),(x,y,z,t),p(x,y,z,t)] = [\widetilde{u}_n(x,y,t),\widetilde{v}_n(x,y,t),\widetilde{p}_n(x,y,t)]\phi_n(z) \tag{I.15}$$

$$w(x,y,z,t) = \widetilde{w}_n(x,y,t)\Phi_n(z) \tag{I.16}$$

for vertical mode number $n$, where $\phi$ describes the vertical structure function for horizontal velocity velocity and pressure and $\Phi$ describes the vertical structure function of vertical velocity for (Kundu et al., 2015). Each vertical mode has a fixed vertical structure and behaves in the horizontal dimension (and in time) the same way as a homogeneous fluid obeying a free surface (Gill, 1982).

Let us consider the governing equations of motion as in Equations I.2 - I.6, but for the non-rotating case. Also, the hydrostatic approximation is applied, i.e.:

$$\frac{\partial u}{\partial x} + \frac{\partial v}{\partial y} + \frac{\partial w}{\partial z} = 0 \tag{I.17}$$

$$\frac{\partial u}{\partial t} = -\frac{1}{\rho_0}\frac{\partial p'}{\partial x} \tag{I.18}$$

$$\frac{\partial v}{\partial t} = -\frac{1}{\rho_0}\frac{\partial p'}{\partial y} \tag{I.19}$$

$$\frac{\partial p'}{\partial z} = -\rho' g \tag{I.20}$$

$$\frac{\partial \rho'}{\partial t} - \frac{\rho_0}{g}N^2 w = 0 \tag{I.21}$$

Eliminating $u$ and $v$ via and combining Equations (I.17), (I.20), and (I.21) gives us two equations that relate $w$ and $p$:

$$\rho_0 \frac{\partial^2 w}{\partial t \partial z} = (\frac{\partial^2}{\partial x^2} + \frac{\partial^2}{\partial y^2})p' \tag{I.22}$$

$$N^2 w = -\frac{1}{\rho_0}\frac{\partial^2 p'}{\partial t \partial z} \tag{I.23}$$

The solution of these two equations are determined by the separation of variables applied to $w$ and $p'$, i.e.:

$$p' = \widetilde{p}_n(x,y,t)\phi_n(z) \tag{I.24}$$

$$w = \widetilde{w}_n(x,y,t)\Phi_n(z) \tag{I.25}$$

Inserting these solutions in I.22 and I.23 gives:

$$\rho_0 \frac{\partial \widetilde{w}_n}{\partial t}\frac{\partial \Phi_n(z)}{\partial z} = \left(\frac{\partial^2}{\partial x^2} + \frac{\partial^2}{\partial y^2}\right)\widetilde{p}_n \phi_n(z) \tag{I.26}$$

$$N^2 \widetilde{w}_n \Phi_n(z) = -\frac{1}{\rho_0}\frac{\partial \widetilde{p}_n}{\partial t}\frac{\partial \phi_n(z)}{\partial z} \tag{I.27}$$

The separation of variables is satisfied by the following two equations:

$$\frac{1}{\rho_0}\phi_n(z) = c_n^2 \frac{d\Phi_n(z)}{dz} \tag{I.28}$$

$$\frac{1}{\rho_0}\frac{d\phi_n(z)}{dz} = -N^2 \Phi_n(z) \tag{I.29}$$

where $c_n$ is a separation constant. Note that the wave equation results from this when inserting the expression $\frac{d\Phi_n(z)}{dz}$ from I.28 in I.26 while applying the Boussinesq approximation, i.e.:

$$\frac{\partial^2 \widetilde{p}_n}{\partial t^2} = c_n^2 \left(\frac{\partial^2}{\partial x^2} + \frac{\partial^2}{\partial y^2}\right)\widetilde{p}_n \tag{I.30}$$

where $\widetilde{w}_n = \frac{\partial \widetilde{p}_n}{\partial t}$. Equations (I.28) and (I.29) can be reduced to a single equation, i.e. one for $\phi_n(z)$ and one for $\Phi_n(z)$ as follows:

$$\frac{d}{dz}\left(\frac{1}{N^2}\frac{d\phi_n(z)}{dz}\right) + \frac{1}{c_n^2}\phi_n(z) = 0 \tag{I.31}$$

$$\frac{d^2\Phi_n(z)}{dz^2} + \frac{N^2}{c_n^2}\Phi_n(z) = 0 \tag{I.32}$$

Note that also here the Boussinesq approximation is applied. These equations form the Sturm-Liouville problem with the following boundary conditions obeying a flat bottom and a linearized free surface:

$$\Phi_n = \frac{c_n^2}{g}\frac{d\Phi_n(z)}{dz} \quad \text{and} \quad \frac{d\phi_n(z)}{dz} = -\frac{N^2}{g}\phi_n(z) \quad \text{at } z = 0 \tag{I.33}$$

$$\Phi_n(z) = 0 \quad \text{and} \quad \frac{d\phi_n(z)}{dz} = 0 \quad \text{at } z = -H \tag{I.34}$$

The horizontal/pressure modes are related to the vertical velocity modes via $\phi_n(z) = \frac{\partial \Phi_n(z)}{\partial z}$. In the continuously stratified case, there is an infinite number of eigenvalues $c_n$ and corresponding eigenfunctions $\phi_n(z)$ and $\Phi_n(z)$. The lowest mode ($n = 0$) refers to the barotropic mode, whereas $n \geq 1$ refers to the baroclinic modes. For the special case $n = 0$, $c_n$ is only a function of depth and can be approximated by $c_0 = \sqrt{gH}$. The barotropic mode acts usually on basin scales. For the baroclinic modes ($n \geq 1$), the eigenspeed $c_n$ is inversely proportional to $n$, i.e. the wave's group velocity $c_{gr}$ is given by:

$$c_{gr} = \frac{(\omega^2 - f^2)^{1/2}}{\omega} c_n. \tag{I.35}$$

Further, baroclinic internal gravity waves are associated with smaller horizontal wavelengths $\lambda_n$ with increasing mode number:

$$\lambda_n = \frac{2\pi}{\left(\frac{\omega^2 - f^2}{c_n^2}\right)^{1/2}} \tag{I.36}$$

where $\omega$ is the wave frequency. Briefly, low vertical modes have typical wavelengths of $O$(100 km) and can propagate over large distances. High vertical modes have typical wavelengths down to $O$(1-10 km), and do not propagate far away from their generation site due to their lower group velocity and higher vertical shear (Arbic et al., 2018). From this, important conclusions can be drawn on the horizontal and vertical scales of internal tides as well as their fate away from the generation site in propagation direction.

### I.2.2 Internal tides as an internal gravity wave forced by the barotropic tide and topography

The transfer of energy from the barotropic to the baroclinic tide can be estimated by considering the simplified barotropic and baroclinic energy equations omitting the tendency term and non-linear advection (Simmons et al., 2004; Carter et al., 2008).

$$\boldsymbol{\nabla}_h \cdot \boldsymbol{F}_{bt} + D_{bt} + C = 0, \tag{I.37}$$

$$\boldsymbol{\nabla}_h \cdot \boldsymbol{F}_{bc} + D_{bc} - C = 0, \tag{I.38}$$

where $\boldsymbol{\nabla}_h \cdot \boldsymbol{F}$ is the energy flux divergence with $\boldsymbol{\nabla}_h = (\partial/\partial x, \partial/\partial y)$ the horizontal gradient operator and $\boldsymbol{F} = (F_x, F_y)$ the energy flux vector, $D$ the energy dissipation, and $C$ the barotropic-to-baroclinic conversion term. The subscripts $_{bt}$ and $_{bc}$ stand for the barotropic and baroclinic tide. In the barotropic energy equation, the conversion is considered a sink of energy, whereas it is an energy source in the baroclinic energy equation. The barotropic-to-baroclinic conversion is defined as:

$$C = \boldsymbol{\nabla}_h H \langle \boldsymbol{u}_{bt}\, p_{bc}(-H) \rangle, \tag{I.39}$$

where $H$ is the bathymetry, $\boldsymbol{u}_{bt} = (u_{bt}, v_{bt})$ the barotropic tidal velocity vector, and $p_{bc}$ the baroclinic tidal pressure at the ocean bottom ($-H$). $\langle\rangle$ denotes the average over a tidal cycle.

The nature of the bathymetric features is believed to play a significant role in the modal content of internal tides. Specifically, tall and steep slopes, like continental slopes, tend to give rise to low-mode internal tides. Conversely, higher modes are favored for a deeper and flatter ocean bottom, though with small-scale bathymetric properties (Laurent and Garrett, 2002; Laurent et al., 2003). An important quantity to describe the character of the sea floor topography is the ratio $\alpha = \gamma/s$ of the seafloor topographic slope ($\gamma = dh/dx$) to the wave ray-path slope $s$. The latter is defined as:

$$s = \sqrt{\frac{\omega^2 - f^2}{N^2 - \omega^2}}, \tag{I.40}$$

where $N$ is taken from near the ocean bottom. Using the definition from de Lavergne et al. (2019), the seafloor can be classified as subcritical ($\alpha < 0.8s$), critical ($0.8s \leq \alpha \leq 1.5s$), and supercritical ($\alpha > 1.5s$).

Internal tide generation and its associated spatial variability is relatively well documented in literature (Garrett and Kunze, 2007). It depends primarily on bottom topography, stratification, and barotropic tidal currents. The fate of the tidal beam depends ultimately on the ratio $\alpha$ of seafloor topographic slope $\gamma$ to the wave ray-path slope $s$. The schematic in Fig. I.12 illustrates the fate of an internal tide beam depending on the slope's criticality. A subcritical slope will cause the beam to reflect forward before it may either shoal on the continental shelf or reflect backward as it encounters a supercritical slopes. A beam impinging on a critical slope will dissipate along the slope through the energy transfer to very high modes and boundary turbulence. Supercritical slopes cause a backward reflection as already indicated above.

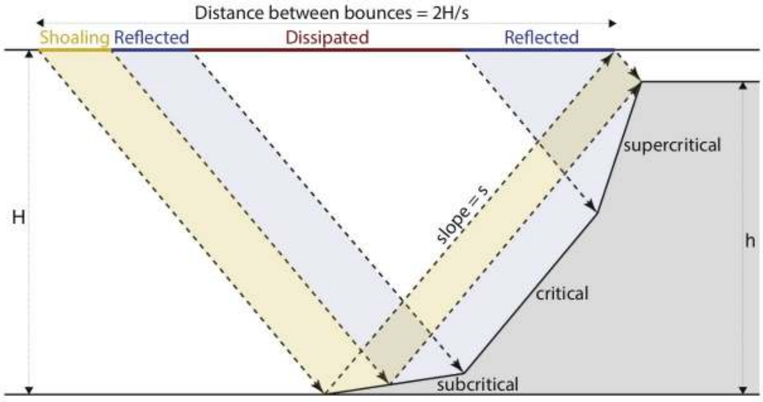

**Figure I.12:** From de Lavergne et al. (2019). Schematic illustrating the forward reflection (shoaling), dissipation, backward reflection of an impinging tidal beam on a subcritical, critical, and supercritical slopes, respectively.

### I.2.3 Generation: a first insight from semi-analytical theory

Semi-analytical modeling provided first insight into internal tide generation on global scales, partitioned into the vertical mode structure (Smith and Young, 2002; Nycander, 2005; Pétrélis et al., 2006; de Lavergne et al., 2019; Vic et al., 2019). These model require only only three key ingredients as stated above: bottom topography, climatological stratification, and barotropic tidal currents (see Equation I.39) allowing for a computationally efficient way to quantify global internal tide generation.

The barotropic-to-baroclinic energy conversion for the M2 tide is shown in Fig. I.13, highlighting internal tide generation hot spots over mid-ocean ridges, seamounts, and continental shelves (Fig I.13a). The dominant mode 1 accounts for 29 % of the total M2 tidal energy conversion (Fig. I.13b). Though, considering a total of 50 modes,

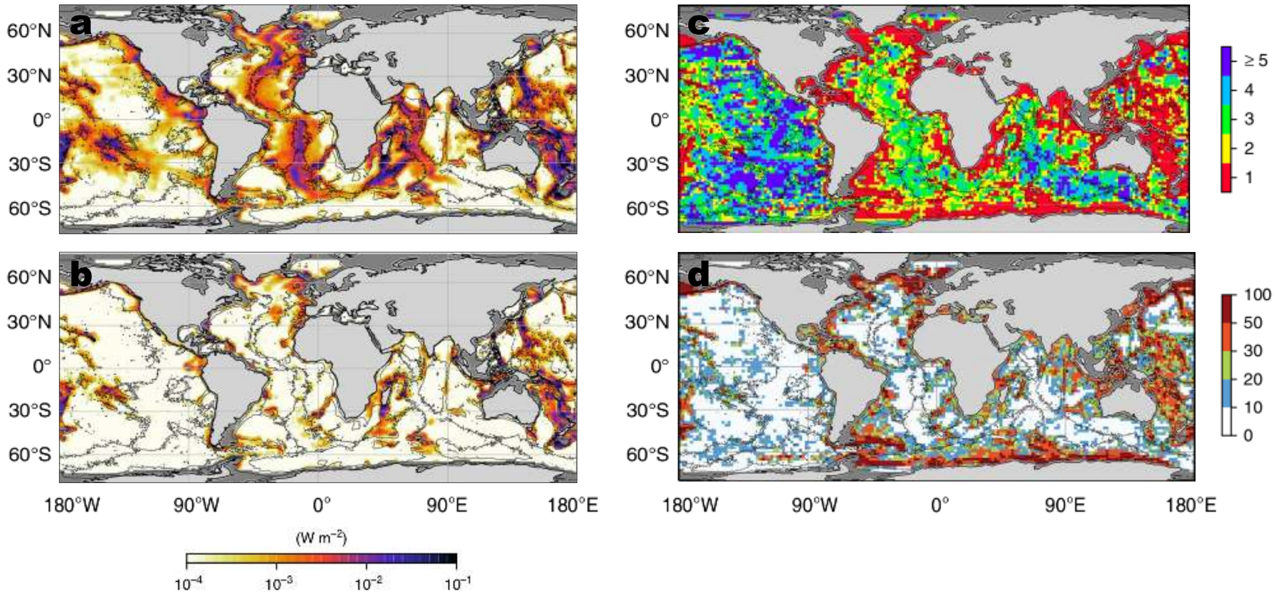

**Figure I.13:** Adapted from Vic et al. (2019). **(a)** Barotropic-to-baroclinic M2 tide energy conversion from the semi-analytical model. **(b)** Same as **(a)** but barotropic-to-baroclinic tide energy conversion into mode 1. **(c)** Most energetic mode, i.e. the mode associated with maximum M2 energy conversion and **(d)** ratio (%) of mode 1 and total M2 energy conversion.

Vic et al. (2019) pointed out that the bulk of energy is associated with modes higher than 1. The vertical mode structure is highly variable in space. Modes higher than 1 seem to govern at the Mid-Atlantic Ridge as well as the Indian and East Pacific basin. In contrast, continental shelves and the West Pacific (namely the Indonesian Seas, the Philippine Sea, and the Coral Sea) are dominated by mode 1 (Fig. I.13c), which explains comprehensively 30 % and locally 50-100 % of the total conversion (Fig. I.13d).

The major drawback of semi-analytical models is that tidal conversion is not valid in regions with bathymetric slopes equal to or larger than the internal tide wave slopes, i.e. critical and supercritical slopes, respectively. Further, tidal conversion in shallow waters are often neglected. This has two reasons. First, stratification in the upper layers is enhanced leading to an increase of critical to supercritical slopes through the wave ray-path slope relationship (Equation I.40). Second, the assumption of horizontal tidal excursion being smaller than the horizontal topographic scale is violated due to elevated barotropic velocities on continental slopes and at shelf breaks. The violation of linear theory may feature unrealistic values, i.e. conversion larger than energy lost by the barotropic tide. Therefore, the products from Falahat et al. (2014) and Vic et al. (2019) discard energy conversion in the upper 400 m and 700 m respectively before applying a correction to account for some part of missing conversion in shallow waters.

### I.2.4 Dissipation: a first insight from semi-analytical theory

Internal tides contribute to vertical mixing and energy dissipation both in the near- and far-field. An important quantity to measure local internal tide dissipation is the parameter $q$. It describes the fraction of locally dissipated tidal energy to local barotropic-to-baroclinic tidal energy conversion providing insight into the fate of the

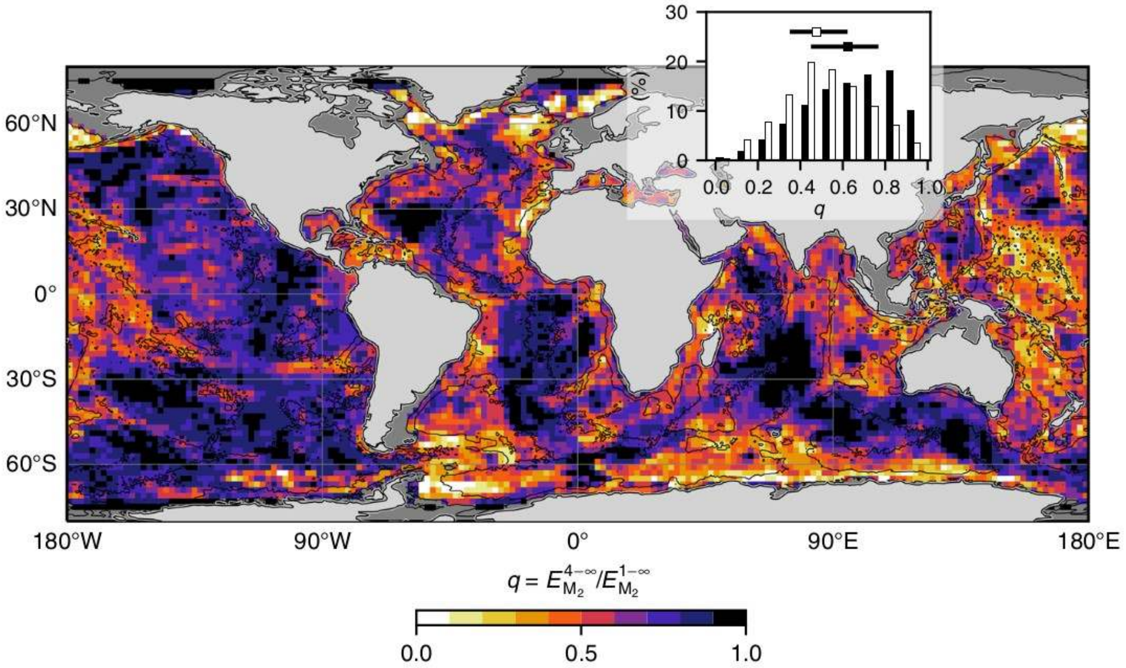

**Figure I.14:** From Vic et al. (2019). Spatial map of the fraction $q$ of locally dissipated tidal energy to local barotropic-to-baroclinic tidal energy conversion for the M2 tide. The inset histogram represents the seafloor area (black) and the energy conversion (white) binned as a function of $q$. Error bars indicate the 25th and 75th percentiles.

internal tide. Generally, topographic properties influence the modal content and, thus, set the conditions for either near-field dissipation by high-mode internal tides or the far-field propagation of baroclinic energy by low-mode internal tides.

Using semi-analytical theory, it has been shown on global scales that tidal mixing in the near-field dominates ($>$50 %) over tidal mixing in the far-field highlighting the importance for high-vertical mode mixing processes (Vic et al., 2019). Further, near-field tidal mixing is highly variable in geographical space as shown in Fig. I.14. The fraction $q$ may vary between 0.45 and 0.77 (25th and 75th percentile). The fraction of locally dissipated energy may reach 0.8-1, especially where higher modes dominate (Mid-Atlantic Ridge, the Indian Ocean Basin, and the East Pacific). It is generally lower where mode 1 dominates (0.3-0.5, continental shelves and the West Pacific). Further drivers that drive near-field tidal energy dissipation include interactions with remotely generated internal tides, internal tide resonance due to adjacent ridges, and topographically trapped internal waves at latitudes where the internal tide becomes subinertial ($>$30° for the diurnal tide and $>$74.5° for the semidiurnal tide).

While the fate of higher vertical modes is relatively well understood, the energy sinks of low-vertical mode tidal energy, which can travel over large distance in the order of $O$(100-1000 km), is an ongoing research topic. Three potential sinks have been considered in literature: nonlinear wave-wave interactions, scattering by abyssal hills, and interactions with topographic slopes (Garrett and Kunze, 2007; de Lavergne et al., 2019). The major driver for low-mode (mode 1) energy dissipation may be linked to ocean topography as found by (Kelly et al., 2013). Specifically, this concerns the interaction of low-mode tidal beam with the topographic slope of continental shelves, mid-ocean ridges, and seamounts.

de Lavergne et al. (2019) have shown at global scales that low-mode internal tides dissipate due to shoaling at shelf breaks and shoreward, at critical slopes around most of the ocean's perimeter as well as ridge crests, fractures, or seamounts. In the meanwhile, continental slopes are subject to supercritical reflection implying that much of the impinging low-mode internal tide is reflected backward to the open ocean. Quantitatively, shoaling and dissipation at critical slopes account globally for the mode-1 M2 internal tide 18 % and 29 %, respectively. An additional energy sink for low-mode internal tides linked to topography is scattering to higher modes by abyssal hills or small-scale seafloor roughness (19 %). Non-linear wave-wave interactions for mode 1 are estimated at 26 %. Non-linear wave-wave interactions gain in importance with increasing mode number. When summing over the modes 1-5, they make up over 60 % of the low-mode tidal energy dissipation, whereas shoaling, critical slopes, and scattering together contribute by only 34 % (compared to 66 % for mode 1; de Lavergne et al., 2019, 2020).

Information obtained from semi-analytical theory on internal tide dissipation is crucial for the parameterization of unresolved sub-grid scale physics in coarse-resolution ocean and climate models such as tidal energy dissipation through wave breaking. Traditionally, a fraction of $q$=1/3 was assumed in the vicinity of internal tide generation sites, bottom-intensified and prescribed to decay exponentially with height above the sea floor (St. Laurent et al., 2002). Assuming a spatially independent parameterization for tidal mixing is highly simplistic and has implications on climate scales as pointed out by Melet et al. (2016), highlighting the need for robust and geographically dependent parameterizations as developed by Vic et al. (2019); de Lavergne et al. (2020).

### I.2.5 Coherent and incoherent propagation

In regions where low-mode internal tides dynamics dominate, the associated baroclinic energy is barely affected by near-field wave breaking and manages to travel over long distances at scales $O$(100-1000 km) (Dushaw et al., 1995; Ray and Cartwright, 2001; Zhao et al., 2010). Internal tide propagation was commonly assumed to a large extent to be coherent, that is to say, maintaining its consistent structure or pattern in amplitude and phase while being well-predictable in time space and space as it is phase-locked to the astronomical tide forcing. As the internal tide propagates, it may lose its coherence or its stationarity with increasing distance to the generation site (Rainville and Pinkel, 2006; Zhao et al., 2010). Any departure from coherence is referred to tidal incoherence or non-stationarity. Specifically, the incoherent or non-stationary internal tide distinguishes from the coherent internal tide mainly by its unpredictability, i.e. temporal variations of amplitude and phase within the tidal frequency band.

#### I.2.5.1 Satellite altimetry observations

Satellite altimetry has proven to be a crucial platform for observing the SSH signature of internal tides, overcoming the previous limitations in spatial coverage linked to in-situ observations. It does so by making use of the internal tides' SSH imprint $O(1\text{ cm})$. The challenge of observing internal tides from space was for a long time limited by the coarse sampling in space and time associated with the satellite ground tracks. Particularly, the satellites' long revisit time caused the aliasing of high-frequency motion, i.e. internal tides, into low-frequency motion. Today, the community has an over 20-year-long record of sea surface height observations at its disposal, which allows for the clean separation of tidal constituents. Global mapping techniques have been developed in recent years that came up with a coherent internal-tide solution.

The extraction of internal tides from sea surface height (SSH) measurements combines methodologies from several studies. Initially, Ray and Zaron (2016) employed point-wise harmonic analysis, along with a high-pass filter to remove non-tidal noise, mapping the filtered data onto a regular grid. Zhao et al. (2016) introduced a plane wave fitting technique, determining internal tide amplitude, phase, and direction by fitting plane waves to SSH data within specific windows. The work done by Zaron

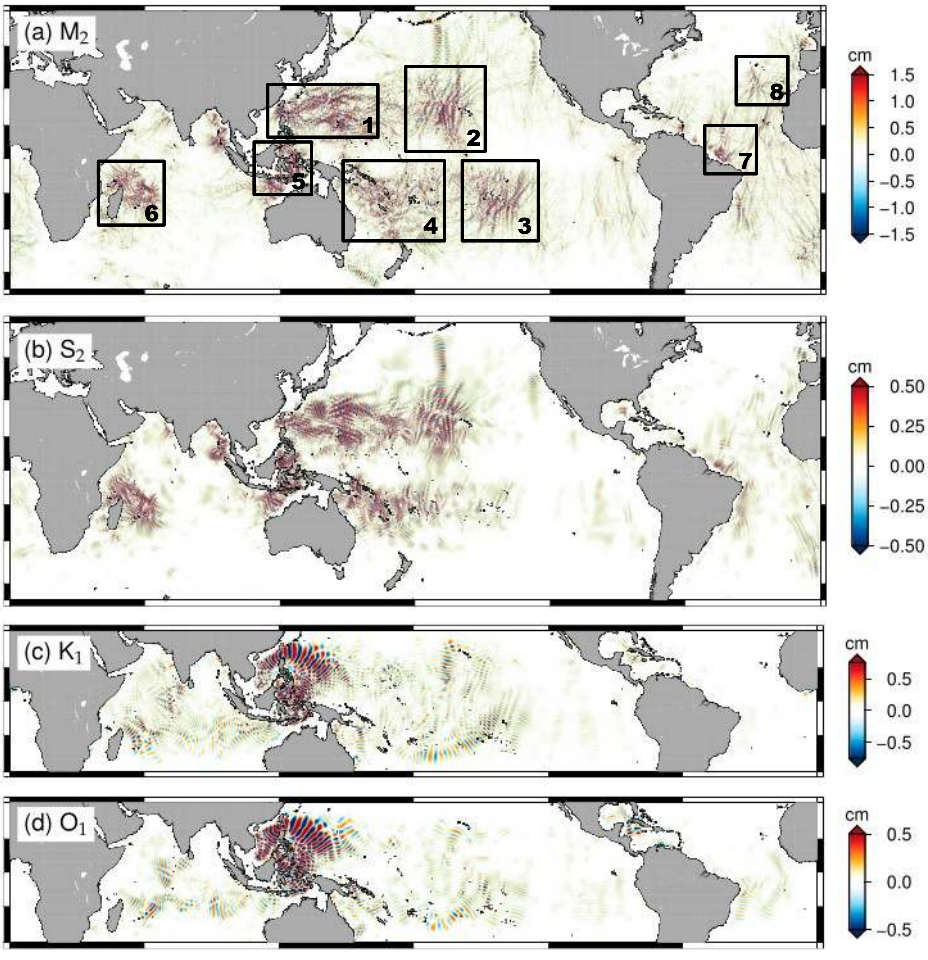

**Figure I.15:** Adapted from Zaron (2019). Coherent **(a)** M2, **(b)**, S2, **(c)** K1, and **(d)** O1 internal tide SSH signature. Note the different colorbar scales. The domains are bounded to the north and south by the critical latitude, i.e the latitude where the inertial frequency equals the tidal frequency. The major hot spots of (M2) internal tide generation are highlighted and number 1-8. 1: Luzon Strait; 2; Hawaii; 3: French Polynesia; 4: Southwestern Tropical Pacific/Coral Sea; 5: Indonesian Seas; 6: Madagascar; 7: Amazonian Shelf Break; 8: Mid-Atlantic-Ridge south of the Azores.

(2019) can be understood as an upgrade to the previous products from Ray and Zaron (2016) and Zhao et al. (2016). Most importantly, it is purely empirical, i.e. it does not require dynamical hypothesis such as linear dynamics, spatial coherence, or the usage of a dispersion relation for internal waves at tidal frequency. What sets the High-Resolution Empirical Tide (HRET) model from Zaron (2019) apart is their use of weighted least squares fitting to obtain coefficients for constructing a second-order polynomial instead of sticking to simple plane waves, modulating the amplitude envelope of all wave components across the $x$ and $y$ directions. For a more comprehensive description and comparison of available empirical models as well as assimilative and hydrodynamic models, the reader is referred to Carrere et al. (2021).

Global estimates from HRET of the coherent M2, S2, K1, O1 internal tides are obtained through the application of the above methodology on overlapping patches, which are finally blended and smoothly interpolated to a regular grid (Fig. I.15). Note the different colorbar scales. Internal tides are ubiquitous in the global ocean. The M2 internal tide is clearly dominant. The major internal tide generations hot spots can be deduced from this: the Luzon Strait, the Hawaiian Islands, French Polynesia, the Southwestern Tropical Pacific, the Indonesian Seas, Madagascar, and the Amazonian shelf break to name a few. From this it appears that energetic tidal beams that propagate from their generation site through the ocean basins over hundreds to thousands of km distance are confined to the following hot spot regions: the Luzon Strait, the Hawaiian Islands, French Polynesia, the Southwestern Tropical Pacific (Coral Sea), the Indonesian Seas, Madagascar, the Amazonian shelf break, and the Mid-Atlantic-Ridge south of the Azores Island.

Satellite altimetry is primarily used to extract the coherent internal tide SSH. The incoherent internal tide is difficult to detect using satellite altimetry due to the following challenges. On the one hand, the applied mapping methodologies and the underlying frequency analyses rely on the extraction of consistent periodic variations. On the other hand, tidal incoherence is generally elevated in regions with mesoscale activity, where non-tidal variance at the tidal alias frequencies make the extraction of tidal signals less accurate (Ray and Zaron, 2011). Moreover, it is assumed that sea surface height is primarily representative for the first baroclinic mode which is associated with the coherent internal tide. The incoherent tide, in turn, is usually associated with higher modes. In other words, sea surface height acts as a "high-mode filter", making the detection of incoherent tides a more difficult task. (Ray and Zaron, 2011; Hendershott, 1981). Despite these challenges, Zaron (2017) attempted to extract the incoherent internal tide SSH using satellite altimetry in the along-track wavenumber domain to provide global estimates of incoherent variance. Briefly, the methodology is based on subtracting the coherent internal tide (obtained through conventional harmonic analysis) from the total tide. An empirical model is then applied to the residual SSH wavenumber spectrum to extract the variance around mode-1 wavenumbers, which remains in the signal and which is associated with the incoherent tide.

The global estimates of the incoherent tide from this analysis is shown in Fig. I.16. It reveals elevated variance in some of the major internal tide generation sites as known from Fig. I.15 (e.g. Luzon Strait, Hawaii, Madagascar, Southwestern Tropical

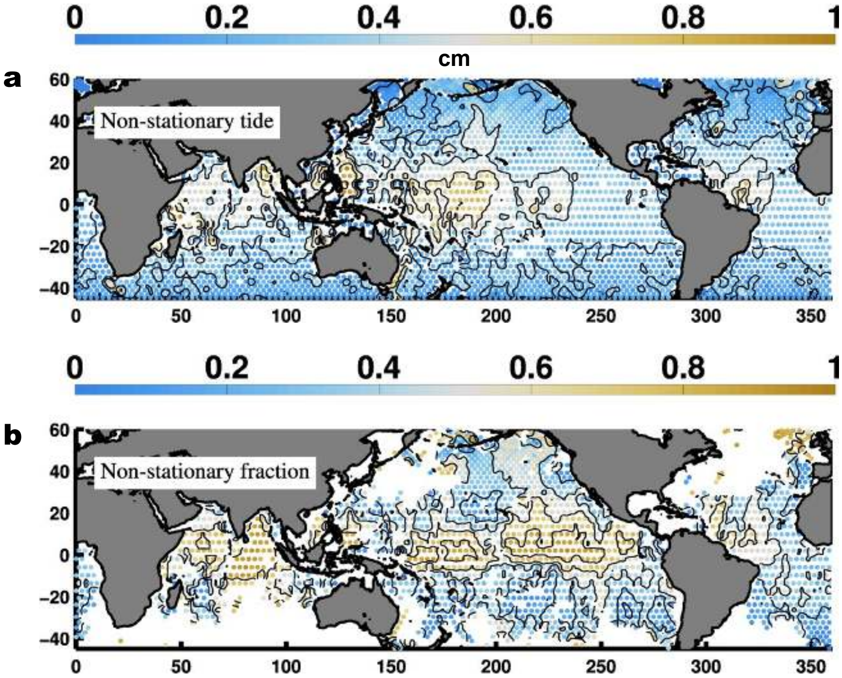

**Figure I.16:** Adapted from Zaron (2017). **(a)** Variability (root mean square) of the incoherent internal tide representative for the semidiurnal frequency band. It is estimated from the along-track sea surface height wavenumber spectra. **(b)** The incoherent fraction of the mode-1 semidiurnal internal tide variance. Areas are blanked where the standard error estimate of the M2 harmonic constant is twice as large as the total semidiurnal band baroclinic tidal standard error.

Pacific, Amazonian Shelf Break). The incoherent internal tide may represent a large fraction of the total tide. This is especially true in the equatorial regions (80-100 %, Fig. I.16b). Poleward, the fraction diminishes, but it still explains >30 % of the signal.

Applications of the above products could lie inter alia in the removal or correction of the baroclinic SSH internal tide signature in satellite altimetry measurements to access the SSH signature associated with mesoscale and submesoscale motions. Though, an incoherent fraction will remain in the signal. Applications can also be found for in-situ observations in order to spatially classify the mostly very local measurements. Finally, these data set can prove valuable for validating internal tide SSH in ocean general circulation models that include tidal forcing (Carrere et al., 2021).

#### I.2.5.2 Realistic numerical modeling

Realistic numerical modeling has largely contributed to our understanding of internal-tide dynamics by overcoming the disadvantages associated with in-situ observations and satellite altimetry. The HYbrid Coordinate Ocean Model (HYCOM) is considered the first realistic, three-dimensional global model with both tidal and atmospheric forcing. Early validation efforts show an overall agreement for the low-mode coherent M2 internal tide when comparing with estimates from satellite altimetry (Fig. I.17). To facilitate a more accurate comparison, the tidal harmonics from HYCOM were first interpolated onto the satellite tracks. Following this interpolation, a spatial band-pass filter was then applied to the along-track data of both satellite altimetry (Fig. I.17a) and HYCOM (Fig. I.17a) to isolate the dominant wavelengths associated with

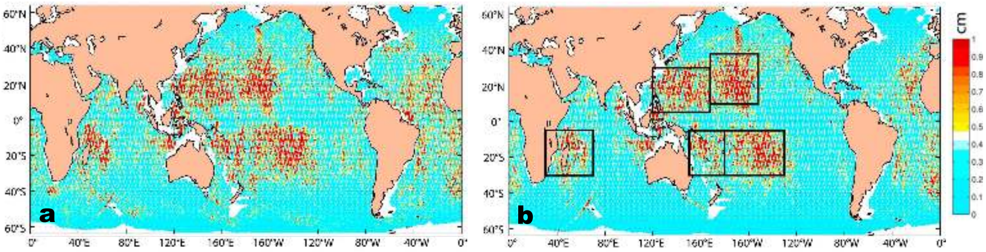

**Figure I.17:** Adapted from Shriver et al. (2012). Global coherent M2 internal tide amplitude as derived from **(a)** along-track satellite altimetry and **(b)** HYCOM. The amplitudes are retrieved by a spatial bandpass filter of along-track SSH data to isolate wavelengths associated with low-mode internal tides. See Shriver et al. (2012) for a more in-depth description and evaluation.

low-mode internal tides. Averaged over the subregions as indicated in Fig. I.17, the internal tide amplitudes in HYCOM compare well with the altimetry-based analysis. The reader is referred to Shriver et al. (2012) for a more in-depth validation.

Numerical modeling played a key role in accessing the incoherent internal tide on regional to basin scales. Using HYCOM output, Buijsman et al. (2017) quantified the importance of tidal incoherence in the equatorial Pacific (Fig. I.18), which turns out be dominant for large parts along the equator (Fig. I.18b). This is in agreement with the findings from Zaron (2019). The equatorial Pacific was previously believed to be tidally non-active and an energy sink for coherent internal tide due to increasing phase variability in propagation direction. However, it is well acknowledged today that it is not related to actual energy dissipation but rather the energy transfer or scattering from the coherent to incoherent internal tide. This is specifically shown for the northward internal tide beam propagating from French Polynesia toward the equator (Fig. I.18). Separating the total semidiurnal internal tide into the coherent

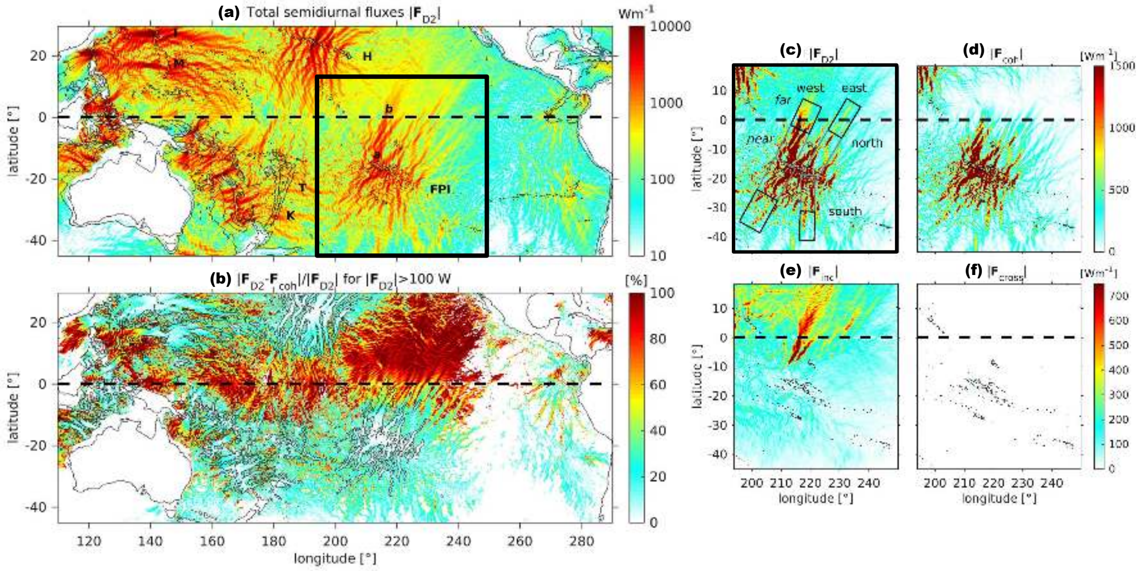

**Figure I.18:** Adapted from Zaron (2019). Adapted from Buijsman et al. (2017). **(a)** Annual mean of total semidiurnal energy flux in the equatorial Pacific mean. **(b)** Percentage of the incoherent semidiurnal energy flux (including cross-terms) to the total semidiurnal energy flux. Areas with fluxes $<1000$ W $m^{-1}$ are masked. **(c)** Total, **(d)** coherent, **(e)** incoherent semidiurnal energy flux zoomed into French Polynesia including **(f)** cross-terms.

and incoherent component as well as the cross-terms, Buijsman et al. (2017) find that the northward tidal beam loses its coherence (Fig. I.18d) while the incoherent energy flux increases (Fig. I.18e) as the beam approaches the equator.

### I.2.6 Mechanisms of tidal incoherence

The mechanisms of emerging tidal incoherence can be numerous and occur in both the near-field and the far-field.

In the near-field, tidal incoherence can arise in the near-field due to local stratification changes or impinging remotely generated internal tides that affect local internal tide generation (Zilberman et al., 2011; Kerry et al., 2014; Pickering et al., 2015; Kerry et al., 2016). The former expresses by variations in the baroclinic pressure amplitude, whereas the latter expresses by variations in the phase difference between the baroclinic pressure and barotropic tidal velocity.

In the far-field, tidal incoherence occurs due to spatial and temporal variations in stratification and background currents such as the mid-latitude or equatorial jets and the mesoscale eddy field (Park and Watts, 2006; Dunphy and Lamb, 2014; Ponte and Klein, 2015; Kelly and Lermusiaux, 2016; Buijsman et al., 2017). The physical mechanism behind the loss of coherence is ultimately linked with the wave's altering phase for a fixed location in the far-field accompanied with varying phase and group speed. It is often expressed by increasing phase variability due to the stochastic nature of the background field.

Idealized numerical experiments have given recent insight into the factors that determine the strength of tidal incoherence (e.g. Dunphy and Lamb, 2014; Ponte and

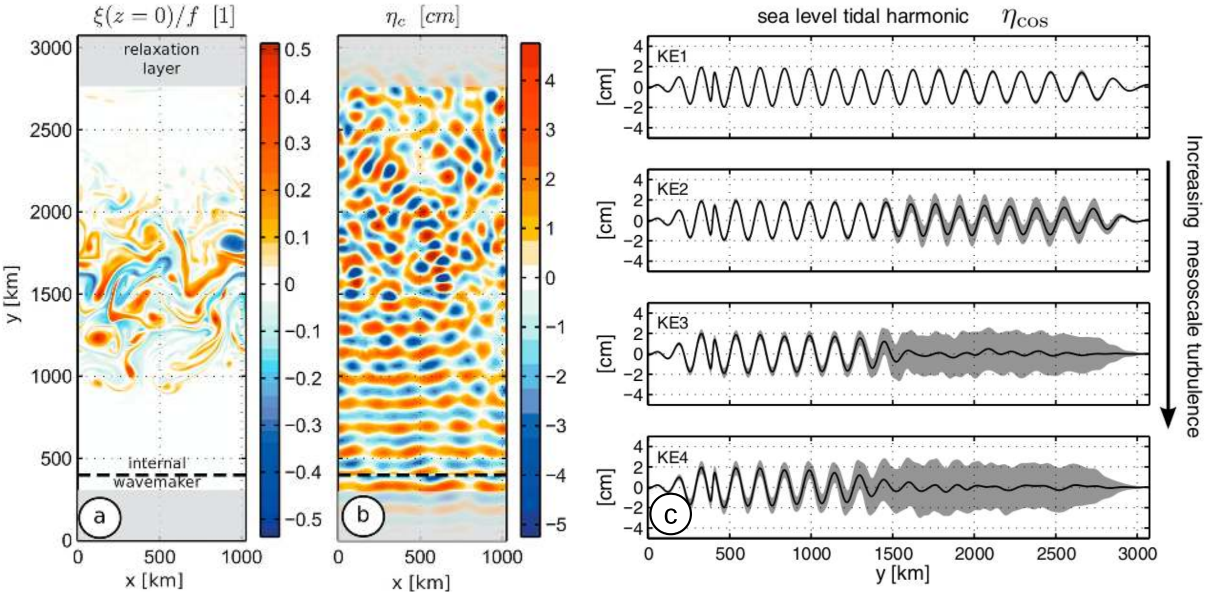

**Figure I.19:** Adapted from Ponte and Klein (2015). **(a)** Snapshot of idealized numerical simulation with strong mesoscale turbulence corresponding to KE4 in **(c)** showing surface relative vorticity normalized by the Coriolis frequency. **(b)** Tidal harmonic of sea level. The internal tide propagates northward originating to the south of the domain (dashed line). **(c)** Time-averaged sea level harmonic at $x = 512$ km as a function of $y$ for four different strengths of mesoscale turbulence (KE1-KE4). The gray shadings stand for values 1.3 times the standard deviation away from the mean value (corresponding to the 80 % percentile of a Gaussian variable). Note the complex interference pattern in **(b)**, when the internal tide crosses the zonal jet.

Klein, 2015; Dunphy et al., 2017). Ponte and Klein (2015) studied the passage of low-mode internal tides through a turbulent mesoscale eddy field as shown in Fig. I.19. The authors state that tidal incoherence emerges in the form of complex interference patterns (Fig. I.19b), which strengthens with increasing background turbulence. The internal tide remains strongly in phase for weak mesoscale turbulence, whereas strong mesoscale turbulence causes the sea level tidal harmonic north of zonal jet (>1500 km) to be fully associated with the incoherent internal tide (Fig. I.19c). Dunphy and Lamb (2014) suggest that the interaction between the eddy field and the low-mode internal tide is favored when they feature comparable length scales resulting in energy scattering towards higher modes.

Ray-tracing techniques have shown that mesoscale turbulence (i.e. eddies) refracts the tidal beam propagation direction (Park and Watts, 2006; Rainville and Pinkel, 2006; Duda et al., 2018; Guo et al., 2023). Guo et al. (2023) correlated the refraction of the internal tide in the Luzon Strait with mesoscale-eddy driven phase speed variations. Further, in their analysis the refraction is rather associated with the currents of the mesoscale eddies rather than mesoscale eddy driven stratification changes. Rainville and Pinkel (2006) found that low-mode internal tides are only little affected by the background eddy field (Fig. I.20a,e). Higher modes experience increasingly stronger refraction and phase variability, even closer to the generation site. (Fig. I.20b-h). The incoherent internal tide may represent a large fraction of the total tide and can reach locally 80-100 % (Zaron, 2017; Buijsman et al., 2017). This is especially true in equatorial regions due to seasonal changes in stratification and the time-varying vertically sheared flow of the equatorial jets and tropical instability waves (Buijsman et al., 2017).

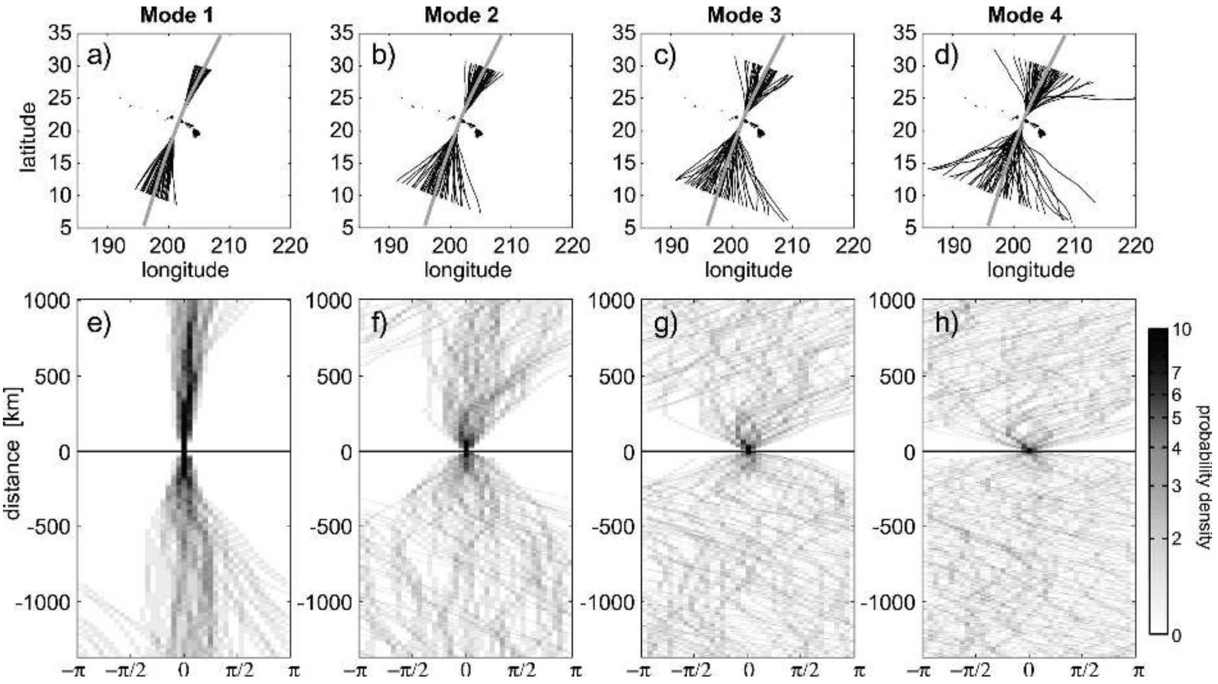

**Figure I.20:** From Rainville and Pinkel (2006). **(a)-(d)** Ray paths of modes 1-4 originating from the Hawaiian Islands and propagating northward and southward through the mesoscale eddy field (representative for the period September 2001-September 2002). **(e)-(h)**. Phase offsets (relative to the ray path without background velocity field) as a function of distance and probability densities.

### I.2.7 Internal tide modeling: a historical perspective and recent progress

Modeling internal tides has historically faced challenges due to the demanding computational requirements associated with high horizontal and vertical resolution, particularly when dealing with higher-vertical mode dynamics characterized by reduced horizontal wavelengths and increasing vertical shear. Despite the fact that current models can generally meet the necessary horizontal and vertical resolutions, the central challenge lies in effectively handling high-frequency components and ensuring numerical simulation output at adequate temporal resolution. This often necessitates the use of intricate time-splitting techniques, coupled with the need for substantial storage capacities on high-performance computing clusters.

Much of the motivation for internal tide modeling arises from the community's interest in the dynamics of internal tides themselves, specifically their impact on ocean mixing and the closure of the oceanic energy cascade. Even though in-situ observations and satellite altimetry, each associated with indispensable benefits, numerical modeling has set new heights in our understanding of the internal tide life cycle, i.e. internal tide generation, dissipation, and propagation.

First attempts of basin- and global-scale simulations of internal tides can be traced back to Niwa and Hibiya (2001) and Arbic et al. (2004),Simmons et al. (2004), respectively. These simulations were idealized in the sense that they did not include atmospheric forcing. As stated in Sect. I.2.5.2, HYCOM is considered the first realistic, three-dimensional global model with both tidal and atmospheric forcing and, particularly, with sufficient resolution in the horizontal (1/12.5° and 1/25°) and vertical (varying from 32 to 41 vertical levels) to resolve both mesoscale variability and internal tides (Arbic et al., 2010, 2012, 2018; Arbic, 2022).
Further simulations were developed in the following years, i.e. the STORMTIDE simulation (Müller et al., 2012) and the Generalized Ocean Layer Model (GOLD; Waterhouse et al., 2014). A widely used model configuration incorporating tides is the Massachusetts Institute of Technology general circulation model (MITgcm) that features a horizontal grid spacing down to 1/48° with 90 vertical levels (e.g. Rocha et al., 2016a,b; Savage et al., 2017; Qiu et al., 2018; Torres et al., 2018, 2019). Basin-scale also exist for the Regional Ocean Modeling System (ROMS) and the Nucleus for European Modeling of the Ocean (NEMO), such as the North Atlantic Basin configuration with 1/60° horizontal grid spacing and 300 vertical levels (`https://github.com/ocean-next/eNATL60`).

Realistic, three-dimensional numerical models played an essential role in our understanding of tidal dynamics and their role on the oceanic circulation and climate. Along-side with satellite altimetry, internal tide generation sites were identified while increasing our understanding of tidal energy propagation. The inclusion of tidal forcing leaded to a partially resolved internal gravity wave continuum. Further, it was shown that the variance at high-frequencies is elevated with increasing resolution in numerical models as shown by Müller et al. (2015) for HYCOM at 1/12.5° and 1/25°

horizontal grid spacing. Moreover, the simulated continuum is increasingly closer to theory and observations, which has also shown for the MITgcm (Savage et al., 2017; Rocha et al., 2016a; Chereskin et al., 2019; Luecke et al., 2020).

Running these high-resolution models including their storage on high-performance computing clusters are extremely costly. Regional models played a crucial role in the last two decades as they require less computational power while providing insight in tidal energetics. Early efforts using analytical modeling date back to Rattray (1969), up to the beginnings of numerical modeling such as Holloway (1996) and Cummins and Oey (1997). Further, important contributions to numerical modeling of internal tides were made by Kang et al. (2000), Merrifield et al. (2001), and Merrifield and Holloway (2002) in the framework of the Hawaiian Ocean Mixing Experiment (HOME).

Today, state-of-the-art models often consist of regional model configurations. Due to their smaller domain, they often require less computational resources allowing for increasing grid spacing in the horizontal and vertical direction. The model set-up generally consists of a nested domain (or a series of nested domains) forced at the lateral boundaries by a host domain or global run. Regional models often enjoy full dedication on understanding local dynamics. Specifically, boundary conditions, forcings, and parameterizations are explicitly tuned for the realism of the region's dynamical regime. Some recent studies that focus on regional internal tide modeling include Jithin et al. (2019); Lahaye et al. (2020); Tchilibou et al. (2020, 2022). A key component in the realistic regional modeling of internal tides lies in the remote forcing of tides as pointed out by several studies, (e.g. Carter et al., 2012; Jeon et al., 2019; Jithin et al., 2019; Nelson et al., 2019; Mazloff et al., 2020; Siyanbola et al., 2023). The remote forcing is considered of high importance since remotely generated high-frequency oceanic variability, i.e internal tides, may represent a non-negligible source of energy in the regional domain. This is supported by regional numerical

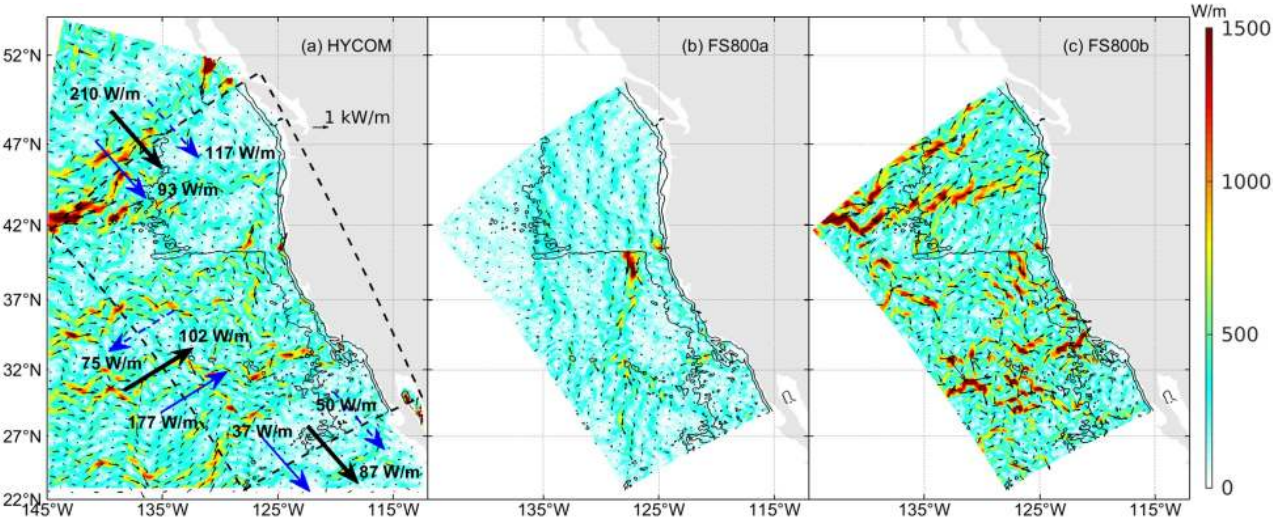

**Figure I.21:** From Siyanbola et al. (2023). Depth-integrated and time-averaged semidiurnal energy flux in the California Current system for **(a)** the global HYCOM simulation, **(b)** the regional ROMS simulation without remote high-frequency baroclinic boundary forcing, and **(c)** the regional ROMS simulation with remote high-frequency baroclinic boundary forcing.

modeling experiments in Siyanbola et al. (2023). It is suggested that remote internal wave forcing at the open boundaries of the regional domain (ROMS) prescribed by a global HYCOM simulation significantly improves the energy content (Fig. I.21. An alternative approach lies in a two-way nesting framework between the high-resolution nesting domain and the lower-resolution host grid for which high-frequency boundary forcing does not to be taken into account. This technique proved to contribute to tidal accuracy and predictability (Jeon et al., 2019).

Regional modeling allows for high horizontal and vertical resolution grid box spacing to due their smaller size. Thus, they are less dependent on parameterizations that account for sub-grid scale physics such as internal wave induced vertical mixing. Recently, Thakur et al. (2022) pointed out that high-resolution model configurations still incorporate parameterization schemes for vertical mixing processes with possible implications for the realism of the internal gravity continuum. This has not necessarily physical reasons, but rather traditional ones. These models configuration were initially set up with lower horizontal and vertical resolution and especially without tidal forcing and, hence, relied on vertical mixing schemes. Because of the model configuration's complexity, these schemes remained almost unchanged even though horizontal and vertical grid spacing has been gradually reduced and tides were included. Specifically, Thakur et al. (2022) point out that keeping the vertical mixing schemes turned on double accounts for internal wave induced mixing leading to decreased energy levels. For sufficient resolution in the horizontal and vertical direction, the authors suggest to turn off the associated parameterizations. By doing so, energy levels of high-frequency motion $> f$ were shown to be closer to in-situ observations.

### I.2.8 Open questions

Numerous efforts have been made to study internal-tide dynamics that range from high-resolution but locally constrained in-situ observations, near-global coverage from satellite altimetry but limited to the SSH signature and large horizontal scales or low-vertical modes, to numerical modeling that provides the full-depth information from regional to basin or global scales at high temporal and spatial resolution but may represent a simplification of the complex reality and do not fully encapsulate the intricacies of the actual physical system.

Internal tides exhibit a strong local dependence, with each geographical area bearing its unique characteristics, shaped by factors such as local bathymetry, stratification, and barotropic tide forcing. These characteristics underscore the importance of conducting regional studies. In the realm of regional modeling, adequate forcing at the lateral boundaries is vital to capture interactions between the internal tide and the background circulation, which is a major source of tidal incoherence. Studying internal-tide dynamics must necessarily encompass both the coherent and incoherent tide component. Further work is needed to understand sources of tidal incoherence through interactions with the varying background circulation, wave-wave and wave-topography interactions, which may vary from one region to another.

However, there are limitations in this endeavor. Achieving a precise knowledge of bathymetry, a critical factor influencing the generation and dissipation of internal tides, remains a challenge. To conclude, internal tide modeling results require extensive validation, especially against in-situ observations which remain, however, sparse despite dedicated efforts in in-situ experiments. Research fields that deserve further attention and associated open questions are summarized below:

**Open questions**

**1)** What is the general realism of internal-tide dynamics in regional numerical model configurations and how does it compare with in-situ observations?

**2)** What is the internal tide's fate close to the generation site and in propagation direction in the open ocean? Where do low-vertical mode internal tides dissipate and what are the exact underlying mechanisms?

**3)** What are regional sources of tidal incoherence? At the generation site, what are the contributions of local stratification changes and remotely propagating internal tides? In the open ocean, what are the contributions of eddy-internal tide interactions?

**4)** Do eddy-internal tide interactions contribute to dissipation? Do eddy-internal tide interactions affect tidal energy transfer to higher vertical modes?

## I.3 The Surface Water and Ocean Topography mission

Satellite altimetry looks back upon a more than three-decade long history. The acquired sea surface height observations of the global ocean have played a key role in our understanding of the large-scale circulation, mesoscale variability, and internal tide dynamics. In some way, satellite altimetry revolutionized our view on the surface ocean as it revealed dynamics that were either not known to us or were not considered of big importance before. Tracking algorithms were developed to identify and quantify mesoscale eddies applied on global and regional scales (Chelton et al., 2011; Le Vu et al., 2018). Sea surface height spectra, derived from both along-track data and gridded two-dimensional maps, have proven to be very useful for determining the spatially-varying and governing dynamical regimes (e.g. Le Traon et al., 2008; Stammer, 1997; Xu and Fu, 2011, 2012; Vergara et al., 2019, 2023). Further, new information was obtained on the redistribution of potential and kinetic energy among spatial scales shedding light on the energy cascade and transfer in the ocean (sco, 2005).

Our present-day view of the surface ocean is largely restricted by the coarse sampling capabilities with ground track distances that are often far larger than the local Rossby deformation radius. This has consequences for the mapping technique of along-track data applied to obtain a two-dimensional grid with a global Cartesian resolution of 1/4° on a daily basis. They rely on gridding and optimal interpolation using objective analysis such as smoothing and latitude dependent spatial and temporal correlation scales (Pujol et al., 2016). Particularly, the mapping procedure was set up in such way that it represents the best compromise between the eddy field characteristics which are desired to be resolved and the available sampling. In practice, this is seen in the representation of eddy field characteristics. Using a high-resolution numerical simulation as a reference data set, it was shown that more than 2/3 of oceanic eddies may be missed by eddy tracking algorithms applied on satellite altimetry derived two-dimensional maps of surface velocity (Amores et al., 2018).

A recently launched satellite mission will set new heights in sea surface height observations: the Surface Water and Ocean Topography (SWOT) mission. Initiated by the American and French space agencies NASA (National Aeronautics and Space Administration) and CNES (Centre National d'Études Spatiales), SWOT represents a new era of oceanographic sea surface height observations. SWOT is expected to provide new insights into small-scale ocean dynamics. Particularly, it has been designed to resolve wavelengths by up to ten times higher resolution (down to 15 km depending on the altimeter's noise; Fu et al., 2012; Fu and Ubelmann, 2014) than conventional altimetry ($O$(100 km); Ballarotta et al., 2019). The primary objective of SWOT from an oceanographic point of view is the characterization of the mesoscale and submesoscale circulation down to scales that have never been accessed before on global scales. The scientific interests and applications are numerous: understanding the redistribution of energy, momentum, tracer (e.g. heat, carbon, nutrients), air-sea interactions, vertical transport of physical and biogeochemical tracers between atmosphere-ocean interface, mixed, and ocean interior (e.g. Lapeyre et al., 2006; Capet et al., 2008; Klein and Lapeyre, 2009). Moreover, it may have major implica-

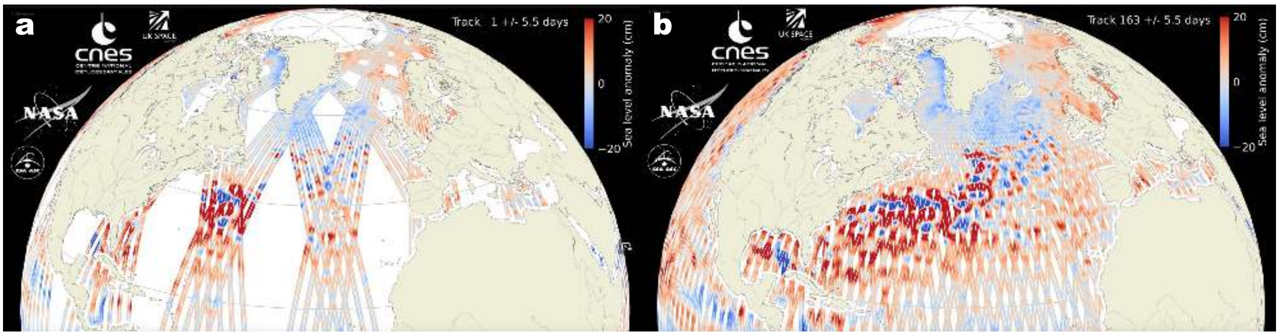

**Figure I.22:** SWOT nominal orbit coverage after **(a)** track 1 ± 5.5 days and **(b)** track 163 ± 5.5 days obtained from a SWOT simulator. A complete cycle encompasses 21 days (Credits: CNES/CLS).

tions for the biological carbon pump and regulation of atmospheric carbon dioxide (Fu and Ferrari, 2008; Lévy et al., 2012; Liu and Levine, 2016).

SWOT will operate in a nominal 21-day repeat orbit for a total of three years (Fig. I.22). The final orbit choice does not only represent the compromise between spatial and temporal coverage. Also, it is supposed to serve the needs for both the hydrology and oceanography community, e.g. the global coverage of rivers and lakes on a monthly time scale for hydrologists and resolving the quickly evolving westward propagating mesoscale instabilities for oceanographers. A key factor in choosing the SWOT inclination and repeat sampling rate is linked to resolving the major tidal constituents dedicated to the observations and study of internal tides (non-sun-synchronous orbit, Morrow et al., 2019).
Prior to the 21-day repeat orbit, SWOT operated in a fast-sampling phase associated with a 1-day repeat orbit, which is subject to a Calibration and Validation (CalVal) phase. From a scientific perspective, this CalVal phase is dedicated to an international consortium, namely SWOT Adopt-A-Crossover (AdAC), which aims to assists in-situ experiment helping to interpret future SWOT SSH measurements.

This section is dedicated to introduce the SWOT mission alongside its scientific objectives, the measuring technique, and associated challenges before highlighting the role of New Caledonia in the evaluation and assessment of SWOT.

### I.3.1 A new era of sea surface height observations

Conventional satellite altimetry relies on the measurement of the round-trip travel time of an emitted radar pulse using a nadir-pointing radar altimeter. The derived range between the altimeter and the ocean's surface, together with the knowledge of the satellite orbital height (relative to the Earth's reference ellipsoid) is then used to estimate the sea surface height. The limitation of the nadir-pointing altimeter consists in the finite foot-print of the backscattered signal. The diameter of this foot-print can vary from 2 km to 10 km depending on the sea conditions. Therefore, nadir-pointing altimetry relies heavily on radar waveform analysis, i.e. the tracking of the radar pulse's leading edge (Fig. I.23). The spatially non-homogeneous conditions of such a foot-print may largely impact the radar waveform analysis, especially near coasts and islands (Fu et al., 2012; Morrow et al., 2023).

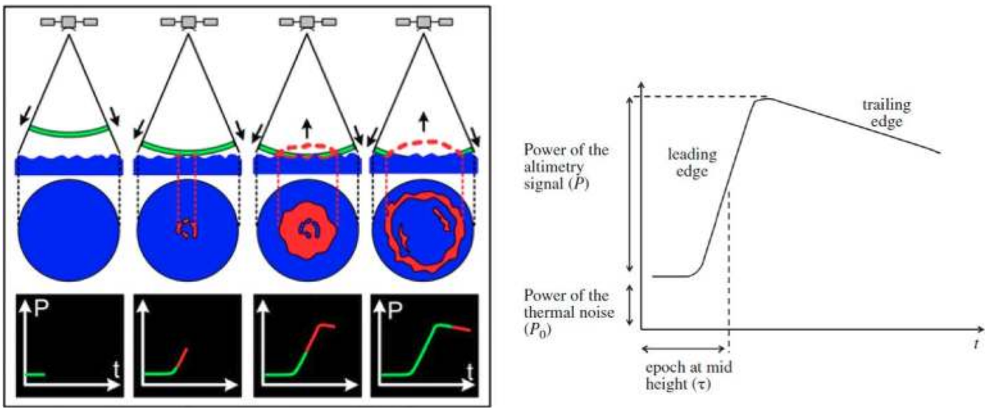

**Figure I.23:** From CNES. **(left)** Schematic illustrating the time series of a characteristic foot-print of a radar pulse bouncing off the ocean's surface with the downward propagating signal in green and the backscattered signal in red. **(right)** The power received over time of the backscattered signal at the radar altimeter indicating the radar pulse's leading edge.

SWOT represents a major improvement to conventional satellite altimetry thanks to the applied wide-swath radar interferometry technique that will provide 2-dimensional SSH observations over two 60-km wide swaths with a 20 km nadir gap (Fig. I.24). In contrast to conventional altimetry, SWOT relies on off-nadir pointing radar altimetry which allows to locate range measurements in the horizontal plane (across the swaths) using triangulation. Doing so, SWOT will provide a pixel-by-pixel estimate for SSH in geographically fixed coordinates with a horizontal resolution of 2 km × 2 km . The data acquisition and basic measurement principle is briefly described in the following (Fig. I.24).

The core instrument is a Ka-band radar interferometer (KaRin) which contains two

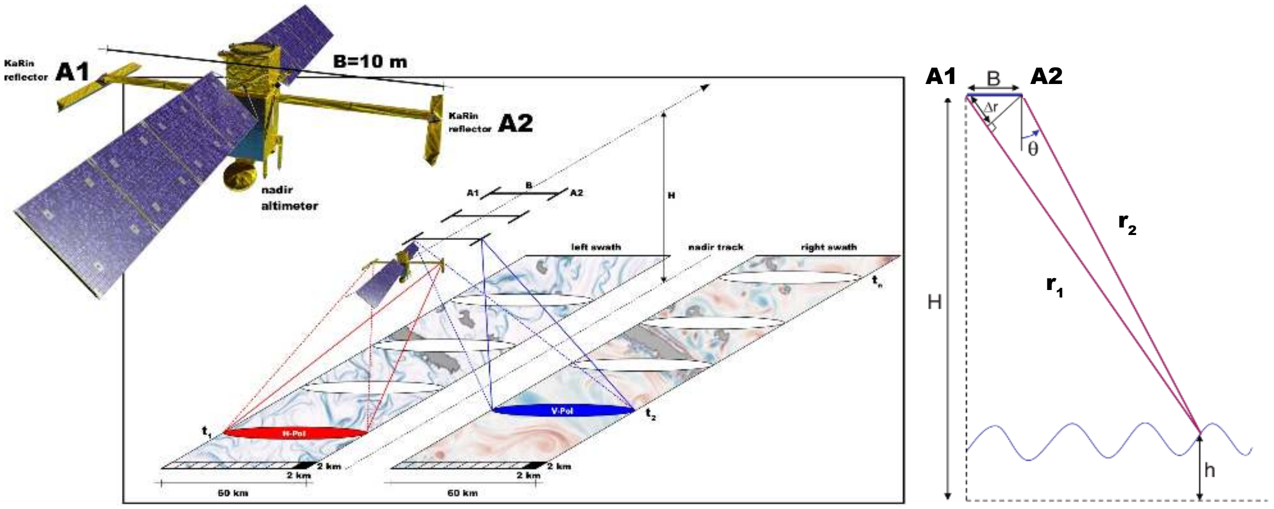

**Figure I.24: (left)** Schematic of the SWOT satellite with the two KaRin reflectors/antennas (A1 and A2) separated by a baseline mast (B) and the nadir altimeter (from `https://science.nasa.gov/toolkits/spacecraft-icons`). Illustration of the acquisition geometry of SWOT with two swaths of 60 km width to the left and right side of the nadir track. The left swath (red) is associated with a horizontal polarization and the right swath (red) with a vertical polarization to allocate the backscattered signals to the corresponding swath. **(right)** Adapted from Fjørtoft et al., 2010. SWOT measurement principle using triangulation (see text for details).

Ka-band SAR antennae (KaRin reflectors) at opposite ends separated by a 10-m baseline mast. In the two-antenna configuration, only one antenna is capable of alternatively illuminating the left and right swath on either side of the nadir track. In the default configuration, this is antenna A2. Specifically, at time step $t_1$, A2 emits a pulse towards the left swath and at time step $t_2$ towards the right swath as the altimeter moves on in time along the nadir track. In both cases, both antennas (A1+A2) receive the backscattered signal. To allocate the backscattered signals to the corresponding swath, they are separated from each other by orthogonal polarization, i.e. the left swath has a horizontal polarization and the right swath a vertical polarization (Fig. I.24).

The basic measurement principle underlies the determination of the range difference $\Delta r = r_2 - r_1$ and the incidence angle $\theta$ (Fig. I.24). The range distance $r_2$ is determined by the round trip travel time of the radar pulse. The range difference $\Delta r$ can be derived by measuring the relative phase shift $\varphi$ that is related to $\Delta r$ via: $\Delta\varphi = 2\pi\lambda^{-1}\Delta r$, where $\lambda$ is the radar wavelength. Note that many $r_1$ are possible for a given $\lambda$. This is solved by a processing called phase unwrapping. Once unwrapped, the phase difference $\Delta\varphi$ is used to estimate the incidence angle $\theta$ via: $\Delta\varphi = kB\sin\theta$, where $k$ is the electromagnetic wavenumber related to $\lambda$ and $B$ =10 m. Finally, sea surface height can be computed as follows: $h = H - r_2\cos\theta$, where H is the satellite orbital height. This is done for each bin providing a pixel-by-pixel estimate of $h$ in 3-dimensional space along the interferogram line.

First SWOT SSH data imply prospective results and the success of the mission as shown for the two SWOT swaths off the American East Coast for the Gulf Stream region for SSH anomaly and geostrophic velocity after noise reduction (Fig. I.25).

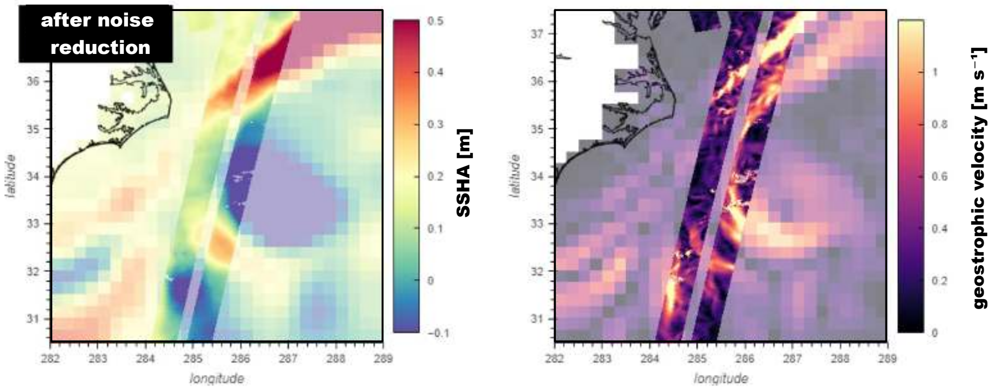

**Figure I.25:** SWOT swaths off the American East Coast for the Gulf Stream region showing **(left)** SSH anomaly and **(right)** geostrophic velocity. The remaining field is field is filled with gridded two-dimensional data from conventional nadir-pointing altimetry (Credits: G. Dibarboure, SWOT Science Team Meeting 2023, Toulouse, France).

### I.3.2 SWOT challenge: disentangling balanced and unbalanced motion

Conventional satellite altimetry allows us to access scales $O(100\,\text{km})$, predominantly governed by rotational, balanced motion. SWOT will access scales an order of magnitude lower, i.e. $O(10\,\text{km})$. Apart from this, SWOT represents a unique oppor-

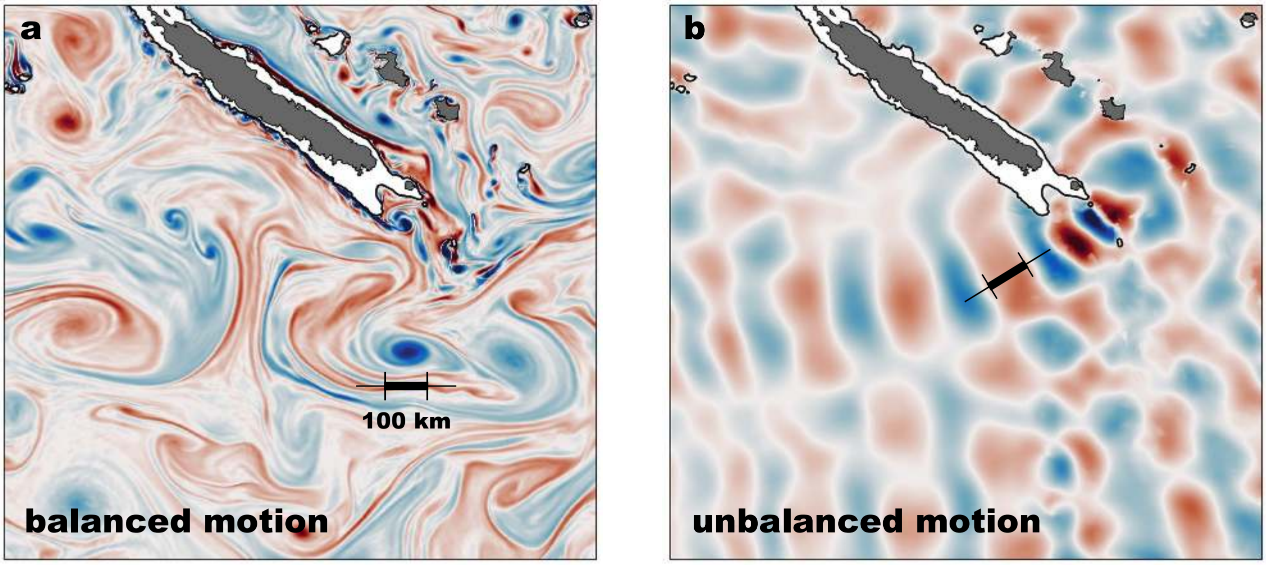

**Figure I.26:** Snapshot of **(a)** relative vorticity normalized by the Coriolis frequency and **(b)** M2-tide induced pressure perturbations, both from realistic numerical simulation output (see Sect. II). Note that mesoscale and submesoscale eddies (balanced motion) expressed by patches of relative vorticity can feature similar wavelengths as internal tides (unbalanced motion).

tunity for combined SSH observations of balanced and unbalanced motion including geostrophic eddy motion, high-frequency internal waves (i.e. internal tides, Morrow et al., 2019).

On the one hand, combined observations of balanced and unbalanced motions open up a lot of possibilities such as the study of energy transfers and scale interactions. Specifically, SWOT will not only enable the study of the inverse energy cascade at mesoscales (as previously accomplished by conventional satellite altimetry) but also at submesoscales (Klein et al., 2019). On the other hand, SWOT is confronted with a major challenge as combined observations of balanced and unbalanced motions represent a challenge for observations of mesoscale and submesoscale sea surface height and their derived dynamics, SWOT's primary objective. Mesoscale eddy characteristics in present-day altimeter products rely on the geostrophic approximation to derive sea surface currents. This approximation, however, is technically not valid anymore when resolving scales down to 15 km wavelengths, at which sea surface height is not purely associate with balanced anymore. Particularly, depending on the region, the signature can be dominated by unbalanced motion such as internal tides, which are not constrained by rotation. Further, the disentangling is complicated by the fact that mesoscale and submesoscale eddies and internal tides can feature similar wavelengths (Fig. I.26). This may implications for limited observability of the mesoscale and submesoscale circulation. Therefore, the challenge of SWOT lies in disentangling the sea surface signatures of the two different regimes.

An important quantity in satellite altimetry is the transition scale which separates in spectral space dominant balanced motion from unbalanced motion. In particular and in the context of SWOT, it represents a valuable measure to disentangle balanced and unbalanced motion. Previous studies using a realistic numerical simulation (MITgcm at 1/48○ resolution, Qiu et al., 2018) and along-track satellite altimetry data (Jason-3

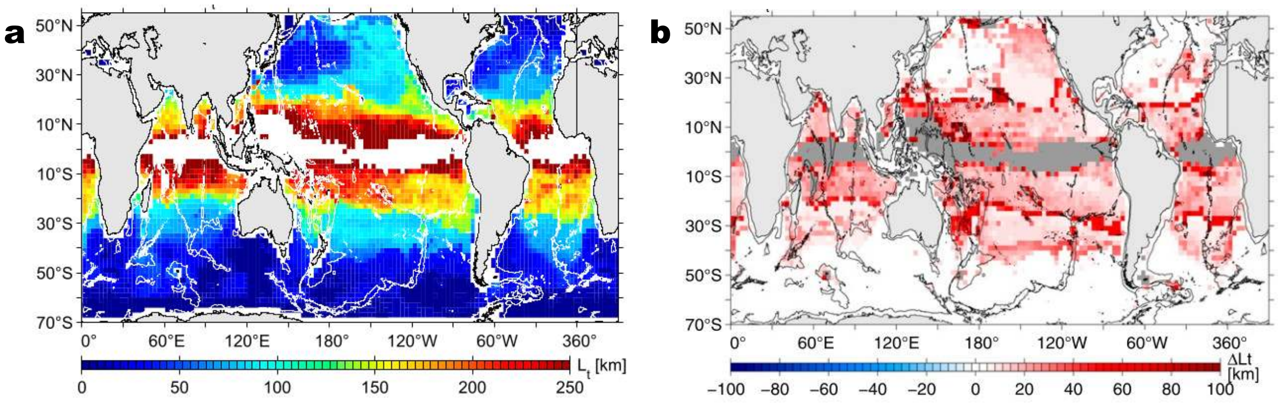

**Figure I.27:** Adapted from Qiu et al. (2018). Spatial maps of **(a)** the transition scale ($L_t$) that separates balanced and unbalanced motions derived from sea surface height from a realistic high-resolution numerical simulation output and **(b)** the transition scale corrected for the coherent internal tide. Specifically, the transition scale is defined for wavelengths with equal contributions to sea surface height variance between balanced and unbalanced motion.

and Sentinal-3A nadir altimetry, Vergara et al., 2023) estimated the transition scale on global scales revealing both seasonal and spatial variability (Fig. I.27a and Fig. I.28).

Some effort has been made in the SWOT science community to tackle the challenge of disentangling balanced from unbalanced motion. A relatively simple approach consists in correcting the measured sea surface height for the coherent internal tide by making use of the empirical internal tide models based on the >20-year long altimeter time series (Zaron and Ray, 2017; Zaron, 2019; Carrere et al., 2021). In Qiu et al. (2018), this method was tested from a realistic numerical modeling perspective (Fig. I.27b). Locally, especially in internal tide hot spot generation sites such as the Hawaiian Island, the Luzon Strait, and the southwestern tropical Pacific Ocean, the transition scale is lowered by up to 80 km allowing for increasing observability of

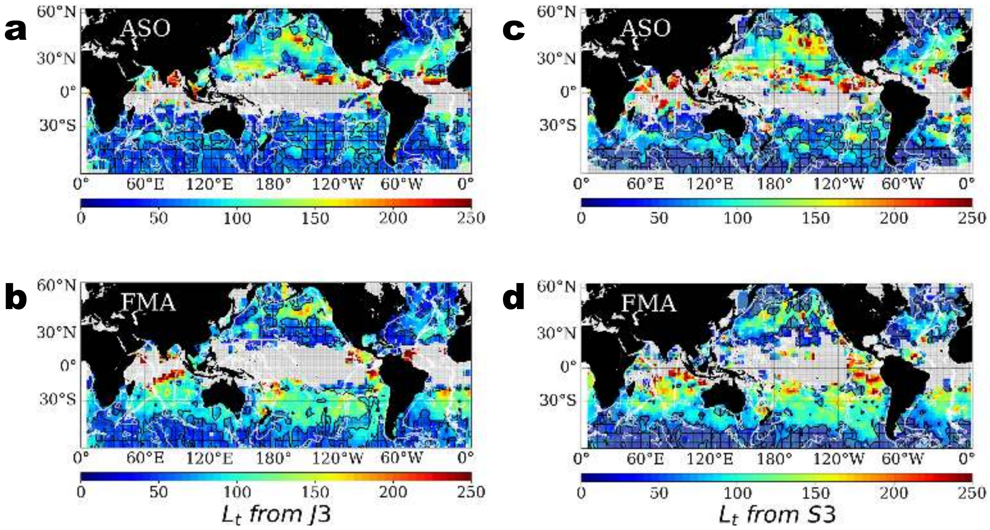

**Figure I.28:** Adapted from Vergara et al. (2023). Seasonal variability of the transition scale in km estimated from along-track sea surface height data from **(a,b)** Jason-3 and **(c,d)** Sentinal-3A covering a 4-year period (2015-2019), shown for August-October **(a,c)** and February-April **(b,d)**.

mesoscale and submesoscale dynamics. The observation-based study from Vergara et al. (2023) is in good agreement the modeling results. However, a correction for the coherent internal tide was reported to have only little impact on the transition scale. Discrepancies may result from the longer time series in the nadir altimeter products and the applied methodologies to determine the transition scale. (Vergara et al., 2023) use the change of spectral slope of SSH observations as a proxy for the separation length scale, whereas (Qiu et al., 2018) use a spectral filter.

However, this approach does not account for the incoherent part. In regions with elevated internal tide activity this may be problematic since tidal incoherence can explain a large fraction of the total signal. Alternatives were developed that aim to extract the both balanced and unbalanced motion of the sea surface height field using idealized simulations. Ponte et al. (2017) suggested a complementary usage of sea level data and sea surface density to differentiate low-mode internal tide and balanced mesoscale eddies. This methodology relies on the assumption that low-mode internal tides have a weak signature on sea surface density, while balanced contributions to the sea level can be derived to some extent from surface density via potential-vorticity inversion. Though, the methodology shows weaknesses in regions where balanced turbulence is high. Le Guillou et al. (2021) used a joint estimation algorithm to simultaneously map and separate balanced motion and internal tides. At any given iteration, the assimilated observations are recursively corrected by from the previously estimated component as illustrated in Fig. I.29. An additional feature of the suggested methodology in Le Guillou et al. (2021) is the extraction of both the coherent and incoherent internal tide. Overall, the authors achieve a reconstruction of around 80 % of the variance of balanced motion and internal tides marking a progress towards disentangling these signals from real wide-swath altimetry data.

Most recently, Wang et al. (2022) presented a deep-learning approach to accurately

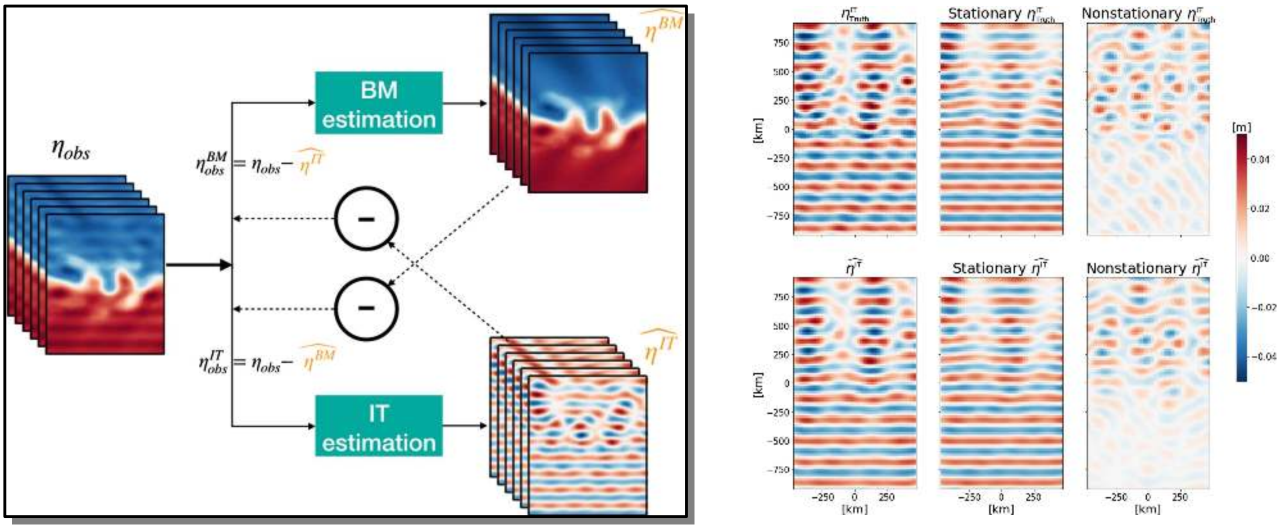

**Figure I.29:** Adapted from Le Guillou et al. (2021). **(left)** Schematic of the joint estimation algorithm that alternates between balanced motions estimates and internal tides estimations with observations recursively corrected from the other component. **(right)** Snapshots of sea surface height of the internal tide field shown for the reference truth (upper panels) and the joint estimation algorithm (lower panels). Note that the total signals $\eta^{IT}_{Truth}$ and $\widehat{\eta^{IT}}$ are decomposed in their coherent and incoherent components.

extract balanced motions and internal tides. Also here, the accuracy of the disentanglement decreases with increasing magnitude of balanced turbulence. Some important work has also been done Savage et al. (2017) and Torres et al. (2018, 2019); Ubelmann et al. (2022) by partitioning oceanic motion in contributions from balanced motions and internal gravity waves.

Briefly summarized, several approaches with developed methodologies exist to separate balanced and unbalanced motion in future wide-swath altimetry. They vary from simple sea surface height corrections for the coherent tide to joint estimation algorithms that map both components using dynamical models, and even complex deep learning techniques. Not accounting for the disentanglement of balanced and unbalanced motion may introduce large errors when calculating geostrophic currents, especially in regions where internal tide activity is high or dominates.

### I.3.3 Regional application: SWOT Adopt-A-Crossover

The CalVal phase of SWOT is essential in its early stage to ensure the instrument performance and corresponding measurements. This CalVal phase is referred to as the fast-sampling phase during which the satellite orbits on a 1-day repeat cycle collecting high-frequency sea surface height measurements along the same ground track for a duration of 90 days (Fig. I.30). This fast-sampling phase with scientifically exploitable data began in April 2023 and officially ended early July.

An important contribution to the CalVal phase is the SWOT Adopt-A-Crossover consortium, which was endorsed by CLIVAR in 2019 (d'Ovidio et al., 2019). This international initiative aims to assist in-situ experiments during the fast-sampling phase. In total, 30 study sites exist of which 16 are dedicated offshore field campaigns and 7 are offshore infrastructure. There is increased interest for ocean areas

**Figure I.30:** SWOT fast-sampling phase 1-day repeat orbit. The participating field campaigns (offshore and coastal/estuary) as well observational infrastructure in the framework of the SWOT-AdAC consortium are also shown (adapted from `https://www.swot-adac.org/science/`). The SWOTALIS in-situ experiment south of New Caledonia was carried out in spring 2023 aboard RV Antéa (inset, Credits: J.-M. Bore, IRD) at crossover sites, i.e. where SWOT's ascending and descending tracks cross. At these locations, the revisit time is maximum (twice a day). Each of these in-situ campaigns and observing systems may address and follow different scientific objectives. However, they all aim to contribute to our understanding how the three-dimensional fine-scale physics, i.e. the fine-scale vertical structure, express in SWOT sea surface height.

This thesis, as introduced in the following section (Sect. I.4), is dedicated to New Caledonia in the southwestern tropical Pacific. Within the context of SWOT-AdAC, a dedicated in-situ experiment named SWOTALIS was conducted in spring 2023 aboard RV Antéa, located south of New Caledonia in an area known for significant internal tide generation, tidal energy dissipation, and propagation (see Fig. I.30). As SWOTALIS represents a region with pronounced internal tide activity, this in-situ experiment aims to contribute to our understanding of how internal tides manifest in SWOT SSH measurements.

### I.3.4 Open questions

The launch of the SWOT mission marks a new era in SSH observations thanks to the wide-swath radar interferometry technique, enabling us to study small-scale ocean dynamics at unprecedented levels on global scales. It represents a unique opportunity to study fine-scale SSH observations of combined balanced and unbalanced motions holding a significant promise for understanding the redistribution of energy among various scales. In the meanwhile, combined observations of balanced and unbalanced motions limit our ability to observe mesoscale and submesoscale dynamics or internal tides in regions where balanced and unbalanced motions have equal importance. Disentangling the balanced from the unbalanced flow regime represents one of the major challenges of SWOT. The SWOT science community has been working with full dedication to tackle this problem. Further, important insight will be provided by the SWOT-AdAC consortium fine-scale in-situ experiments, which will help interpreting SWOT SSH data. Open research questions are as follows:

**Open questions**

**1**) What is the SWOT SSH observability of internal tides in various regions with different dynamics?

**2**) To what extent does a correction for the coherent internal tide modify the transition scale between balanced and unbalanced motions around New Caledonia?

**3**) How do eddy-internal tide interactions or the incoherent internal tide express in SWOT SSH and how much of the variance do they explain? When correcting for the coherent internal tide SSH signature, to what extent does the incoherent internal tide limit the observability of mesoscale and submesoscale dynamics?

## I.4 New Caledonia

This study is dedicated to New Caledonia, an archipelago located in the southwestern tropical Pacific at the entrance of the Coral Sea. New Caledonia is a unique study site to address eddy-internal tide interactions in the context of SWOT SSH observability for three primary reasons. 1) It is characterized by complex regional circulation and mesoscale eddy activity. 2) It represents a hot spot for internal tide generation due complex bathymetry. 3) The study area is located beneath the two swaths of SWOT's fast sampling phase.

In Sect. I.3.3, New Caledonia was introduced as a SWOT-AdAC CalVal site. In the following, our present-day knowledge of the area's governing dynamics ranging from the large-scale circulation down to mesoscale and submesoscale motions are recapitulated while pointing out the importance of high-frequency motion such as internal tides for the New Caledonia marine biodiversity.

### I.4.1 Regional circulation and mesoscale variability

The Coral Sea plays a key role of the westward inflow of subtropical thermocline waters and the subsequent equator- and poleward redistribution of heat and salt (Fig. I.31, Qu and Lindstrom, 2002; Kessler and Cravatte, 2013). This region was recently subject to observational efforts in the framework of the international research program

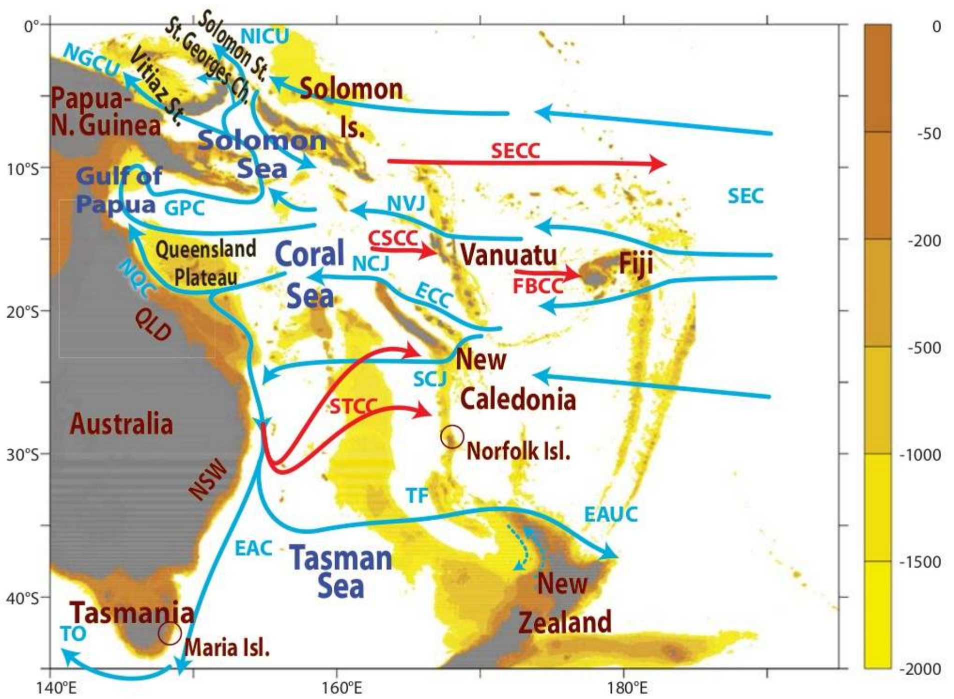

**Figure I.31:** From Ganachaud et al. (2014). Schematic of the regional circulation (blue arrows: thermocline circulation; red arrows: surface-trapped circulation) in the Coral Sea in the Southwestern Tropical Pacific including bathymetry (shading) shallower than 2000 m. Relevant abbreviations are as follows: SEC (South Equatorial Current), NVJ (North Vanuatu Jet), NCJ and SCJ (North and South Caledonian Jet), STCC (SubTropical Counter Current), GPC (Gulf of Papua Current), EAC (East Australian Current) and ECC (East Caledonian Current). The main islands and countries are given.

SPICE (Southwest Pacific Ocean Circulation and Climate Experiment), endorsed by CLIVAR (Variability and Predictability of the Ocean-Atmosphere System) program (Ganachaud et al., 2007, 2008, 2014). The complexity of the region in terms of accessibility, data acquisition, and challenges for numerical modeling initiated this international coordinated program to understand inter alia the circulation patterns, the water mass transformation and mixing, as well as the underlying variability with implications on climate.

Using ARGO floats, ship-based hydrography and acoustic current velocity profiler data as well as autonomous underwater gliders, the complex circulation in the Coral

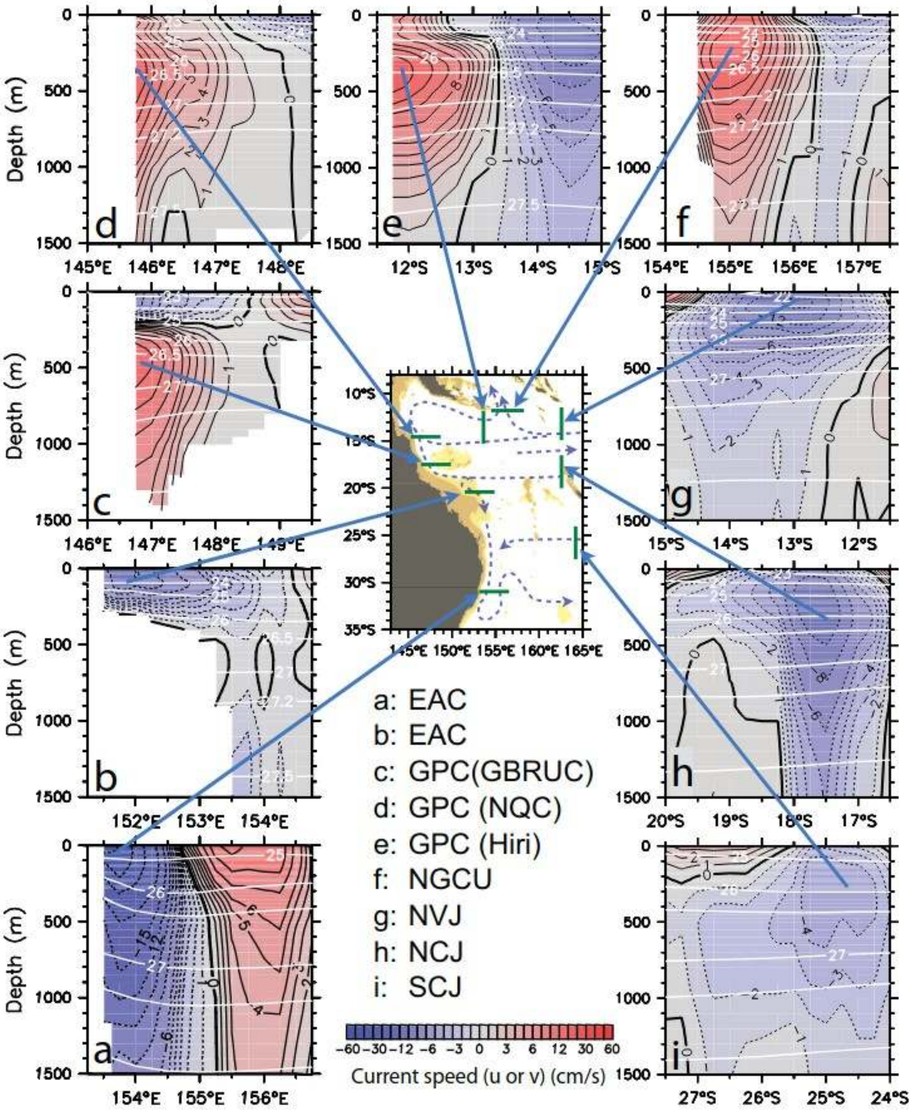

**Figure I.32:** From Kessler and Cravatte (2013). Regional circulation pattern in the Coral Sea with the key geostrophic velocity sections (referenced to a known level of motion at 1000 m depth) derived from climatological hydrography and Argo drift data. Eastward and northward velocities are shown in red. Westward and southward velocities are shown in blue. The panels **(g)**-**(i)** represent the westward inflow of the South Equatorial Current (SEC) split into the North Vanuatu Jet (NVJ), the North Caledonian Jet (NCJ), and the South Caledonian Jet (SCJ). The background potential density field in kg $m^{-3}$ is also shown (white contours).

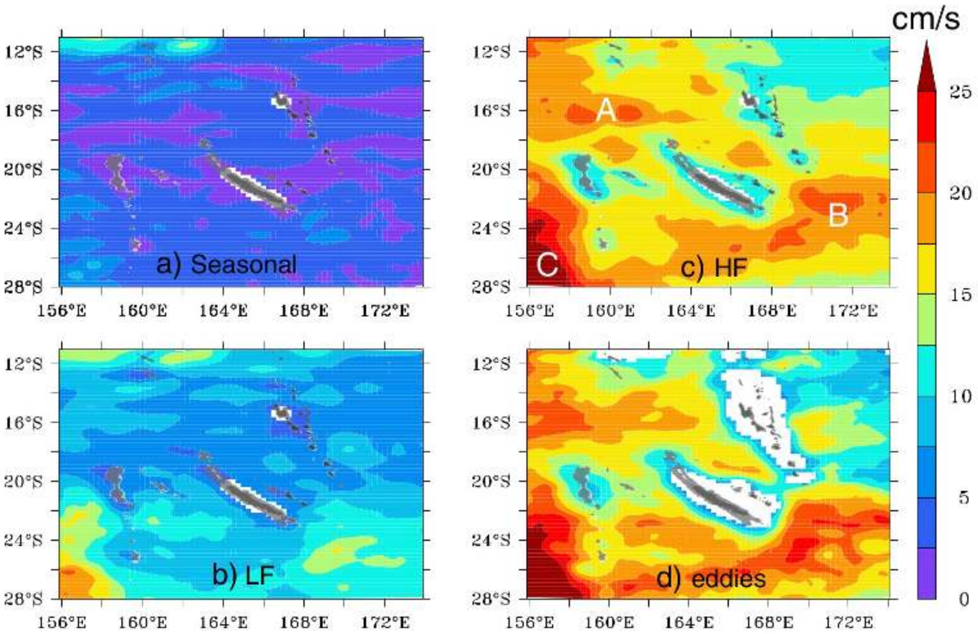

**Figure I.33:** From Cravatte et al. (2015). Kinetic energy (root mean square) of **(a)** seasonal, **(b)** low-pass filtered, **(c)** and high-pass filtered AVISO surface geostrophic velocities. **(d)** Mean rotational speed of mesoscale eddies as obtained from an eddy tracking. Areas of high intraseasonal variability are denoted A (NCJ), B (STCC), and C( EAC).

Sea was described in a series of observational studies (Gourdeau et al., 2008; Gasparin et al., 2011; Kessler and Cravatte, 2013; Ganachaud et al., 2014; Cravatte et al., 2015). The main findings and conclusions are well put together and summarized in Fig. I.31 from Cravatte et al. (2015) and Fig. I.32 from Kessler and Cravatte (2013). Together with the Fiji and Vanuatu islands, New Caledonia represents an obstacle for the large-scale westward flowing South Equatorial Current (SEC). As a consequence, the SEC splits into westward jets such as the North Vanuatu Jet (NVJ), North Caledonian Jet (NCJ), and the South Caledonian Jet (SCJ) (Fig. I.32g-i). The NVJ can be regarded as the westward limb of the shallow thermocline (subtropical) gyre, whereas the latter two (even though the SCJ to a smaller extent) are narrow, deep-reaching zonal jets down to 1500 m of more barotropic nature (Couvelard et al., 2008; Gourdeau et al., 2008; Kessler and Cravatte, 2013). When approaching the Australian coast, the zonal jets supply the the East Australian Current (EAC) and the Gulf of Papua Current (GPC) forming recirculation and counter currents such as the SubTropical Counter Current (STCC) and the Coral Sea Counter Current (CSCC; Fig. I.31).

The horizontal and vertical shear of the zonal current systems play an essential role in the Coral Sea mesoscale variability due to barotropic and baroclinic instabilities giving rise to elevated eddy kinetic energy levels (Qiu and Chen, 2004; Qiu et al., 2008, 2009). As a consequence, time variability of the regional circulation is enhanced on intraseasonal timescales, which is in accordance with mesoscale eddy activity (Fig. I.33c,d, Cravatte et al., 2015). Three regions with high variability in the high or intraseasonal frequency band are identified: northwest (A), southeast (B), and in the far southwest of New Caledonia. The latter corresponds with the EAC. (A) has its origin in the horizontal shear and associated barotropic instabilities of the NCJ/NVJ-CSCC current system. In contrast, (B) has its origin in the vertical shear and associated baroclinic instabilities of the vertically aligned SEC/SCJ-STCC current system. The mesoscale eddy field was investigated in more detail in Keppler et al. (2018). The authors find elevated eddy kinetic energy levels of up to 300 cm $s^{-1}$ south/southeast of New Caledonia, where eddies are most pronounced with an average radius of 100 km and an amplitude of 9 cm. The eddy field is overall more energetic and long-lived compared to the equatorward regions highlighting the regime shift from non-linear eddy motion south of New Caledonia to a more linear dynamical regime north of New Caledonia.

Qiu and Chen (2004) investigated temporal variability of mesoscale EKE in the Southwestern Tropical Pacific. The vertically aligned SEC(/SCJ)-STCC current system was found to undergo seasonal variability featuring maximum shear in August corresponding with the surface cooling induced tilt of the seasonal thermocline. The maximum eddy kinetic energy lags by 3 months peaking in November/December. The 3-month lag corresponds with the growth rate of 81 days for the most unstable mode as suggested by 2 1/2-layer reduced-gravity model. Minimum shear is found in May when the surface ocean is capped by a flat and well-stratified seasonal thermocline followed by minimum eddy kinetic energy in June/July. Even though the study region (21°-29° S and 180°-160° W) is located significantly east of New Caledonia (1500-3500 km) it sheds light into the temporal modulation of mesoscale variability.

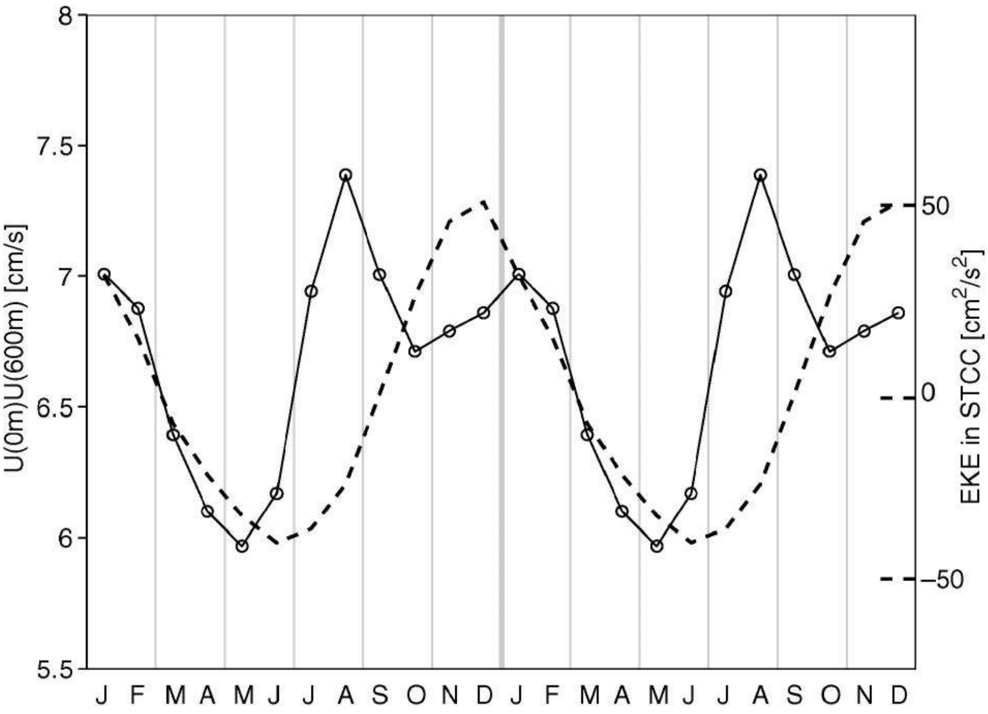

**Figure I.34:** From Qiu and Chen (2004). Time series of the zonal velocity shear between 0 and 600 m of the vertically aligned SEC/SCJ-STCC current system averaged over 21°-29° S and 180°-160° W (solid line). The time series of monthly eddy kinetic energy is also shown. Note the 3-month lag between peak zonal velocity shear and maximum eddy kinetic energy.

### I.4.2 Submesoscale circulation

From an observational point of view, the mesoscale circulation has been relatively well studied around New Caledonia. The major currents have been surveyed and characterized; sources of mesoscale turbulence identified and quantified. In general, accessing the submesoscale regime is a challenge due to the spatially smaller and temporally higher time scales. Sérazin et al. (2020) made use of all available in-situ data sets in the region, i.e. ship-board Acoustic Doppler Current Profiler (sADCP) data, to compute structure functions while decomposing the flow into its rotational and divergent component using Helmholtz decomposition. Doing so, the velocity field along the ship tracks was analyzed in terms of their governing dynamics while distinguishing between balanced (rotational) and unbalanced (divergent) motion. The high-resolution

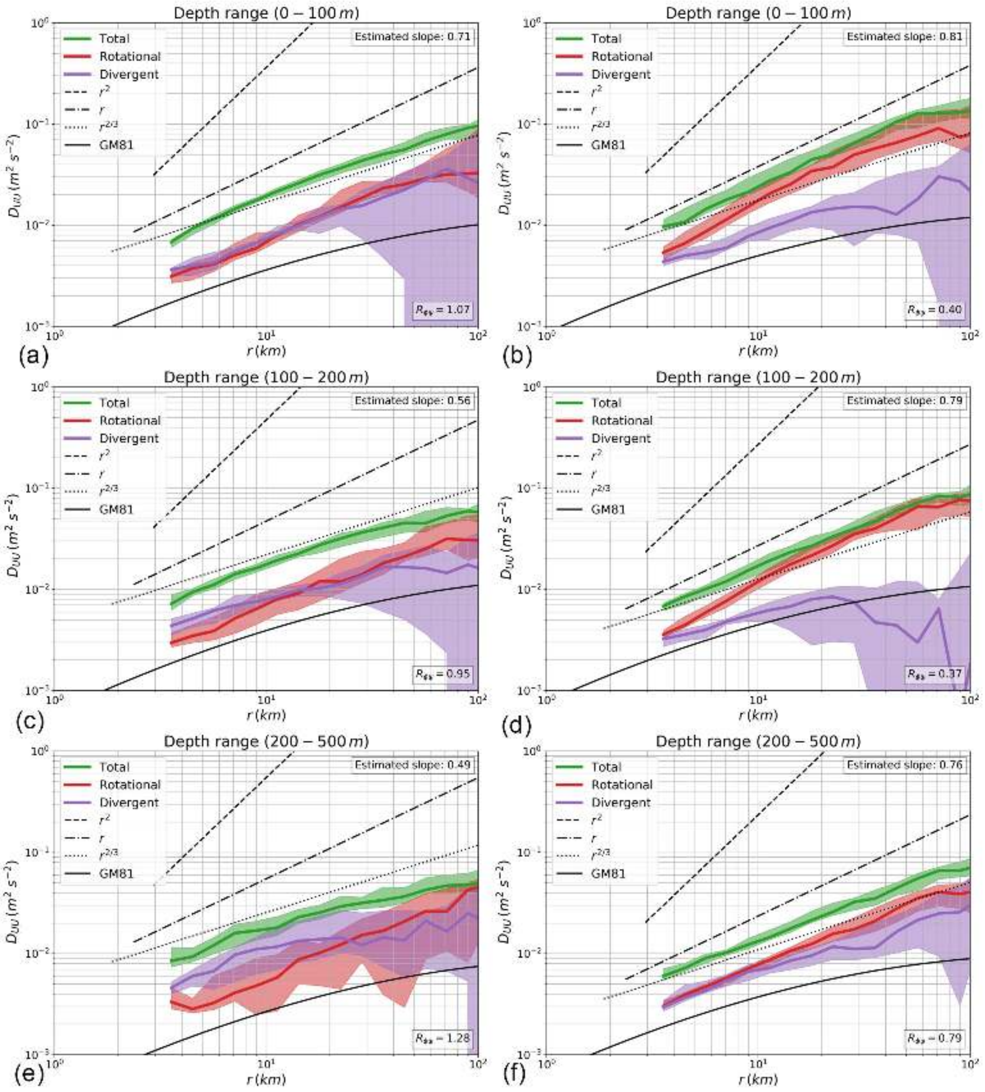

**Figure I.35:** From Sérazin et al. (2020). Mean velocity structure functions computed for the region north **(a,c,e)** and south **(b,d,f)** of New Caledonia for three different depth ranges (0-100 m, 100-200 m, 200-500 m. Shown are the velocity structure functions for the full (green), rotation (red), and divergent(purple) regime. Following oceanic turbulence, the classic power laws $r^2$, $r$, $r^{2/3}$ as well as the Garrett-Munk spectrum (GM81) are given as reference.

in along-ship track direction allows to access wavelengths in the range 3-100 km, thereby enabling the study of submesoscale dynamics. Their analysis suggests the predominance of rotational contributions from submesoscale dynamics associated with frontogenesis and mixed layer instabilities south/southeast of New Caledonia near the surface (Fig. I.35b,d). With increasing depth, the rotational component decreases in importance, i.e. the ratio of the rotational and the divergent component is close to unity (Fig. I.35f). North of New Caledonia, rotational and divergent motion feature similar contributions suggestive for a more turbulent regime involving internal gravity waves (Fig. I.35a,c,e). Seasonal variability has been reported for submesoscale dynamics using thermosalinograph (TSG) data. Submesoscale turbulence peaks in late winter/early spring energized by mixed layer instabilities that are associated with the maximum available potential energy in the cool season.

Given the general scarcity of in-situ observations dedicated to submesoscales, most studies are based on numerical modeling. Prior to this thesis, dedicated modeling studies have not existed for the study region south of New Caledonia. Some high-resolution modeling has been conducted in the northern Coral Sea, i.e. the Solomon Sea (Hristova et al., 2014; Srinivasan et al., 2017). Even though not directly representative for the governing dynamics around New Caledonia, these studies gave first insight into submesoscale dynamics such mixed layer instabilities and frontogenesis. Submesoscale motion was found to follow the seasonal wind stress and surface heat flux cycle. Further, the region's complex bathymetry gives rise to highly non-linear submesoscale coherent vortices.

### I.4.3 Hot spot of internal tide generation and marine biodiversity

The southwestern tropical Pacific Ocean has been long considered as a potential site for strong internal tide generation due to the complex bathymetry such as oceanic ridges, continental shelf breaks, seamounts, and island chains. Early model efforts supported this view (Niwa and Hibiya, 2001), being confirmed by the first efforts in global internal tide mapping using satellite altimetry (Ray and Zaron, 2016). The sea surface height amplitude of the M2 internal tide from Ray and Zaron (2016) is explicitly shown for the southwestern tropical Pacific Ocean in Fig. I.36. These estimates first shed light on the large-scale spatial distribution of tidal energy from an observational perspective. Focusing on New Caledonia, two distinct generation sites have become apparent north and south of New Caledonia that express in sea surface height amplitude of more than 4 cm (red stars in Fig. I.36) with possible tidal energy propagation southwestward and northeastward. No dedicated studies exist up to this date that investigate the tidal dynamics in full detail around New Caledonia.

Internal tides are considered to have important implications for coastal temperatures and marine ecosystems, thriving biological productivity, biodiversity, and overall ecological processes. In particular, internal tides enhance upwelling of cold, oxygen-, and nutrient-rich waters to the surface with implications for the chlorophyll content (Wolanski and Pickard, 1985; Leichter et al., 2003; Wolanski et al., 2004; Wang et al., 2007; Jan and Chen, 2009; Muacho et al., 2013). The upwelling of colder waters plays an active role mitigating heat stress (Wyatt et al., 2020, 2023). Thus, they are

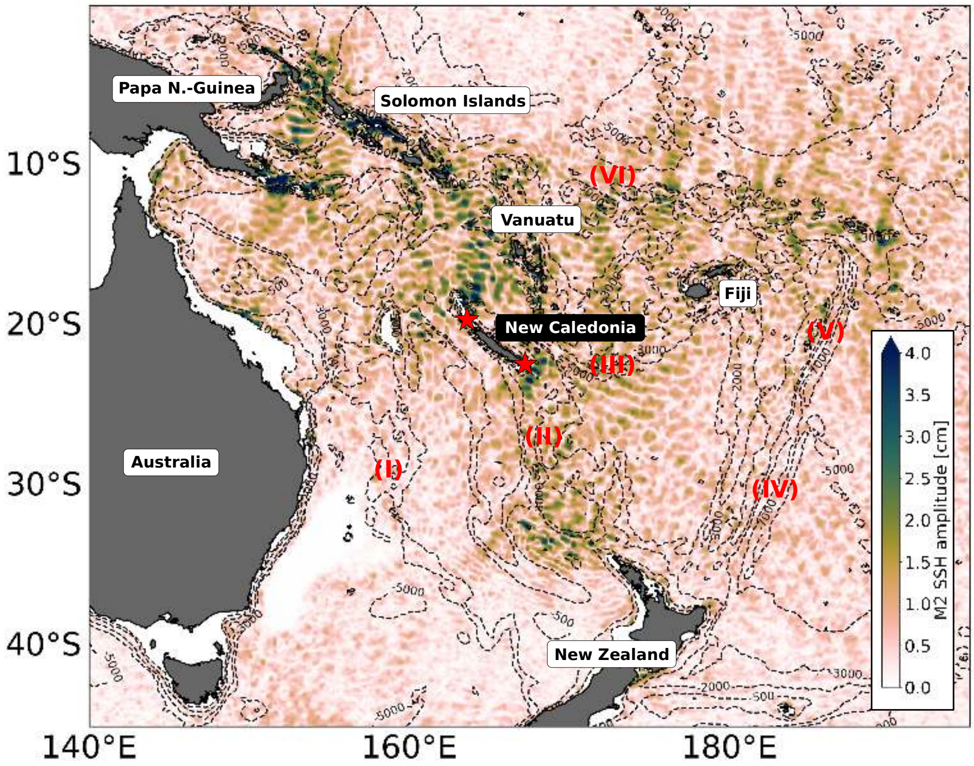

**Figure I.36:** Reproduced from Ray and Zaron (2016). Amplitude of M2 coherent internal tide in the Southwestern Tropical Pacific estimated from satellite altimetry. The main islands and countries are given. The red stars represent internal tide generation sites north and south of New Caledonia. Some of the large-scale bathymetric features are highlighted: (I) Lord Howe Rise, (II) Norfolk Ridge, (III) New Hebrides Trench, (IV) Kermadec Trench, (V) Tonga Trench, (VI) Vitiaz Trench.

considered important in partly counteracting the increasingly progressive bleaching of coral reefs due to climate change induced rising sea surface temperatures by acting as a thermal buffer (Green et al., 2019; Storlazzi et al., 2020).

New Caledonia is recognized for its outstanding marine biodiversity and coral reef systems as it holds world heritage status. It stands out by a 750-km long barrier reef surrounding New Caledonia while enclosing a shallow lagoon. South of New Caledonia, seamounts and ridges are also hot spots of biodiversity providing marine habitats for marine mammals, fish, and small-scale organisms (Fig. I.37; Payri and de Forges, 2006; Gardes et al., 2014; Payri et al., 2019). Traditionally, hot spots of biodiversity in the relatively unproductive water of the tropical ocean are explained by the island mass effect (Doty and Oguri, 1956). This was more recently shown for the tropical island of the Pacific Ocean including New Caledonia pointing out the importance of mixing and upwelling processes for the islands' biogeochemical properties (Ganachaud et al., 2010; Menkès et al., 2015; Messié et al., 2022).

Observing and understanding the local impact of internal tides on the ecosystem up to trophic levels is of large socio-economic interest for the island's conservation management of marine protected areas and the associated maintenance of the food web dynamics and food security related to commercial fishing. Several projects have been initiated recently that aim to understand the impact of tidally-driven mixing on temperature, tracer fields, and biogeochemical properties. The ScInObs (Science, Innovation and Observatories of seamounts) project led by the French Research Institute for Exploitation of the Sea (IFREMER) and in collaboration with the Japan Agency for Marine–Earth Science and Technology (JAMSTEC) south of New Caledonia at the Stylaster seamount is an example for such an effort.

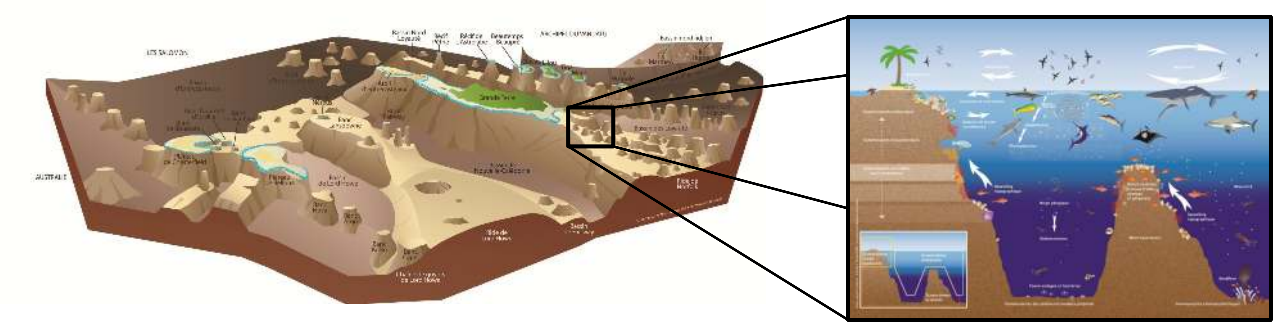

**Figure I.37:** Adapted from Gardes et al. (2014). Three-dimensional schematic of the New Caledonia bathymetry illustrating the large-scale Lord Howe Rise and the Norfolk Ridge system, where the latter gives rise to the main New Caledonia island (denoted Grande Terre). Seamounts are ubiquitous in the region, i.e. south of New Caledonia along the Norfolk Ridge. The inset visualizes the role and importance of bathymetric features and seamounts for the marine ecosystem and biodiversity.

## I.5 Objectives of this thesis

The scientific interest in high-frequency motion such as internal waves or, specifically, internal tides has continuously increased among in-situ observations, satellite altimetry, and numerical modeling. Internal tides are ubiquitous in the global ocean, though they are intensified at specific generation hot spots. Internal tides are considered an important source of unbalanced baroclinic energy while providing a potential route to energy dissipation. In the context of the SWOT mission, internal tides represent a challenge for SWOT's SSH observability of mesoscale and submesoscale dynamics since they can feature wavelengths and SSH variance similar to these balanced motions in regions of pronounced tidal activity.

**The objective of this thesis lies in the understanding of how SWOT's SSH observability of mesoscale and submesoscale dynamics may be limited around New Caledonia, an internal tide generation hot spot in the southwestern tropical Pacific with moderate to elevated mesoscale activity.**

A tailored state-of-art regional modeling effort, explicitly designed for this thesis, will be used to address the above objective. A valuable in-situ data set from autonomous underwater gliders will complement the numerical simulation output to assess the regional model's realism of internal tide dynamics and SSH signature. Consequently, the thesis is subdivided into three different subjects (A, B, and C) as listed below along with their corresponding research questions. In addition, this thesis consists of a perspectival section with preliminary results that motivate future investigations.

### A Coherent internal-tide dynamics and sea surface height signature around New Caledonia

As a first step, this part addresses the first comprehensive description of coherent internal-tide characteristics around New Caledonia using high-resolution regional modeling. This region is known as an internal-tide generation hot spot from satellite altimetry and basin to global-scale ocean general circulation models. A detailed description of high-frequency internal tide motion around New Caledonia does not exist in literature yet. The gained knowledge will not only help quantifying the governing dynamics at place but aims to contribute to future studies concerning the role of internal tides on marine biodiversity around New Caledonia. The following scientific questions will be addressed:

**1) What regions and bathymetric structures are subject to strong internal- tide generation around New Caledonia?**

**2) In what regions do we expect elevated tidal energy dissipation? What fraction of locally generated tidal energy is dissipated in the near-field?**

**3) Is the internal tide dominated by low- or high-vertical mode dynamics?**

**4) How do internal tides express in SSH variance and at what wavelengths? How do SSH variance and wavelengths compare with balanced motion?**

## B Tidal incoherence and implications for sea surface height observability around New Caledonia

As a second step, building upon the high-resolution regional modeling effort above, the temporal variability of the internal tide, i.e. tidal incoherence, is investigated. Tidal incoherence is known to arise from stratification changes or interactions with background currents such as mesoscale eddies. The analysis aims to provide insight into the fate of the internal tide as it propagates from the generation site toward the open ocean. Insight is given into the following questions:

**1) What regions are expected to feature increased levels of tidal incoherence around New Caledonia and what is its fraction to the total tidal variance?**

**2) What are sources of tidal incoherence around New Caledonia both close to the generation site and toward the open ocean?**

**3) How does tidal incoherence manifest in SSH? How much does it contribute to SSH variance? What are potential implications for SSH observability of balanced motion?**

## C Internal tides inferred from autonomous underwater gliders around New Caledonia

As a third step, insight into internal-tide dynamics is given by available in-situ observations from autonomous underwater gliders. Glider observations are used to infer internal-tide motion within a specific region with a large spatial extent. In addition, the glider observations may serve to assess the regional model's realism of internal tide. The following question are considered:

**1) Are glider observations around New Caledonia suitable to infer internal-tide characteristics? How do glider observations compare with regional modeling?**

**2) Can glider observations serve as an in-situ observation platform to deduce the SSH signature of internal tides?**

## D Impact of internal tides on cross-scale energy exchanges

Finally, in a dedicated section, this thesis also gives an outlook on eddy-internal tide interactions in a wider context by making use of a twin regional model configuration with and without tidal forcing. In detail, this section aims to contribute to our understanding of how internal tides affect cross-scale energy exchanges. Literature and some pioneer modeling studies suggested that unbalanced wave motion may provide a route to energy dissipation. Particularly, they break the geostrophically constrained flow and the associated inverse energy cascade and promote a downscale energy flux to smaller scales where three-dimensional dissipation acts. The following questions are addressed:

**1) Do internal tides affect cross-scale energy exchanges by modifying kinetic energy fluxes?**

**2) Do internal tides affect the length scale at which the inverse energy cascade transitions into the forward energy cascade?**

The thesis manuscript is organized as follows. Chapter II introduces the high-resolution regional numerical modeling effort and the underlying methodologies for the tidal analysis. In addition, the available glider observations are presented along-side a description of how internal tides were extracted from the given data sets. Chapter III presents the results acquired during the thesis, subdivided into **(A)** the coherent internal tide characteristics (Sect. III.1) , **(B)** tidal incoherence (Sect. III.2), **(C)** the in-situ glider approach (Sect. III.3), and **(D)** the impact of internal tides on cross-scale energy exchanges (Sect. III.4). The thesis is being wrapped up by a final conclusion along with a description of potential routes for future work in the Conclusion and Perspectives.

## Chapter II

# Methodology

---

## Contents

# II

# Methodology

This thesis is dedicated to two different approaches to deduce into internal-tide dynamics around New Caledonia: regional numerical modeling and in-situ observations from autonomous underwater gliders. While the focus lies on the regional numerical modeling effort, the glider observations play a important role to gain insight from in-situ perspective. That being said, these two data sets do not stand alone, but they will complement each other to the largest extent possible. This chapter aims to introduce the numerical modeling effort, along with the key analyses conducted to deduce tidal and mesoscale to submesoscale motions, as well as the available glider surveys alongside their specific data analysis.

## II.1 Model description and dedicated simulations

In the framework of this thesis, a tailored high-resolution modeling effort has been initiated in cooperation with OceanNext (Grenoble, France) and the MultiscalE Ocean Modeling (MEOM) research group at the Institute des Géosciences de l'Environment (IGE), Grenoble (France). The model is based on the Nucleus for European Modeling of the Ocean (NEMO, code version 4.0.6, Madec and Team) and solves the three-dimensional primitive equations, i.e. the Navier-Stokes equations, on a staggered Arakawa-C type grid.

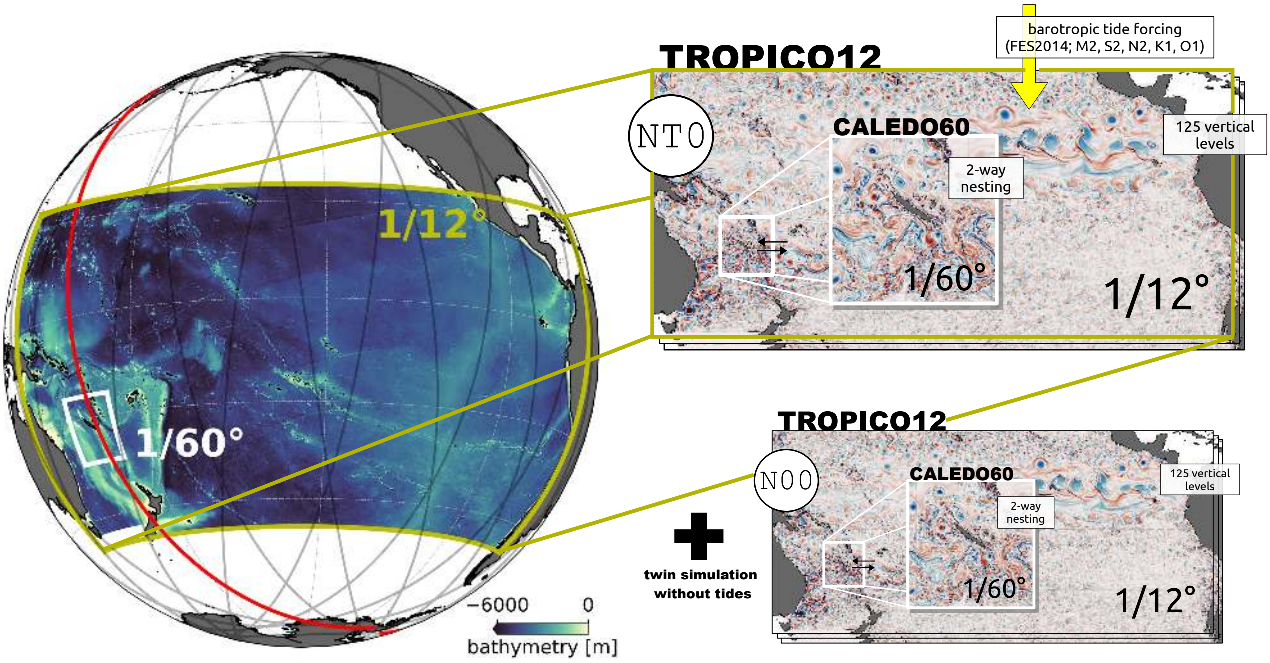

**Figure II.1:** Schematic of the model configuration showing bathymetry (shading) and the domain extent for TROPICO12 (1/12°, host grid) in the Pacific Ocean basin and CALEDO60 (1/60°, nesting grid) in the southwestern tropical Pacific encompassing New Caledonia. The 1-day repeat orbit of SWOT's fast-sampling phase is also shown (gray line) with the highlighted ground track which passes by New Caledonia (red line). The inset schematic shows a snapshot of relative vorticity. The model configuration consists of 125 vertical levels. The model explicitly resolves tidal motion (NT0). Within the domain, it is forced by the tidal potential of the five major tidal constituents. At the lateral boundaries of TROPICO12, barotropic SSH and currents are forced by the same tidal constituents taken from the global tide atlas FES2014 (Finite Element Solution 2014, Lyard et al., 2021). A twin simulation also exists. If features identical forcing and parameterization but without barotropic tide forcing (N00).

### II.1.1 Model configuration

The model grid consists of a host grid, denoted as TROPICO12, which spans the Pacific Ocean basin from 142° E - 290° E and 24° N - 46° S using a curvilinear orthogonal grid with 1775 and 926 grid points in longitude and latitude, respectively (Fig. II.1). It features 1/12° horizontal resolution and 125 vertical levels with 0.5 m thickness at the surface increasing toward 150 m in the deep ocean with 75 vertical levels in the upper 1000 m. Further, the model employs a partial step z-coordinate with a non-linear free surface.

In order to study fine-scale processes around New Caledonia, the model configuration features a horizontal grid refinement, named CALEDO60. At 1/60° horizontal resolution, equivalent to ∼1.7 km grid-box spacing, the model is expected to be submesoscale-permitting in this particular region. Located in the Southwestern Tropical Pacific, the nesting grid spans from 159.2° E - 172.4° E and 15.7° S - 28.8° S, encompassing New Caledonia with 788 and 853 grid points in longitude and latitude. The nesting grid's location is sketched in Fig. II.1 and explicitly shown in Fig. II.2 with southern hemisphere representative summer and winter snapshots of surface relative vorticity illustrating the emergence of small-scale dynamics in winter.

For such regional simulations, the influence of remote motions on high-frequency oceanic variability holds significant importance as it can represent a substantial source of energy, as previously demonstrated by studies such as Nelson et al. (2020), Mazloff et al. (2020), and Siyanbola et al. (2023). The nesting was set up using an Adaptive Grid Refinement in Fortran (AGRIF, Debreu et al., 2008). AGRIF is explicitly designed for NEMO to set up a regional simulation embedded a in pre-defined configuration. Specifically, it enables the two-way lateral boundary coupling between the host (TROPICO12) and nesting grid (CALEDO60) during the whole length of the simulation. The two-way nesting has been favored over one-way nesting (from the host grid to the nesting grid) because of its ability to conserve mass and energy with

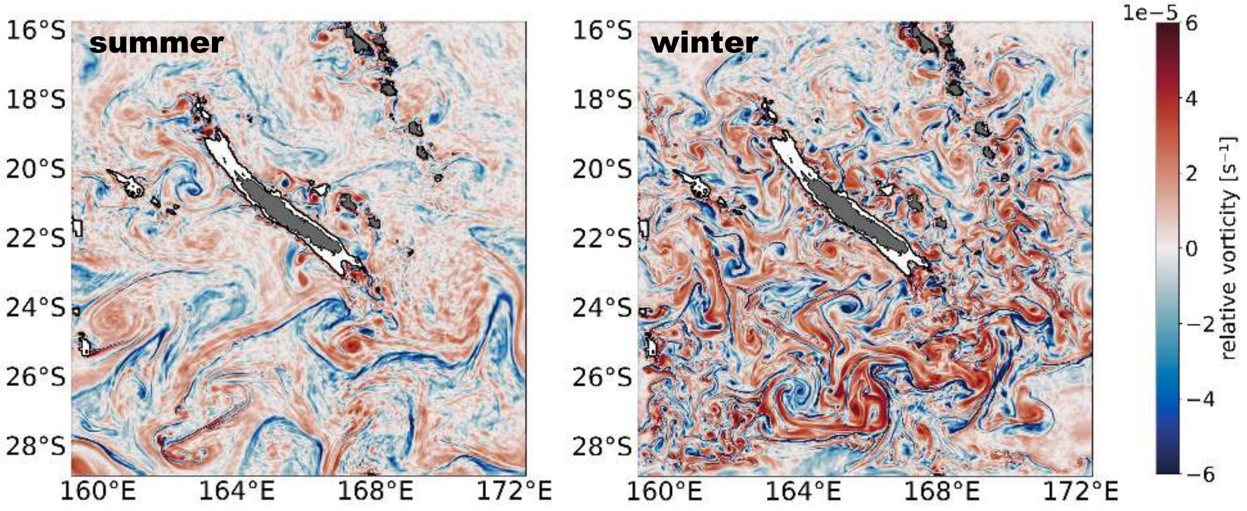

**Figure II.2:** CALEDO60 (1/60°) surface relative vorticity from the simulation with tides (NT0) for southern hemisphere representative **(left)** summer and **(right)** winter snapshots. Note the emergence of small-scale dynamics in winter.

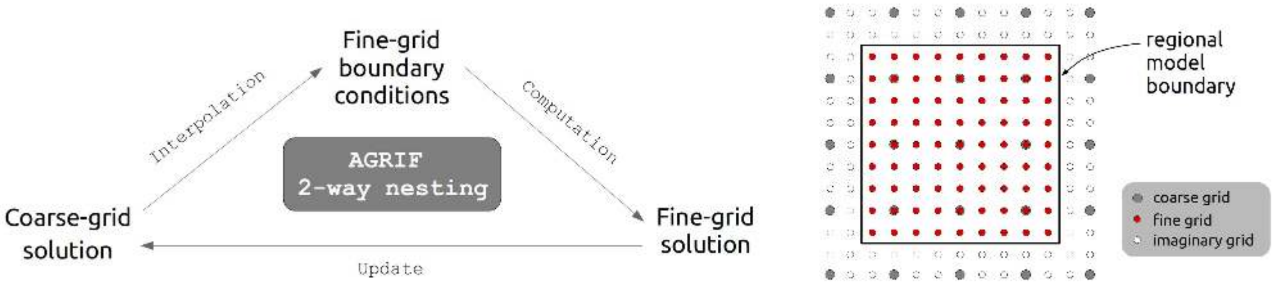

**Figure II.3:** Schematic illustrating the two-way lateral boundary coupling between the host and nesting grid. The coarse-grid solution and fine-grid solution refer to TROPICO12 and CALEDO60, respectively.

no evident discontinuities along the nesting boundaries (Jeon et al., 2019).

The two-way coupling and its mechanism are sketched in Fig. II.3. The coarse-grid solution (TROPICO12) is interpolated to define the open fine-grid boundary conditions before computing the fine-grid solution (CALEDO60) at a given time step. The fine-grid solution is then used to update the coarse-grid solution for coarse grid points that lie within the fine grid. At the regional model boundary, the lateral boundary conditions are subject to a relaxation zone to smooth the transition between the host and nesting grids. It is gradually imposed from the boundary over $N$ cells into the nesting domain. Here, the width of the relaxation zone was chosen to be over $N$=10 cells, where the relaxation becomes gradually weaker as one moves into the regional domain away from the boundary line.

In the following, some aspects of the simulation such as boundary forcing, parameterization, and bathymetry are discussed. Table II.1.5 summarizes the model specifications.

### II.1.2 Boundary conditions and forcings

The initial conditions for temperature and salinity in both the TROPICO12 and CALEDO60 domains are prescribed based on the GLORYS2V4 oceanic reanalysis (`https://doi.org/10.48670/moi-00023`). Atmospheric forcing is taken from ERA5 produced by the European Centre for Medium-Range Weather Forecast (ECMWF, Hersbach et al., 2020) provided at an hourly temporal resolution and at a spatial resolution of 1/4° to compute surface fluxes using bulk formulae and the prognostic sea surface temperature from the model. Wind stress is computed following the methodology outlined in Renault et al. (2016), which involves subtracting surface currents from wind speed.

In the tidal simulation (NT0), both domains are forced by the tidal potential of the five major tidal constituents (M2, S2, N2, K1, O1). This limited choice was made to allow the separation of these constituents at monthly timescales. TROPICO12 is forced at its open lateral boundaries with daily currents, temperature, and salinity, likewise using GLORYS2V4. In addition, it is forced by SSH and barotropic currents of the same five tidal constituents taken from the global tide atlas FES2014 (Finite Element Solution 2014, Lyard et al., 2021).

### II.1.3 Sub-grid scale parameterizations

Parameterizations for sub-grid scale physics are essential for accounting for vertical mixing processes and energy dissipation that cannot be physically resolved by the model. These parameterizations typically exhibit significant variability and are fine-tuned based on factors such as the study region and model resolution. They encompass various aspects, including horizontal and vertical diffusivity/viscosity, bottom friction, and mixing resulting from breaking of internal waves, among others. Parameterizations for sub-grid scale physics are presented in the following differentiating between eddy diffusivity for tracers and eddy viscosity for momentum advection.

On the horizontal, a second-order Laplacian diffusion scheme is applied along isopycnal surfaces. The lateral diffusion coefficients for tracers were chosen to be mesh-size dependent such that tracer diffusion is scaled down from the host grid of 93 $m^2$ $s^{-1}$ to the nesting grid of 4 $m^2$ $s^{-1}$. In the vertical direction, eddy diffusivity is estimated using a Turbulent Kinetic Energy (TKE) closure scheme (Madec and Team). This scheme is based on a prognostic equation for turbulent kinetic energy and employs a closure assumption that considers factors such as vertical shear, stratification, vertical diffusion, and dissipation. To parameterize momentum advection, a third-order Upstream-Biased Scheme (UBS) is employed that relies on parabolic interpolation (Madec and Team). This scheme effectively accounts for both lateral and vertical mixing replacing the second-order Laplacian operator and the TKE closure scheme, respectively.

In NEMO, the hydrostatic assumption is made, i.e. the vertical momentum equation represents the balance between the vertical pressure gradient and the buoyancy force. Thus, convective processes are not accounted for and must be parameterized. Traditionally, an enhanced vertical diffusion (EVD) scheme is used. It relies on the assignment of very large values of vertical eddy mixing coefficients in regions where stratification is unstable. Here, a non-penetrative convection (NPC) scheme was chosen, which is computationally more expensive, but a more physical representation of convection processes (Madec and Team). It mixes conservatively and iteratively water properties from cell $k$ down to cell $k + N$ until the whole water column has become statically stable. In practice, sensitivity experiments conducted by the NEMO community have revealed minimal to negligible distinctions between the two schemes. The primary advantage of the NPC scheme lies in its ability to produce a clean vertical eddy diffusivity output, which can be susceptible to contamination in the EVD scheme due to the enforced increase of eddy mixing coefficients (Laurent Brodeau, personal communication).

Bottom friction was parameterized using a logarithmic boundary layer with a drag coefficient of $3{\times}10^{-3}$ (maximum value of 0.1), a roughness of $2.5{\times}10^{-3}$ m, and a background kinetic energy of $1{\times}10^{-2}$ $m^2$ $s^{-2}$. These values were ultimately selected because, when tested against the output of the model's primary spin-up phase, they exhibited the most favorable visual agreement with the mean regional circulation, i.e. the location and magnitude of zonal jets in the Coral Sea.

The parameterization of mixing induced by breaking internal waves, as originally developed by St. Laurent et al. (2002) is commonly employed in NEMO simulations. Here, it is disabled. Typically, this parameterization is used in coarse-grid ocean general circulation models to account for the mixing contribution of breaking internal waves. But recent advances in numerical simulation resolution have enabled increasingly detailed representations of the internal gravity wave continuum. Despite these advancements, many model configurations still incorporate parameterization schemes for ocean interior mixing, such as the K-Profile Parameterization (KPP) scheme used in the MITgcm (LLC4320). This practice can potentially lead to double accounting for internal wave-induced mixing. To address this concern, Thakur et al. (2022) demonstrated that deactivating the background components of the vertical mixing scheme can enhance modeled energy levels. This adjustment brings the model into closer agreement with in-situ observations, particularly as the model's vertical resolution increases.

### II.1.4 Bathymetry

Particular emphasis was placed on achieving a realistic representation of the bathymetry within the nesting grid, a crucial factor in enhancing the predictability of tidal dynamics. To achieve this, we utilized a specific bathymetry data set derived from GEBCO_2019 and a compilation of multibeam echosounder data collected over the years in the New Caledonia economic zone (Roger et al., 2021). The initial multibeam echosounder data, with a horizontal resolution of 200 m, covers the region spanning from 155° to 175.1° E and 14.1° to 26.6° S. To encompass the entire nesting grid, we integrated this dataset with the GEBCO_2019 bathymetry product (GEBCO, 2019). This comprehensive approach ensures that fine-scale bathymetric features, including ridges and seamounts around New Caledonia, which are potential sources of internal tide generation, are accurately represented. The bathymetry is explicitly shown for

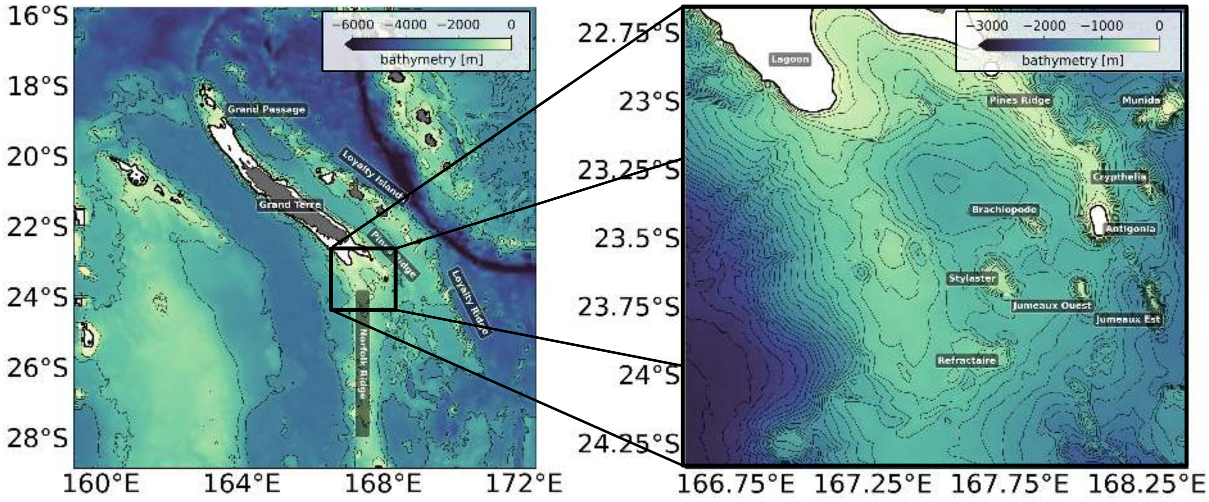

**Figure II.4:** CALEDO60 bathymetry with the main bathymetric features. The thin black lines represent the 1000 m, 2000 m, and 3000 m depth contours. The thick black line is the 100 m depth contour representative for the New Caledonia lagoon. A zoom is given for the region south of New Caledonia close to Pines Ridge. Prominent seamounts are also shown. The depth contour interval is 100 m. This region is characterized by major internal tide generation and it is subject to the SWOTALIS in-situ experiment carried out in the SWOT-AdAC framework. Note the different colorbar scales.

**Table II.1:** Model specifications for CALEDO60 and TROPICO12. Note that the simulation without tides (N00) differs to the simulation with tides (NT0) only by the tidal forcing.

| | **TROPICO12** | **CALEDO60** |
|---|---|---|
| **Domain** | (Sub)tropical Pacific | New Caledonia |
| | 142° W - 70° E<br>46° S - 24 ° N | 159.2° W - 172.4° W<br>15.7° S - 28.8° S |
| **Horizontal resolution** | 1/12° | 1/60° |
| **Vertical resolution** | 125 levels | |
| | 0.5 m (surface)<br>150 m (bottom) | |
| **Output** | | |
| - 3D fields | daily averaged | hourly instantaneous |
| - surface fields | hourly averaged | hourly instantaneous |
| **Boundary conditions** | GLORYS2V4 | |
| **Atmospheric forcing** | ERA5 ECMWF | |
| **Tidal forcing** | M2, S2, N2, K1, O1 | |
| **Bottom drag** | $3 \times 10^{-3}$ | |
| **Bottom roughness** | $2.5 \times 10^{-3}$ m | |
| **Background kinetic energy** | $1 \times 10^{-2}$ m$^2$ s$^{-2}$ | |
| **Lateral eddy diffusivity** | 93 m$^2$ s$^{-1}$ | 4 m$^2$ s$^{-1}$ |
| **Lateral eddy viscosity** | UBS advection scheme | |
| **Vertical eddy diffusivity** | TKE closure scheme | |
| **Vertical eddy viscosity** | UBS advection scheme | |
| **Bathymetry** | GEBCO2019 | GEBCO2019 &<br>multibeam echosounder |

the CALEDO60 domain in Fig. II.4 including a zoom for the region south of New Caledonia, which will be shown to be a major internal tide generation site.

### II.1.5 Numerical integration, data storage, and challenges

The model was run and stored on the high-performance computing machine Occigen at CINES (Centre Informatique National de l'Enseignement Supérieur) with support from the MEOM/IGE group. The model configuration was spun-up for 2 years (model years 2012-2013) before being run for a total of five years (model years 2014-2018) providing daily averaged outputs for TROPICO12 and hourly instantaneous output for CALEDO60. The variables saved are potential temperature, practical salinity, the three-dimensional velocity vector, vertical momentum diffusivity, vertical heat diffusivity, and the time-varying three-dimensional metric for the vertical cell thickness at w-points in addition to SSH, sea surface temperature, sea surface salinity, and surface fluxes and wind stress. We have performed a twin simulation experiment with (NT0) and without tidal forcing (N00). The objective of these two simulations lies in the deeper understanding of how tides, i.e. internal tides, impact mesoscale and submesoscale processes including energy transfers among spatial scales.

The numerical integration and the model output required large computational resources. The CALEDO60 (TROPICO12) output accounts for 10.2 TB (1.6 TB) per year and simulation for the five years (2014-2018). This gives for the five years of simulation together with the two-year spin-up a total of 165 TB for both simulations (NT0 and N00). This amount of data requires large computational resources both for the actual model integration and offline post-processing. Because of a renewal of the computing resources at CINES starting early 2022, i.e. the replacement of Occigen by Adastra, a smooth work flow could no longer be guaranteed anymore due to lacking computational resources, server maintenance, and finally a complete shutdown of Occigen.

Consequently, the model simulation was migrated on the high-performance computing center of CNES (Centre national d'Études spatiales, HAL cluster). However, due to limited storage capacity on HAL, the data transfer was restricted to one year of model data. The choice was made to use the full-model calendar year 2014 for both simulations N00 and NT0 where the tidal analysis presented in the following have been performed. Another data migration occurred due to the closure of the HAL cluster which is undergoing a gradual replacement by the TREX cluster scheduled for completion by the end of 2023. The migration and file synchronization between HAL and TREX began in spring/summer 2023. It is worth noting that the data analysis in this thesis limited to the full-model calendar year 2014 is due to the shutdown of the CINES Occigen machine.

### II.1.6 Deficiency of the simulated K1 tide

A comprehensive model validation encompassing the large-scale circulation, mesoscale eddy variability, and high-frequency motion is provided in Chapter III.1.2. A key factor for the model's realism of internal tide motion is the correct forcing of astronomical tidal potential and the forcing at the open lateral boundaries of TROPICO12. Here, we report a bug that was encountered in the K1 tidal constituent.

TROPICO12 SSH amplitude and phase for the five major semidiurnal (M2, S2, N2) and diurnal (K1, O1) tidal constituents are compared with the empirical estimates from the barotropic tide model FES2014 by which the tidal simulation is forced (Fig. II.5). Note that the modeled tides encompass both barotropic and baroclinic tidal signatures, and even if the main signature is barotropic, modulations at shorter wavelengths of the baroclinic tide are clearly visible. Overall, there is good agreement between TROPICO12 and FES2014 for the semidiurnal M2, S2, and N2 and the diurnal O1 tidal constituents. The amphidromic points are well located and SSH amplitudes are of the same order of magnitude.

However, there is a clear disagreement between TROPICO12 and FES2014 for the

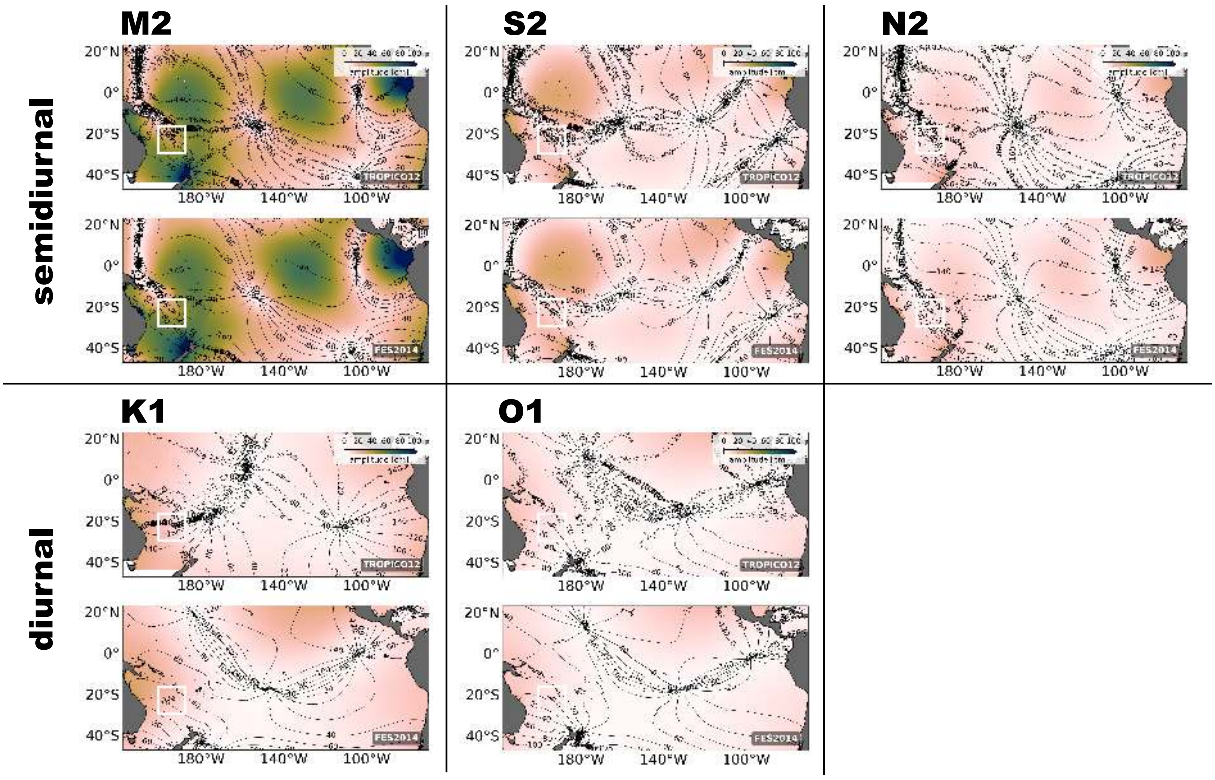

**Figure II.5:** TROPICO12 SSH amplitude (shading) and phase (contour) based on a harmonic analysis of the full-model calendar year time series (model year 2014) for the five major semidiurnal (M2, S2, N2) and diurnal (K1, O1) tidal constituents. Note that the harmonic analysis on the full-model SSH is treated to be representative for the dominant barotropic tide. TROPICO12 semidiurnal and diurnal SSH amplitude are compared with the global barotropic tide atlas FES2014. Note the K1 disagreement between TROPICO12 and FES2014. The white box represents the CALEDO60 domain.

diurnal K1 tide with amphidromic points not located at the right place (Fig. II.5). It clearly impacts the reconstructed time series as illustrated in Fig.II.6 with K1 signatures out of phase between the model and FES2014. This bug went unnoticed until after the completion of the numerical simulation run. The error was eventually found in the tidal potential forcing file for the K1 tide, which was assigned by incorrect astronomical constants. Unfortunately, we were unable to rerun the simulation due to constraints related to computing resources and time limitations. For now, we assume that the erroneous K1 tide plays minor role for the internal tide field since the region around New Caledonia is highly dominated by the semidiurnal internal tide, the M2 tide to be more specific, as shown later.

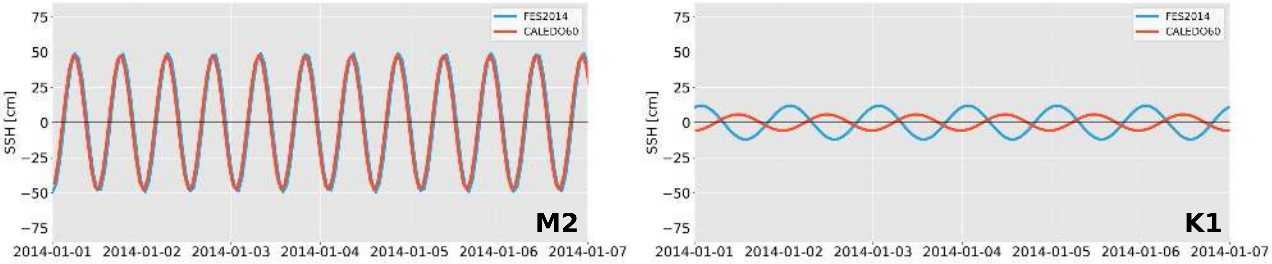

**Figure II.6:** Reconstructed SSH time series shown for **(left)** the M2 **(right)** K1 for an exemplary location within the CALEDO60 domain (171° E, 18° S).

## II.2 Tidal analysis

To investigate the tidal dynamics at play, the full-model three-dimensional regional model (CALEDO60) output at hourly resolution was subject to a tidal analysis including a vertical model decomposition to accurately separate barotropic and baroclinic tides, the extraction of the different tidal components including their coherent and incoherent parts, and the calculation of the different energy terms. The analysis was performed to large part using the COMODO-SIROCCO tools, which are developed and maintained by the SIROCCO national service (CNRS/INSU), funded by INSU and Observatoire Midi-Pyrénées/Université Paul Sabatier and receives project support from CNES, SHOM, IFREMER, and ANR.

Tidal analyses are based on the three-dimensional velocity and pressure fields. Since pressure $p$ is not a direct output of the model simulation, it must be computed from potential density $\rho$ and the surface displacements $\eta_{\mathrm{surf}}$. The pressure was computed individually at each grid point and time step via

$$p = \underbrace{\left[\frac{1}{2}\rho g dz_{\mathrm{surf}} + \eta_{\mathrm{surf}}\right]}_{p_{\mathrm{surf}}} + \sum_{z=1}^{z=-H} \frac{1}{2}\left(\rho^{z+1} - \rho^{z}\right) g dz, \tag{II.1}$$

where $dz$ is the grid cell thickness of the vertical coordinate $z$ and $p_{\mathrm{surf}}$ is the hydrostatic pressure contribution at the surface with $dz_{\mathrm{surf}}$ the grid cell thickness of the uppermost layer.

### II.2.1 Tidal harmonics: the coherent tidal signature

Tidal harmonic analysis is a useful and classic technique to extract the coherent signature (constant amplitude and phase over the period of analysis) of a tidal signal at a given frequency. It is applied to the three-dimensional velocity and pressure fields over the full-model calendar time series (model year 2014) to extract the semidiurnal (M2, S2, N2) and diurnal (K1, O1) tidal constituents. The choice of a full-model calendar year time series relies upon the representative extraction of the coherent tide through a time series long enough to isolate seasonal and mesoscale variability.

Thus, and if not noted otherwise, the harmonic analysis referenced to the full-model calendar year time series is referred to the coherent tide component. Note that at this stage the coherent tide component includes both the barotropic and baroclinic signatures. The separation between barotropic and baroclinic tides is done through a vertical mode decomposition as described below.

### II.2.2 Barotropic-baroclinic vertical mode decomposition

To accurately examine internal tides, it is essential to distinguish between barotropic and baroclinic tides. The barotropic tide is directly influenced by astronomical tidal forcing. Unlike baroclinic tides, it remains unaffected by depth and density stratification (Hendershott, 1981). Here, barotropic and baroclinic tides are separated by a vertical-mode decomposition approach by considering a separation of variables:

$$u(x,y,z,t) = \sum_{n=0}^{9} \widetilde{u}_n(x,y,t)\phi_n(z) \tag{II.2}$$

$$v(x,y,z,t) = \sum_{n=0}^{9} \widetilde{v}_n(x,y,t)\phi_n(z) \tag{II.3}$$

$$p(x,y,z,t) = \sum_{n=0}^{9} \widetilde{p}_n(x,y,t)\phi_n(z) \tag{II.4}$$

and

$$w(x,y,z,t) = \sum_{n=0}^{9} \widetilde{w}_n(x,y,t)\Phi_n(z) \tag{II.5}$$

where $\phi_n$ describes the vertical structure of horizontal velocity and pressure and $\Phi_n$ describes the vertical structure of vertical velocity (see Sect. II.2.2). Individual modes exhibit horizontal propagation characteristics, the sum of multiple modes with different phase relationships give rise to vertical propagation in the resulting composite structure. The modes are defined by solving the Sturm-Liouville problem obeying a linearized free surface and a flat bottom (see Equations I.31 - I.34).

In practice, we have solved the Sturm-Liouville eigenvalue problem individually at every grid point within the regional model domain. This was achieved by utilizing the annual mean density field. We focused on computing the solutions for the ten lowest modes, where the lowest mode ($n = 0$) corresponds to the barotropic tide, and $n \geq 1$ corresponds to the baroclinic modes. Based on the tidal harmonics determined in Sect. II.2.1, the model variables were projected onto the orthogonal, discrete set of normal vertical modes. The baroclinic tide is defined as the sum of modes 1-9.

### II.2.3 Energy equations

The barotropic and baroclinic energy equations, as defined in Sect. I.2.2, were used to study the coherent internal-tide characteristics in Sect. III.1.2. They are applied on the harmonically fitted variables (see Sect. II.2.1), decomposed into their barotropic and baroclinic components.

Recalling Equation I.39, $\langle \boldsymbol{u}_{bt}\, p_{bc}(-H)\rangle$ is computed following Zilberman et al. (2009):

$$\langle \boldsymbol{u}_{bt}\, p_{bc}(-H)\rangle = \frac{1}{2}\, A_{p_{bc}(-H)}\, A_{\boldsymbol{u}_{bt}}\, \cos(\varphi_{p_{bc}(-H)} - \varphi_{\boldsymbol{u}_{bt}}), \tag{II.6}$$

where $A$ and $\varphi$ are the respective amplitude and phase of the tidal harmonic obtained from $p_{bc}$ and $\boldsymbol{u}_b t$. The conversion for each mode $n$ is given by:

$$C^n = \boldsymbol{\nabla}_h H \langle \boldsymbol{u}_{bt}\, p^n_{bc}(-H)\rangle, \tag{II.7}$$

where $p^n_{bc}(-H)$ is the baroclinic pressure at the ocean bottom $(-H)$ for mode $n$. Equivalent to Equation II.6, we compute for each mode $n$:

$$\langle \boldsymbol{u}_{bt}\, p^n_{bc}(-H)\rangle = \frac{1}{2}\, A_{p^n_{bc}(-H)}\, A_{\boldsymbol{u}_{bt}}\, \cos(\varphi_{p^n_{bc}(-H)} - \varphi_{\boldsymbol{u}_{bt}}) \tag{II.8}$$

The propagation of barotropic and baroclinic tide energy is expressed by the energy flux ($\boldsymbol{F}_{bt}$ and $\boldsymbol{F}_{bc}$) and is considered here as a depth-integrated quantity:

$$\boldsymbol{F}_{bt} = \int_{-H}^{\eta} \langle \boldsymbol{u}_{bt}\, p_{bt}\rangle\, dz, \tag{II.9}$$

$$\boldsymbol{F}_{bc} = \int_{-H}^{\eta} \langle \boldsymbol{u}_{bc}\, p_{bc}\rangle\, dz, \tag{II.10}$$

where $p_{bt}$ is the barotropic pressure, and $\boldsymbol{u}_{bc} = (u_{bc}, v_{bc})$ is the baroclinic velocity vector. The baroclinic energy flux for each mode $n$ is defined as:

$$\boldsymbol{F}^n_{bc} = \int_{-H}^{\eta} \langle \boldsymbol{u}^n_{bc}\, p^n_{bc}\rangle\, dz, \tag{II.11}$$

where $\boldsymbol{u}^n_{bc}$ is the baroclinic velocity vector for mode $n$. Note that the average over a tidal cycle follows the same methodology as for the conversion term above. The barotropic ($D_{bt}$) and baroclinic ($D_{bc}$) dissipation is regarded as the residual of the energy flux divergence and conversion and, hence, obtained through Equation I.37 and I.38, respectively:

$$D_{bt} = -C - \boldsymbol{\nabla}_h \cdot \boldsymbol{F}_{bt}, \tag{II.12}$$

$$D_{bc} = C - \boldsymbol{\nabla}_h \cdot \boldsymbol{F}_{bc}, \tag{II.13}$$

### II.2.4 Tidal incoherence

By definition, the harmonic analysis as described in Sect. II.2.1 is mostly representative of the coherent component. This thesis also gives insight into tidal incoherence, i.e. temporal variations of the internal tide. The easiest approach to infer temporal variability is to apply a harmonic analysis on monthly data subsets of the full-model calendar year time series (see Sect. II.2.4.1). As described above, this can be taken as a proxy of tidal incoherence since seasonal and mesoscale variability is not sufficiently isolated on monthly timescales. By doing so, we obtain the monthly evolution of the barotropic and baroclinic energy equations from Sect. II.2.3.
A more dedicated approach relies on separating the tidal signal explicitly into its coherent and incoherent part using a bandpass filtering technique.

#### II.2.4.1 Monthly tidal analysis

The tidal analysis, i.e. the harmonic analysis and the barotropic-baroclinic modal decomposition, was not only performed on the full-model calendar year time series, but also on monthly data subsets of that same calendar year. It follows, otherwise, the exact procedure as described in Sect. II.2.1 and Sect. II.2.2, except the coherent tide is referenced to the respective monthly data sets. Note that the monthly time series is just sufficient to separate the semidiurnal and diurnal tidal constituents from each other. In contrast to the full-model calendar year harmonic analysis, the monthly harmonic analysis was only performed for the strongly dominant semidiurnal M2 tide. Even though a harmonic analysis often refers to the coherent component of a signal, the term coherent needs to be taken with caution here since the harmonic analysis on monthly timescales is not expected to be long enough to isolate seasonal and mesoscale variability. The harmonic analysis performed on monthly data subsets will be considered as a proxy for tidal incoherence in Sect. III.2.

### II.2.4.2 Bandpass filtering technique

The incoherent semidiurnal component is deduced from bandpass filtering. This is explained in detail in the following by taking the horizontal velocity component $u$ as example. The full model $u$ is first corrected for the barotropic (depth-average) that gives the baroclinic signal, i.e. $u_{bc}$. Then, the baroclinic signal is bandpass-filtered in the semidiurnal frequency band (10-14 h) to give $u_{bc}^{\mathrm{sd}}$. The incoherent component $u_{bc}^{\mathrm{inc}}$ is finally obtained by subtracting the coherent component $u_{bc}^{\mathrm{coh}}$, reconstructed by summing the M2, N2, and S2 harmonics to obtain a time series for the semidiurnal frequency band, from $u_{bc}^{\mathrm{sd}}$. This approach is commonly used in different papers (e.g. Buijsman et al., 2017).

Our methodology to compute the incoherent component slightly differs from common approaches, such as in Buijsman et al. (2017). We first corrected the full-model $u$ for both the coherent semidiurnal barotropic and baroclinic as obtained from the harmonic analysis and vertical mode decomposition in Sect. II.2.1 and Sect. II.2.2. The resulting variable is then bandpass-filtered in the semidiurnal frequency band (10-14 h) to obtain $u_{bc}^{\mathrm{inc}}$. The differing methodology was pointed out by an anonymous reviewer during the paper review. Comparing both methodologies for an exemplary time series of $u$ reveals that both methodologies give the same result (Fig. II.7).

Here, this method was addressed to compute the incoherent semidiurnal baroclinic energy flux in Sect. III.2. Let $\boldsymbol{u}_{bc}^{sd}$ and $p_{bc}^{sd}$ be the total semidiurnal signal for the horizontal velocity vector and pressure, respectively. Then, the signal can be decomposed into the coherent ($^{\mathrm{coh}}$) and incoherent ($^{\mathrm{inc}}$) semidiurnal contribution, i.e.:

$$\boldsymbol{u}_{bc}^{sd} = \boldsymbol{u}_{bc}^{\mathrm{coh}} + \boldsymbol{u}_{bc}^{\mathrm{inc}} \tag{II.14}$$

$$p_{bc}^{sd} = p^{\mathrm{coh}} + p^{\mathrm{inc}} \tag{II.15}$$

The resulting total semidiurnal baroclinic energy flux can then be written as follows:

$$\boldsymbol{F}_{bc}^{sd} = \frac{1}{T}\int_{t_1}^{t_2}\left[\int_{-H}^{\eta} \overbrace{\boldsymbol{u}_{bc}^{\mathrm{coh}}\, p_{bc}^{\mathrm{coh}}}^{\text{coherent}} + \overbrace{\boldsymbol{u}_{bc}^{\mathrm{inc}}\, p_{bc}^{\mathrm{inc}} + \underbrace{\boldsymbol{u}_{bc}^{\mathrm{coh}}\, p_{bc}^{\mathrm{inc}} + \boldsymbol{u}_{bc}^{\mathrm{inc}}\, p_{bc}^{\mathrm{coh}}}_{\text{cross terms}}}^{\text{incoherent}}\, dz\right] dt, \tag{II.16}$$

$$= \boldsymbol{F}_{bc}^{\mathrm{coh}} + \boldsymbol{F}_{bc}^{\mathrm{inc}}, \tag{II.17}$$

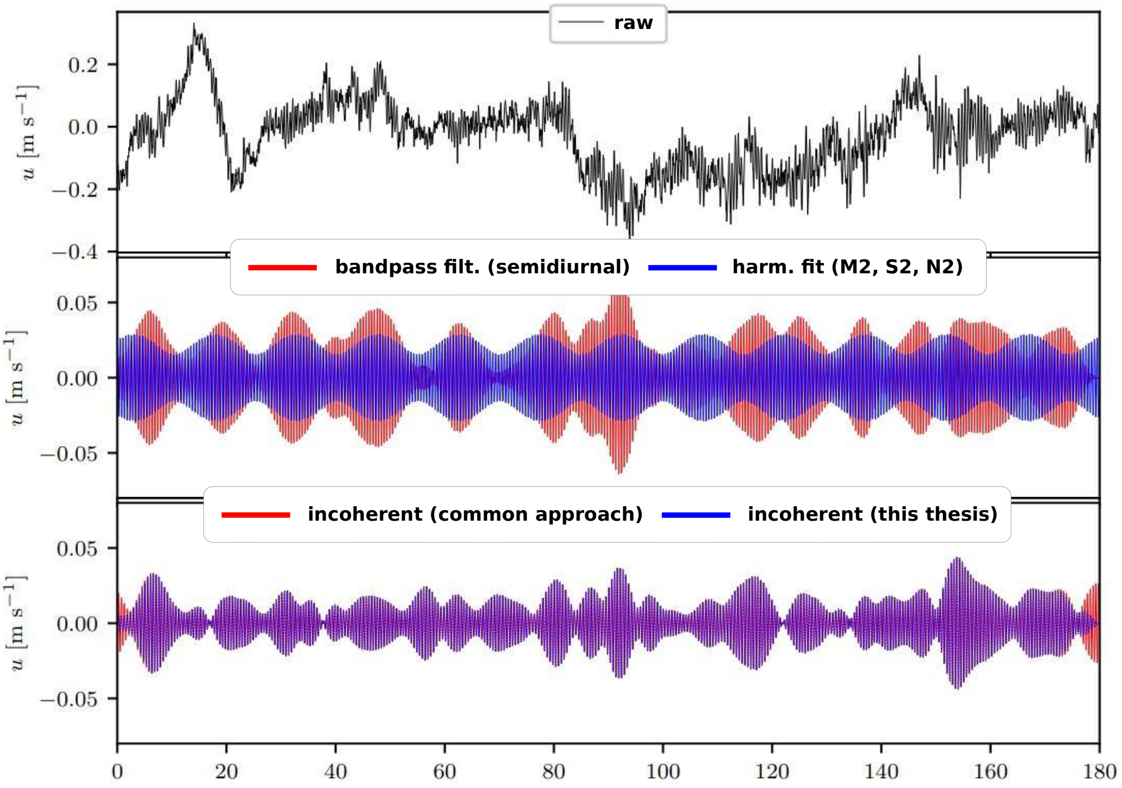

**Figure II.7:** Computation of the incoherent tide component for an exemplary time series (raw, upper panel). (middle panel) Semidiurnal bandpass filter (red) and harmonic analysis (blue) on the raw signal. (lower panel) Incoherent component derived by subtracting the harmonic fit from the bandpassed signal (common approach, red) and incoherent component derived by bandpass-filtering the raw signal corrected by the harmonic fit (this thesis, blue).

for a given averaging time period $[t_1,t_2]$, where the terms $\boldsymbol{u}^{\mathrm{coh}}\ p_{bc}^{\mathrm{inc}}$ and $\boldsymbol{u}^{\mathrm{inc}}\ p_{bc}^{\mathrm{coh}}$ represent the cross terms which are considered to contribute to the incoherent flux. These cross terms were also computed in Sect. III.2, but similarly to Nash et al. (2012) and Buijsman et al. (2017), they are negligible in the annual mean. However, they are not negligible when averaging over shorter time periods.

## II.3 Mesoscale diagnostics

Two main tools have been used to get some insight on mesoscale dynamics and their role on internal-tide dynamics: a ray tracing technique to study the refraction of a tidal beam as it propagates through the mesoscale eddy field and an eddy tracking algorithm to characterize mesoscale eddy properties. Details are provided in the following.

### II.3.1 Ray tracing

A ray tracing technique is applied to study the horizontal propagation of internal gravity modes, primarily, through the mesoscale eddy field around New Caledonia. Particularly, we investigate the refraction of an internal tide beam and the departure from tidal coherence due to mesoscale background currents. We use the methodology proposed by Rainville and Pinkel (2006), which considers the horizontal propagation of a ray for spatially varying topography, climatological stratification, planetary vorticity, and depth-independent currents. Bathymetry is taken from ETOPO2v2 (Smith and Sandwell, 1997). Internal gravity wave speeds are predefined and solved by the Sturm-Liouville problem for stratification from the World Ocean Atlas (Locarnini et al., 2018; Zweng et al., 2019). In the applied approach following Rainville and Pinkel (2006), the propagation of internal waves including information about their trajectories, angles of propagation are ultimately derived from the Hamiltonian function $H$ in the presence of depth-averaged velocities, i.e.:

$$H \equiv \left(c_n^2 - U^2\right) p_x^2 + \left(c_n^2 - V^2\right) p_y^2 + 2Up_x + 2Vp_y - 2UVp_xp_y - 1 + \frac{f^2}{\omega^2}, \quad \text{(II.18)}$$

where $p_x$, $p_y$ are the horizontal momentum components of the wave in the horizontal plane. See Rainville and Pinkel (2006) for a derivation of the above Hamilton function and a detailed description of the ray tracing methodology.

In this thesis, we finally use this ray tracing technique to model the ray path for a range of vertical modes initialized at internal tide generation hot spots and for a given propagation angle. In an iterative procedure, the ray tracing considers for each step size (1 km) bathymetry, climatological buoyancy and planetary vorticity effects, and the background currents. Through the dispersion relation from the Helmholtz equation for internal wave modes assuming a local wave expression, the ray's group and phase velocity are obtained, which are then used to update the ray's position and direction (angle of propagation). To identify the effects of background currents on the ray's path, a no-currents scenario is also given.

In this thesis, the ray tracing is applied on CALEDO60 daily-mean depth-averaged currents (model year 2014) to track the semidiurnal ray path for vertical modes 1-2 initialized at two internal tide generation hot spots north and south of New Caledonia and for a given propagation angle. The results obtained and possible limitations of the ray tracing technique are discussed in more detail in Sect. III.2.3.1. Further, the ray tracing is applied to altimetry-derived geostrophic surface currents from CMEMS to infer tidal beam refraction in in-situ observations (see Sect. III.3).

### II.3.2 Eddy tracking

For various purposes throughout this thesis, an eddy tracking was applied. The choice fell on the Angular Momentum Detection and tracking Algorithm (AMEDA), which is described in full detail in Le Vu et al. (2018). AMEDA provides eddy location as well as eddy characteristics based on the physical parameters and the velocity field geometrical properties. The algorithm first identifies an eddy center which correspond to an extreme of the local normalized angular momentum (LNAM; +1 for cyclonic and -1 for anticyclonic). Streamlines surrounding the LNAM extreme are then computed and mean radius and velocity for each streamline are evaluated. The radius of a circular disc with an area delimited by the closed streamline is analogous to the mean radius, while the circulation along the closed streamline is used to derive the mean velocity. The azimuthal speed increases towards the eddy boundary until maximum speed is reached, whose corresponding radius being equivalent to the speed radius (Chelton et al., 2011; Laxenaire et al., 2018; Le Vu et al., 2018). This closed contour of maximum speed is the "characteristic contour" of the detected eddy. Subsequently, the azimuthal speed decreases within the eddy's outer ring until the last closed streamline is reached. In this thesis, the eddy tracking was mainly applied on CALEDO60 daily-mean depth-averaged currents (model year 2014) to infer spatial variations of eddy rotational speeds in the regional model domain in Sect. III.2.3.1.

## II.4 Submesoscale diagnostics

Submesoscale diagnostics are presented in the following that allow to better characterize the governing dynamics at smaller scales, i.e. scales where rotational (balanced) and non-rotational (unbalanced) effects have equal contribution. Here, we focus on quantities that are potential indicators for submesoscale activity, such as relative vorticity, horizontal divergence, lateral buoyancy gradients, and frontogenesis. In Sect. III.4.2, these quantities are subject to analysis to study seasonal variations of submesoscale processes.

### II.4.1 Relative vorticity

Enhanced values of relative vorticity $\zeta$ are indicative of submesoscale coherent vortices accompanied by large $Ro$ numbers due to increasing importance of fluid inertia at small-scales. It is computed as $\zeta = \frac{\partial v}{\partial x} - \frac{\partial u}{\partial y}$.

### II.4.2 Horizontal divergence

Submesoscale motion also expresses by frontal dynamics, i.e. front and filaments. They have a clear signature in horizontal divergence $\delta = \frac{\partial u}{\partial x} + \frac{\partial v}{\partial y}$ and tend to be positively skewed.

### II.4.3 Lateral buoyancy gradient

The lateral buoyancy gradient was computed as $\boldsymbol{\nabla}_h b = \left(\frac{\partial b}{\partial x}, \frac{\partial b}{\partial y}\right)$, where $b = g((1 - \rho)/\rho_0)$ is the buoyancy. Buoyancy gradients are elevated in regions of submesoscale fronts and filaments. They are required for the computation of frontogenesis.

### II.4.4 Frontogenesis

Following Srinivasan et al. (2017), frontogenesis or frontogenetic tendency $F$ was computed as $F = \boldsymbol{Q} \cdot \boldsymbol{\nabla}_h b$, where $\boldsymbol{Q}$

$$\boldsymbol{Q} = -\left(\frac{\partial u}{\partial x}\frac{\partial b}{\partial x} + \frac{\partial v}{\partial x}\frac{\partial b}{\partial y}, \frac{\partial u}{\partial y}\frac{\partial b}{\partial x} + \frac{\partial v}{\partial y}\frac{\partial b}{\partial y}\right) \qquad \text{(II.19)}$$

For values $F > 0$, the system is denoted frontogenetic and accompanied by the formation of submesoscale fronts and filaments.

## II.5 Kinetic energy spectra and spectral energy fluxes calculations

In Sect. III.4, we investigated the distribution of kinetic energy and cross-scale kinetic energy fluxes. This was done by computing power spectral density of kinetic energy and energy fluxes of the instantaneous horizontal velocity field using two-dimensional horizontal Fourier transformation for an area southwest of New Caledonia. The chosen domain is free of missing data points caused by islands or shallow bathymetric features and it is sufficiently large to encompass a broad wavenumber range, spanning from the large-scale and mesoscale circulation down to submesoscale processes, and high-frequency unbalanced motions (Fig. II.8). This domain has a size of 725 km × 725 km.

The uniform spacing of data points are crucial prerequisites for performing a Fourier transform, as irregular or non-uniformly spaced data can introduce spectral leakage and aliasing artifacts. The data preprocessing follows closely the methodology described in Schubert et al. (2020). We first interpolated the horizontal velocity vector $\boldsymbol{u}_h = (u, v)$ onto the tracer grid points of an Arakawa-C type grid. Second, the geographical coordinates (WGS84, EPSG:4326) are transformed into Cartesian coordinates $x$, $y$ (EPSG:3395). $\boldsymbol{u}_h = (u, v)$ is then interpolated onto a regular 1-km grid. Prior to the Fourier transformation, the horizontal velocity field is corrected for its temporal mean (model year 2014) and it is linearly detrended in both horizontal directions. Since the considered data set is not periodic, nor infinitely large, a hanning window with an amplitude correction factor of 1.5 is applied (Fig. II.8). A tukey window with a shape parameter of 0.5 was also tested. However, it did not yield any notable differences. The computation of power spectral density and spectral energy fluxes is briefly described below.

In Sect. III.4, the focus lies on seasonal variations of kinetic energy spectra and

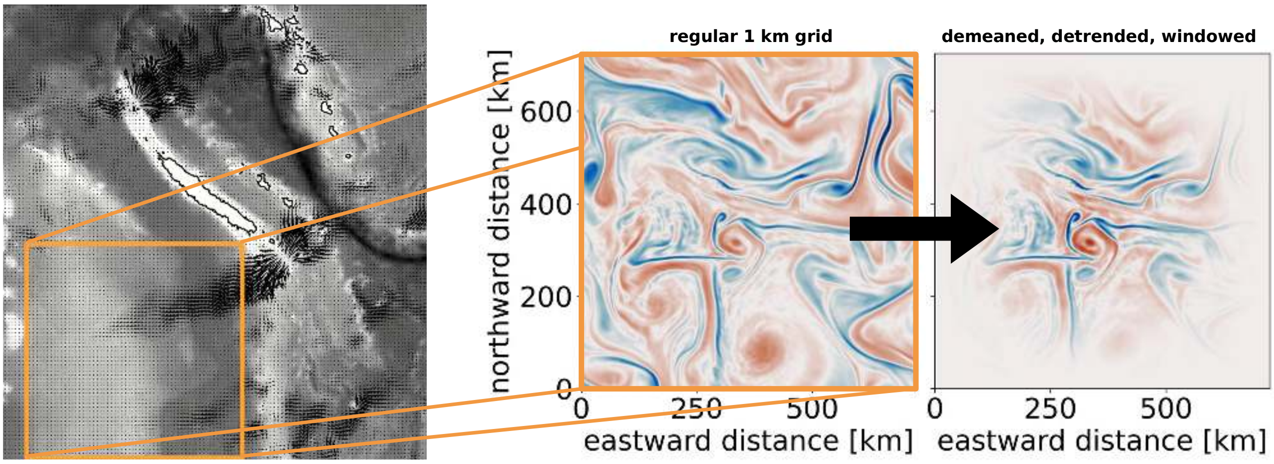

**Figure II.8: (left)** CALEDO60 bathymetry (shading, white: shallow, black: deep) and the depth-integrated semidiurnal coherent internal tide energy flux (vectors). Power spectral density and spectral energy flux are computed the horizontal velocity field extracted for a square-shaped domain of size 725 km × 725 km (orange box). **(right)** The horizontal velocity field, here expressed by relative vorticity, is being transformed to Cartesian coordinates and interpolated on a regular 1 km grid. The two-dimensional Fourier transformation is applied on the demeaned, detrended, and windowed field.

spectral kinetic energy flux. The spectra are subsequently averaged for summer (January-March) and winter (July- September) months. The computation of power spectral density and spectral energy fluxes is briefly described below.

### II.5.1 Kinetic energy spectra

The Fourier transformation of the horizontal velocity field $\boldsymbol{u}_h$, which is given by:

$$\hat{\boldsymbol{u}}_h(k,l) = \frac{1}{(2\pi)^2}\int_{-\infty}^{\infty} \boldsymbol{u}_h(x,y)e^{-i(kx+ly)}dxdy \tag{II.20}$$

where $\hat{\boldsymbol{u}}_h = (\hat{u}, \hat{v})$ is the Fourier transforms of $\boldsymbol{u}_h$, and $k$ and $l$ are the zonal and meridional wavenumber components, respectively. The kinetic energy cumulative power spectrum $\mathrm{E}_{\mathrm{PS}}(K)$ is computed as follows:

$$\mathrm{E}_{\mathrm{PS}}(K) = \frac{1}{N_x^2 N_y^2}\int_0^K \frac{1}{2}\left(\mathrm{Re}\{\hat{u}^*\hat{u}\} + \mathrm{Re}\{\hat{v}^*\hat{v}\}\right) dK, \tag{II.21}$$

where $\hat{u}^*$ and $\hat{v}^*$ are the complex conjugates from $\hat{u}$ and $\hat{v}$. $N_x$ and $N_y$ represent the number of grid points in $x$ and $y$ direction, $K = \sqrt{k^2 + l^2}$ is the isotropic wavenumber, and $\mathrm{Re}$ accounts for the real part. In fact, kinetic energy spectra $E(K)$ are represented by their power spectral density obtained by differentiating the cumulative power spectrum $E_{\mathrm{PS}}(K)$ with respect to $K$:

$$\mathrm{E}(K) = 2\pi\frac{dE_{\mathrm{PS}}}{dK}. \tag{II.22}$$

### II.5.2 Spectral flux calculation

The cross-scale kinetic energy flux quantifies the exchange of kinetic energy by non-linear interactions between current systems of varying horizontal scales. An easy way based on Fourier transformation in spectral space, building upon the preceding section, lies in integrating the Fourier-transform of the non-linear advection term (sco, 2005). Doing so, the spectral kinetic energy flux is defined as:

$$\Pi_{\mathrm{sp}}(K) = -\frac{\rho_0}{N_x^2 N_y^2}\int_0^K \hat{\boldsymbol{u}}_h^* \cdot \left(\widehat{\boldsymbol{u}_h \boldsymbol{\nabla}_h \boldsymbol{u}_h}\right) dK \tag{II.23}$$

$$= -\frac{\rho_0}{N_x^2 N_y^2}\int_0^K \mathrm{Re}\left\{\hat{u}^*\left(\widehat{u\frac{du}{dx} + v\frac{du}{dy}}\right) + \hat{v}^*\left(\widehat{u\frac{dv}{dx} + v\frac{dv}{dy}}\right)\right\} dK, \tag{II.24}$$

where $\widehat{\boldsymbol{u}_h \boldsymbol{\nabla}_h \boldsymbol{u}_h}$ is the Fourier transform of the nonlinear advection term.

As for kinetic energy spectra, the spectral kinetic energy flux is represented by its power spectral density. To minimize computational expenses, spectral energy fluxes are computed on instantaneous snapshots of horizontal velocities at every sixth hour and for every second depth level down to 600 m.

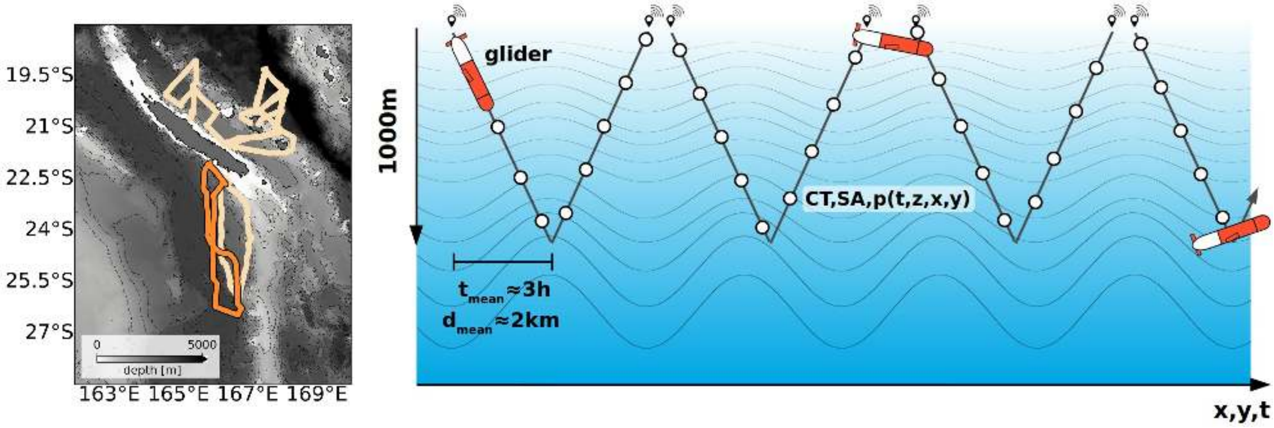

**Figure II.9: (Left)** Available glider surveys around New Caledonia. The highlighted glider track refers to glider mission 2014-1. It is of particular interest as it overlaps in time with the numerical model output of CALEDO60. It is subject to a detailed analysis in Sect. III.3. **(right)** Schematic of a typical glider sampling. Before each descending and after each ascending profile, the glider sends its GPS locations.

## II.6 Glider observations

A unique set of glider surveys is available which provides high-resolution/frequency in-situ measurements of hydrography around New Caledonia. This data set was acquired as part of the Southwest Pacific Ocean Circulation and Climate Experiment (SPICE, Ganachaud et al., 2014; Durand et al., 2017). A total of seven glider missions (notably 2011-5, 2012-1, 2013-3, 2013-4, 2013-5, 2014-1, and 2014-2) are at disposal in the time period between 2011 and 2014 around New Caledonia measuring continuously temperature, salinity, and pressure to a maximum depth of 1000 m in a saw-tooth pattern. The glider tracks are shown in Fig. II.9.

In this thesis, particular interest exists in the glider mission 2014-1 (highlighted in Fig. II.9) since it surveys the region of increased tidal activity. In addition, it overlaps in time with regional numerical simulation output of CALEDO60 allowing for a complementary analysis of numerical modeling and in-situ observations (see Sect. III.3). The primary objective of the glider observations is to study amplitude and phase of internal-tide induced vertical displacements of isopycnals. The underlying methodology is presented in the following.

Glider sampling represents spatio-temporal measurements of hydrography traveling simultaneously in horizontal and vertical direction within the water column while sending its GPS location before each descending and after each ascending profile. This is schematically shown in Fig. II.9. Assuming a dive depth of 1000 m, a typical glider dive (profile) duration is 6 h (3 h) associated with a horizontal displacement of 6 km (3 km). Simple statistics of glider maximum dive depth, dive duration, and horizontal displacement is given in the histograms for glider mission 2014-1 in Fig. II.10.

For further analysis, the collected time series of temperature, salinity, and pressure were divided into descending and ascending profiles by allocating the glider time stamp with the maximum dive depth. The profiles were then gridded into vertical 10 m bins.

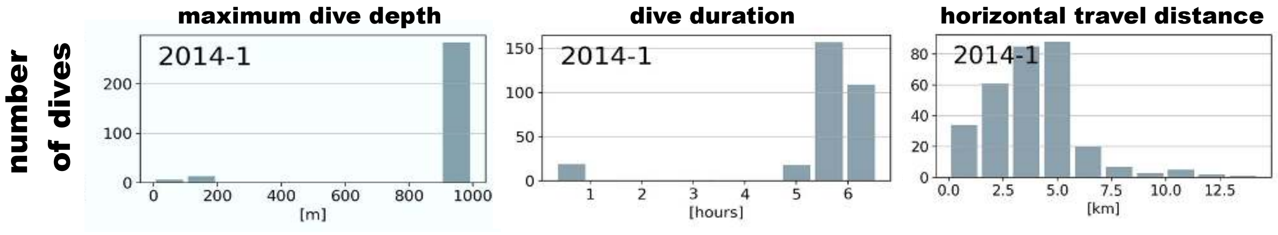

**Figure II.10:** Histograms for **(left)** glider dive depth, **(middle)** dive duration, and **(right)** the horizontal displacement during a glider dive for glider mission 2014-1.

### II.6.1 Least-squares sinusoidal fit of internal tide induced vertical displacements

Internal tide amplitude and phase are deduced by fitting a sinusoidal function on glider vertical displacement using a least-squares method in 3-day running windows. It closely follows the methodology described in Rainville et al. (2013). The fit applied on 3-day running windows accounts for the glider irregular spatio-temporal sampling. The choice of the 3-day window length is ultimately linked to a compromise between (1) a minimum time series length that captures the diurnal period between 18 and 36 h and the semidiurnal period between 10.3 and 14.4 h, (2) an adequate number of tidal cycles within 3 days for the statistical analysis, and (3) a time period during which the internal tide amplitude and phase do not vary significantly during the glider's horizontal displacement. In our case, assuming a dive depth of 1000 m, the corresponding travel distance over 3 days is approximately 50 km. The vertical displacements are calculated for each depth level as follows:

$$\eta = g\frac{\sigma_s - \overline{\sigma}}{\sigma_s \overline{N^2}}, \tag{II.25}$$

where g is the gravitational acceleration, $\sigma_s$ is the sample density, and $\overline{\sigma}$ and $\overline{N^2}$ are the mean density and mean squared buoyancy frequency relative to the 3-day running window, respectively. Further, a linear trend was subtracted which we attribute to sloping isopycnals of low-frequency motion. We fit simultaneously the K1 ($\omega_d$ = $2\pi$/23.9345 h$^{-1}$) and M2 ($\omega_{sd}$ = $2\pi$/12.4206 h$^{-1}$) internal tide for each depth layer and each 3-day time window, i.e.

$$\eta(t,z) = A_d(z)e^{iw_dt+\phi_d(z)} + A_{sd}(z)e^{iw_{sd}t+\phi_{sd}(z)}, \tag{II.26}$$

where $A_d$ and $A_{sd}$ are the diurnal and semidiurnal amplitude, respectively. Equivalently, $\phi_d$ and $\phi_{sd}$ are the diurnal and semidiurnal phases, relative to the Unix epoch (00:00:00 UTC on 1 January 1970). Equation II.26 is solved using a least-squares fit, i.e. we solve for $\mathbf{A}v = \eta(t)$, where $\mathbf{A}$ is the design matrix expressed in terms of its sinusoidal components:

$$\mathbf{A} = \begin{bmatrix} \cos(w_dt_1) & \sin(w_dt_1) & 1 & \cos(w_{sd}t_1) & \sin(w_{sd}t_1) \\ \cos(w_dt_2) & \sin(w_dt_2) & 1 & \cos(w_{sd}t_2) & \sin(w_{sd}t_2) \\ \vdots & \vdots & 1 & \vdots & \vdots \\ \cos(w_dt_n) & \sin(w_dt_n) & 1 & \cos(w_{sd}t_n) & \sin(w_{sd}t_n) \end{bmatrix} \tag{II.27}$$

$v$ is the vector of unknown parameters, i.e. the amplitudes of the cosine and sine components associated with the frequencies $w_d$ and $w_{sd}$, $\eta$ the observed vertical displacements. $n$ is the number of measurements within the 3-day fitting window. Note that even though we solve for the peak frequencies of the K1 and M2 tide, the fitted amplitude and phase are representative for the diurnal and semidiurnal frequency band since the 3-day window does not allow for a separation among the diurnal or semidiurnal tidal constituents. This methodology allows us to exploit the irregular glider sampling to study the spatio-temporal distribution of diurnal and semidiurnal amplitude and phase around New Caledonia in Sect. III.3.

# Chapter III

# Results

---

## Contents

# III Results

## III.1 Coherent internal tides around New Caledonia: a numerical model approach

### III.1.1 Introduction

This thesis begins with a comprehensive description of the internal tide field around New Caledonia - an internal tide generation hot spot in the southwestern tropical Pacific which has received very limited attention in literature and remains to be fully quantified. Using regional numerical modeling output from a full-model calendar year time series, this section aims to provide a general overview of internal tide characteristics around New Caledonia laying the foundation for the rest of this manuscript. We will answer the following questions as stated in Sect. I.5:

**A Coherent internal-tide dynamics and sea surface height signature around New Caledonia**

**1)** What regions and bathymetric structures are subject to strong internal- tide generation around New Caledonia?

**2)** In what regions do we expect elevated tidal energy dissipation? What fraction of locally generated tidal energy is dissipated in the near-field?

**3)** Is the internal tide dominated by low- or high-vertical mode dynamics?

**4)** How do internal tides express in SSH variance and at what wavelengths? How do SSH variance and wavelengths compare with balanced motion?

The following work was initially submitted as a preprint for publication *Ocean Science* which covered both the coherent and incoherent tidal analyses. During the review process and based on the suggestions from two anonymous reviewers and the editor, we decided to explicitly divide the study of coherent and incoherent internal tides. We start with the results for the coherent internal-tide dynamics, which are presented in the form of the associated publication (Bendinger et al., 2023):

**Publication**

**Bendinger, A.**, Cravatte, S., Gourdeau, L., Brodeau, L., Albert, A., Tchilibou, M., Lyard, F., Vic, C.: Regional modeling of internal-tide dynamics around New Caledonia - Part 1. Coherent internal-tide characteristics and sea surface height signature. Ocean Sci, 19(4), 1315–1338, https://doi:10.5194/os-19-1315-2023, 2023 (**Published**).

### III.1.2 Regional modeling of internal-tide dynamics around New Caledonia - Part 1. Coherent internal-tide characteristics and sea surface height signature (Publication)

Ocean Sci., 19, 1315–1338, 2023
https://doi.org/10.5194/os-19-1315-2023
© Author(s) 2023. This work is distributed under
the Creative Commons Attribution 4.0 License.

Ocean Science

# Regional modeling of internal-tide dynamics around New Caledonia – Part 1: Coherent internal-tide characteristics and sea surface height signature

**Arne Bendinger**[1], **Sophie Cravatte**[1,2], **Lionel Gourdeau**[1], **Laurent Brodeau**[3,a], **Aurélie Albert**[3], **Michel Tchilibou**[1,b], **Florent Lyard**[1], **and Clément Vic**[4]

[1]Université de Toulouse, LEGOS (CNES/CNRS/IRD/UPS), Toulouse, France
[2]IRD, Centre IRD de Nouméa, New Caledonia
[3]Université Grenoble Alpes, CNRS, INRAE, IRD, Grenoble INP, Institut des Géosciences de l'Environnement, Grenoble, France
[4]Laboratoire d'Océanographie Physique et Spatiale, Univ. Brest, CNRS, Ifremer, IRD, Plouzané, France
[a]now at: DATLAS, Grenoble, France
[b]now at: CLS, Ramonville-Saint-Agne, France

**Correspondence:** Arne Bendinger (arne.bendinger@univ-tlse3.fr)

Received: 27 February 2023 – Discussion started: 7 March 2023
Revised: 6 July 2023 – Accepted: 10 July 2023 – Published: 29 August 2023

**Abstract.** The southwestern tropical Pacific exhibits a complex bathymetry and represents a hot spot of internal-tide generation. Based on a tailored high-resolution regional model, we investigate for the first time the internal-tide field around the New Caledonia islands through energy budgets that quantify the coherent internal-tide generation, propagation, and dissipation. A total of 15.27 GW is converted from the barotropic to the baroclinic M2 tide with the main conversion sites associated with the most prominent bathymetric structures such as continental slopes and narrow passages in the north (2.17 GW) and ridges and seamounts south of New Caledonia (3.92 GW). The bulk of baroclinic energy is generated in shallow waters around 500 m depth and on critical to supercritical slopes, highlighting the limitations of linear semi-analytical models in those areas. Despite the strongly dominant mode-1 generation, more than 50 % of the locally generated energy either dissipates in the near field close to the generation sites or loses coherence. The remaining baroclinic energy propagates within well-defined tidal beams with baroclinic energy fluxes of up to 30 kW $m^{-1}$ toward the open ocean. The New Caledonia site represents a challenge for SWOT (Surface Water and Ocean Topography) observability of balanced motion in the presence of internal tides with sea surface height (SSH) signatures > 6 cm at similar wavelengths. We show for our study region that a correction of SSH for the coherent internal tide potentially increases the observability of balanced motion from wavelengths > 160 km to well below 100 km.

## 1 Introduction

The flow of barotropic tidal oceanic currents over bathymetry such as continental slopes, ridges, and seamounts represents a major source of baroclinic energy in the global ocean in the form of internal tides (i.e., internal waves at tidal frequency) expressed by high-frequency fluctuations and vertical displacements of isopycnal surfaces (Bell, 1975; Smith and Young, 2002; Garrett and Kunze, 2007). From a global point of view, internal tides have received increasing attention in recent decades as they provide a route to energy dissipation away from lateral boundaries and the surface through diapycnal mixing with important implications for open-ocean mixing and the global oceanic energy budget (e.g., Munk and Wunsch, 1998; Melet et al., 2013; Waterhouse et al., 2014; Kunze, 2017a, b).

Internal tides express themselves in vertical oscillations of density surfaces with strong baroclinic velocities. They

Published by Copernicus Publications on behalf of the European Geosciences Union.

are characterized by a complex vertical structure that can be described by a discrete set of vertical normal modes via the Sturm–Liouville problem (Gill, 1982; Arbic et al., 2018; Buijsman et al., 2020). Low vertical modes have large horizontal wavelengths ($\mathcal{O}(150\,\mathrm{km})$), usually form over large-scale topographic features, and propagate over large distances ($\mathcal{O}(1000\,\mathrm{km})$; Dushaw et al., 1995; St. Laurent and Garrett, 2002; Alford, 2003; Zhao et al., 2010, 2016). In contrast, high vertical modes feature smaller horizontal wavelengths that are generated over smaller-scale topographic features. They tend to dissipate locally not far away from the formation sites due to their lower group velocities and higher vertical shear (Zhao et al., 2016; Vic et al., 2019). Characterizing internal tides, their vertical structure, and propagation is thus key to better understanding their contribution to mixing.

Yet, it is still challenging through both observations and model experiments. Some scattered in situ observations with high-frequency sampling, such as moorings, can help to characterize these processes at some locations (e.g., Zilberman et al., 2011; Vic et al., 2018), but they do not provide a global view. Alternatively, altimetric sea surface height (SSH) observations have been extensively used to globally estimate the SSH imprint of internal tides by using, e.g., empirical models that are based on an up to 20-year-long record of conventional altimeter missions (Zhao et al., 2016; Ray and Zaron, 2016; Zaron, 2019; Ubelmann et al., 2022). These estimates have provided us with a robust representation of the coherent internal tide, which is defined here as a phase-locked internal tide constant in amplitude and phase that is determined over a long time series. However, satellite altimetry generally provides very limited information about internal-tide vertical structure, allowing the detection of the first and second vertical modes only.

The characterization of internal tides with their vertical modes (each associated with a different wavelength) and their signature in SSH is an important task for the Surface Water and Ocean Topography (SWOT) satellite mission (launched in December 2022). SWOT is expected to provide new insights into small-scale ocean dynamics by resolving wavelengths at up to 10 times higher resolution (down to 15 km; Fu et al., 2012; Fu and Ubelmann, 2014) than conventional altimetry ($\mathcal{O}100\,\mathrm{km}$; Ballarotta et al., 2019) with SSH imprints from mesoscale and submesoscale dynamics down to high-frequency internal wave motion, as well as the interaction between them (Fu and Ferrari, 2008; Morrow et al., 2019). From an oceanographic point of view, the characterization of the mesoscale and submesoscale circulation is the primary objective of SWOT (Morrow et al., 2019). The challenge lies in disentangling the measured SSH signal associated with balanced and unbalanced motions, i.e., eddies and gravity waves, since they can feature similar spatial scales. This highlights the need for a detailed picture of internal-tide dynamics to properly derive mesoscale and submesoscale motions (Zaron, 2019; Carrere et al., 2021). Numerical modeling has been playing an important role in partly overcoming the constraints of in situ observations and altimetry. Dedicated studies of internal-tide characteristics and energetics near internal-tide generation hot spots have been conducted in various regions such as the Hawaiian Ridge (Carter et al., 2008), Luzon Strait (Kerry et al., 2013), Solomon Sea (Tchilibou et al., 2020), Amazonian Shelf (Tchilibou et al., 2022), and Mid-Atlantic Ridge (Lahaye et al., 2020). The energy converted from barotropic to baroclinic tides, the distribution of the vertical modes generated, the local ratio between dissipation and conversion, and the energy propagation all heavily depend on the local bathymetric features and the background state, emphasizing the need for a regional focus with high-resolution regional simulations.

Here, we provide the first comprehensive description of the internal-tide field around New Caledonia in the southwestern tropical Pacific using the output of a tailored high-resolution regional simulation from a full-model calendar year (Fig. 1). This region has not received much attention despite being known as an internal-tide generation hot spot from numerical modeling of internal tides in early stages (Niwa and Hibiya, 2001). It is characterized by complex bathymetry of large-scale ridges, very steep slopes, shelf breaks, basins, and seamounts at mid-depths and in the near surface that give rise to propagating tidal beams over several hundred kilometers and significant signatures in SSH as deduced from satellite altimetry (Ray and Zaron, 2016).

New Caledonia also represents an interesting site to study eddy–internal-tide interactions due to a complex regional circulation (Qu and Lindstrom, 2002; Kessler and Cravatte, 2013; Cravatte et al., 2015). Through the interaction with the background currents, the internal-tide field around New Caledonia is potentially subject to temporal variability, also referred to as tidal incoherence in the literature (e.g., Dunphy and Lamb, 2014; Dunphy et al., 2017; Ponte et al., 2017; Lamb and Dunphy, 2018; Shakespeare and Hogg, 2019). An additional reason to study the internal tides around New Caledonia is their potential role in the marine biodiversity for which the region is internationally recognized (Payri et al., 2019). This is especially true south of New Caledonia where seamounts and ridges are hot spots of biodiversity providing marine habitats for marine mammals, fish, and small-scale organisms (Payri and de Forges, 2006; Ganachaud et al., 2010; Gardes et al., 2014; Menkès et al., 2015). Internal tides may also have important implications for coastal ecosystems, mitigating heat stress (Wyatt et al., 2020, 2023) or enhancing upwelling of nutrient-rich waters to the surface (Wolanski and Pickard, 1985; Leichter et al., 2003).

Lastly, the region is crossed by the SWOT swaths during SWOT's fast sampling phase (1 d repeat orbit, Fig. 1a). In this context, New Caledonia serves as a calibration and validation (CalVal) site within the SWOT program and the associated Adopt-A-Crossover (AdAC) consortium. A dedicated field campaign was carried out in spring 2023 to collect high-frequency measurements of the governing fine-scale physics.

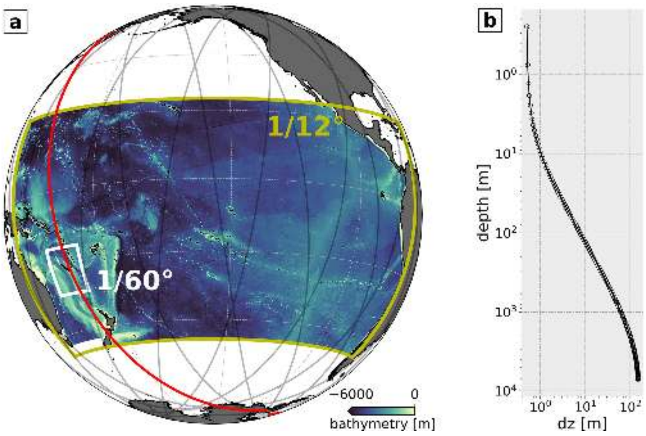

**Figure 1. (a)** Model setup showing the host grid domain (TROPICO12, yellow box) and the nesting grid (CALEDO60, white box) including the bathymetry (shading) and the SWOT CalVal orbit (black transparent lines) with the highlighted ground track (red line) that crosses the CALEDO60 domain. **(b)** TROPICO12 and CALEDO60 vertical resolution among 125 vertical levels.

It thus represents a unique opportunity to address SSH observability of mesoscale and submesoscale dynamics, internal tides, and their interaction.

Due to the study's extent, this work is subject to a series of two papers. Part 1 focuses on stationary, coherent internal tides, whereas Part 2 focuses on nonstationary, incoherent internal tides addressing mesoscale activity as a source of this incoherence.

This study's overall objective for Part 1 is twofold: (1) a detailed introduction to the regional modeling effort that has been explicitly designed to shed light on the internal-tide dynamics around New Caledonia in the framework of SWOT–AdAC, including a model assessment; (2) a detailed description of the coherent internal-tide energetics providing a first picture of the local dynamics at work. Here, we will address the following scientific questions. What areas around New Caledonia are subject to internal-tide generation and dissipation? What is the internal tide's modal content? How is the internal tide expressed in SSH, and at which wavelengths are we able to observe mesoscale and submesoscale processes?

The study is organized as follows. In Sect. 2, we introduce the high-resolution modeling strategy, the tidal analyses and diagnostics used in this study, and the different datasets or products used to assess our simulation. The model assessment is presented in Sect. 3, where we estimate the model ability to realistically simulate the mean circulation, the mesoscale activity, and the barotropic tides. In Sect. 4, we quantify the energetics of the dominant internal tide in the region around New Caledonia and in the hot spots of internal-tide generation. Internal-tide SSH signature is investigated in Sect. 5 in the context of SWOT observability. We finish with a summary and discussion in Sect. 6.

## 2 Data and methods

### 2.1 Model setup

The model used in this study is based on the Nucleus for European Modelling of the Ocean (NEMO, code version 4.0.6, Madec and Team, 2023), which solves the three-dimensional primitive equations on a staggered Arakawa-C-type grid. The model grid consists of a host grid (TROPICO12) at 1/12° horizontal resolution that spans the Pacific Ocean basin from 142–290° E and 24° N–46° S (Fig. 1a). The ridge features 125 vertical levels with 0.5 m thickness at the surface increasing toward 150 m in the deep ocean with 75 vertical levels in the upper 1000 m (Fig. 1b). In the vertical, the model uses a partial-step $z$ coordinate with a nonlinear free surface.

Further, the model setup features a horizontal grid refinement (nesting), named CALEDO60, at 1/60° horizontal resolution ($\sim 1.7$ km grid box spacing). In this particular region, it is expected to allow the model to be submesoscale-permitting. The nesting grid is located in the southwestern tropical Pacific from 159.2–172.4° E and 15.7–28.8° S and encompasses New Caledonia (see Fig. 1a). The nesting was set up using an Adaptive Grid Refinement In Fortran (AGRIF, Debreu et al., 2008), a tool explicitly designed for NEMO to set up regional simulations embedded in a predefined configuration. AGRIF enables the two-way lateral boundary coupling between the host and the nesting grid to be integrated sequentially during the whole length of the simulation.

Laplacian isopycnal diffusion coefficients for tracers were chosen to be mesh-size-dependent such that the tracer diffusion is scaled down from the host grid of $93\,\mathrm{m^2\,s^{-1}}$ to the nesting grid of $4\,\mathrm{m^2\,s^{-1}}$. Vertical eddy diffusivity is estimated by a turbulent kinetic energy (TKE) closure scheme (Gaspar et al., 1990). It is based on a prognostic equation for turbulent kinetic energy and a closure assumption for turbulent length scales depending on vertical shear, stratification, vertical diffusion, and dissipation. The advection of momentum is parameterized by means of a third-order scheme based on upstream-biased parabolic interpolation (UBS).

Initial conditions for temperature and salinity for TROPICO12 and CALEDO60 are prescribed by the GLORYS2V4 oceanic reanalysis (https://doi.org/10.48670/moi-00023). Atmospheric forcing is taken from ERA5 produced by the European Centre for Medium-Range Weather Forecasts (ECMWF, Hersbach et al., 2020) provided at hourly temporal resolution and a spatial resolution of 1/4° to compute surface fluxes using bulk formulae and the prognostic sea surface temperature from the model. Wind stress is computed following the methodology from Renault et al. (2016), i.e., wind speed minus surface currents.

Both domains are forced by the tidal potential of the five major tidal constituents (M2, S2, N2, K1, O1). TROPICO12 is forced at its open lateral boundaries with daily currents, temperature, and salinity, likewise using GLORYS2V4. In addition, TROPICO12 is forced at the open lateral boundaries by SSH and barotropic currents of the same five tidal constituents taken from the global tide atlas FES2014 (Finite Element Solution 2014, Lyard et al., 2021). We made this limited choice to allow the separation of these constituents at monthly timescales.

Recent studies have highlighted the importance of taking into account remote forcing of high-frequency oceanic variability for regional simulations, as it may represent a non-negligible source of energy (Jeon et al., 2019; Nelson et al., 2020; Mazloff et al., 2020; Siyanbola et al., 2023). Further, it was suggested that tidal accuracy and predictability increase when implementing a two-way nesting framework between the high-resolution regional domain and the lower-resolution host grid (Jeon et al., 2019). The authors show that mass and energy are conserved with no evident discontinuities along the nesting boundaries.

Apart from increasing predictability through higher horizontal resolution of the nesting grid, it is argued that a realistic bathymetry product is also essential. For the CALEDO60 domain, we used a specific bathymetric product based on the GEBCO_2019 grid (GEBCO, 2019) and a compilation of multibeam echosounder data acquired over the years in the New Caledonia economic zone (Roger et al., 2021). The latter product, initially at 200 m resolution, only covers the area 155° E–175.1° N, 14.1–26.6° S. It has been combined with the GEBCO_2019 bathymetry product to cover the full domain.

Internal tides represent a large source of diapycnal mixing in the open ocean. The associated parameterization scheme developed by St. Laurent et al. (2002) is usually used in NEMO simulations. Here, it has been turned off because our simulation has a resolution large enough to resolve the internal wave dynamics. In fact, it has been recently suggested that turning off background components of the vertical mixing scheme improves the modeled kinetic energy levels (Thakur et al., 2022).

The bottom friction is parameterized using a logarithmic boundary layer with a drag coefficient of $3 \times 10^{-3}$ (maximum value of 0.1), a roughness of $2.5 \times 10^{-3}$ m, and a background kinetic energy of $1 \times 10^{-2}\,\mathrm{m}^2\,\mathrm{s}^{-2}$. These values yielded the best visual agreement with respect to the mean regional circulation, i.e., the location and magnitude of zonal jets.

The model has been spun up for 2 years (model years 2012–2013) before being run for a total of 5 years (model years 2014–2018). Here, if not noted otherwise, we only focus on 2014 (neutral El Niño–Southern Oscillation conditions) with instantaneous fields saved hourly for the three-dimensional temperature, salinity, velocity, and surface fields (including SSH) for CALEDO60. For TROPICO12, the instantaneous three-dimensional variables are given at daily resolution, whereas the surface fields are saved at hourly resolution. A twin experiment with identical forcing and parameterization has been initialized, but without barotropic tide forcing. Being subject to a future study, here, it is only used to compare the energy spectrum with the tidal simulation.

## 2.2 Tidal analysis and diagnostics

### 2.2.1 Tidal harmonics

In order to investigate the tidal dynamics at play in the regional CALEDO60 simulation, we first apply a harmonic analysis to a full-model calendar year time series (model year 2014) of the three-dimensional velocity and pressure fields to extract the semi-diurnal (M2, S2, N2) and diurnal (K1, O1) tidal constituents. The choice of a full-model calendar year relies upon a compromise between high computational expenses and the representative extraction of the coherent tide through a time series long enough to isolate seasonal and mesoscale variability. Therefore and if not noted otherwise, we define the coherent internal tide as a phase-locked internal tide with constant amplitude and phase referenced to the full-model calendar year time series.

### 2.2.2 Barotropic–baroclinic modal decomposition

The study of internal tides requires an accurate separation of the barotropic and baroclinic tides. The barotropic tide is directly linked to the astronomical tide forcing. In contrast to baroclinic tides, it is independent of depth and density stratification (Hendershott, 1981, see Sect. 1). Several approaches to separate barotropic and baroclinic tides have been discussed in detail, for example in Kelly et al. (2010), Nugroho (2017), and Tchilibou et al. (2020). Here, we use a vertical-mode decomposition approach by solving the Sturm–Liouville problem obeying a linear free surface while assuming a flat bottom:

$$\frac{\partial^2 \Phi_n}{\partial z^2} + \frac{N^2}{c_n^2}\Phi_n = 0, \tag{1}$$

$$\Phi_n = \frac{c_n^2}{g}\frac{\partial \Phi_n}{\partial z} \quad \text{at} \quad z = 0, \quad \text{and} \tag{2}$$

$$\Phi_n = 0 \quad \text{at} \quad z = -H, \tag{3}$$

with the given buoyancy frequency $N$ defined as

$$N^2 = -\frac{g}{\rho_0}\frac{\partial \rho}{\partial z}, \tag{4}$$

where $\rho$ is the potential density, $z$ the vertical coordinate, $g$ the gravitational acceleration, and $\rho_0$ the reference density. $c_n$ is the eigenspeed and $\Phi_n$ the eigenfunction describing the vertical structure for vertical velocity and displacement (McDougall and Barker, 2011). It is related to the eigenfunction describing the vertical structure for horizontal velocity and pressure via

$$\phi_n = \rho_0\, c_n^2\, \frac{\partial \Phi_n}{\partial z}. \tag{5}$$

In practice, the Sturm–Liouville eigenvalue problem has been solved at each grid point of the model, using the annual mean density field referenced to the same period as the harmonic analysis above, for the 10 lowest modes, where the lowest mode ($n=0$) refers to the barotropic tide and $n \geq 1$ represents the baroclinic modes. Based on the tidal harmonics determined in Sect. 2.2.1, the model variables are projected onto the orthogonal, discrete set of normal vertical modes, i.e.,

$$[\boldsymbol{u}(x,y,z,t), p(x,y,z,t)] = \sum_{n=0}^{9} [\boldsymbol{u}_n(x,y,t), p_n(x,y,t)]\phi_n(z), \tag{6}$$

for the horizontal velocity vector $\boldsymbol{u}=(u,v)$ and pressure $p$, as well as

$$w(x,y,z,t) = \sum_{n=0}^{9} w_n(x,y,t)\Phi_n(z), \tag{7}$$

for the vertical velocity $w$ using a least squares fit method. If not specified otherwise, we define the baroclinic tide as the sum of modes 1–9. As will be seen in Sect. 4, this is sufficient in our study region, where low baroclinic modes are strongly dominant.

### 2.2.3 Energy equations

The redistribution and transfer of energy from the barotropic tide to the internal tide can be approximated by the barotropic and baroclinic energy equation neglecting the tendency term and nonlinear advection following Simmons et al. (2004), Carter et al. (2008), and Buijsman et al. (2014, 2017) since both terms were found to be at least 1 order of magnitude smaller:

$$\nabla_\mathrm{h} \cdot \boldsymbol{F}_\mathrm{bt} + D_\mathrm{bt} + C = 0, \tag{8}$$

$$\nabla_\mathrm{h} \cdot \boldsymbol{F}_\mathrm{bc} + D_\mathrm{bc} - C = 0, \tag{9}$$

where $\nabla_\mathrm{h} \cdot \boldsymbol{F}$ is the energy flux divergence with $\nabla_\mathrm{h} = (\partial/\partial x, \partial/\partial y)$ the horizontal gradient operator and $\boldsymbol{F} = (F_x, F_y)$ the energy flux vector, $D$ is the energy dissipation, and $C$ is the barotropic-to-baroclinic conversion term. The subscripts bt and bc stand for the barotropic and baroclinic tide. In the barotropic energy equation, the conversion is considered a sink of energy, whereas it is an energy source in the baroclinic energy equation. The conversion term is defined as

$$C = \nabla_\mathrm{h} H \langle \boldsymbol{u}\ p_\mathrm{bc}(-H)\rangle, \tag{10}$$

where $H$ is the bathymetry, $\boldsymbol{u} = (u_\mathrm{bt}, v_\mathrm{bt})$ the barotropic tidal velocity vector, and $p_\mathrm{bc}$ the baroclinic tidal pressure at the ocean bottom ($-H$). $\langle\rangle$ denotes the average over a tidal cycle. Following Zilberman et al. (2009), we compute $\langle \boldsymbol{u}_\mathrm{bt}\ p_\mathrm{bc}(-H)\rangle$ via

$$\langle \boldsymbol{u}_\mathrm{bt}\ p_\mathrm{bc}(-H)\rangle = \frac{1}{2}\ A_{p_\mathrm{bc}(-H)}\ A_{\boldsymbol{u}}\ \cos(\varphi_{p_\mathrm{bc}(-H)} - \varphi_{\boldsymbol{u}}), \tag{11}$$

where $A$ and $\varphi$ are the respective amplitude and phase of the tidal harmonic obtained from $p_\mathrm{bc}$ and $\boldsymbol{u}_\mathrm{bt}$. The conversion for each mode $n$ is given by

$$C^n = \nabla_\mathrm{h} H \langle \boldsymbol{u}_\mathrm{bt}\ p^n_\mathrm{bc}(-H)\rangle, \tag{12}$$

where $p^n_\mathrm{bc}(-H)$ is the baroclinic pressure at the ocean bottom ($-H$) for mode $n$. Equivalent to Eq. (11), we compute for each mode $n$:

$$\langle \boldsymbol{u}_\mathrm{bt}\ p^n_\mathrm{bc}(-H)\rangle = \frac{1}{2}\ A_{p^n_\mathrm{bc}(-H)}\ A_{\boldsymbol{u}_\mathrm{bt}}\ \cos(\varphi_{p^n_\mathrm{bc}(-H)} - \varphi_{\boldsymbol{u}_\mathrm{bt}}). \tag{13}$$

The propagation of barotropic and baroclinic tide energy is expressed by the energy flux ($\boldsymbol{F}_\mathrm{bt}$ and $\boldsymbol{F}_\mathrm{bc}$) and is considered here to be a depth-integrated quantity:

$$\boldsymbol{F}_\mathrm{bt} = \int_{-H}^{\eta} \langle \boldsymbol{u}_\mathrm{bt}\ p_\mathrm{bt}\rangle\ \mathrm{d}z, \tag{14}$$

$$\boldsymbol{F}_\mathrm{bc} = \int_{-H}^{\eta} \langle \boldsymbol{u}_\mathrm{bc}\ p_\mathrm{bc}\rangle\ \mathrm{d}z, \tag{15}$$

where $p_\mathrm{bt}$ is the barotropic pressure, and $\boldsymbol{u}_\mathrm{bc} = (u_\mathrm{bc}, v_\mathrm{bc})$ is the baroclinic velocity vector. The baroclinic energy flux for each mode $n$ is defined as

$$\boldsymbol{F}^n_\mathrm{bc} = \int_{-H}^{\eta} \langle \boldsymbol{u}^n_\mathrm{bc}\ p^n_\mathrm{bc}\rangle\ \mathrm{d}z, \tag{16}$$

where $\boldsymbol{u}^n_\mathrm{bc}$ is the baroclinic tidal velocity vector for mode $n$. Note that the average over a tidal cycle follows the same methodology as for the conversion term above. The barotropic ($D_\mathrm{bt}$) and baroclinic ($D_\mathrm{bc}$) dissipation is regarded as the residual of the energy flux divergence and conversion and is, hence, obtained through Eqs. (8) and (9), respectively. As will be discussed later, $D_\mathrm{bc}$ may contain both true baroclinic energy dissipation and scattering to the incoherent tide.

In the following, we mainly focus our study on the M2 semi-diurnal tide, which explains in the nesting domain more than 80 % of the total energy conversion from the barotropic to the baroclinic tide while representing about 84 % of the semi-diurnal energy conversion (see Table 1).

## 2.3 Other data

### 2.3.1 CARS climatology and merged Argo–CARS velocity product

The model used in this study is evaluated using climatology and observations. Model stratification and water mass

**Table 1.** Full CALEDO60 domain, area-integrated barotropic-to-baroclinic conversion in gigawatts (GW) for each tidal constituent (M2, S2, N2, K1, O1) with their respective contribution to the total in percent.

| | Total | M2 | S2 | N2 | K1 | O1 |
|---|---|---|---|---|---|---|
| Conversion (GW) | 19.03 (100 %) | 15.27 (80.2 %) | 2.04 (10.7 %) | 0.92 (4.8 %) | 0.64 (3.4 %) | 0.16 (0.8 %) |

vertical structure are evaluated using climatological hydrography data taken from the CSIRO Atlas of Regional Seas (CARS2009) that provides gridded maps of temperature and salinity by combining a variety of datasets (Ridgway et al., 2002, http://www.marine.csiro.au/~dunn/cars2009/, last access 21 February 2021). The large-scale regional mean circulation in the Coral Sea is compared to the Argo–CARS merged velocity product from Kessler and Cravatte (2013). This product derives absolute geostrophic currents using climatological hydrographic data from CARS2009 referenced to a level of known motion of 1000 m obtained by drifting trajectories of Argo floats.

### 2.3.2 Altimetry-derived EKE

Surface mesoscale eddy kinetic energy (EKE) during the period 2014–2018 is evaluated using global ocean gridded maps (1/4°) of SSH generated and processed by the EU Copernicus Marine Environment Monitoring Service (CMEMS, https://doi.org/10.48670/moi-00148). In detail, we use the multimission Data Unification and Altimeter Combination System (DUACS) product in delayed time and daily resolution with all satellite missions available at a given time. Mesoscale EKE was derived from the geostrophic velocity field as follows:

$$\mathrm{EKE} = \frac{1}{2}\,\overline{u_g'^2 + v_g'^2}, \tag{17}$$

where $u_g = -\frac{g}{f}\frac{\partial \eta}{\mathrm{d}y}$, $v_g = \frac{g}{f}\frac{\partial \eta}{\mathrm{d}x}$ with $f$ the Coriolis parameter and $\eta$ the SSH above geoid (also referred to as absolute dynamic topography), and $(u_g', v_g') = (u_g - \overline{u_g}, v_g - \overline{v_g})$ where the overbar denotes the temporal average over the period 2014–2018. Additionally, the geostrophic velocities were high-pass-filtered at a cut-off period of 180 d to account for the mesoscale (Qiu and Chen, 2004). We computed the modeled EKE as closely as possible to the altimetric EKE.

### 2.3.3 In situ mooring

As part of an assessment of the SARAL/ALtiKa satellite altimeter for the monitoring of the East Caledonian Current flowing along Loyalty Ridge, moorings and gliders have been deployed along the satellite ground track (Durand et al., 2017). Here, we take advantage of the current meter mooring at 167.26° E, 20.44° S (about 30 km off the northern tip of Lifou island in the core of the ECC; see Fig. 2a). The mooring was deployed from November 2010 to October 2011 at the bottom of the continental slope in 3300 m water depth. It was equipped with an upward-looking LinkQuest FlowQuest 300 kHz acoustic Doppler current profiler (ADCP; with 4 m bins) located at a mean depth of 80 m and five RCM7 Aanderaa rotor current meters at 300, 400, 500, 600, and 1000 m. The mooring provided hourly records of the 1 min averaged ocean velocity over the upper 1000 m. Here, it is used to compare in situ kinetic energy with the model (see Sect. 3.3)

### 2.3.4 FES2014

The FES2014 global ocean tidal atlas (Lyard et al., 2021) is the latest release to improve tidal predictions based on the hydrodynamic modeling of tides (Toulouse Unstructured Grid Ocean model, further denoted T-UGOm) coupled to an ensemble data assimilation code (spectral ensemble optimal interpolation, denoted SpEnOI). It is a very significant upgrade compared to the previous atlases, thanks to the improvement of the assimilated data accuracy and the model performance. FES2014 has been integrated in satellite altimetry geophysical data records (GDRs). It also provides very accurate open-boundary tidal conditions for regional and coastal modeling. Here, it is used to ensure the correct representation of the barotropic tide for SSH in both the host and nesting grid.

### 2.3.5 HRET

The expression of internal tides in SSH in our model simulation is evaluated by the High Resolution Empirical Tide version 8.1 (HRET8.1, https://ingria.ceoas.oregonstate.edu/~zarone/downloads.html, last access 12 September 2022, Zaron, 2019; Carrere et al., 2021). The product uses essentially all exact-repeat altimeter mission data in the period 1992–2017 (TOPEX/Jason, GEOSAT, ERS, Envisat). In contrast to other previous approaches, HRET differs by the subtraction of the mesoscale sea level anomaly from the SSH along the ground tracks. This ensures having as little non-tidal variability as possible. This is followed by a harmonic analysis applied to a time series at each point along the ground track for missions with the same orbit.

### 2.3.6 Semi-analytical models of tidal energy conversion

Semi-analytical models have been developed to obtain a global estimate of energy conversion rates from the barotropic to the baroclinic tide using bottom topography, climatological stratification, and tidal barotropic velocity (e.g., Nycander, 2005; Falahat et al., 2014; Vic et al., 2019). Doing so, they are highly valuable for tidal mixing param-

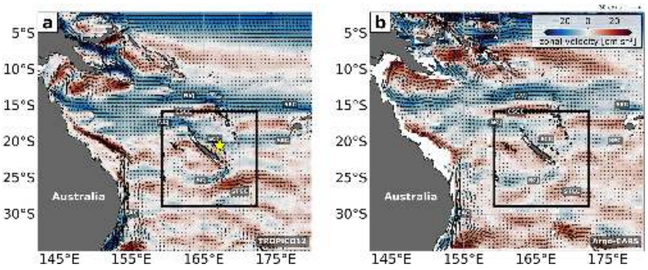

**Figure 2.** Coral Sea near-surface (20–100 m) regional circulation illustrating zonal velocity (shading) and velocity vectors from **(a)** TROPICO12 (2014–2018 mean) and **(b)** the Argo–CARS merged velocity product (Kessler and Cravatte, 2013). The black box indicates the CALEDO60 domain. The major currents are labeled: South Equatorial Current (SEC), North Vanuatu Jet (NVJ), Coral Sea Countercurrent (CSCC), North Caledonian Jet (NCJ), East Caledonian Current (ECC), South Caledonian Jet (SCJ), Subtropical Countercurrent (STCC), and East Australian Current (EAC). The location of the in situ mooring (see Sect. 2.3.3) is indicated by the yellow star.

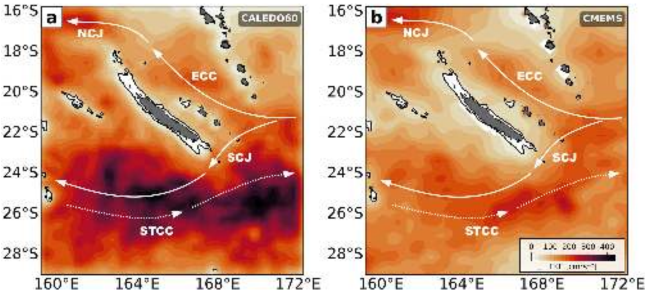

**Figure 3.** Surface mesoscale EKE derived from SSH for **(a)** CALEDO60 and **(b)** CMEMS altimeter products and averaged for the period 2014–2018. Currents are labeled as in Fig. 2.

eterizations in ocean and climate models that do not have the ability to explicitly resolve tidal processes (MacKinnon et al., 2017; de Lavergne et al., 2019, 2020). Here, we make use of the products from Falahat et al. (2014) and Vic et al. (2019) to evaluate our model energy conversion. At the same time, we emphasize the limited capability of semi-analytical models to accurately predict internal-tide generation in shallow waters and in areas of complex bathymetry such as New Caledonia. Specifically, semi-analytical models break down for bathymetric slopes that are equal to or larger than the internal-tide wave slopes, i.e., critical to supercritical slopes. The wave ray-path slope $s$ is obtained from the dispersion relation as follows:

$$s = \sqrt{\frac{\omega^2 - f^2}{N^2 - \omega^2}}, \tag{18}$$

where $\omega$ is the tidal frequency. The buoyancy frequency $N$ is taken from near the ocean bottom. The steepness parameter $\alpha$, defined as the ratio of the seafloor topographic slope to the ray-path slope, qualifies the seafloor topography as subcritical ($\alpha < 0.8$ s), critical ($0.8\,\mathrm{s} \leq \alpha \leq 1.5$ s), and supercritical ($\alpha > 1.5$ s), following de Lavergne et al. (2019). Semi-analytical models are often corrected for energy conversion in the shallow waters due to violation of linear theory. Initially corrected for the upper 400 m in Falahat et al. (2014) and the upper 700 m in Vic et al. (2019), we also correct Falahat et al. (2014) for the upper 700 m to ensure the best comparison between the two products.

## 3 Model assessment

In the following, we will assess the model's capability to realistically reproduce motion from the large-scale circulation down to high-frequency motion while justifying the model's eligibility to simulate internal-tide dynamics.

### 3.1 Mean circulation

The modelization of the regional circulation in the Coral Sea represents a challenge due to the numerous islands that serve as obstacles, forming boundary currents and westward jets as well as recirculation and eastward countercurrents (Couvelard et al., 2008; Qiu et al., 2009). The main feature is a westward inflow from the South Pacific subtropical gyre, which splits into strong zonal jets, western boundary currents, and eastward countercurrents when encountering bathymetric features (Couvelard, 2007; Kessler and Cravatte, 2013; Cravatte et al., 2015; Qiu and Chen, 2004). The 2014–2018 mean near-surface (20–100 m) simulated velocity field (Fig. 2a) is compared to the Argo–CARS merged velocity (see Sect. 2.3.1 for a description, Fig. 2b). The model 5-year mean shows good agreement with the observed regional circulation. The westward zonal jets are well represented with the South Equatorial Current (SEC) being split into the North Vanuatu Jet (NVJ) and the North Caledonian Jet (NCJ) north of New Caledonia and the South Caledonian Jet (SCJ) south of New Caledonia. West of the main islands (New Caledonia, Vanuatu, Fiji), the observed surface eastward countercurrents are also well simulated (Qiu et al., 2009). The circulation south of New Caledonia seems more variable, with less clearly defined mean currents in both products. There is evidence of the presence of the surface-intensified eastward Subtropical Countercurrent (STCC) that emerges from the East Australian Current (EAC) recirculation (Ridgway and Dunn, 2003). It is clearly intensified in the model, but the Argo merged product south of New Caledonia should be taken with caution since limited observations do not average out the signatures of ubiquitous mesoscale eddies. Overall, the mean circulation is well simulated, which is essential for the proper description of eddy–internal-tide interactions that are the subject of Part 2 of this study.

## 3.2 Mesoscale variability

The large-scale circulation around New Caledonia is subject to barotropic and baroclinic instability of horizontally and vertically sheared currents (Qiu and Chen, 2004; Qiu et al., 2008, 2009) giving rise to mesoscale eddy variability. Here, the spatial pattern of the surface model mesoscale EKE (Fig. 3a) is compared to the mesoscale EKE as observed by satellite altimetry (Fig. 3b). We computed the modeled EKE as closely as possible to the altimetric EKE. To do so, we computed the 5 d mean of the model SSH to eliminate high-frequency variability such as tidal and inertial motions before horizontally binning the data onto the grid of present-day altimetry (1/4°). For proper comparison between model and altimeter observations, we also computed the 5 d average for altimetric SSH before the derivation of mesoscale EKE. Mesoscale EKE is maximum south of New Caledonia where mesoscale activity is expected to be generated through baroclinic instabilities of the vertically sheared SEC and SCJ–STCC (Qiu et al., 2009; Keppler et al., 2018). Elevated levels of EKE are also found along the eastern boundary current system between New Caledonia and Vanuatu as well as in the northwest of the domain through horizontal shear between the westward NCJ and the eastward Coral Sea Countercurrent (Figs. 2, 3a). The spatial pattern of simulated EKE is in good agreement with satellite altimetry (Fig. 3b). Maximum levels of EKE in the southern domain where mesoscale activity is high are essentially lower than in the model ($> 250\,\mathrm{cm^2\,s^{-2}}$ compared to $> 400\,\mathrm{cm^2\,s^{-2}}$). We argue that this can be attributed to the present-day two-dimensional gridded satellite altimetry products. They are derived by gridding and optimal interpolation of available along-track SSH data, projected onto a 1/4° horizontal grid, and do not resolve wavelengths smaller than 150–200 km in our study region (Ballarotta et al., 2019). The model, even though gridded to 1/4° resolution, might contain dynamics that are associated with smaller scales.

## 3.3 Kinetic energy frequency spectra

In situ observations are also used to validate energy levels from seasonal down to tidal frequencies obtained from a full-year in situ current meter mooring (see Sect. 2.3.3, Fig. 4). Model energy levels are very close to observations from seasonal to inertial timescales (180 d to 36 h), i.e., for mesoscale and submesoscale processes. Inertial and tidal energy peaks are also in good agreement. For higher frequencies, the simulation with tidal forcing (red line) introduces a major improvement to the simulation without tidal forcing (blue line). This is especially true for the internal wave continuum raising the energy levels closer to the observations for frequencies $> f$. This validation, even if only performed at one location, gives us confidence in the ability of the numerical simulation to correctly represent the tides and their interaction with mesoscale processes.

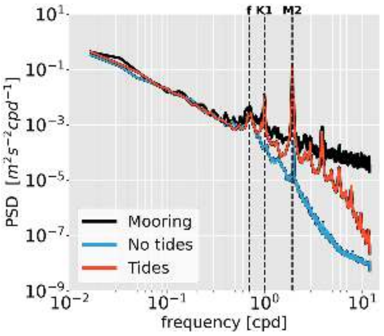

**Figure 4.** Power spectral density of near-surface (20–100 m) horizontal kinetic energy for CALEDO60 without (blue) and with (red) tidal forcing for the full-model time series near 167.25° E, 20.43° S in the New Caledonian eastern boundary current (see Fig. 3a). The energy spectra are compared to a mooring time series that was deployed between November 2010 and October 2011 (Durand et al., 2017). The vertical dashed black lines are representative of the inertial frequency $f$, the peak frequency of the K1 diurnal tide, and the peak frequency of the M2 semi-diurnal tide. Note that the signal at the semi-diurnal frequency (2 cpd) evident in the simulation with and without tides as well as in the mooring data is primarily linked to the atmospheric S2 tide, which is contained in the atmospheric forcing of ERA5 (not shown; Chapman and Lindzen, 1969; Balidakis et al., 2022).

## 3.4 Barotropic M2 tide validation

The barotropic tide in both the host grid (TROPICO12) and the nesting grid (CALEDO60) is compared with the empirical estimates from the barotropic tide model FES2014 (see Sect. 2.3.4) by applying a harmonic analysis to the full-model hourly SSH. Note that the daily output of the three-dimensional variables from TROPICO12 does not allow for a decomposition between the barotropic and baroclinic tide through the projection onto vertical modes. Therefore, we treat the full-model SSH as a proxy for the barotropic tide. For the sake of consistency, we treat CALEDO60 similarly. The M2 tides of TROPICO12 (Fig. 5a) and CALEDO60 (Fig. 5c) are in overall accordance with FES2014 (Fig. 5c and Fig. 5d, respectively). The amphidromic points are well located and amplitudes of SSH are of the same order of magnitude. Note that the modulations at shorter wavelengths in Fig. 5c and d are attributed to the baroclinic SSH signatures, which are presented at a later stage in Sect. 6.1.

## 3.5 Stratification

Finally, in order to study internal-tide dynamics, a correct representation of the ocean's stratification is essential. Internal tides are expressed inter alia in the vertical displacement of isopycnal surfaces (Arbic et al., 2018), which can be decomposed by a sum of discrete baroclinic modes that only depend on buoyancy frequency and water depth (see Sect. 2.2.1). We compare the vertical hydrographic

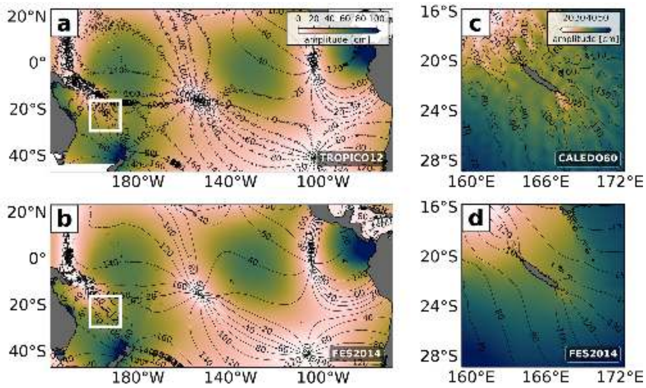

**Figure 5.** M2 SSH amplitude (shading) and phase (contour) for **(a)** TROPICO12 and **(c)** CALEDO60 based on a 1-year (2014) harmonic analysis (assuming that the model SSH is dominated by the barotropic tide) and in comparison to the global tide atlas FES2014 for **(b)** TROPICO12 and **(d)** CALEDO60. The boxes in **(a)** and **(b)** indicate the location of the CALEDO60 domain.

structure of CALEDO60 with a hydrographic climatology (CARS2009, see Sect. 2.3.1). The model mean density was horizontally binned to the climatological grid (1/2°), whereas the climatological density was vertically interpolated onto the model grid. The water masses (not shown) and buoyancy frequency profiles correspond well to each other. An example of such a comparison is illustrated by looking at a stratification profile south of New Caledonia (166° E, 26° S, Fig. 6a). The maximum stratification around 100 m depth is slightly reduced in the model compared to climatology. This is attributed to a reduced salinity maximum in the thermocline in the model (not shown). The normalized modal structures for the four lowest modes and for both the displacement and vertical velocity (Fig. 6b) agree well with climatology. In particular, the depths of the zero crossings correspond well to each other.

Overall, we conclude that our model simulation is capable of realistically simulating both background ocean dynamics and internal tides. This encourages us to study the internal-tide field around New Caledonia in detail including its tidal energy budget, its vertical structure, and finally its SSH signature.

## 4 Barotropic–baroclinic coherent M2 tide energy budget

In the following, we first analyze the M2 internal-tide field around New Caledonia by quantifying the energy conversion from the barotropic to the baroclinic tide while linking it to the local bathymetry. We also discuss the overall energy budget of the coherent M2 internal tide. We start with a regional overview before focusing on the regional hot spots of internal-tide generation.

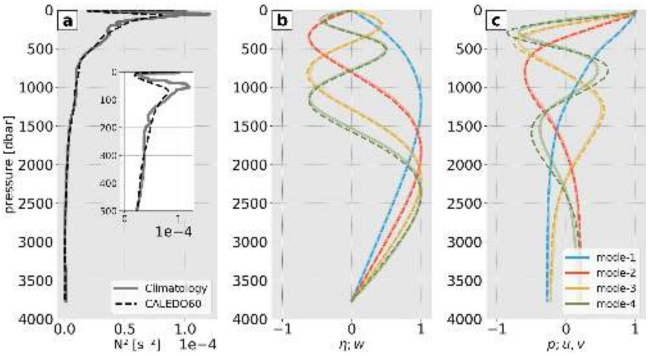

**Figure 6. (a)** Squared buoyancy frequency ($N^2$) for a representative profile at 166° E, 26° S from the CARS2009 climatology (solid) and CALEDO60 (dashed). A zoom for the upper 500 m is given in the inset. Normalized baroclinic modal structures for **(b)** displacement $\eta$ and vertical velocity $w$, as well as **(c)** pressure $p$ and horizontal velocity $u$ and $v$, for the four lowest modes are also shown.

### 4.1 Regional overview

Tidal energy conversion from the barotropic to baroclinic tide is closely linked to the bathymetry that is shortly presented in the following for the regional model domain (Fig. 7a). It is characterized by a complex northwest–southeast-extending ridge system, deep-reaching trenches, small-scale basins, seamounts, and shallow lagoons. The ridge system is composed of two major ridges, Norfolk Ridge and Loyalty Ridge. Norfolk Ridge extends from north of the Grand Passage all the way to the northern tip of New Zealand. The main New Caledonia island (Grande Terre) is located on the northern segment of Norfolk Ridge, also referred to as the New Caledonia Ridge. Loyalty Ridge stretches parallel to Norfolk Ridge, giving rise to the Loyalty Islands (Payri and de Forges, 2006). Seamounts are ubiquitous around New Caledonia and most prominent south of Grande Terre (Samadi et al., 2006).

As the M2 barotropic tidal energy flux curves southwestward around New Caledonia, the region is subject to barotropic-to-baroclinic energy conversion (Fig. 8a). Positive conversions represent energy transfer from the barotropic to the baroclinic tide; negative conversions are argued to be a measure of the energy transfer from the baroclinic tide to the barotropic tide due to pressure work (Zilberman et al., 2009). However, they may also reflect limitations in the baroclinic–barotropic decomposition (Lahaye et al., 2020). Thus, they remain difficult to explain physically and will not be further discussed here.

In the full-model domain, a total 21.16 GW of barotropic tidal energy is lost, 72 % (15.27 GW) of which is transferred to baroclinic tidal energy, whereas 28 % (5.89 GW) is dissipated due to bottom friction. This is a significant loss of barotropic tidal energy. For comparison, barotropic tidal energy loss has been estimated at 18.35 and 2.73 GW, 94 % and

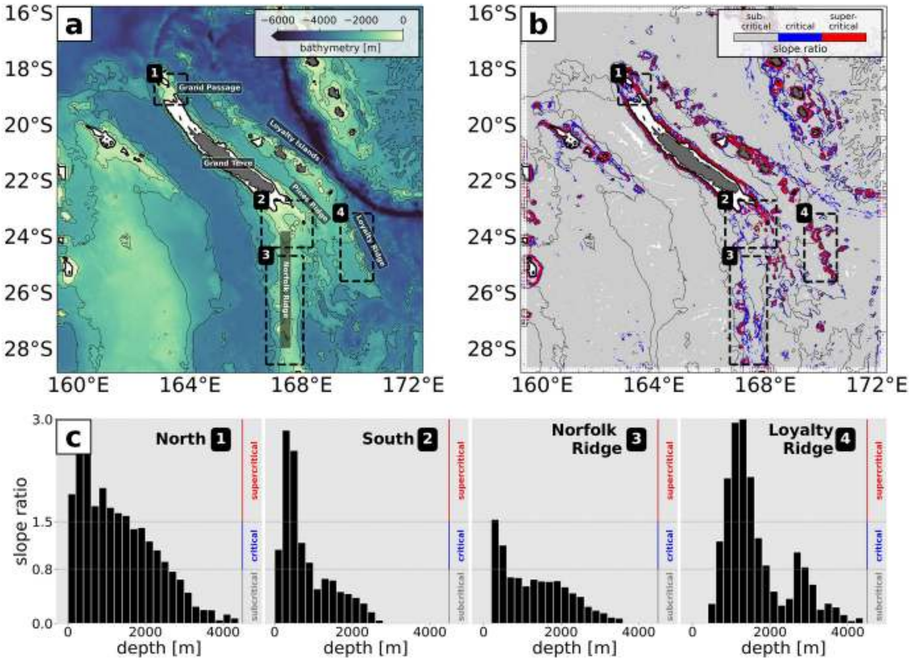

**Figure 7.** CALEDO60 **(a)** bathymetry and **(b)** M2 tide slope ratio $\alpha$ between topographic slope and wave slope $s$, divided into subcritical (gray, $\alpha < 0.8\,s$), critical (blue, $0.8\,s < \alpha < 1.5\,s$), and supercritical (red, $\alpha > 1.5\,s$) slopes. Note that white shaded grid points are associated with a zero bathymetry gradient. The thin black lines represent the 1000, 2000, and 3000 m depth contours. The thick black line is the 100 m depth contour representative for the New Caledonian lagoon. The numbered black boxes represent the hot spots of internal-tide generation (1: North, 2: South, 3: Norfolk Ridge, 4: Loyalty Ridge) for which the distribution of the slope ratio as a function of depth (divided into 200 m depth bins) is given in **(c)**.

84 % of which are converted to baroclinic tidal energy for the Luzon Strait (Kerry et al., 2013) and the Hawaiian Ridge (Carter et al., 2008), respectively.

In the whole domain (not shown), conversion is observed at all depths up to 4000 m and over a broad range of slopes. However, tidal conversion peaks in shallow waters with overall 25 % of the area-integrated energy that is associated with the upper 500 m. Moreover, two-thirds of the tidal conversion occurs on critical and supercritical slopes. Mode 1 clearly dominates, explaining almost 70 % of the total tidal energy conversion. Higher modes play only a minor role (15 % for mode 2 and 7 % for mode 3). For the whole domain, 93 % of this generated baroclinic energy is finally dissipated inside the domain, while little energy (1.06 GW) leaves the domain (Fig. 8a). Note that this quantity is representative of the net baroclinic flux of inward and outward energy propagation.

### 4.2 Subregional analyses

Here, we identify four regions of internal-tide generation which together represent roughly 60 % of the full-domain area-integrated M2 barotropic-to-baroclinic conversion. These hot spots are illustrated by the black boxes in Fig. 7a–b and Fig. 8a and defined as North (1), South (2), Norfolk Ridge (3), and Loyalty Ridge (4). The conversion and energy budget are discussed for each area in light of its topographic characteristics (Fig. 7). The energy budget and the part dissipated locally are also provided for each subregion to better infer where the dissipation occurs and where tidal mixing is expected (Fig. 9, see also Table A1).

The North (1) domain is characterized by a very steep (with critical and supercritical slopes) shelf break at the eastern flank of the New Caledonia Ridge and a 500 m deep, 50 km wide passage (Grand Passage) that is located between the d'Entrecasteaux Reef and the main island reef (Fig. 7a–b). Two-thirds of the tidal energy conversion occurs at depths shallower than 500 m (Fig. 8b), predominantly on critical and supercritical slopes (Fig. 7b–c). The region features the highest dissipation rate of barotropic energy compared to the other three regions. Of the 3.83 GW that is lost by the barotropic tide, 1.66 GW (43 %) is directly lost through bottom friction (Fig. 9a). Of the 2.17 GW that is converted to baroclinic energy, 32 % (0.70 GW) dissipates locally, while the remaining 68 % (1.47 GW) radiates away.

The South (2) domain has similar bathymetric characteristics in terms of depth and slopes. It represents the southward extension of the New Caledonia Ridge, just south of the New Caledonian lagoon. The most prominent bathymetric feature is Pines Ridge: it is a very steep (critical and supercritical slopes) and narrow ridge (a few tens of kilometers wide) of 100 km length that may be as shallow as 500 m (Fig. 7a–b). This region will be analyzed in more detail in Sect. 4.5

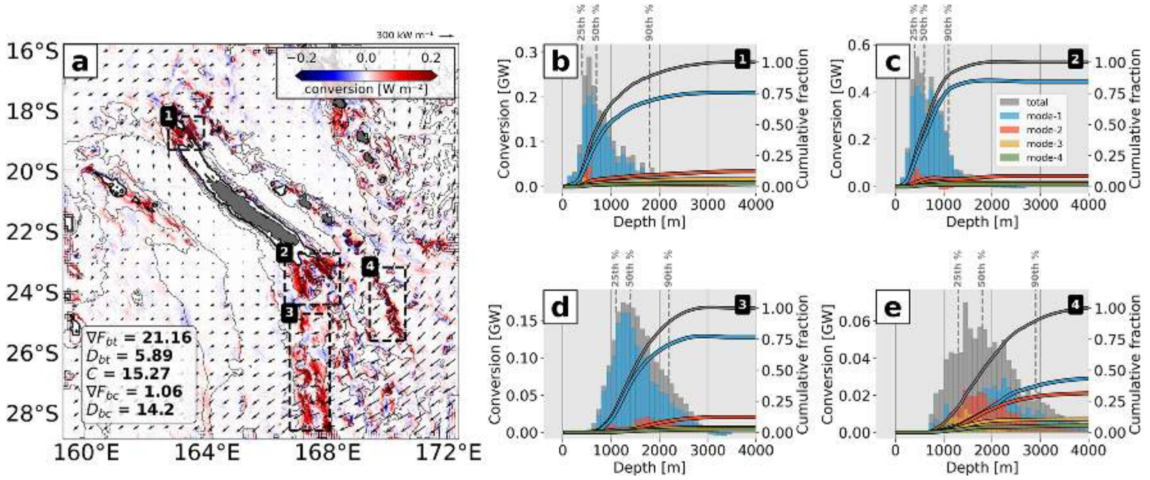

**Figure 8. (a)** M2 barotropic-to-baroclinic conversion including barotropic energy flux vectors and the full-domain area integral of the barotropic energy flux divergence ($\nabla F_{\mathrm{bt}}$), barotropic energy dissipation ($D_{\mathrm{bt}}$), barotropic-to-baroclinic conversion ($C$), baroclinic energy flux divergence ($\nabla F_{\mathrm{bc}}$), and baroclinic energy dissipation ($D_{\mathrm{bc}}$) in gigawatts (GW). Bathymetry contours and the black boxes are given as in Fig. 7. Histograms of the regional area-integrated conversion (total baroclinic and four lowest modes) as a function of generation depth divided into 100 m depth bins for **(b)** North (1), **(c)** South (2), **(d)** Norfolk Ridge (3), and **(e)** Loyalty Ridge (4). The 25th, 50th, and 90th percentiles as well as the normalized cumulative fraction are also shown.

since it is subject to the most intense energy conversion with a total of 3.92 GW (Fig. 9b), primarily in depths shallower than 500 m (Fig. 8c). Further, local dissipation is essentially higher than in the North (1) domain.

Norfolk Ridge (3) exhibits different bathymetric characteristics. It is defined as the > 100 km wide north–south-stretching ridge between 24.5 and 28.5° S. It is dominated by subcritical slopes at depths > 1000 m (Fig. 7c) and also features steep (critical) slopes at mid-depths (400–700 m) which are mostly associated with seamounts. It is mainly characterized by energy conversion at subcritical slopes peaking at depths in the range 1000–2000 m with the 50th percentile at around 1500 m and the 90th percentile below 2000 m (Fig. 8d). Similarly to South (2), approximately half (53 %) of the converted baroclinic energy (2.04 GW) is dissipated locally (1.07 GW), while the other half (47 %) is radiated away (0.96 GW, Fig. 9c).

Loyalty Ridge (4) is a deep and narrow ridge composed of seamounts and guyots (Pelletier, 2007). These seamounts and guyots are located between 1000 and 2000 m depth, but deeper ones are also found between 2500 and 3000 m. They are characterized by supercritical and critical slopes, respectively (Fig. 7b–c). It features the most efficient energy conversion from the barotropic to baroclinic tide. Of the 1.28 GW that is lost by the barotropic tide, only 0.31 GW (24 %) is directly lost through bottom friction (Fig. 9d). The area-integrated baroclinic energy accounts for 0.97 GW, 45 % of which dissipates within the region (0.44 GW) and 55 % leaves the domain (0.53 GW).

Most of the tidal energy conversion discussed above is dominated by mode 1, explaining 75 %, 84 %, and 76 % for North (1), South (2), and Norfolk Ridge (3), respectively (Fig. 9a–c). In these, regions, mode 2 (7 %–12 %) and mode 3 (4 %–6 %) contribute little to the total baroclinic energy conversion. Loyalty Ridge (4) represents an exception with notable contributions of higher vertical modes: 43 %, 31 %, 11 %, and 6 % associated with mode 1 through mode 4, respectively (Fig. 9d).

These findings are partly consistent with the literature. In shallow depth ranges, the tidal energy conversion is expected to be largest for mode 1 (Falahat et al., 2014). Also, we expect mode 1 to be dominant for steep, tall, narrow structures such as in the North (1) and South (2) domains, similarly found for the Hawaiian Ridge (Laurent et al., 2003; Laurent and Nash, 2004). In the case of a deeper ocean bottom with small-scale bathymetric structures, such as Loyalty Ridge (4), higher modes are expected to become more important. The general presence of critical and subcritical slopes suggests a superposition of numerous vertical modes forming beams (Gerkema, 2001; Balmforth et al., 2002; Legg and Huijts, 2006). Nevertheless, we did not find any clear relationship between the bathymetric slope and excitement of vertical modes. The high dissipation rates in South (2) and Norfolk Ridge (3) could be explained by the successive bathymetric obstacles encountered by the internal-tide beams emanating from the generation spots with low modes scattered to higher modes before being dissipated locally (Lahaye et al., 2020). Surprisingly, the fraction of energy dissipation around Loyalty Ridge (4) is slightly reduced even though higher vertical modes are generated, which should imply more local dissipation.

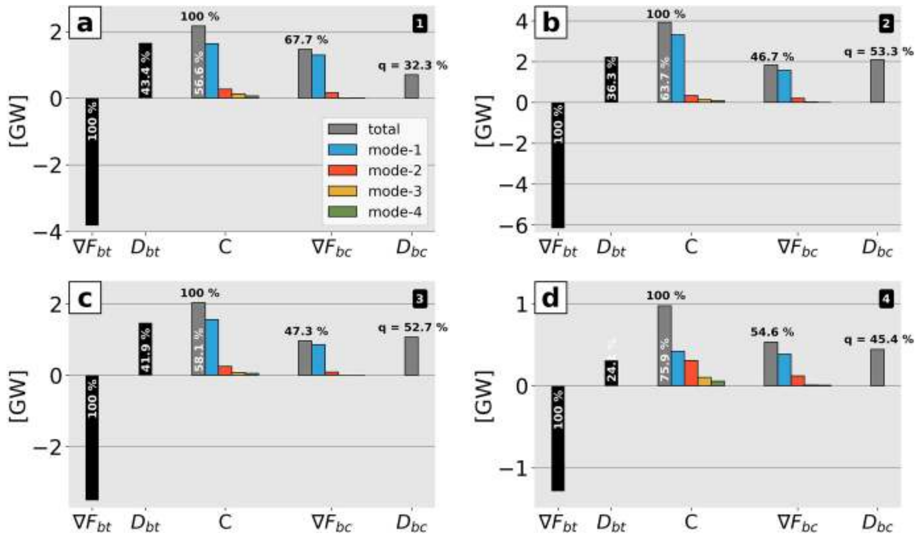

**Figure 9.** Bar plots of the regional barotropic–baroclinic M2 energy budgets for **(a)** North (1), **(b)** South (2), **(c)** Norfolk Ridge (3), and **(d)** Loyalty Ridge (4) including the barotropic energy flux divergence ($\nabla F_{\mathrm{bt}}$) and barotropic energy dissipation ($D_{\mathrm{bt}}$) as well as conversion ($C$) and baroclinic energy flux divergence ($\nabla F_{\mathrm{bc}}$) for the total baroclinic and the four lowest modes. The baroclinic energy dissipation ($D_{\mathrm{bc}}$) determined by the residual of $\nabla F_{\mathrm{bc}}$ and $C$ is also given. The percentage values (i) in white give the ratio of the barotropic energy flux divergence that is either dissipated through bottom friction or converted to baroclinic energy. The values (ii) in black give the ratio of the energy conversion term that is either radiated away or dissipated ($q$).

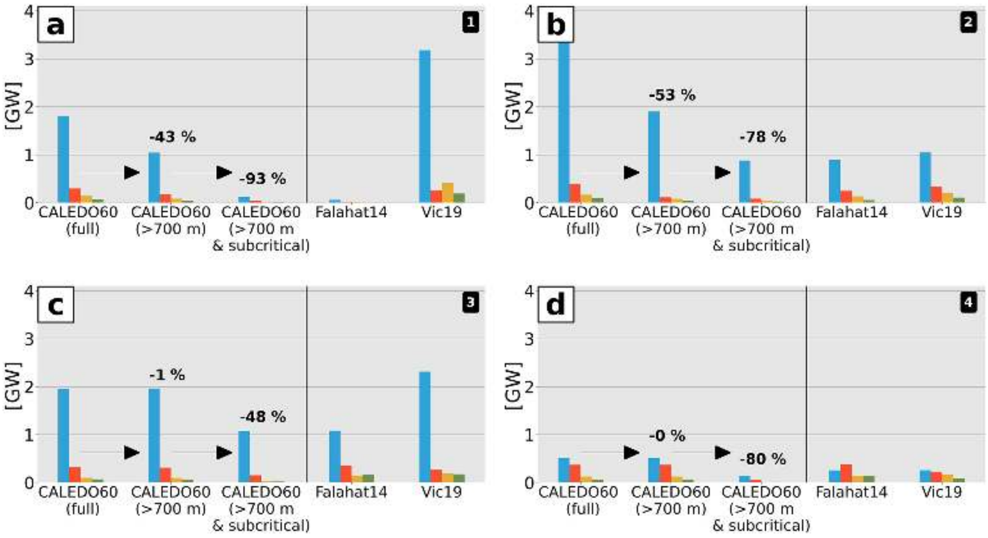

**Figure 10.** M2 barotropic-to-baroclinic energy conversion in gigawatts (GW) for the four lowest modes integrated over **(a)** North (1), **(b)** South (2), **(c)** Norfolk Ridge (3), and **(d)** Loyalty Ridge (4) for the full model, corrected for the upper 700 m, and corrected for both the upper 700 m and critical to supercritical slopes. The associated percentage decrease for the given correction is also shown. Energy conversion is compared to the semi-analytical estimates from Falahat et al. (2014) (Falahat14) and Vic et al. (2019) (Vic19) corrected for the upper 700 m. The color code is as in Fig. 9.

Briefly summarized, the bulk of energy conversion from the barotropic to the baroclinic tide is confined to four hot spot regions in shallow waters (500 m), closely linked to the complex bathymetry (i.e., shelf breaks, ridges, and seamounts), and dominated by mode 1. Approximately half of the locally generated energy dissipates in the near field, whereas the other half propagates outside the hot spot regions. This suggests a quick attenuation of baroclinic energy. Our model results show that the fraction of coherent internal tides that loses energy locally ($q = D_{\mathrm{bc}}/C$) is elevated in our study region compared to 36 % and 20 % for the Luzon Strait (Kerry et al., 2013) and the Hawaiian Ridge (Carter et al., 2008), respectively. Potential factors that may contribute to this loss of energy will be discussed later in Sect. 6.2. Particularly, we will point out that the high dissipation rates observed in our analysis may not be solely associated with actual energy dissipation, but also with a loss of tidal coherence. This will be explored in more detail in Part 2 of this study.

### 4.3 Comparison with semi-analytical model estimates

In the following, we compare our M2 modal conversion for the four subregions with the semi-analytical model estimates from Falahat et al. (2014) (Falahat14) and Vic et al. (2019) (Vic19) in Fig. 10. Recall that both products represent the energy conversion in depths $> 700$ m and on subcritical slopes only (see Sect. 2.3.6). The model conversion is given for the full model (considering the full water column and subcritical, critical, and supercritical slopes), the full model but only considering depths $> 700$ m, and the full model but only considering both depths $> 700$ m and subcritical slopes. The latter ensures the best comparison between the semi-analytical and numerical model estimates.

Overall, there is good agreement between our full-model estimates and those from semi-analytical theory concerning the conversion's modal content, with mode 1 being clearly dominant. Higher modes appear to only increase in relative importance for Loyalty Ridge (4) (Fig. 10d). The full-model energy conversion tends to be excessive in the South (2) domain (Fig. 10b). When correcting the full model for conversion in the upper 700 m in addition to conversion on critical and supercritical slopes, our model conversion compares better with the semi-analytical estimates. Even though corrected for the upper 700 m, there is no good comparison with Vic19 in the North (1) domain (Fig. 10a). This could be related to violation of linear theory that leads to unrealistic conversion rates larger than the energy lost by the barotropic tide. Remaining discrepancies among the products may be attributed to the associated bathymetry products that differ in both horizontal resolution and the correct representation of those bathymetric structures that are key for internal-tide generation.

While semi-analytical theory has proven very valuable in providing a first-order estimation of internal-tide generation on global scales, it reaches its limits in regions with shallow and complex bathymetry with critical to supercritical slopes. In fact, we find for the subregions around New Caledonia that roughly 50 %–90 % of the energy conversion may be missed locally when not allowing for conversion in the upper 700 m and on critical to supercritical slopes. This highlights the need for realistic, high-resolution numerical simulations to more faithfully represent the local internal-tide generation and dynamics.

### 4.4 Regional overview of tidal energy propagation and dissipation

The propagation of baroclinic tidal energy is expressed mainly by two predominant tidal beams that emerge from the North (1) and South (2) domains (Fig. 11a). They are 100–200 km in width and feature magnitudes well above $20\,\mathrm{kW\,m^{-1}}$ (locally up to $30\,\mathrm{kW\,m^{-1}}$) near the respective generation sites but propagate not more than 800 km toward the open ocean. In contrast to the southern tidal beam that propagates from its generation site at Pines Ridge southwestward and northeastward (though the northeastward beam is more limited), the northern tidal beam mainly propagates northeastward. This is attributed to the energy conversion that is confined to the shelf break east of the Grand Passage, whereas the Grand Passage itself is subject to only minor energy conversion (not shown). Tidal beams also emerge from Norfolk Ridge (3) and Loyalty Ridge (4). However, they are overall less pronounced and smaller in magnitude ($5\,\mathrm{kW\,m^{-1}}$).

The rather quick attenuation of the tidal beams may be associated with the high dissipation rates, which are in large part constrained to the hot spot regions (Fig. 11b). This is reflected in the regional energy budgets and sheds light on the high fraction ($\sim 50\,\%$) between local energy dissipation and generation (see Sect. 4.2). Dissipation also occurs away from the hot spot regions, but to a lower degree.

### 4.5 Zoom-in of the South (2) domain

The South (2) domain deserves special attention for two reasons: first, it represents a study area of the SWOT–AdAC program accompanied by an extensive field campaign. This will be further addressed in Sect. 6.4. Second, it represents the predominant hot spot of internal-tide generation contributing more than 40 % and 25 % to the area-integrated barotropic-to-baroclinic energy conversion associated with the four subregions and full regional domain, respectively.

In total, 6.16 GW is lost by the barotropic tide, 64 % (3.92 GW) of which is converted to internal tides (Fig. 12a). The bulk of energy is generated when the incoming barotropic tidal flow encounters Pines Ridge, featuring conversion rates well above $1\,\mathrm{W\,m^{-2}}$ on both its western and eastern flanks. Further internal-tide generation is localized downstream along a secondary ridge parallel to Pines Ridge and across the western shelf break. Locally, positive conversion is also evident around seamounts that are present in the area, namely, Munida, Antigonia, Jumeaux Est, and Stylaster.

In contrast to the conversion map which shows isolated spots, baroclinic energy dissipation is observed throughout the domain, accounting for a total of 2.09 GW (Fig. 12b). In other words, well above 50 % of the locally generated energy dissipates within the South (2) domain. Dissipation maxima are located near the generation sites such as Pines Ridge and

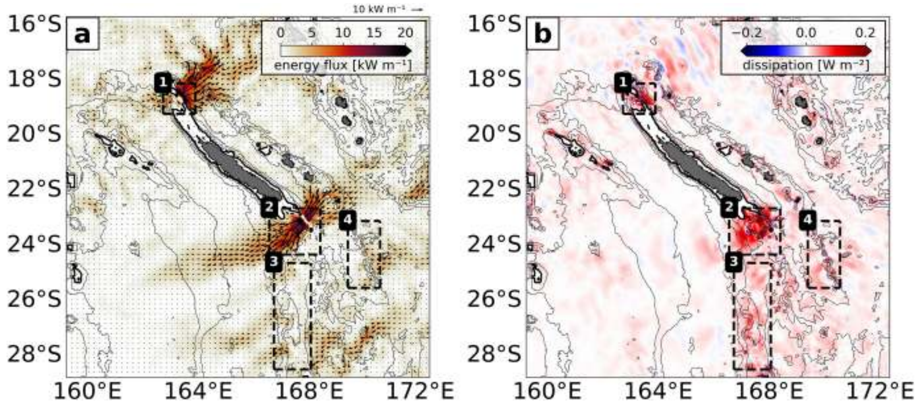

**Figure 11.** **(a)** M2 coherent energy flux (shading) including flux vectors. **(b)** M2 coherent energy dissipation (residual between the energy flux divergence and conversion). Bathymetry contours and the black boxes are given as in Fig. 7.

around the seamounts with dissipation rates $> 0.5\,\mathrm{W\,m^{-2}}$, i.e., around Munida, Brachiopode, Jumeaux Ouest, and Stylaster. Increased levels of dissipation are also found along the barrier reef that encloses the southern Caledonian lagoon. Further energy dissipation occurs uniformly westward and eastward of Pines Ridge across the shelf break with constant dissipation rates $> 0.1\,\mathrm{W\,m^{-2}}$.

The non-dissipated energy propagates away from the main generation site within well-confined tidal beams in southwestern and northeastern directions characterized by energy fluxes $> 20\,\mathrm{kW\,m^{-1}}$ which attenuate gradually to roughly $10\,\mathrm{kW\,m^{-1}}$ within 100 km distance of the generation site in the annual mean. A net energy flux of 1.83 GW leaves the South (2) domain, accounting for 47 % of the locally generated baroclinic tidal energy.

## 5 Internal-tide SSH signature

The expression of internal tides in SSH is of major interest for SWOT observability of mesoscale to submesoscale dynamics. Here, we first investigate the M2 tide amplitude around New Caledonia before addressing the tidal signature in spectral space. The questions of interest are the following. (1) What are the processes in our study region that dominate the SSH signal in the mesoscale to submesoscale range? (2) What is the contribution of the coherent internal tide to these SSH signals? (3) To what extent are we able to increase observability of the mesoscale to submesoscale when correcting for the coherent internal tide?

### 5.1 SSH amplitude of the M2 internal tide around New Caledonia

We present the spatial maps of mode 1 and mode 2 of the M2 SSH amplitude in Fig. 13a and b in comparison with the satellite-altimetry-derived empirical estimates from the HRET model (see Sect. 2.3.5) in Fig. 13c and d for mode 1 and mode 2, respectively. Dominated by mode 1, the spatial distribution of SSH reveals multiple interference patterns with M2 tidal waves emanating from multiple generation sites and summing constructively and destructively as they propagate (Fig. 13a). Amplitudes may reach more than 6 cm in the internal-tide hot spot regions. Following a similar pattern but strongly reduced in amplitude, mode 2 features significant amplitudes of up to 2 cm at some locations. Overall, the M2 SSH signature resembles the energy flux in Fig. 11a with the predominant tidal beams to the north and south of New Caledonia. There is good agreement with the HRET model concerning the spatial representation of the M2 SSH for both mode 1 (Fig. 13c) and mode 2 (Fig. 13d). Overall, mode 1 seems to be enhanced in our model, whereas mode 2 is underestimated in some regions. Note that the given differences may be associated with the different time periods the datasets are referenced to as well as the length of the time series for the model (1 year) and altimetry (25 years).

### 5.2 SSH spectral signature

Wavenumber SSH spectra are commonly used to investigate dynamical regimes at work and to explore the relative importance of balanced and unbalanced motions which may feature similar wavelengths: the wavenumber slopes and relative levels of variance both provide information on these issues (e.g., Le Traon et al., 2008; Dufau et al., 2016; Savage et al., 2017; Tchilibou et al., 2020, 2022; Vergara et al., 2022, and many more).

Here the objective is to describe for two given transects in the tidal beam direction (red lines in Fig. 13a) the SSH signature with regard to the different dynamics that are separated in terms of frequency bands: subinertial frequencies ($\omega < f$, $\mathrm{SSH_{subinertial}}$) for mesoscale and submesoscale dynamics, as well as superinertial frequencies ($\omega > f$, $\mathrm{SSH_{superinertial}}$) for internal gravity waves while distinguishing between the coherent internal-tide ($\mathrm{SSH_{coh}}$) and supertidal frequencies ($\omega > 1/10\,\mathrm{h}$, $\mathrm{SSH_{supertidal}}$).

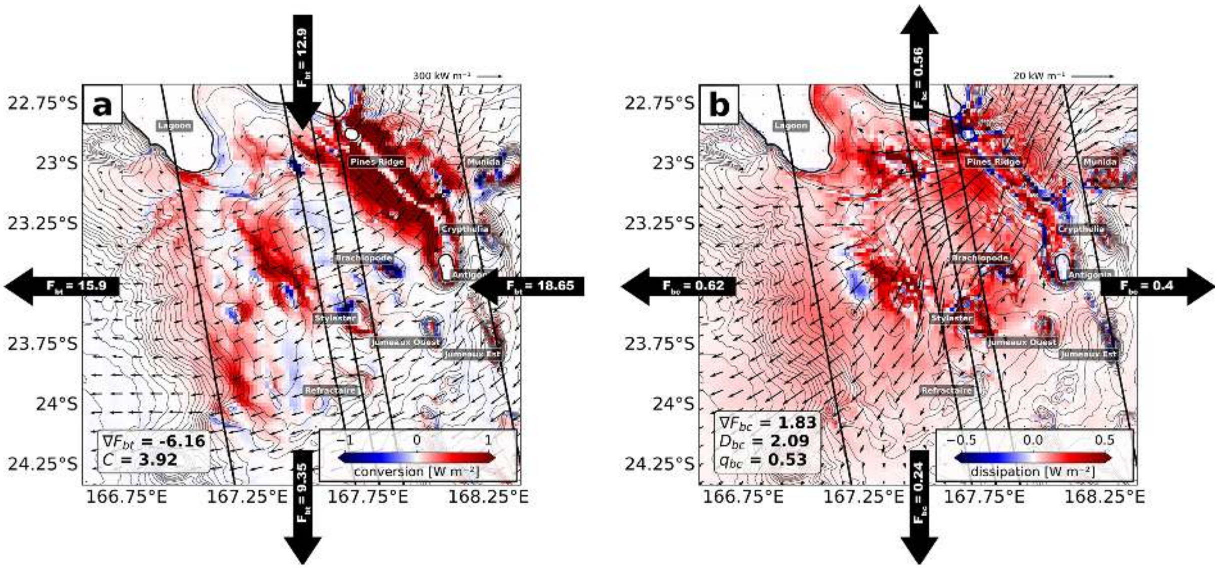

**Figure 12.** Regional M2 energy budget for the South (2) domain showing **(a)** the barotropic-to-baroclinic conversion (shading) overlaid by the barotropic energy flux (vectors) and **(b)** the depth-integrated baroclinic energy dissipation overlain by the depth-integrated baroclinic energy flux (vectors). The area-integrated values for the barotropic energy flux divergence ($\nabla F_{\mathrm{bt}}$) and barotropic-to-baroclinic conversion $C$ in **(a)** as well as the baroclinic energy flux divergence ($\nabla F_{\mathrm{bc}}$), the baroclinic energy dissipation $D_{\mathrm{bc}}$, and the ratio of locally dissipated baroclinic energy $q_{\mathrm{bc}}$ in **(b)** are also given. The incoming and outgoing **(a)** barotropic and **(b)** baroclinic energy fluxes with integrated values along the boundary are illustrated at the lateral boundaries of the domain, indicating the net direction of energy propagation. All integrated quantities are given in gigawatts (GW). Pines Ridge, the lagoon, and the most prominent seamounts are labeled. The depth contour interval is 100 m. The SWOT swaths and nadir track (solid black lines) during the fast sampling phase (1 d repeat orbit) are also shown.

Further, we will examine how SWOT observability may be limited in a region with strong internal tides. SWOT observability of mesoscale and submesoscale dynamics (balanced motion in this case) is ultimately governed by the transition scale $L_{\mathrm{t}}$ that separates balanced from unbalanced motion. The transition scale is a quantitative measure to estimate above which scales in spectral space the geostrophic balance is valid to derive balanced motion. Here, we define it as the intersection of subinertial and superinertial spectra. In other words, the transition scale is set to wavelengths where subinertial variance equals superinertial variance.

For both regions, subinertial processes explain almost all of the SSH variance for scales larger than 200 km (Fig. 13e, f). For scales smaller than 200 km, SSH variance is governed by superinertial processes, which are largely dominated by the coherent internal tide clearly expressed in spectral space with mode 1 and mode 2 around 160 and 80 km wavelength. In the annual mean, $L_{\mathrm{t}}$ is set to (i) 204 km and (ii) 163 km, meaning that the observability of balanced motion is largely limited below these scales as unbalanced motion dominates the SSH variance.

The correction of the total SSH for the coherent internal tide may be a promising attempt to assess balanced SSH dynamics. Doing so, $L_{\mathrm{t}}$ is reduced (i) from 204 km to 92 km and (ii) from 163 to 83 km. The right sub-panels of Fig. 13e and Fig. 13f show the monthly evolution of $L_{\mathrm{t}}$ and the corrected transition scale $L_{\mathrm{t}}^{\mathrm{corr}}$ over 1 model year. Temporal variations of the transition scale may be the result of the relative importance of subinertial motion, which undergoes seasonal variability (Callies et al., 2015; Rocha et al., 2016). This was explicitly shown for New Caledonia by Sérazin et al. (2020), who attributed the increasing importance of mixed layer instabilities and frontogenesis to more available potential energy in the Southern Hemisphere winter months.

Other temporal variations of the transition scale may be related to temporal variability of the internal tide. The coherent internal tide is by definition constant, but the incoherent internal tide (not shown here) depends on the seasonally varying stratification (Lahaye et al., 2019) and/or the interaction with the background currents (see Sect. 1 for references). Moreover, the incoherent signal remains in the corrected SSH signal. Therefore, the extent to which we can increase observability of mesoscale and submesoscale dynamics in areas with internal-tide activity depends on the amplitude of the incoherent internal tide. Understanding the temporal variations of the transition scale, its link to the incoherent internal tide, and its implication for SWOT SSH measurements is beyond this scope of this paper's objective, but it will be specifically addressed in Part 2.

Briefly, the dominance of unbalanced motion in the mesoscale to submesoscale band strongly restricts SSH observability of geostrophic dynamics to large eddy scales in our study regions. However, a correction for the coherent

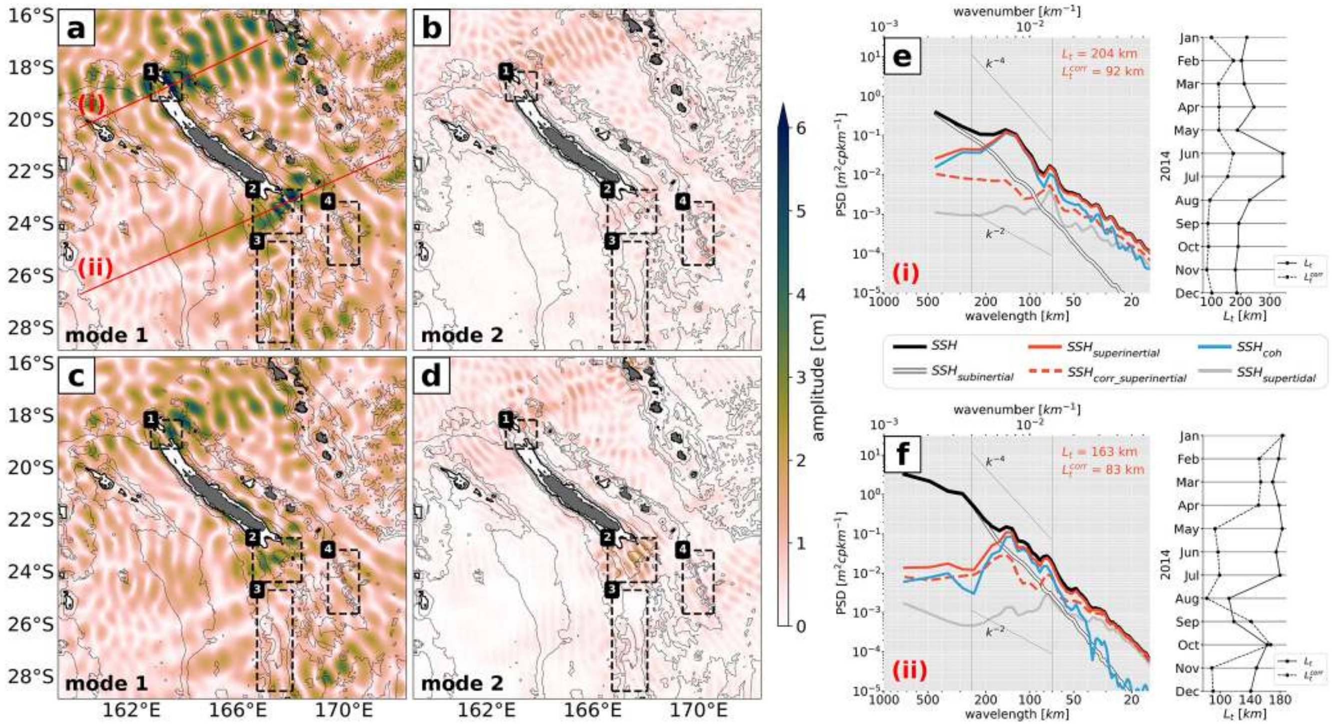

**Figure 13.** CALEDO60 M2 SSH amplitude for **(a)** mode 1 and **(b)** mode 2 in comparison with the empirical estimates of the High Resolution Empirical Tide (HRET) model for **(c)** mode 1 and **(d)** mode 2. Bathymetry contours and the black boxes are given as in Fig. 7. Annually averaged SSH wavenumber spectra for two transects **(e)** north and **(f)** south of New Caledonia, denoted (i) and (ii), respectively, in **(a)** (red lines). SSH spectra are presented for the altimetry-like SSH (corrected for the barotropic tide, SSH, black) with regard to the different dynamics that are separated in terms of frequency bands: subinertial ($\omega < f$, $\mathrm{SSH_{subinertial}}$, white) for mesoscale and submesoscale dynamics, as well as superinertial frequencies ($\omega > f$, $\mathrm{SSH_{subinertial}}$, solid red) for internal gravity waves decomposed into the coherent ($\mathrm{SSH_{coh}}$, blue) internal-tide and supertidal frequencies ($\omega > 1/10\,\mathrm{h}$, $\mathrm{SSH_{supertidal}}$, gray). The altimetry-like SSH corrected for both the barotropic and baroclinic tide and filtered for motions at superinertial frequencies ($\mathrm{SSH_{corr\_superinertial}}$, dashed red) is also given. The characteristic wavenumber slopes $k^{-2}$ and $k^{-4}$ are represented by the dotted black lines encompassing the mesoscale band (70–250 km, vertical dotted black lines). The transition scale $L_\mathrm{t}$ (i.e., where $\mathrm{SSH_{superinertial}} > \mathrm{SSH_{subinertial}}$) and the transition scale corrected for $\mathrm{SSH_{coh}}$ ($L_\mathrm{t}^\mathrm{corr}$, i.e., where $\mathrm{SSH_{corr\_superinertial}} > \mathrm{SSH_{subinertial}}$) for the annually averaged SSH spectra are specified by the red numbers. The right sub-panels in **(e)** and **(f)** show the temporal evolution of $L_\mathrm{t}$ (solid) and $L_\mathrm{t}^\mathrm{corr}$ (dashed). These are computed similarly to the annually averaged SSH spectra above (i.e. $\mathrm{SSH_{corr\_superinertial}}$ is still corrected for the annual coherent tide), but are determined by the monthly averaged spectra of $\mathrm{SSH_{superinertial}}$ / $\mathrm{SSH_{corr\_superinertial}}$ and $\mathrm{SSH_{subinertial}}$.

internal tide may improve the observability to well below 100 km.

## 6 Summary and discussion

Prominent topographic structures such as oceanic ridges, continental shelf breaks, seamounts, and island chains give rise to major internal-tide formation in large parts of the Pacific Ocean (Niwa and Hibiya, 2001). The majority of recent studies on internal tides focused mainly on two regions: the Luzon Strait (e.g., Niwa and Hibiya, 2004; Alford et al., 2011; Kerry et al., 2013) and the Hawaiian Ridge (e.g., Merrifield and Holloway, 2002; Zaron and Egbert, 2006; Carter et al., 2008). Here, we present for the first time the internal-tide dynamics around New Caledonia in the southwestern tropical Pacific Ocean using the output of a tailored high-resolution regional numerical model. Being subject to strong internal tides and elevated mesoscale eddy activity, New Caledonia represents an area of high interest for the upcoming SWOT altimeter mission to evaluate observability of mesoscale and submesoscale dynamics in the presence of unbalanced motion at wavelengths of similar scale. This is primarily true for the SWOT fast sampling phase, when the satellite sampled this region of interest every day. In this context, a dedicated field campaign (SWOTALIS, March–April 2023) was carried out in the framework of the SWOT–AdAC program (Morrow et al., 2019; d'Ovidio et al., 2019). The model results we obtained provide new and key information for the New Caledonia study region, but also more globally for the understanding of the generation and life cycle of internal tides. We were also able to gain insights into SWOT observability in a challenging region with strong internal tidal waves. These findings are summarized and discussed below.

### 6.1 New Caledonia: a hot spot of mode-1 internal-tide generation in the Pacific

The barotropic and baroclinic energy budget of the dominant M2 tide shows that in the regional model domain surrounding New Caledonia, 21.16 GW of the barotropic tidal energy is lost, 72 % (15.27 GW) of which is converted into baroclinic tidal energy. The main conversion zones are associated with the most prominent bathymetric structures such as the Grand Passage (2.17 GW) and Pines Ridge (3.92 GW) north and south of New Caledonia, respectively. This confirms that New Caledonia is a hot spot of internal-tide generation. The amount of energy converted is comparable to what has been estimated in the Luzon Strait (Kerry et al., 2013) and the Hawaiian Ridge (Carter et al., 2008), taking into account that the exact numbers depend on the size of the domain. The area-integrated M2 conversion is estimated as 15.27 GW around New Caledonia, 16.97 GW in the Luzon Strait, and 2.34 GW along the Hawaiian Ridge. Conversion integrated in the smaller subregions North (1) and South (2) are similar to the Hawaiian Ridge (2.17 and 3.92 GW, respectively). Local conversion rates are of the same order of magnitude (well above 1 W $m^{-2}$) among all regions. Further, all regions feature similar energy propagating away from the formation site within well-defined tidal beams. Maximum M2 baroclinic energy fluxes vary from 10 kW $m^{-1}$ at the Hawaiian Ridge up to 30 kW $m^{-1}$ around New Caledonia and 40 kW $m^{-1}$ at the Luzon Strait.

Interestingly, the New Caledonia region stands out compared to other previously studied regions in terms of modal content. Our modeling results suggest that barotropic tidal energy is converted, overwhelmingly, into baroclinic mode 1 (75 % of the full-domain energy conversion and up 85 % in the South (2) domain). Modes 2–4 represent a comparable amount of energy only at Loyalty Ridge (4) characterized by deep topography. For comparison, this mode-1 conversion percentage was estimated to be around 30 % at global scale, 35 % for the Pacific basin (Falahat et al., 2014; Vic et al., 2019), 30 %–60 % around Hawaii (Merrifield and Holloway, 2002; Zilberman et al., 2011), and about 9 % over the northern Atlantic Ridge (Vic et al., 2018). The reasons behind this strongly dominant mode 1 are not completely understood. A dominance of mode 1 in the western Pacific has been previously suggested with semi-analytical models (Falahat et al., 2014; Vic et al., 2019), but not to that extent. Mode 1 has been suggested to be dominantly generated in shallow depths (Falahat et al., 2014). Apart from topographic characteristics such as height, width, and depth (Legg and Huijts, 2006; Falahat et al., 2014), the modal content is argued to be primarily governed by roughness and, thus, by the topography's spectral shape (Laurent and Nash, 2004). On the other hand, it has been observed and argued by many that critical and supercritical slopes are conducive to beam-like patterns, requiring the presence of higher vertical modes (Gerkema, 2001; Balmforth et al., 2002; Legg and Huijts, 2006). Fully understanding the strong dominance of mode 1 in our region characterized by the presence of steep, tall, and shallow ridges with critical and supercritical slopes, as well as 25 % of the conversion taking place above 500 m, would require further analyses.

An important lesson learned is that New Caledonia represents a complex area for linear semi-analytical models that break down for critical and supercritical slopes and shallow bathymetry, which in turn are key for internal-tide generation at our study site. Such semi-analytical models, although very useful and widely used to estimate tidal energy conversion, its modal distribution, and tidal mixing (e.g., Falahat et al., 2014; Vic et al., 2019; de Lavergne et al., 2019, 2020), miss a significant part of the conversion (50 %–90 %) in our area, pointing out the limitation of these approaches in such complex areas. This issue was also presented in Buijsman et al. (2020). However, it was only addressed on global scales, highlighting the relevance of realistic numerical simulations on regional scales.

### 6.2 A hot spot of internal-tide dissipation

Our model results suggest elevated ratios ($q$) between local tidal energy dissipation and generation of $\sim 50\,\%$ compared to other internal-tide generation hot spots in the Luzon Strait (36 %, Kerry et al., 2013) and the Hawaiian Ridge (20 %, Carter et al., 2008). This is surprising considering the clear dominance of mode 1 in most parts of our nesting model domain where mode 1 dominates the baroclinic tidal energy propagation. Nonetheless, the elevated levels of local energy dissipation provide an explanation for the relatively small propagation distance of the tidal beams (e.g., around 800 km for the tidal beam emanating from South (2)), essentially smaller compared to the tidal beams emanating from the Luzon Strait and the Hawaiian Ridge that may propagate several thousand kilometers toward the open ocean. Several processes of tidal energy dissipation have been discussed in the literature that are well summarized in de Lavergne et al. (2019, 2020): nonlinear wave–wave interactions, wave breaking through shoaling, dissipation on critical slopes, and scattering by abyssal hills. The interaction with the topography may explain the largest fraction of energy dissipation (Kelly et al., 2013). This especially concerns the scattering and energy transfer of the low-mode internal tide to higher modes leading to increasing dissipation. Nonlinear wave–wave interactions were shown to facilitate the energy transfer of low-mode internal tides to both superharmonic (Baker and Sutherland, 2020; Sutherland and Dhaliwal, 2022) and subharmonic frequencies (Ansong et al., 2018; Olbers et al., 2020). Particularly the latter, which is associated with parametric subharmonic instability, can be an important energy sink for low-mode internal tides near the critical latitude band (around 29° N/S for the semi-diurnal tide) south of New Caledonia. The mechanisms of tidal energy dissipation and their relative contributions in our study area remain an open question. This is beyond the scope of this study and requires further investigation.

Recall that here the tidal energy dissipation (residual between energy flux divergence and conversion) corresponds to a coherent tidal analysis. Due to the length of the harmonically analyzed time series (full-model calendar year), it must be assumed that a non-negligible fraction of the coherent dissipation is not associated with true dissipation but with a loss of coherence or scattering of energy to the incoherent tide, i.e., with increasing distance from the internal-tide generation site (Rainville and Pinkel, 2006; Alford et al., 2019). The actual fraction of true energy dissipation will be addressed in more detail in Part 2 of this study involving the full semi-diurnal signal and tidal incoherence. A potentially important contribution to elevated dissipation rates could also be linked to the chosen bottom friction and drag parameterization (see Sect. 2.1). The tidal dissipation's sensitivity to the given parameterization, however, was not addressed and would require a dedicated analysis.

### 6.3 A challenging spot for SWOT observability

The SWOT mission is dedicated to documenting two-dimensional fine-scale features down to 15 km wavelength that include both subinertial (mesoscale to submesoscale dynamics) and superinertial (such as internal tides) frequencies. Disentangling these different dynamics in terms of SSH is of interest for SWOT observability. Here, we have investigated the transition scale that separates the larger scale dominated by balanced geostrophic motion from the smaller scale dominated by unbalanced wave motions in the two main pathways of the internal-tide energy flux. Further, we analyzed what impact the correction for the coherent tide in the SSH signal has on the transition scale.

Wavenumber spectra of SSH reveal the dominance of unbalanced, rapidly changing motion, largely governed by the internal tide, in the mesoscale band at spectral wavelengths below 200 km. The separation length scale between balanced and unbalanced motion is in good agreement with estimates deduced from along-track satellite altimetry in Vergara et al. (2022, see their Fig. 6). Our findings also align with the global model analysis from Qiu et al. (2018), where the SSH-derived transition scale is estimated to be slightly below 200 and 160 km north and south of New Caledonia, respectively.

Correcting our model for the coherent internal tide, we are able to improve the observability of mesoscale and submesoscale SSH around New Caledonia to well below 100 km in the annual mean. The limited observability even after the correction of the coherent internal tide is potentially linked to the temporally varying tide. The study region may be subject to strong interactions between internal tides and mesoscale eddies, giving rise to tidal incoherence. This is especially true south of the New Caledonia that is characterized by elevated levels of EKE (see Fig. 3).

### 6.4 Perspectives of this work

This work is the first modeling approach to characterize the internal-tide dynamics around New Caledonia. Part 1 focuses on the coherent part of the main M2 component. Giving first insight into internal-tide generation, propagation, and dissipation as well as SSH observability, this study is meant to serve as a basis for future studies such as eddy–internal-tide interactions and their expression in SSH. Internal tides may be strongly sensitive to the background currents both at the generation sites and along propagation, with implications for tidal energy conversion from the barotropic to baroclinic tide and tidal energy dissipation. This will be the subject of Part 2 of this study. Further, a twin simulation experiment, with the same forcing and parameterizations but without tidal forcing, has been performed. Comparing the two simulations will help us understand how tides impact the mesoscale and submesoscale fields, as well as the forward and inverse energy cascades among spatial scales (work in progress).

The results obtained will play an important role when confronted with in situ observations. The dedicated SWOTALIS in situ experiment was carried out in March–May 2023 during the SWOT fast sampling phase (related to SWOT–AdAC) beneath the SWOT swaths and nadir track. Observational platforms such as moorings, repeated hydrographic sections, and long fixed stations spanning several semi-diurnal tidal cycles with microstructure measurements in the hot spots of internal-tide generation and dissipation as well as in the propagation direction will provide further insight into the internal-tide life cycle south of New Caledonia, in combination with the SWOT data. Our simulations will help link the full water column dynamics and the SSH measurements.

Finally, this study provided first hints on internal-tide dissipation spatial variability. Yet, the impact of tidally driven mixing on temperature, other tracer fields, and biological variables in this area of high biodiversity remains to be quantified. It is expected that strong vertical velocities along bathymetric slopes, reefs, and seamounts may influence nutrient inputs into the euphotic layer and primary production, potentially up to high trophic levels and marine fauna (Derville et al., 2020). Such effort has been recently initialized in the framework of the ScInObs (Science, Innovation and Observatories of seamounts) project led by the French Research Institute for Exploitation of the Sea (IFREMER) and in collaboration with the Japan Agency for Marine–Earth Science and Technology (JAMSTEC) south of New Caledonia at the Stylaster seamount (Fig. 12). Overall, observing and understanding the local impact of internal tides on the ecosystem are of large socioeconomic interest for the island's conservation management. We hope that our results will pave the way to a better understanding of the processes and ultimately help marine conservation.

## Appendix A

**Table A1.** Regional M2 barotropic energy flux divergence $\nabla F_{\mathrm{bt}}$, barotropic energy dissipation $D_{\mathrm{bt}}$, barotropic-to-baroclinic conversion $C$, baroclinic energy flux divergence $\nabla F_{\mathrm{bc}}$, and baroclinic dissipation $D_{\mathrm{bc}}$ integrated over the North (1), South (2), Norfolk Ridge (3), and Loyalty Ridge (4) domains. The vertical structures for modes 1–4 are given for $C$ and $\nabla F_{\mathrm{bc}}$.

| | | North | South | Norfolk Ridge | Loyalty Ridge |
|---|---|---|---|---|---|
| $\nabla F_{\mathrm{bt}}$ | | −3.83 | −6.16 | −3.51 | −1.28 |
| $D_{\mathrm{bt}}$ | | 1.66 | 2.24 | 1.47 | 0.31 |
| $C$ | total | 2.17 | 3.92 | 2.04 | 0.97 |
| | mode 1 | 1.63 | 3.31 | 1.56 | 0.42 |
| | mode 2 | 0.27 | 0.33 | 0.25 | 0.31 |
| | mode 3 | 0.13 | 0.14 | 0.08 | 0.10 |
| | mode 4 | 0.06 | 0.08 | 0.05 | 0.05 |
| $\nabla F_{\mathrm{bc}}$ | total | 1.47 | 1.83 | 0.96 | 0.53 |
| | mode 1 | 1.30 | 1.58 | 0.86 | 0.38 |
| | mode 2 | 0.16 | 0.20 | 0.09 | 0.12 |
| | mode 3 | $< -0.01$ | 0.02 | $< 0.01$ | 0.01 |
| | mode 4 | 0.01 | 0.01 | $< 0.01$ | 0.01 |
| $D_{\mathrm{bc}}$ | total | 0.70 | 2.09 | 1.07 | 0.44 |

All units are given in gigawatts (GW).

*Code availability.* The tidal analysis was performed using the COMODO-SIROCCO tools, which are developed and maintained by the SIROCCO national service (CNRS/INSU). SIROCCO is funded by INSU and Observatoire Midi-Pyrénées/Université Paul Sabatier and receives project support from CNES, SHOM, IFREMER, and ANR. Figures were created using Python 3.9, Matplotlib 3.5.1, and color maps provided by Thyng et al. (2016) and van der Velden (2020).

*Data availability.* This study has been conducted using EU Copernicus Marine Service Information CMEMS (https://doi.org/10.48670/moi-00148, last access: 18 January 2023). Climatological hydrography data were obtained from CARS (http://www.marine.csiro.au/~dunn/cars2009/, last access: 21 February 2021). The Argo-CARS product from Kessler and Cravatte (2013) was made available upon request. FES2014 was produced by Noveltis, LEGOS, and CLS and distributed by Aviso+, with support from CNES (https://www.aviso.altimetry.fr/, last access: 21 June 2021). The publicly available HRET products from Edward Zaron ((Zaron and Egbert, 2006)) were downloaded from https://ingria.ceoas.oregonstate.edu/~zarone/downloads.html (last access: 12 September 2022). Barotropic-to-baroclinic M2 conversion rates from Falahat et al. (2014) are freely available at https://www.seanoe.org/data/00470/58153/ (Falahat et al., 2018, last access 23 September 2022). Barotropic-to-baroclinic M2 conversion rates from Vic et al. (2019) were made available upon request (last access: 23 September 2022).

*Author contributions.* AB performed the analysis and drafted the paper under the supervision of LG and SC. LB and AA performed the numerical simulations. The tidal analysis was performed with the help of MT and FL including fruitful discussions with CV. All co-authors reviewed the paper and contributed to the writing and final editing.

*Competing interests.* The contact author has declared that none of the authors has any competing interests.

*Disclaimer.* Publisher's note: Copernicus Publications remains neutral with regard to jurisdictional claims in published maps and institutional affiliations.

*Acknowledgements.* Simulations presented in this study were performed at the Centre Informatique National de l'Enseignement Supérieur (CINES). We thank the MEOM/IGE (MultiscalE Ocean Modeling/Institut des Géosciences de l'Environnement) group for allowing us to be part of their allocation of computational resources. We thank Mathilde Cancet for the preparation of the bathymetry dataset and Amélie Ferran for preliminary work on the modeling and analysis of internal tides around New Caledonia. Further, we appreciate the fruitful discussions with Jerome Chanut and Julien Le Sommer as well as Ritabrata Thakur and Brian Arbic with helpful comments on the modeling part. We also thank the SWOT Science Teams including the High-Resolution Ocean Modeling Group (led by Brian Arbic, Florent Lyard, and Lionel Renault) and the

Tides, Internal Tides, and Internal Gravity Waves Group (led by Edward Zaron and Brian Arbic) for providing a platform for scientific exchange and discussion. Finally, we thank two anonymous reviewers for the insightful suggestions that improved the paper.

*Financial support.* This research has been supported by the Université Toulouse III – Paul Sabatier (grant from the Ministère de l'Enseignement supérieur de la Recherche et de l'Innovation, MESRI) carried out within the PhD program of AB at the Faculty of Science and Engineering and the Doctoral School Geosciences, Astrophysics, Space and Environmental Sciences (SDU2E). Lionel Gourdeau and Sophie Cravatte are funded by the Institut de Recherche pour le Développement (IRD); Laurent Brodeau and Aurélie Albert were funded by OceanNext, Grenoble; Michel Tchilibou was funded by the Centre National d'Études Spatiale (CNES); Florent Lyard was funded by the Centre National de la Recherche Scientifique (CNRS); and Clément Vic was funded by the Institut français de recherche pour l'exploitation de la mer (IFREMER). Further, this study has been partially supported through grant EUR TESS no. ANR-18-EURE-0018 in the framework of the Programme des Investissements d'Avenir. This work is a contribution to the joint CNES–NASA project SWOT in the tropics and is supported by the French TOSCA (la Terre, l'Océan, les Surfaces Continentales, l'Atmosphère) program and the French national program LEFE (Les Enveloppes Fluides et l'Environnement).

*Review statement.* This paper was edited by Katsuro Katsumata and reviewed by two anonymous referees.

## References

Alford, M. H.: Redistribution of energy available for ocean mixing by long-range propagation of internal waves, Nature, 423, 159–162, https://doi.org/10.1038/nature01628, 2003.

Alford, M. H., MacKinnon, J. A., Nash, J. D., Simmons, H., Pickering, A., Klymak, J. M., Pinkel, R., Sun, O., Rainville, L., Musgrave, R., et al.: Energy flux and dissipation in Luzon Strait: Two tales of two ridges, J. Phys. Ocean., 41, 2211–2222, https://doi.org/10.1175/JPO-D-11-073.1, 2011.

Alford, M. H., Simmons, H. L., Marques, O. B., and Girton, J. B.: Internal tide attenuation in the North Pacific, Geophys. Res. Lett., 46, 8205–8213, https://doi.org/10.1029/2019GL082648, 2019.

Ansong, J. K., Arbic, B. K., Simmons, H. L., Alford, M. H., Buijsman, M. C., Timko, P. G., Richman, J. G., Shriver, J. F., and Wallcraft, A. J.: Geographical distribution of diurnal and semidiurnal parametric subharmonic instability in a global ocean circulation model, J. Phys. Ocean., 48, 1409–1431, https://doi.org/10.1175/JPO-D-17-0164.1, 2018.

Arbic, B. K., Alford, M. H., Ansong, J. K., Buijsman, M. C., Ciotti, R. B., Farrar, J. T., Hallberg, R. W., Henze, C. E., Hill, C. N., Luecke, C. A., Menemenlis, D., Metzger, E. J., Muller, M., Nelson, A. D., Nelson, B. C., Ngodock, H. E., Ponte, R. M., Richman, J. G., Savage, A. C., Scott, R. B., Shriver, J. F., Simmons, H. L., Souopgui, I., Timko, P. G., Wallcraft, A. J., Zamudio, L., and Zhao, Z.: Primer on global internal tide and internal gravity wave continuum modeling in HYCOM and MITgcm, New Front. Operat. Oceanogr., 307–392, https://doi.org/10.17125/gov2018.ch13, 2018.

Baker, L. E. and Sutherland, B. R.: The evolution of superharmonics excited by internal tides in non-uniform stratification, J. Fluid Mech., 891, https://doi.org/10.1017/jfm.2020.188, 2020.

Balidakis, K., Sulzbach, R., Shihora, L., Dahle, C., Dill, R., and Dobslaw, H.: Atmospheric contributions to global ocean tides for satellite gravimetry, J. Adv. Model. Earth Syst., 14, e2022MS003193, https://doi.org/10.1029/2022MS003193, 2022.

Ballarotta, M., Ubelmann, C., Pujol, M.-I., Taburet, G., Fournier, F., Legeais, J.-F., Faugère, Y., Delepoulle, A., Chelton, D., Dibarboure, G., and Picot, N.: On the resolutions of ocean altimetry maps, Ocean Sci., 15, 1091–1109, https://doi.org/10.5194/os-15-1091-2019, 2019.

Balmforth, N., Ierley, G., and Young, W.: Tidal conversion by subcritical topography, J. Phys. Ocean., 32, 2900–2914, https://doi.org/10.1175/1520-0485(2002)032<2900:TCBST>2.0.CO;2, 2002.

Bell Jr., T.: Topographically generated internal waves in the open ocean, J. Geophys. Res., 80, 320–327, https://doi.org/10.1029/JC080i003p00320, 1975.

Buijsman, M. C., Klymak, J. M., Legg, S., Alford, M. H., Farmer, D., MacKinnon, J. A., Nash, J. D., Park, J.-H., Pickering, A., and Simmons, H.: Three-dimensional double-ridge internal tide resonance in Luzon Strait, J. Phys. Ocean., 44, 850–869, https://doi.org/10.1175/JPO-D-13-024.1, 2014.

Buijsman, M. C., Arbic, B. K., Richman, J. G., Shriver, J. F., Wallcraft, A. J., and Zamudio, L.: Semidiurnal internal tide incoherence in the equatorial p acific, J. Geophys. Res.:-Oceans, 122, 5286–5305, https://doi.org/10.1002/2016JC012590, 2017.

Buijsman, M. C., Stephenson, G. R., Ansong, J. K., Arbic, B. K., Green, J. M., Richman, J. G., Shriver, J. F., Vic, C., Wallcraft, A. J., and Zhao, Z.: On the interplay between horizontal resolution and wave drag and their effect on tidal baroclinic mode waves in realistic global ocean simulations, Ocean Modell., 152, 101656, https://doi.org/10.1016/j.ocemod.2020.101656, 2020.

Callies, J., Ferrari, R., Klymak, J., et al.: Seasonality in submesoscale turbulence, Nat. Commun., 6, 6862, https://doi.org/10.1038/ncomms7862, 2015.

Carrere, L., Arbic, B. K., Dushaw, B., Egbert, G., Erofeeva, S., Lyard, F., Ray, R. D., Ubelmann, C., Zaron, E., Zhao, Z., Shriver, J. F., Buijsman, M. C., and Picot, N.: Accuracy assessment of global internal-tide models using satellite altimetry, Ocean Sci., 17, 147–180, https://doi.org/10.5194/os-17-147-2021, 2021.

Carter, G. S., Merrifield, M., Becker, J. M., Katsumata, K., Gregg, M., Luther, D., Levine, M., Boyd, T. J., and Firing, Y.: Energetics of M2 barotropic-to-baroclinic tidal conversion at the Hawaiian Islands, J. Phys. Ocean., 38, 2205–2223, https://doi.org/10.1175/2008JPO3860.1, 2008.

Chapman, S. and Lindzen, R. S.: Atmospheric tides: thermal and gravitational, Vol. 15, Springer Science & Business Media, https://doi.org/10.1007/978-94-010-3399-2, 1969.

Couvelard, X.: Structure et dynamique des jets barotropes créés pas les îles du Pacifique Sud-Ouest., PhD thesis, Université Paul Sabatier-Toulouse III, 2007.

Couvelard, X., Marchesiello, P., Gourdeau, L., and Lefèvre, J.: Barotropic zonal jets induced by islands in the southwest Pacific, J. Phys. Ocean., 38, 2185–2204, https://doi.org/10.1175/2008JPO3903.1, 2008.

Cravatte, S., Kestenare, E., Eldin, G., Ganachaud, A., Lefèvre, J., Marin, F., Menkes, C., and Aucan, J.: Regional circulation around New Caledonia from two decades of observations, J. Mar. Syst., 148, 249–271, https://doi.org/10.1016/j.jmarsys.2015.03.004, 2015.

de Lavergne, C., Falahat, S., Madec, G., Roquet, F., Nycander, J., and Vic, C.: Toward global maps of internal tide energy sinks, Ocean Modell., 137, 52–75, https://doi.org/10.1016/j.ocemod.2019.03.010, 2019.

de Lavergne, C., Vic, C., Madec, G., Roquet, F., Waterhouse, A. F., Whalen, C., Cuypers, Y., Bouruet-Aubertot, P., Ferron, B., and Hibiya, T.: A parameterization of local and remote tidal mixing, J. Adv. Model. Earth Syst., 12, e2020MS002065, https://doi.org/10.1029/2020MS002065, 2020.

Debreu, L., Vouland, C., and Blayo, E.: AGRIF: Adaptive grid refinement in Fortran, Comput. Geosci., 34, 8–13, https://doi.org/10.1016/j.cageo.2007.01.009, 2008.

Derville, S., Torres, L. G., Zerbini, A. N., Oremus, M., and Garrigue, C.: Horizontal and vertical movements of humpback whales inform the use of critical pelagic habitats in the western South Pacific, Sci. Rep., 10, 4871, https://doi.org/10.1038/s41598-020-61771-z, 2020.

Dufau, C., Orsztynowicz, M., Dibarboure, G., Morrow, R., and Le Traon, P.-Y.: Mesoscale resolution capability of altimetry: Present and future, J. Geophys. Res.-Oceans, 121, 4910–4927, https://doi.org/10.1002/2015JC010904, 2016.

Dunphy, M. and Lamb, K. G.: Focusing and vertical mode scattering of the first mode internal tide by mesoscale eddy interaction, J. Geophys. Res.-Oceans, 119, 523–536, https://doi.org/10.1002/2013JC009293, 2014.

Dunphy, M., Ponte, A. L., Klein, P., and Le Gentil, S.: Low-mode internal tide propagation in a turbulent eddy field, J. Phys. Ocean., 47, 649–665, https://doi.org/10.1175/JPO-D-16-0099.1, 2017.

Durand, F., Marin, F., Fuda, J.-L., and Terre, T.: The east caledonian current: a case example for the intercomparison between altika and in situ measurements in a boundary current, Mar. Geodesy, 40, 1–22, https://doi.org/10.1080/01490419.2016.1258375, 2017.

Dushaw, B. D., Howe, B. M., Cornuelle, B. D., Worcester, P. F., and Luther, D. S.: Barotropic and baroclinic tides in the central North Pacific Ocean determined from long-range reciprocal acoustic transmissions, J. Phys. Ocean., 25, 631–647, https://doi.org/10.1175/1520-0485(1995)025<0631:BABTIT>2.0.CO;2, 1995.

d'Ovidio, F., Pascual, A., Wang, J., Doglioli, A. M., Jing, Z., Moreau, S., Grégori, G., Swart, S., Speich, S., Cyr, F., et al.: Frontiers in fine-scale in situ studies: Opportunities during the swot fast sampling phase, Front. Mar. Sci., 6, 168, https://doi.org/10.3389/fmars.2019.00168, 2019.

Falahat, S., Nycander, J., Roquet, F., and Zarroug, M.: Global calculation of tidal energy conversion into vertical normal modes, J. Phys. Ocean., 44, 3225–3244, https://doi.org/10.1175/JPO-D-14-0002.1, 2014.

Falahat, S., Nycander, J., De Lavergne, C., Roquet, F., Madec, G., and Vic, C.: Global estimates of internal tide generation rates at 1/30° resolution, SEANOE [data set], https://doi.org/10.17882/58153, 2018.

Fu, L.-L. and Ferrari, R.: Observing oceanic submesoscale processes from space, EOS T. Am. Geophys. Un., 89, 488–488, https://doi.org/10.1029/2008EO480003, 2008.

Fu, L.-L. and Ubelmann, C.: On the transition from profile altimeter to swath altimeter for observing global ocean surface topography, J. Atmos. Ocean. Tech., 31, 560–568, https://doi.org/10.1175/JTECH-D-13-00109.1, 2014.

Fu, L.-L., Alsdorf, D., Morrow, R., Rodriguez, E., and Mognard, N.: SWOT: the Surface Water and Ocean Topography Mission: wide-swath altimetric elevation on Earth, Tech. rep., Pasadena, CA: Jet Propulsion Laboratory, National Aeronautics and Space, http://hdl.handle.net/2014/41996 (last access: 16 May 2023), 2012.

Ganachaud, A., Vega, A., Rodier, M., Dupouy, C., Maes, C., Marchesiello, P., Eldin, G., Ridgway, K., and Le Borgne, R.: Observed impact of upwelling events on water properties and biological activity off the southwest coast of New Caledonia, Mar. Pollut. Bull., 61, 449–464, https://doi.org/10.1016/j.marpolbul.2010.06.042, 2010.

Gardes, L., Tessier, E., Allain, V., Alloncle, N., Baudat-Franceschi, J., Butaud, J., Collot, J., Etaix-Bonnin, R., Hubert, A., Jourdan, H., Loisier A., Menkès, C., Rouillard, P., Samadi, S., Vidal, E., and Yokohama, Y.: Analyse stratégique de l'Espace maritime de la Nouvelle-Calédonie–vers une gestion intégrée, Nouméa: Agence des aires marines protégées, https://doi.org/10.13140/RG.2.1.2888.0803, 2014.

Garrett, C. and Kunze, E.: Internal tide generation in the deep ocean, Annu. Rev. Fluid Mech., 39, 57–87, https://doi.org/10.1146/annurev.fluid.39.050905.110227, 2007.

Gaspar, P., Grégoris, Y., and Lefevre, J.-M.: A simple eddy kinetic energy model for simulations of the oceanic vertical mixing: Tests at station Papa and Long-Term Upper Ocean Study site, J. Geophys. Res.-Oceans, 95, 16179–16193, https://doi.org/10.1029/JC095iC09p16179, 1990.

GEBCO, B.: The GEBCO_2019 Grid–a Continuous Terrain Model of the Global Oceans and Land, BODC [data set], 2019.

Gerkema, T.: Internal and interfacial tides: beam scattering and local generation of solitary waves, J. Mar. Res., 59, 227–255, https://doi.org/10.1357/002224001762882646, 2001.

Gill, A. E.: Atmosphere-ocean dynamics, Vol. 30, Academic press, ISBN 9780122835223, 1982.

Hendershott, M. C.: Long waves and ocean tides, in: Warren, B., Wunsch, C. (Eds.), Evolution of Physical Oceanography, Scientific Surveys in Honor of Henry Stommel, MIT Press, Cambridge, MA, 292–341, 1981.

Hersbach, H., Bell, B., Berrisford, P., Hirahara, S., Horányi, A., Muñoz-Sabater, J., Nicolas, J., Peubey, C., Radu, R., Schepers, D., Simmons, A., Soci, C., Abdalla, S., Abellan, X., Balsamo, G., Bechtold, P., Biavati, G., Bidlot, J., Bonavita, M., De Chiara, G., Dahlgren, P., Dee, D., Diamantakis, M., Dragani, R., Flemming, J., Forbes, R., Fuentes, M., Geer, A., Haimberger, L., Healy, S., Hogan, R. J., Hólm, E., Janisková, M., Keeley, S., Laloyaux, P., Lopez, P., Lupu, C., Radnoti, G., de Rosnay, P., Rozum, I., Vamborg, F., Villaume, S., and Thépaut, J.-N.: The ERA5 global reanalysis, Q. J. Roy. Meteor. Soc., 146, 1999–2049, https://doi.org/10.1002/qj.3803, 2020.

Jeon, C.-H., Buijsman, M. C., Wallcraft, A. J., Shriver, J. F., Arbic, B. K., Richman, J. G., and Hogan, P. J.: Improving surface tidal accuracy through two-way nesting in a global ocean model, Ocean Modell., 137, 98–113, https://doi.org/10.1016/j.ocemod.2019.03.007, 2019.

Kelly, S., Nash, J., and Kunze, E.: Internal-tide energy over topography, J. Geophys. Res.-Oceans, 115, https://doi.org/10.1029/2009JC005618, 2010.

Kelly, S., Jones, N., Nash, J., and Waterhouse, A.: The geography of semidiurnal mode-1 internal-tide energy loss, Geophys. Res. Lett., 40, 4689–4693, https://doi.org/10.1002/grl.50872, 2013.

Keppler, L., Cravatte, S., Chaigneau, A., Pegliasco, C., Gourdeau, L., and Singh, A.: Observed characteristics and vertical structure of mesoscale eddies in the southwest tropical Pacific, J. Geophys. Res.-Oceans, 123, 2731–2756, https://doi.org/10.1002/2017JC013712, 2018.

Kerry, C. G., Powell, B. S., and Carter, G. S.: Effects of remote generation sites on model estimates of M2 internal tides in the Philippine Sea, J. Phys. Ocean., 43, 187–204, https://doi.org/10.1175/JPO-D-12-081.1, 2013.

Kessler, W. S. and Cravatte, S.: Mean circulation of the Coral Sea, J. Geophys. Res.-Oceans, 118, 6385–6410, https://doi.org/10.1002/2013JC009117, 2013.

Kunze, E.: Internal-wave-driven mixing: Global geography and budgets, J. Phys. Ocean., 47, 1325–1345, https://doi.org/10.1175/JPO-D-16-0141.1, 2017a.

Kunze, E.: The internal-wave-driven meridional overturning circulation, J. Phys. Ocean., 47, 2673–2689, https://doi.org/10.1175/JPO-D-16-0142.1, 2017b.

Lahaye, N., Gula, J., and Roullet, G.: Sea surface signature of internal tides, Geophys. Res. Lett., 46, 3880–3890, https://doi.org/10.1029/2018GL081848, 2019.

Lahaye, N., Gula, J., and Roullet, G.: Internal Tide Cycle and Topographic Scattering Over the North Mid-Atlantic Ridge, J. Geophys. Res.-Oceans, 125, e2020JC016376, https://doi.org/10.1029/2020JC016376, 2020.

Lamb, K. G. and Dunphy, M.: Internal wave generation by tidal flow over a two-dimensional ridge: Energy flux asymmetries induced by a steady surface trapped current, J. Fluid Mech., 836, 192–221, https://doi.org/10.1017/jfm.2017.800, 2018.

Laurent, L. C. S. and Nash, J. D.: An examination of the radiative and dissipative properties of deep ocean internal tides, Deep-Sea Res. Pt. I, 51, 3029–3042, https://doi.org/10.1016/j.dsr2.2004.09.008, 2004.

Laurent, L. S., Stringer, S., Garrett, C., and Perrault-Joncas, D.: The generation of internal tides at abrupt topography, Deep-Sea Res. Pt. I, 50, 987–1003, https://doi.org/10.1016/S0967-0637(03)00096-7, 2003.

Le Traon, P.-Y., Klein, P., Hua, B. L., and Dibarboure, G.: Do altimeter wavenumber spectra agree with the interior or surface quasigeostrophic theory?, J. Phys. Ocean., 38, 1137–1142, https://doi.org/10.1175/2007JPO3806.1, 2008.

Legg, S. and Huijts, K. M.: Preliminary simulations of internal waves and mixing generated by finite amplitude tidal flow over isolated topography, Deep-Sea Res. Pt. II, 53, 140–156, https://doi.org/10.1016/j.dsr2.2005.09.014, 2006.

Leichter, J. J., Stewart, H. L., and Miller, S. L.: Episodic nutrient transport to Florida coral reefs, Limnol. Oceanogr., 48, 1394–1407, https://doi.org/10.4319/lo.2003.48.4.1394, 2003.

Lyard, F. H., Allain, D. J., Cancet, M., Carrère, L., and Picot, N.: FES2014 global ocean tide atlas: design and performance, Ocean Sci., 17, 615–649, https://doi.org/10.5194/os-17-615-2021, 2021.

MacKinnon, J. A., Zhao, Z., Whalen, C. B., Waterhouse, A. F., Trossman, D. S., Sun, O. M., Laurent, L. C. S., Simmons, H. L., Polzin, K., Pinkel, R., Pickering, A., Norton, N. J., Nash, J. D., Musgrave, R., Merchant, L. M., Melet, A. V., Mater, B., Legg, S., Large, W. G., Kunze, E., Klymak, J. M., Jochum, M., Jayne, S. R., Hallberg, R. W., Griffies, S. M., Diggs, S., Danabasoglu, G., Chassignet, E. P., Buijsman, M. C., Bryan, F. O., Briegleb, B. P., Barna, A., Arbic, B. K., Ansong, J. K., and Alford, M. H.: Climate process team on internal wave–driven ocean mixing, B. Am. Meteorol. Soc., 98, 2429–2454, https://doi.org/10.1175/BAMS-D-16-0030.1, 2017.

Madec, G. and Team, N. S.: NEMO ocean engine, no. 27 in Scientific Notes of Climate Modelling Center, Zenodo, https://doi.org/10.5281/zenodo.1464816, backup Publisher: Institut Pierre-Simon Laplace (IPSL) ISSN 1288-1619, 2023.

Mazloff, M. R., Cornuelle, B., Gille, S. T., and Wang, J.: The Importance of Remote Forcing for Regional Modeling of Internal Waves, J. Geophys. Res.-Oceans, 125, e2019JC015623, https://doi.org/10.1029/2019JC015623, 2020.

McDougall, T. J. and Barker, P. M.: Getting started with TEOS-10 and the Gibbs Seawater (GSW) oceanographic toolbox, Scor/Iapso WG, 127, 1–28, 2011.

Melet, A., Hallberg, R., Legg, S., and Polzin, K.: Sensitivity of the ocean state to the vertical distribution of internal-tide-driven mixing, J. Phys. Ocean., 43, 602–615, https://doi.org/10.1175/JPO-D-12-055.1, 2013.

Menkès, C. E., Allain, V., Rodier, M., Gallois, F., Lebourges-Dhaussy, A., Hunt, B. P., Smeti, H., Pagano, M., Josse, E., Daroux, A., Lehodey, P., Senina, I., Kestenare, E., Lorrain, A., and Nicol, S.: Seasonal oceanography from physics to micronekton in the south-west Pacific, Deep-Sea Res. Pt. II, 113, 125–144, https://doi.org/10.1016/j.dsr2.2014.10.026, 2015.

Merrifield, M. A. and Holloway, P. E.: Model estimates of M2 internal tide energetics at the Hawaiian Ridge, J. Geophys. Res.-Oceans, 107, 5–1, https://doi.org/10.1029/2001JC000996, 2002.

Morrow, R., Fu, L.-L., Ardhuin, F., Benkiran, M., Chapron, B., Cosme, E., d'Ovidio, F., Farrar, J. T., Gille, S. T., Lapeyre, G., Le Traon, P.-Y., Pascual, A., Ponte, A., Qiu, B., Rascle, N., Ubelmann, C., Wang, J., Zaron, and E. D.: Global observations of fine-scale ocean surface topography with the Surface Water and Ocean Topography (SWOT) mission, Front. Mar. Sci., 6, 232, https://doi.org/10.3389/fmars.2019.00232, 2019.

Munk, W. and Wunsch, C.: Abyssal recipes II: Energetics of tidal and wind mixing, Deep-Sea Res. Pt. I, 45, 1977–2010, https://doi.org/10.1016/S0967-0637(98)00070-3, 1998.

Nelson, A., Arbic, B., Menemenlis, D., Peltier, W., Alford, M., Grisouard, N., and Klymak, J.: Improved internal wave spectral continuum in a regional ocean model, J. Geophys. Res.-Oceans, 125, e2019JC015974, https://doi.org/10.1029/2019JC015974, 2020.

Niwa, Y. and Hibiya, T.: Numerical study of the spatial distribution of the M2 internal tide in the Pacific Ocean, J. Geophys. Res.-Oceans, 106, 22441–22449, https://doi.org/10.1029/2000JC000770, 2001.

Niwa, Y. and Hibiya, T.: Three-dimensional numerical simulation of M2 internal tides in the East China Sea, J. Geophys. Res.-Oceans, 109, https://doi.org/10.1029/2003JC001923, 2004.

Nugroho, D.: The tides in a general circulation model in the indonesian sras, PhD thesis, Université Paul Sabatier-Toulouse III, 2017.

Nycander, J.: Generation of internal waves in the deep ocean by tides, J. Geophys. Res.-Oceans, 110, https://doi.org/10.1029/2004JC002487, 2005.

Olbers, D., Pollmann, F., and Eden, C.: On PSI interactions in internal gravity wave fields and the decay of baroclinic tides, J. Phys. Ocean., 50, 751–771, https://doi.org/10.1175/JPO-D-19-0224.1, 2020.

Payri, C.-E. and de Forges, B. R.: Compendium of marine species from New Caledonia, IRD (Institut de recherche pour le développement), 1297-9635, 2006.

Payri, C. E., Allain, V., Aucan, J., David, C., David, V., Dutheil, C., Loubersac, L., Menkes, C., Pelletier, B., Pestana, G., and Samadi, S.: New caledonia, in: World Seas: An Environmental Evaluation, Elsevier, 593–618, https://doi.org/10.1016/B978-0-08-100853-9.00035-X, 2019.

Pelletier, B.: Geology of the New Caledonia region and its implications for the study of the New Caledonian biodiversity, Compendium of marines species from New Caledonia, Dossiers Scientifiques et Techniques, II7, 19–32, 2007.

Ponte, A. L., Klein, P., Dunphy, M., and Le Gentil, S.: Low-mode internal tides and balanced dynamics disentanglement in altimetric observations: Synergy with surface density observations, J. Geophys. Res.-Oceans, 122, 2143–2155, https://doi.org/10.1002/2016JC012214, 2017.

Qiu, B. and Chen, S.: Seasonal modulations in the eddy field of the South Pacific Ocean, J. Phys. Ocean., 34, 1515–1527, https://doi.org/10.1175/1520-0485(2004)034<1515:SMITEF>2.0.CO;2, 2004.

Qiu, B., Scott, R. B., and Chen, S.: Length scales of eddy generation and nonlinear evolution of the seasonally modulated South Pacific Subtropical Countercurrent, J. Phys. Ocean., 38, 1515–1528, https://doi.org/10.1175/2007JPO3856.1, 2008.

Qiu, B., Chen, S., and Kessler, W. S.: Source of the 70-day mesoscale eddy variability in the Coral Sea and the North Fiji Basin, J. Phys. Ocean., 39, 404–420, https://doi.org/10.1175/2008JPO3988.1, 2009.

Qiu, B., Chen, S., Klein, P., Wang, J., Torres, H., Fu, L.-L., and Menemenlis, D.: Seasonality in transition scale from balanced to unbalanced motions in the world ocean, J. Phys. Ocean., 48, 591–605, https://doi.org/10.1175/JPO-D-17-0169.1, 2018.

Qu, T. and Lindstrom, E. J.: A climatological interpretation of the circulation in the western South Pacific, J. Phys. Ocean., 32, 2492–2508, https://doi.org/10.1175/1520-0485(2002)032<2492:ACIOTC>2.0.CO;2, 2002.

Rainville, L. and Pinkel, R.: Propagation of low-mode internal waves through the ocean, J. Phys. Ocean., 36, 1220–1236, https://doi.org/10.1175/JPO2889.1, 2006.

Ray, R. D. and Zaron, E. D.: M2 internal tides and their observed wavenumber spectra from satellite altimetry, J. Phys. Ocean., 46, 3–22, https://doi.org/10.1175/JPO-D-15-0065.1, 2016.

Renault, L., Molemaker, M. J., McWilliams, J. C., Shchepetkin, A. F., Lemarié, F., Chelton, D., Illig, S., and Hall, A.: Modulation of wind work by oceanic current interaction with the atmosphere, J. Phys. Ocean., 46, 1685–1704, https://doi.org/10.1175/JPO-D-15-0232.1, 2016.

Ridgway, K. and Dunn, J.: Mesoscale structure of the mean East Australian Current System and its relationship with topography, Prog. Oceanogr., 56, 189–222, https://doi.org/10.1016/S0079-6611(03)00004-1, 2003.

Ridgway, K., Dunn, J., and Wilkin, J.: Ocean interpolation by four-dimensional weighted least squares–Application to the waters around Australasia, J. Atmos. Ocean. Tech., 19, 1357–1375, https://doi.org/10.1175/1520-0426(2002)019<1357:OIBFDW>2.0.CO;2, 2002.

Rocha, C. B., Gille, S. T., Chereskin, T. K., and Menemenlis, D.: Seasonality of submesoscale dynamics in the Kuroshio Extension, 43, 11304–11311, https://doi.org/10.1002/2016GL071349, 2016.

Roger, J., Pelletier, B., Duphil, M., Lefèvre, J., Aucan, J., Lebellegard, P., Thomas, B., Bachelier, C., and Varillon, D.: The $M_{\mathrm{W}}$ 7.5 Tadine (Maré, Loyalty Islands) earthquake and related tsunami of 5 December 2018: seismotectonic context and numerical modeling, Nat. Hazards Earth Syst. Sci., 21, 3489–3508, https://doi.org/10.5194/nhess-21-3489-2021, 2021.

Samadi, S., Bottan, L., Macpherson, E., De Forges, B. R., and Boisselier, M.-C.: Seamount endemism questioned by the geographic distribution and population genetic structure of marine invertebrates, Mar. Biol., 149, 1463–1475, https://doi.org/10.1007/s00227-006-0306-4, 2006.

Savage, A. C., Arbic, B. K., Alford, M. H., Ansong, J. K., Farrar, J. T., Menemenlis, D., O'Rourke, A. K., Richman, J. G., Shriver, J. F., Voet, G., Wallcraft, A. J., and Zamudio, L.: Spectral decomposition of internal gravity wave sea surface height in global models, J. Geophys. Res.-Oceans, 122, 7803–7821, https://doi.org/10.1002/2017JC013009, 2017.

Sérazin, G., Marin, F., Gourdeau, L., Cravatte, S., Morrow, R., and Dabat, M.-L.: Scale-dependent analysis of in situ observations in the mesoscale to submesoscale range around New Caledonia, Ocean Sci., 16, 907–925, https://doi.org/10.5194/os-16-907-2020, 2020.

Shakespeare, C. J. and Hogg, A. M.: On the momentum flux of internal tides, J. Phys. Ocean., 49, 993–1013, https://doi.org/10.1175/JPO-D-18-0165.1, 2019.

Simmons, H. L., Hallberg, R. W., and Arbic, B. K.: Internal wave generation in a global baroclinic tide model, Deep-Sea Res. Pt. II, 51, 3043–3068, https://doi.org/10.1016/j.dsr2.2004.09.015, 2004.

Siyanbola, O. Q., Buijsman, M. C., Delpech, A., Renault, L., Barkan, R., Shriver, J. F., Arbic, B. K., and McWilliams, J. C.: Remote internal wave forcing of regional ocean simulations near the US West Coast, Ocean Modell., 181, 102154, https://doi.org/10.1016/j.ocemod.2022.102154, 2023.

Smith, S. G. L. and Young, W.: Conversion of the barotropic tide, J. Phys. Ocean., 32, 1554–1566, https://doi.org/10.1175/1520-0485(2002)032<1554:COTBT>2.0.CO;2, 2002.

St. Laurent, L. and Garrett, C.: The role of internal tides in mixing the deep ocean, J. Phys. Ocean., 32, 2882–2899, https://doi.org/10.1175/1520-0485(2002)032<2882:TROITI>2.0.CO;2, 2002.

St. Laurent, L., Simmons, H., and Jayne, S.: Estimating tidally driven mixing in the deep ocean, Geophys. Res. Lett., 29, 21-1-21-4, https://doi.org/10.1029/2002GL015633, 2002.

Sutherland, B. R. and Dhaliwal, M. S.: The nonlinear evolution of internal tides, Part 1: the superharmonic cascade, J. Fluid Mech., 948, A21, https://doi.org/10.1017/jfm.2022.689, 2022.

Tchilibou, M., Gourdeau, L., Lyard, F., Morrow, R., Koch Larrouy, A., Allain, D., and Djath, B.: Internal tides in the Solomon Sea in contrasted ENSO conditions, Ocean Sci., 16, 615–635, https://doi.org/10.5194/os-16-615-2020, 2020.

Tchilibou, M., Koch-Larrouy, A., Barbot, S., Lyard, F., Morel, Y., Jouanno, J., and Morrow, R.: Internal tides off the Amazon shelf during two contrasted seasons: interactions with background circulation and SSH imprints, Ocean Sci., 18, 1591–1618, https://doi.org/10.5194/os-18-1591-2022, 2022.

Thakur, R., Arbic, B. K., Menemenlis, D., Momeni, K., Pan, Y., Peltier, W. R., Skitka, J., Alford, M. H., and Ma, Y.: Impact of vertical mixing parameterizations on internal gravity wave spectra in regional ocean models, Geophys. Res. Lett., 49, e2022GL099614, https://doi.org/10.1029/2022GL099614, 2022.

Thyng, K. M., Greene, C. A., Hetland, R. D., Zimmerle, H. M., and DiMarco, S. F.: True colors of oceanography: Guidelines for effective and accurate colormap selection, Oceanography, 29, 9–13, https://doi.org/10.5670/oceanog.2016.66, 2016.

Ubelmann, C., Carrere, L., Durand, C., Dibarboure, G., Faugère, Y., Ballarotta, M., Briol, F., and Lyard, F.: Simultaneous estimation of ocean mesoscale and coherent internal tide sea surface height signatures from the global altimetry record, Ocean Sci., 18, 469–481, https://doi.org/10.5194/os-18-469-2022, 2022.

van der Velden, E.: CMasher: Scientific colormaps for making accessible, informative and 'cmashing' plots, The Journal of Open Source Software, 5, 2004, https://doi.org/10.21105/joss.02004, 2020.

Vergara, O., Morrow, R., Pujol, M.-I., Dibarboure, G., and Ubelmann, C.: Global submesoscale diagnosis using alongtrack satellite altimetry, EGUsphere [preprint], https://doi.org/10.5194/egusphere-2022-1073, 2022.

Vic, C., Garabato, A. C. N., Green, J. M., Spingys, C., Forryan, A., Zhao, Z., and Sharples, J.: The lifecycle of semidiurnal internal tides over the northern Mid-Atlantic Ridge, J. Phys. Ocean., 48, 61–80, https://doi.org/10.1175/JPO-D-17-0121.1, 2018.

Vic, C., Naveira Garabato, A. C., Green, J. M., Waterhouse, A. F., Zhao, Z., Melet, A., de Lavergne, C., Buijsman, M. C., and Stephenson, G. R.: Deep-ocean mixing driven by small-scale internal tides, Nat. Commun., 10, 2099, https://doi.org/10.1038/s41467-019-10149-5, 2019.

Waterhouse, A. F., MacKinnon, J. A., Nash, J. D., Alford, M. H., Kunze, E., Simmons, H. L., Polzin, K. L., Laurent, L. C. S., Sun, O. M., Pinkel, R., Talley, L. D., Whalen, C. B., Huussen, T. N., Carter, G. S., Fer, I., Waterman, S., Naveira Garabato, A. C., Sanford, T. B., and Lee, C. M.: Global patterns of diapycnal mixing from measurements of the turbulent dissipation rate, J. Phys. Ocean., 44, 1854–1872, https://doi.org/10.1175/JPO-D-13-0104.1, 2014.

Wolanski, E. and Pickard, G.: Long-term observations of currents on the central Great Barrier Reef continental shelf, Coral Reefs, 4, 47–57, 1985.

Wyatt, A. S., Leichter, J. J., Toth, L. T., Miyajima, T., Aronson, R. B., and Nagata, T.: Heat accumulation on coral reefs mitigated by internal waves, Nat. Geosci., 13, 28–34, https://doi.org/10.1038/s41561-019-0486-4, 2020.

Wyatt, A. S., Leichter, J. J., Washburn, L., Kui, L., Edmunds, P. J., and Burgess, S. C.: Hidden heatwaves and severe coral bleaching linked to mesoscale eddies and thermocline dynamics, Nat. Commun., 14, 25, https://doi.org/10.1038/s41467-022-35550-5, 2023.

Zaron, E. D.: Baroclinic tidal sea level from exact-repeat mission altimetry, J. Phys. Ocean., 49, 193–210, https://doi.org/10.1175/JPO-D-18-0127.1, 2019.

Zaron, E. D. and Egbert, G. D.: Estimating open-ocean barotropic tidal dissipation: The Hawaiian Ridge, J. Phys. Ocean., 36, 1019–1035, https://doi.org/10.1175/JPO2878.1, 2006.

Zhao, Z., Alford, M. H., MacKinnon, J. A., and Pinkel, R.: Long-range propagation of the semidiurnal internal tide from the Hawaiian Ridge, J. Phys. Ocean., 40, 713–736, https://doi.org/10.1175/2009JPO4207.1, 2010.

Zhao, Z., Alford, M. H., Girton, J. B., Rainville, L., and Simmons, H. L.: Global observations of open-ocean mode-1 M 2 internal tides, J. Phys. Ocean., 46, 1657–1684, https://doi.org/10.1175/JPO-D-15-0105.1, 2016.

Zilberman, N., Becker, J., Merrifield, M., and Carter, G.: Model estimates of M2 internal tide generation over Mid-Atlantic Ridge topography, J. Phys. Ocean., 39, 2635–2651, https://doi.org/10.1175/2008JPO4136.1, 2009.

Zilberman, N., Merrifield, M., Carter, G., Luther, D., Levine, M., and Boyd, T. J.: Incoherent nature of M2 internal tides at the Hawaiian Ridge, J. Phys. Ocean., 41, 2021–2036, https://doi.org/10.1175/JPO-D-10-05009.1, 2011.

### III.1.3 Conclusion

This study gave a first comprehensive description of the coherent internal tide characteristics around New Caledonia based on high-resolution regional numerical modeling, specifically designed to quantify high-frequency motion in this area. We showed that New Caledonia is major major internal generation hot spot, comparable with other prominent generation sites in the Pacific Ocean such as Luzon Strait or the Hawaiian Ridge.

Internal tide generation is associated with the most prominent bathymetric structures, i.e. continental slopes, shelf breaks, small- and large-scale ridges, and seamounts, in predominantly shallow depths. The Grand Passage and Pines Ridge to the north and south of New Caledonia stand out as generation hot spots. Strongly dominated by the semidiurnal M2 internal tide, New Caledonia is predominantly governed by low-vertical mode dynamics. Internal tides feature a signature in SSH reaching locally amplitudes of more than 6 cm making New Caledonia an interesting study site for SWOT SSH observability as unbalanced wave motions may dominate SSH variance at wavelengths similar to those of balanced motions.

The conducted study should be understood as a general overview of internal-tide dynamics around New Caledonia and serves as a base for the following work in this thesis. One aspect that has been disregarded so far in the above study are temporal variations of the internal tides, also referred to as the incoherent internal tide. As reported in literature, the incoherent tide may represent an important fraction of the total tide signal depending on various factors such as a seasonally changing stratification or mesoscale eddy variability, and deserves full consideration.

The following section focuses on the investigation of tidal incoherence. Our goal is to determine the overall importance of the incoherent tide around New Caledonia and its contribution to the total tide signal. Further, we attempt to identify the potential mechanisms responsible for the loss of coherence. By doing so, we attempt to complement the results of the current section.

## III.2 Incoherent internal tides around New Caledonia: a numerical model approach (in preparation for submission)

### III.2.1 Introduction

The previous section provided a general overview of coherent internal tide characteristics, focusing on regional hot spots of internal tide generation, dissipation, tidal energy propagation, and the internal tide SSH signature. This marked an essential initial step. However, the investigation of tidal incoherence, which involves temporal variations of the internal tide or deviations from tidal coherence, remains to be investigated.

Existing literature highlights the significance of incoherent internal tides, which can often dominate the total tidal signal (see Sect. I.2.6). Various mechanisms contributing to tidal incoherence are documented. The relevance of studying tidal incoherence around New Caledonia stems from the coexistence of internal tide generation and tidal energy propagation with elevated mesoscale eddy variability - a potential source of arising incoherence due the refraction of tidal beams by mesoscale currents.

The upcoming section aims to complement the results on coherent internal-tide dynamics gained in Sect. III.1 by expanding the analysis to incoherent internal tides. In doing so, we will address the following question, as outlined in Sect. I.5:

**B Tidal incoherence and implications for sea surface height observability around New Caledonia**

**1)** What regions are expected to feature increased levels of tidal incoherence around New Caledonia and what is its fraction to the total tidal variance?

**2)** What are sources of tidal incoherence around New Caledonia both close to the generation site and toward the open ocean?

**3)** How does tidal incoherence manifest in SSH? How much does it contribute to SSH variance? What are potential implications for SSH observability of balanced motion?

As mentioned in Sect. III.1, a significant part of the following work was initially included in a paper preprint alongside the coherent tidal analysis. However, due to our and the editor's decision to separate the study of coherent and incoherent tides, the results presented in the upcoming section will now serve as a companion paper with Bendinger et al. (2023). Part of the results have been under review and are currently in preparation for resubmission.

**Publication**

**Bendinger, A.**, Cravatte, S., Gourdeau, L., Brodeau, L., Albert, A., Tchilibou, M., Lyard, F., Vic, C.: Regional modeling of internal-tide dynamics around New Caledonia - Part 2. Tidal incoherence and implications for sea surface height observability **(in preparation for submission in Ocean Science)**

### III.2.2 First evidence of incoherent internal tides

Tidal incoherence was inferred using two different methodologies, as described in Sect. II.2.4. The first methodology involved harmonic analysis applied to monthly data subsets of the full-model calendar year time series. This was followed by the barotropic-baroclinic vertical mode decomposition and the computation of the barotropic and baroclinic energy equations (see Sect. II.2.4.1). We refer to this methodology as the monthly harmonic analysis, which serves as a proxy for estimating tidal incoherence, allowing us to infer month-to-month variations. It's important to note that this approach provides insights into temporal variations specifically for the M2 barotropic and baroclinic energy equations, independent of other tidal constituents. The month-to-month variations in the M2 baroclinic energy flux, obtained through the monthly harmonic analysis, are exemplarily shown for two consecutive months (July and August 2014) in Fig. III.1a,e. Apparent variability is visible southwest of New Caledonia with distinct differences of the westward propagating tidal beam as well as finer-scale tidal signatures in the open ocean (far-field).

The second methodology is based on a bandpass-filtering technique applied to the full-model calendar year time series for selected variables, which have been corrected for the barotropic and baroclinic tides (as explained in Sect. II.2.4.2). The barotropic and baroclinic tides are determined through the harmonic analysis referenced to the full-model calendar time series (as detailed in Sect. II.2.1). We refer to this methodology

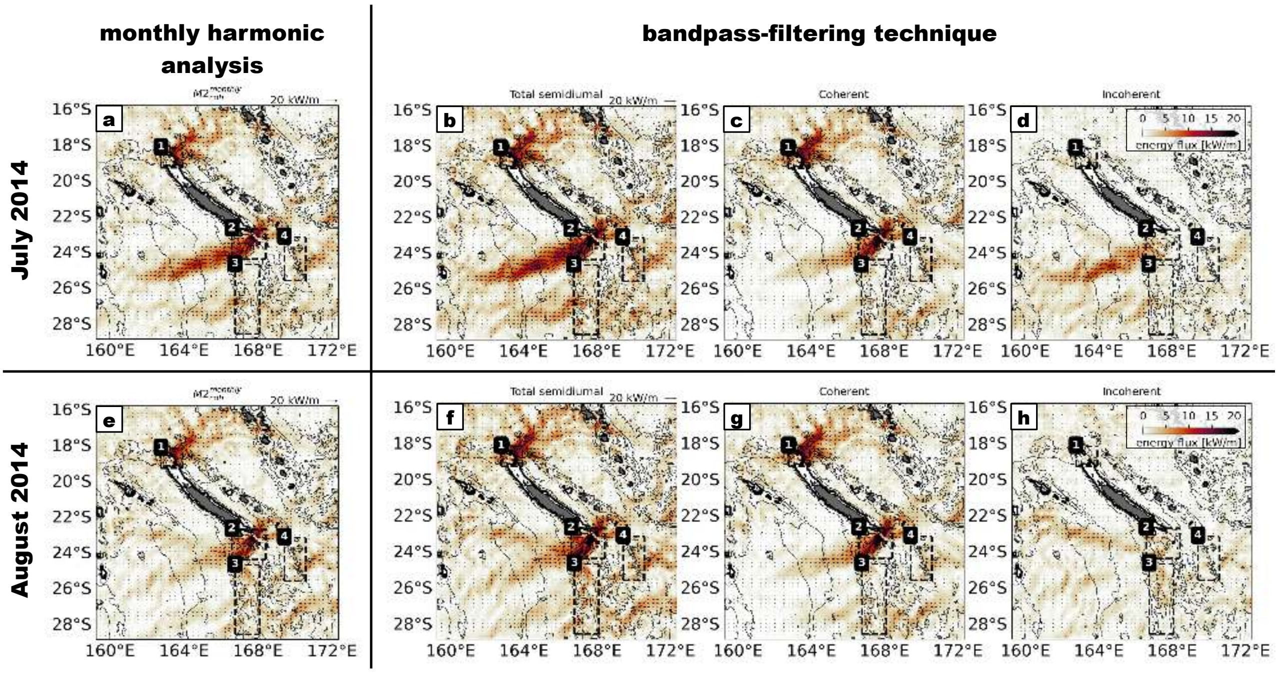

Figure III.1: **(left hand side)** M2 baroclinic energy flux for **(a)** July and **(e)** August 2014 as obtained from the monthly harmonic analysis referenced to the monthly data subsets of the full-model calendar year time series. **(right hand side)** Semidiurnal baroclinic energy flux decomposed into its total, coherent, and incoherent components as obtained from the bandpass-filtering technique, monthly averaged for **(b-d)** July and **(f-h)** August 2014. For a detailed explanation, please refer to corresponding section in the text. The thin black lines represent the 1000 m, 2000 m, and 3000 m depth contours. The thick black line is the 100 m depth contour representative for the New Caledonia lagoon. The numbered, black boxes represent the hot spots of internal tide generation as defined in Sect. III.1.2, i.e. 1: North, 2: South, 3: Norfolk Ridge, 4: Loyalty Ridge.

as the bandpass-filtering technique. It's important to note that the bandpass-filtering technique was applied specifically in the semidiurnal frequency band (M2, S2, N2) and was used solely for inferring the semidiurnal baroclinic energy flux, decomposed into its total, coherent, and incoherent components.

The total, coherent, and incoherent semidiurnal energy flux are presented as monthly averages for July and August 2014 in Fig. III.1b-d and Fig. III.1f-h, respectively. The M2 energy flux obtained from the monthly harmonic analysis closely resembles the spatial pattern of the total semidiurnal energy flux (compare Fig. III.1a,b for July 2014 and Fig. III.1e,f for August 2014). Month-to-month variations in the total semidiurnal energy flux must result from the incoherent internal tide since the monthly averages of the coherent semidiurnal signal are by definition constant (Fig. III.1b-d and Fig.III.1f-h). For the semidiurnal frequency band, the coherent internal tide is only subject to spring-neap tide variability which, however, cancels out in the monthly averages. From this, we can conclude that the month-to-month variations inferred from the monthly harmonic analysis in Fig. III.1a,e should be associated with the incoherent tide. Two key conclusions can be drawn from this analysis. First, it underscores that data sets spanning just one month or even multiple months are insufficient for extracting a robust signal that accurately represents the coherent tide. Second, the variations observed on a month-to-month scale are indicative of the time scales of mesoscale variability.

In the following, we will identify more quantitatively regions of increased tidal incoherence around New Caledonia making use of the bandpass-filtering technique.

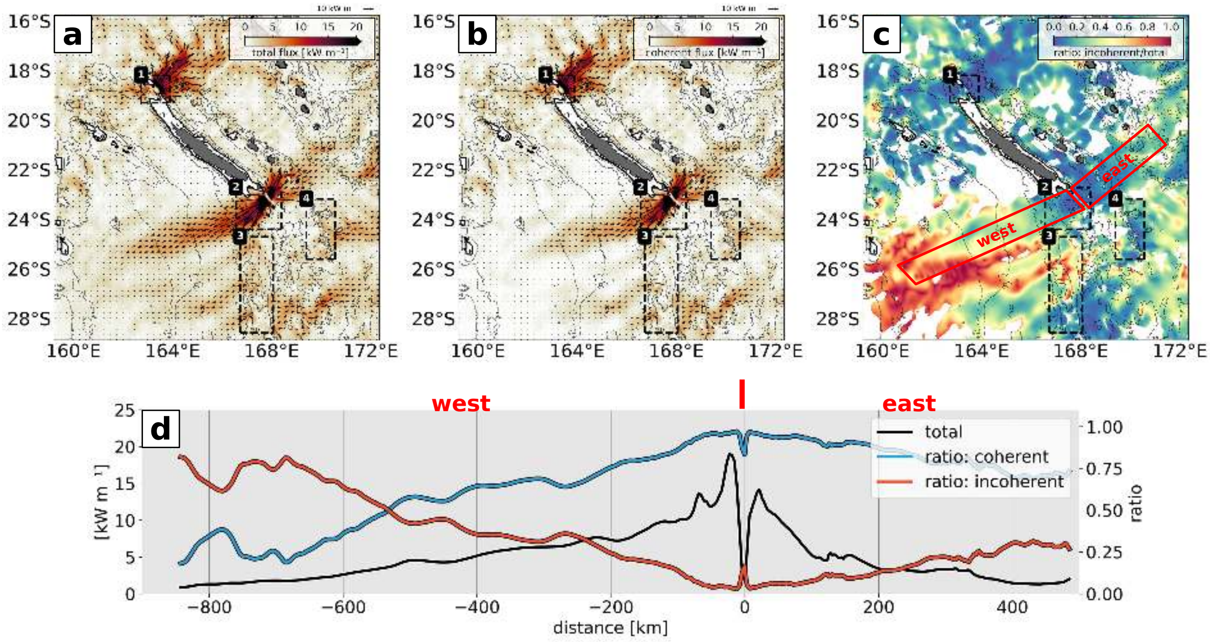

**Figure III.2:** Annual mean of the **(a)** total and **(b)** coherent semidiurnal baroclinic energy flux including flux vectors. **(c)** The incoherent semidiurnal baroclinic energy flux is expressed by the ration to the total semidiurnal internal tide. Regions with a total semidiurnal energy flux of <1 kW $m^{-1}$ are masked. Bathymetry contours and the black boxes are given as in Fig.III.1. **(d)** Total semidiurnal energy flux and the ratio of the coherent/incoherent tide to the total tide as a function of distance to the generation site (0 km, Pines Ridge), and averaged for the red boxes as indicated in **(c)**.

The annually averaged (model year 2014) total semidiurnal energy flux decomposed into the coherent and incoherent components is shown in Fig. III.2. The incoherent semidiurnal tide is presented as the ratio to the total semidiurnal energy flux (Fig. III.2c). Note that we masked regions, where the total semidiurnal energy flux does not exceed 1 kW $m^{-1}$. As shown in Bendinger et al. (2023), the propagation of semidiurnal baroclinic tidal energy is expressed mainly by two predominant tidal beams that emerge from the internal tide generation hot spots north and south of New Caledonia (Fig. III.2b). The northern tidal beam is predominantly coherent. Tidal incoherence is enhanced in the southern half of the regional domain, within the largest beam propagating westward (Fig. III.2c). Plotted as a function of distance to the generation site at Pines Ridge (0 km) in the South (2) domain, tidal incoherence gradually increases in importance with increasing distance. In southwestward propagation direction, the incoherent tide accounts for about 25 % of the total semidiurnal signal beyond 200 km distance, before being dominant at 500 km distance (Fig. III.2d). In the following, we will explore possible mechanisms of tidal incoherence which will help understand the discrepancies seen in the levels of tidal incoherence north and south of New Caledonia and the gradually increasing tidal incoherence with increasing distance to the internal tide generation sites.

### III.2.3 Arising tidal incoherence through mesoscale eddy variability

In this section, we will demonstrate that tidal incoherence around New Caledonia is strongly linked with mesoscale eddy variability in both the far-field and near-field. This hypothesis is strongly supported by elevated eddy kinetic energy levels in regions where we expect tidal incoherence to dominate, i.e. south of New Caledonia, as shown by Bendinger et al. (2023) (see their Fig. 3) and Keppler et al. (2018). To the north of New Caledonia, eddy kinetic energy levels are generally reduced, which makes this regions less favorable for a loss of coherence. We will first give a broad overview of how mesoscale eddy variability may play role in arising incoherence in the far-field and near-field before turning to a more in-depth analysis of the exact underlying mechanism.

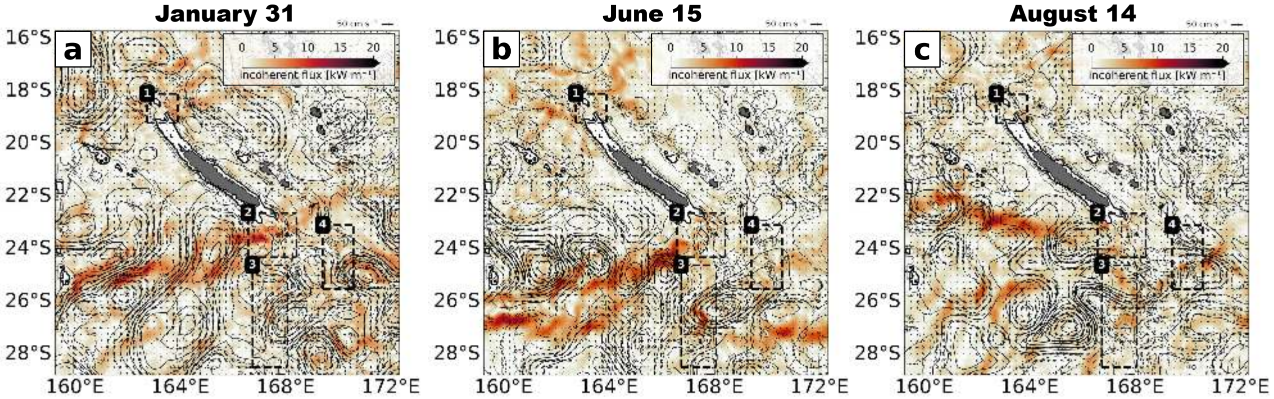

**Figure III.3:** Snapshots of the 5-day mean depth-integrated semidiurnal incoherent energy flux (shading) overlaid by the associated snapshot of the mesoscale eddy field, i.e. surface geostrophic velocity and sea level anomaly (SLA) contours (solid: SLA $> 0$, dashed: SLA $< 0$) for **(a)** January 31, **(b)** June 15, and **(c)** August 14, 2014. Bathymetry contours and the black boxes are given as in Fig.III.1.

In the far-field, the relationship of increasing tidal incoherence and high mesoscale eddy activity is specifically shown by 5-day mean snapshots of the incoherent semidiurnal energy flux overlaid by 5-day mean snapshot of the surface geostrophic velocity field in Fig. III.3. In the influence area of the tidal beams, elevated incoherent energy levels $>10$ kW m$^{-1}$ are clearly linked with intensified mesoscale currents associated with high gradients in sea level anomaly. This suggests that the tidal energy flux becomes incoherent as it propagates through the eddy field. Reduced levels of incoherent energy fluxes north of New Caledonia correspond with weak mesoscale surface currents.

In the near-field, i.e. near the internal tide generation sites, mesoscale eddy variability may affect the internal tide generation itself. A representative illustration is given by the barotropic-to-baroclinic M2 conversion anomaly for April 2014 as obtained from the monthly harmonic analysis (see Sect. II.2.4.1) in Fig. III.4. The internal tide generation hot spot around Pines Ridge is characterized by a strong conversion anomaly. Similarly to Fig. III.3, a 5-day mean snapshot of the mesoscale eddy field is shown. The negative conversion anomaly clearly coincides with the passage of a mesoscale eddy which remains in the region for almost the entirety of the month.

The underlying mechanisms linked to mesoscale eddy variability for arising tidal incoherence are presented in the following, divided into the far-field and near-field.

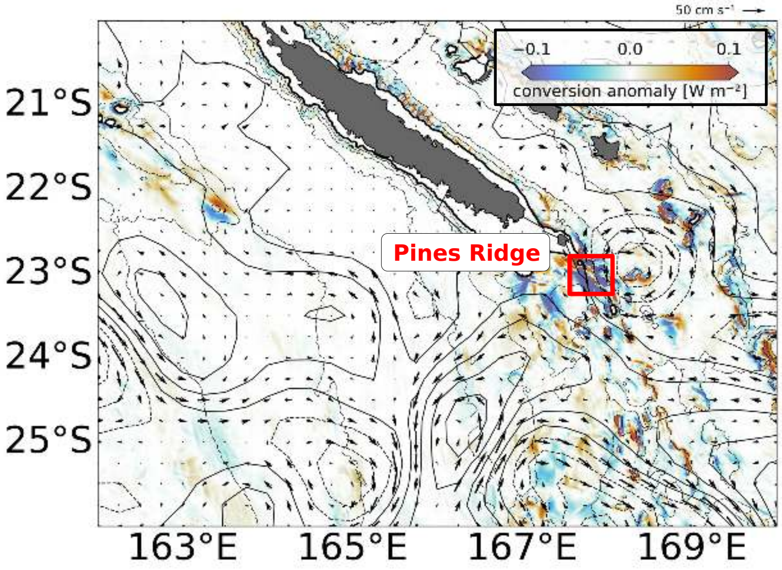

**Figure III.4:** M2 barotropic-to-baroclinic conversion anomaly for April 2014 as obtained from the monthly harmonic analysis (see Sect. II.2.4.1). The red square indicates the internal tide generation hot spot around Pines Ridge. Overlaid is the geostrophic surface eddy field as in Fig. III.3, but for a 5-day mean snapshot on April 26, 2014. Bathymetry contours are given as in Fig.III.1.

### III.2.3.1 Refraction of tidal beam energy propagation

To study the effect of mesoscale eddy variability in the far-field, we applied a simplistic ray tracing method following Rainville and Pinkel (2006), as introduced in Sect. II.3.1. Briefly, the ray tracing models the ray's horizontal propagation for a set of vertical modes, a given initialization region, and a propagation angle while considering spatially varying topography, climatological stratification, planetary vorticity, and depth-independent currents. We initiated a semidiurnal ray for two initialization regions in the internal tide generation hot spots north (163.75° E, 18.4° S) and south (167.65° E, 23.35° S) of New Caledonia (Fig. III.5).

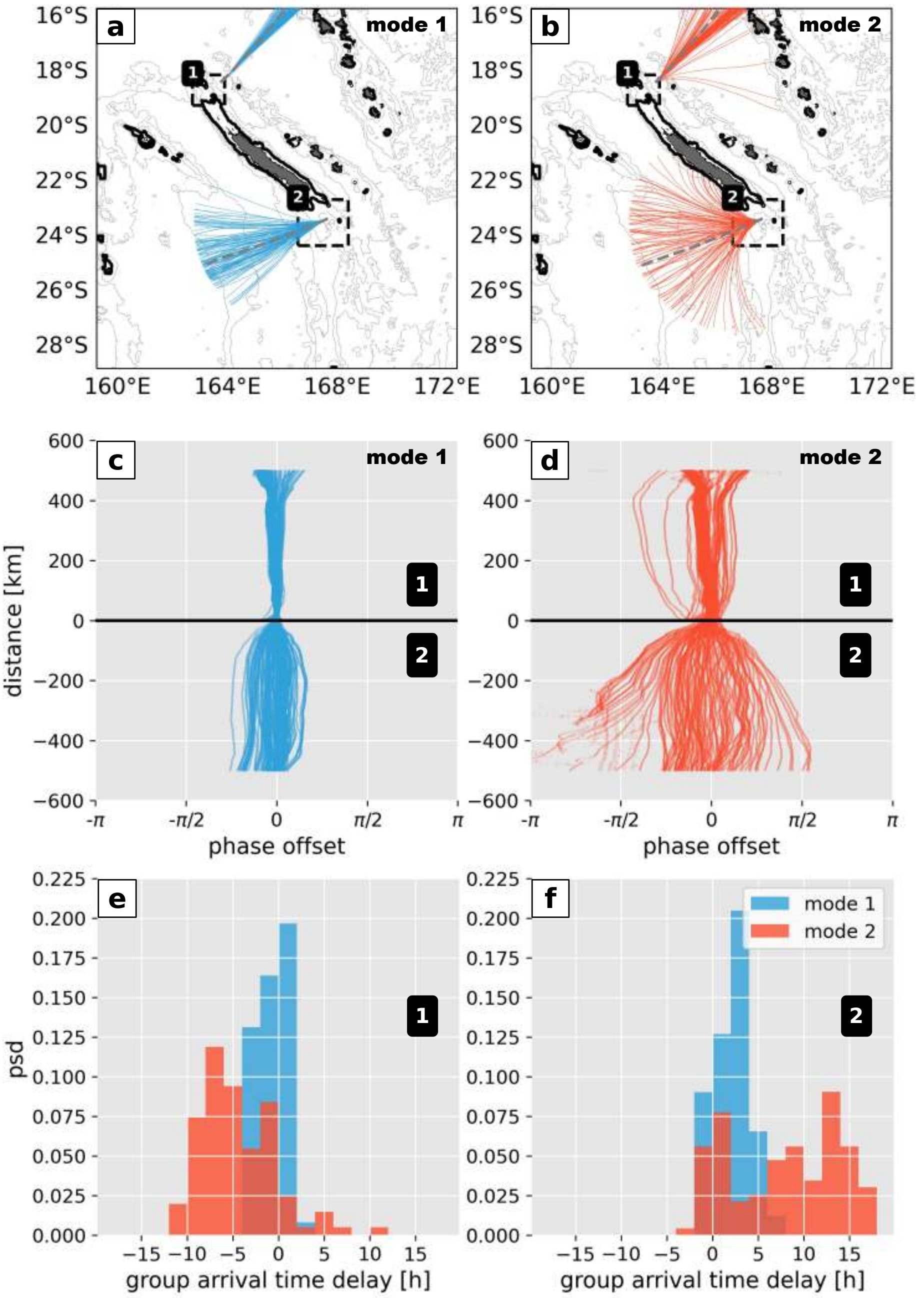

**Figure III.5:** Modeled semidiurnal ray paths for **(a)** mode 1 and **(b)** mode 2 propagating through the mesoscale eddy field, from their initialization north (163.75° E, 18.4° S) and south (167.65° E, 23.35° S) of New Caledonia. The no-currents scenario is also given (dashed gray). Bathymetry contours and the black boxes are given as in Fig.III.1. The phase offset in propagation direction relative to the no-currents scenario as a function of distance is shown for **(c)** mode 1 and **(d)** mode 2. Histograms of group arrival time delay (relative to the no-currents scenario) for the **(e)** northern and **(f)** southern tidal beam.

**Table III.1:** Semidiurnal ray's mean group arrival time for vertical modes 1-2 with (w/) and without (wo/) currents. The average group arrival time delay relative to the no-currents scenario is also given.

| **North (1)** | mode 1 | mode 2 |
|---|---|---|
| wo/currents [days] | 2.29 | 4.38 |
| w/currents [days] | 2.38±0.08 | 4.71±0.26 |
| delay [hours] | 2.19±1.82 | 8.08±6.19 |
| **South (2)** | mode 1 | mode 2 |
| wo/currents [days] | 2.68 | 5.4 |
| w/currents [days] | 2.65±0.06 | 5.23±0.2 |
| delay | -0.71±1.39 | -4.25±4.85 |

The primary objective is to study the refraction of tidal beam energy propagation, by considering only effects of depth-independent currents. Here, the ray tracing is applied on the depth-averaged, 1-day mean currents over the course of a full-model calendar year. Note that the background currents are frozen throughout the rays' propagation. A no-currents scenario is also given (dashed gray line in Fig. III.5a-b) for which the tidal ray's propagation only depends on bathymetry, climatological stratification, and planetary vorticity.

The ray tracing yields profoundly different results for the propagation of tidal beam energy north and south of New Caledonia (Fig. III.5a-b). North of New Caledonia, tidal energy propagation in northeastward direction is confined to a well-defined and narrow tidal beam, which closely aligns with the theoretical propagation direction for a semidiurnal ray in the absence of background currents. In contrast, south of New Caledonia, the semidiurnal rays experience significant refraction in propagation direction. For both regions, mode 2 is more affected by the background currents, leading to increased dispersion (Fig. III.5b).

The phase offset in propagation direction relative to the no-currents scenario underlines increasing incoherence with increasing distance to the generation site. It expresses by an increase of phase variability that becomes more random in the far-field, particularly south of New Caledonia (Fig. III.5c-d) representing the stochastic nature of the mesoscale eddy field.

For a given propagation distance (500 km), the internal wave group arrival time delay (relative to the no-currents scenario) is illustrated for modes 1-2 for all rays in the histogram in Fig. III.5e-f and listed in Table III.1. In the northern (southern) domain, the mean group arrival time for mode 1 is 2.38±0.08 d (2.65±0.06 d), corresponding with a delay of 2.19±1.89 h (-0.71±1.39 h) relative to the arrival time in the absence of background currents. Mode 2 is significantly more delayed than mode 1, roughly a factor of 4 larger. Here, we only considered a maximum of two modes since mode 1 is largely dominant around New Caledonia (Bendinger et al., 2023).

Following Rainville and Pinkel (2006), the ray tracing applied in this study is a simplistic approach to study internal tide propagation through a background velocity field. First, the background velocity is held constant during each ray's propagation. This is a weak approximation since low vertical modes considered here propagate faster and over distances larger than mesoscale eddies do. In our analysis, the semidiurnal rays travel a maximum distance of 500 km, which they reach within 2.5 days for mode 1 and within 5 days for mode 2.

Second, the ray tracing is applied on depth-independent currents. It was recently stated that the rays' horizontal propagation differs significantly from those in baroclinic currents (Duda et al., 2018). Even though we used depth-independent currents, we do not expect the conclusions drawn from our analysis to change. However, the analysis could be extended by analysing the ray propagation through baroclinic currents.

Third, internal tide propagation can be affected by both background currents and stratification. In this study, we used climatological stratification. Spatial variations of climatological stratification have only little impact on tidal beam refraction around New Caledonia. It is only of importance when considering the ray propagation over basin scales as shown by Rainville and Pinkel (2006).

The above analysis suggests that phase variations along the ray's path accompanied by changes in phase/group speed induced by background currents cause a refraction of the tidal beam while altering its propagation direction. To understand why tidal beam refraction is enhanced south of New Caledonia, we further quantify the difference in mesoscale eddies encountered by the internal tides during their propagation. It has already been shown that eddies are more energetic south of New Caledonia in Keppler et al. (2018). Based on an eddy tracking of geostrophic surface currents from AVISO/CMEMS, eddies south of New Caledonia feature slightly higher swirl

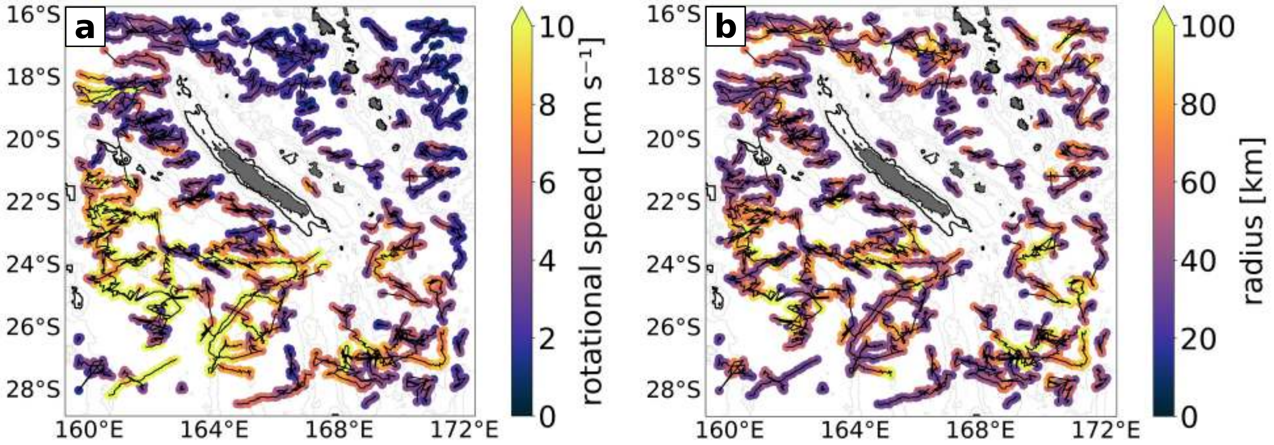

**Figure III.6:** (a) Rotational speed and (b) radius along eddy tracks as tracked by the eddy tracking algorithm AMEDA, applied on 1-day mean depth-averaged/integrated velocities on a full-calendar model year (2014). Here, only eddies with life times >1 week are considered. The theoretical semidiurnal ray paths for mode 1 (black) and the no-currents scenario (white) from Fig. III.5a are also shown.

velocities than eddies north of New Caledonia. We applied an eddy tracking (see Sect. II.3.2) on the same background currents than those on which the ray tracing was applied, i.e. depth-averaged 1-day mean currents for the full-model calendar year.

Assuming a minimum radius of 15 km, we tracked the swirl velocities and radii of eddies as they propagated mainly westward within the regional model domain, as shown in Figure III.6. In total, we detected 573 eddies, of which 176 had a life time exceeding one week. Note that eddies with a life time $<$1 week are not considered in the subsequent analysis. The key finding of this analysis is that the area southwest of New Caledonia is characterized by long-lived eddies with enhanced rotational speeds exceeding 10 cm $s^{-1}$ (Fig. III.6a) and radii ranging from 60 to 100 km (Fig. III.6b). While eddy radii in the northern region are of a similar order of magnitude, rotational speeds are notably reduced.

When averaging for latitudinal bands, those in the southern domain exhibit a mean radius of 65km and a mean swirl velocity of 8 cm $s^{-1}$. On the other hand, eddies in the northern domain have a mean radius of 50km and a mean swirl velocity of 4 cm $s^{-1}$. These values differ from those reported by Keppler et al. (2018), who found a mean radius of 95 km (110 km) and a mean swirl velocity of 25 cm $s^{-1}$ (19 cm $s^{-1}$) for eddies south (north) of New Caledonia. Our eddy tracking results are not necessarily comparable with those from Keppler et al. (2018). First, we expect our model to resolve smaller scales compared to AVISO/CMEMS. Second, the data sets on which the eddy tracking is applied represent different dynamics and flow characteristics. While we use depth-averaged currents representative for the barotropic vertical mode, in Keppler et al. (2018) the AVISO/CMEMS geostrophic surface velocities are more likely to express in baroclinic mode-1. In our model, the decrease in swirl velocities as ones moves northward (by 50 %) is more pronounced than reported in Keppler et al. (2018). This is possibly linked to the the fact that eddies in the northern domain are highly surface-intensified (trapped to the upper 200 m) and thus have a weaker signature in the depth-averaged currents. Contrarily, the signature of eddies in the southern domain extends to greater depth (trapped to the upper 800 m) and, thus, feature a stronger signal in the depth-average.

It is important to note that the eddy tracking applied in this section is not dedicated to the study of actual eddy properties and its comparison to other data products such as Keppler et al. (2018). Rather, we used the eddy tracking as a quantitative tool to allocate enhanced tidal beam refraction to more energetic currents in the southern domain. In this context, the ray tracing and eddy tracking demonstrated a posteriori why tidal incoherence induced by mesoscale eddy variability in the far-field is favored south of New Caledonia.

#### III.2.3.2 Local stratification changes

As demonstrated, tidal energy flux can become incoherent as it propagates through an eddy field with intensified mesoscale currents. Mesoscale eddy variability can also affect the barotropic-to-baroclinic conversion term at the internal tide generation site. This conversion is governed by barotropic tidal currents and baroclinic pressure perturbations at the ocean bottom ($p_{bc}(-H)$), as described in Equation II.6 in Sect. II.2.3. This equation is represented as:

$$\langle \boldsymbol{u}_{bt}\, p_{bc}(-H)\rangle = \frac{1}{2}\, A_{p_{bc}(-H)}\, A_{\boldsymbol{u}_{bt}}\, \cos(\varphi_{p_{bc}(-H)} - \varphi_{\boldsymbol{u}_{bt}}),$$

This relationship has been previously discussed in Zilberman et al. (2011) and Kerry et al. (2014, 2016). Variations in the conversion term are associated with local changes in stratification, represented by pressure amplitude variations $A_{p_{bc}(-H)}$, and the influence of remotely generated internal tides, represented by pressure phase variations $\varphi_{p_{bc}(-H)}$. In the following, we give insight into temporal variations of the M2 conversion term making use of the monthly harmonic analysis as described in Sect. II.2.4.1.

We focus on the four generation zones and consider only locations with a conversion rate $>0.1$ W m$^{-2}$ associated with the internal tide generation hot spots. The corresponding monthly normalized standard deviation of the area-integrated conversion (not shown) is globally rather low ranging from 5-8 % within the North (1) and South (2) domains to 9-14 % within the Norfolk Ridge (3) and Loyalty Ridge (4) domains. However, it can be much higher locally, potentially reaching 100 %. This is evident from the spatial maps of conversion variability that are shown for each subregion in Fig. III.7. They reveal locations of high variability, particularly near small-scale bathymetric structures. Here, the month-to-month variability of the local conversion term appears to be largely governed by pressure amplitude variations, especially in

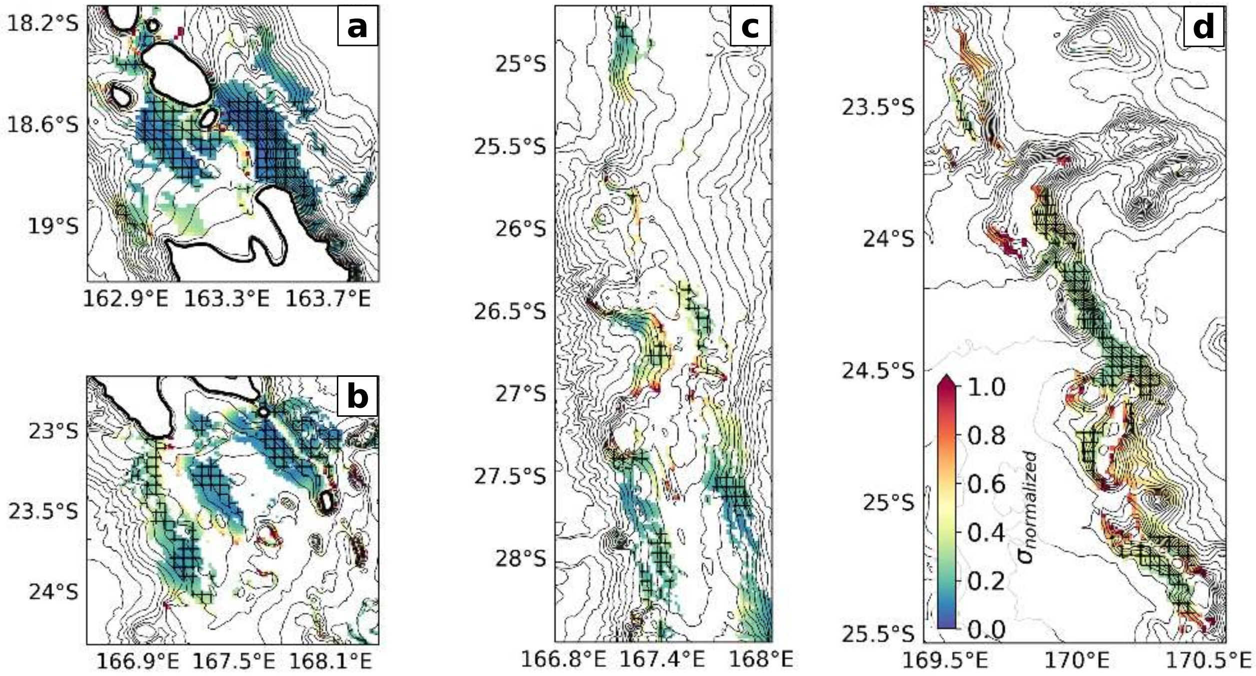

**Figure III.7:** Standard deviation of the M2 barotropic-to-baroclinic conversion term normalized by the annual mean conversion for **(a)** North (1), **(b)** South **(2)**, **(c)** Norfolk Ridge (3), and **(d)** Loyalty Ridge (4). Grid points with conversion rates $<0.1$ W m$^{-2}$ are neglected from the analysis to account only for conversion that is associated with the generation hot spots. The hatched contours represent the regions where conversion variability is dominated by pressure amplitude variations. The depth contour interval is 200 m, where the thick black line is the 100 m depth contour representative for the New Caledonia lagoon.

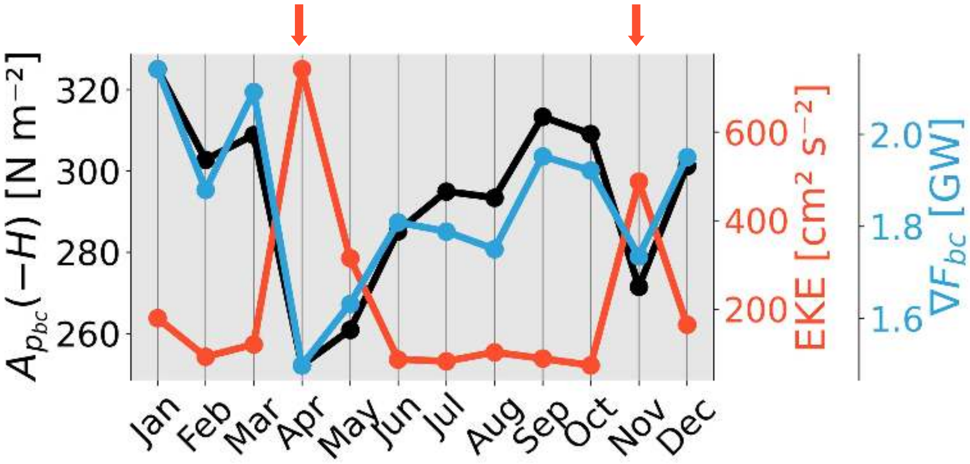

**Figure III.8:** Month-to-month M2 baroclinic pressure amplitude $p_{bc}(-H)$ as obtained from the monthly harmonic analysis (see Sect. II.2.4.1) and the mesoscale eddy kinetic energy averaged for the Pines Ridge region (red box in Fig. III.4. Also shown is the month-to-month M2 depth-integrated baroclinic flux divergence $\nabla_h \boldsymbol{F}_{bc}$ integrated over the Pines Ridge. The red arrows mark the time periods when a mesoscale eddy is located over Pines Ridge.

the North (1) and South (2) domains (illustrated by the hatched contours in Fig. III.7), suggesting that local stratification effects dominate. Variations of the phase differences tend to be enhanced in the Norfolk Ridge (3) suggesting that remotely generated incoherent tides effects dominate.

We could not associate variations of pressure amplitude and phase to a seasonal cycle. Rather, as for the energy flux in the far-field, we suggest that stratification changes and associated pressure amplitude variations are linked with mesoscale eddy variability as highlighted in Fig. III.4. The negative conversion anomaly observed in April 2014 in Fig. III.4 corresponds with a decrease of $p_{bc}(-H)$ in Fig. III.8. Moreover, it coincides with elevated levels of eddy kinetic energy. This leads to a temporal decrease of tidal energy conversion and consequently a decline in baroclinic energy flux divergence. Another event of reduced tidal energy conversion along with increased eddy kinetic energy levels is evident in November (Fig. III.8). These results should be considered as preliminary, but they indicate that the barotropic-to-baroclinic conversion term is relatively constant over time. Though, some sporadic events like mesoscale eddies close to the internal tide generation sites may temporally influence the internal tide generation.

### III.2.4 Incoherent SSH signature

The coherent tide SSH signature and implications for SWOT observability of mesoscale and submesoscale motions were investigated in Bendinger et al. (2023). The main findings include the dominance of internal-tide dynamics in the mesoscale band at spectral wavelengths below 200 km. Correcting the model SSH for the coherent internal tide proved to be partially effective to improve observability down to wavelengths around 100 km. The limited observability below 100 km, even after the correction of the coherent internal tide, was linked to the temporally varying tide. Here, we extend the analysis to quantify the SSH signature of the incoherent internal tide. Equiva-

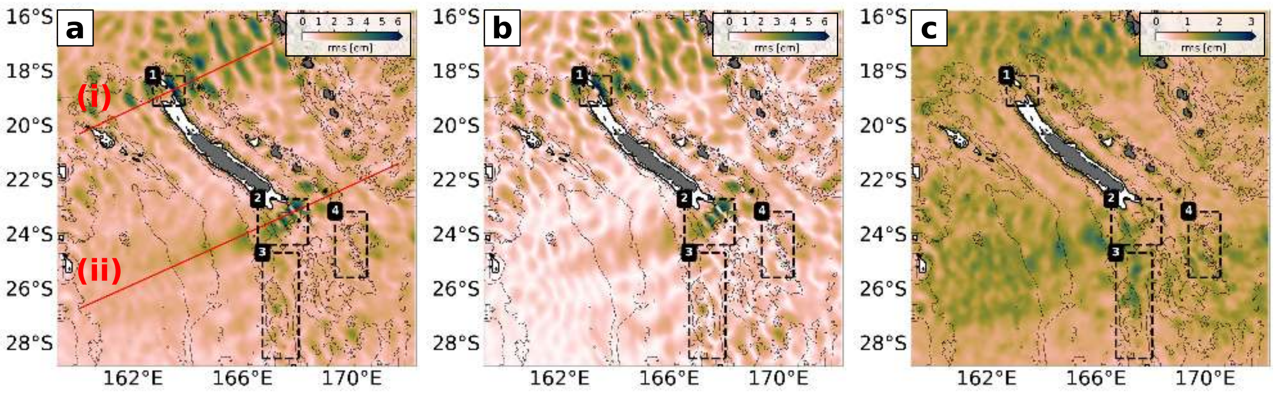

**Figure III.9:** Annual root-mean square (rms) of the **(a)** total, **(b)** coherent, and **(c)** incoherent semidiurnal SSH. Note the different colorbar scales. The red line indicates the transect in along-beam direction for which the SSH spectra are computed. Bathymetry contours and the black boxes are given as in Fig. III.1.

lently to Bendinger et al. (2023), we first investigate the spatial distribution around New Caledonia before addressing the incoherent tide signature in spectral space.

Spatial maps of the SSH root-mean-square of the total, coherent, and incoherent semidiurnal internal tide (relative to the full-model calendar year) are presented in Fig. III.9. The overall signature resembles the semidiurnal energy flux in Fig. III.2 with the predominant tidal beams to the north and south of New Caledonia clearly visible in SSH with a root-mean-square of >6 cm. The incoherent semidiurnal internal tide SSH manifestation is characterized by an overall smaller root-mean-square with a maximum of locally 2 cm (Fig. III.9c). The incoherent SSH is less confined to the tidal beams and it seems overall more widespread both north and south of New Caledonia. This tidal signature outside the energy flux tidal beams has a rather low root-mean-square of 0.5-1 cm, and expresses the dispersion of internal waves propagating through the domain. This implies that the internal tide SSH signature is not purely confined in energetic tidal beams.

Wavenumber spectra in along-beam direction are revisited in the following. In Sect. III.1.2, the annual mean SSH signature was described with regard to different dynamics that are separated in terms of frequency bands: subinertial frequencies ($\omega < f$, $\mathrm{SSH}_{\mathrm{subinertial}}$) for mesoscale and submesoscale dynamics, as well as superinertial frequencies ($\omega > f$, $\mathrm{SSH}_{\mathrm{superinertial}}$) for internal gravity waves while distinguishing between the coherent internal-tide ($\mathrm{SSH}_{\mathrm{coh}}$), and supertidal frequencies ($\omega >$1/10 h, $\mathrm{SSH}_{\mathrm{supertidal}}$). SWOT SSH observability of mesoscale and submesoscale dynamics in a region of strong internal tides was addressed by identifying the transition scale $L_{\mathrm{t}}$. The transition scale is a quantitative measure that separates balanced from unbalanced motions which specifies the length scale at which unbalanced motion become dominant over balanced motions. Here, it is defined as the intersection of subinertial and superinertial spectra. The main findings are briefly summarized and revisited in Fig. III.10 for the northern (Fig. III.10a) and southern transect (Fig. III.10d):

- Subinertial processes explains almost all of the SSH variance for scales larger than 200 km.

- For scales smaller than 200 km, SSH variance is governed by superinertial processes, dominated by the coherent internal tide in the mesoscale band (70-250 km) and clearly expressed in spectral space with mode 1 and mode 2 around 160 and 80 km wavelength.
- The correction for the coherent internal tide lowered the transition scale (seen in Fig. III.10 by the intersection of the white and dashed red curves), from $L_{\mathrm{t}}$ =204 km to $L_{\mathrm{t}}^{\mathrm{corr}}$ =92 km for the northern transect and from $L_{\mathrm{t}}$ =163 km to $L_{\mathrm{t}}^{\mathrm{corr}}$ =83 km for the southern transect.
- The limited observability was attributed to the remaining signal of motions at superinertial frequencies $\mathrm{SSH}_{\mathrm{superinertial}}^{\mathrm{corr}}$, specifically the temporally varying internal tide as well as non-tidal superinertial internal gravity waves.

Next, we explicitly show the contribution of the incoherent internal tide ($\mathrm{SSH}_{\mathrm{inc}}$) in spectral space in the superinertial frequency band for northern (Fig. III.10a) and southern transect (Fig. III.10b). It's important to note that the remaining signal after correcting for the coherent internal tide comprises contributions from the incoherent internal tide, near-inertial internal gravity waves, and motions at supertidal frequencies.

Specifically, for the northern transect, within the mesoscale band of 70-250 km, the incoherent internal tide (shown by the the yellow curve in Fig. III.10a) predominantly governs motions at superinertial frequencies (when corrected for the coherent internal tide) down to wavelengths of 100 km. Below 100 km, the incoherent tide shares equal importance with motions at supertidal frequencies (represented by the gray curve in

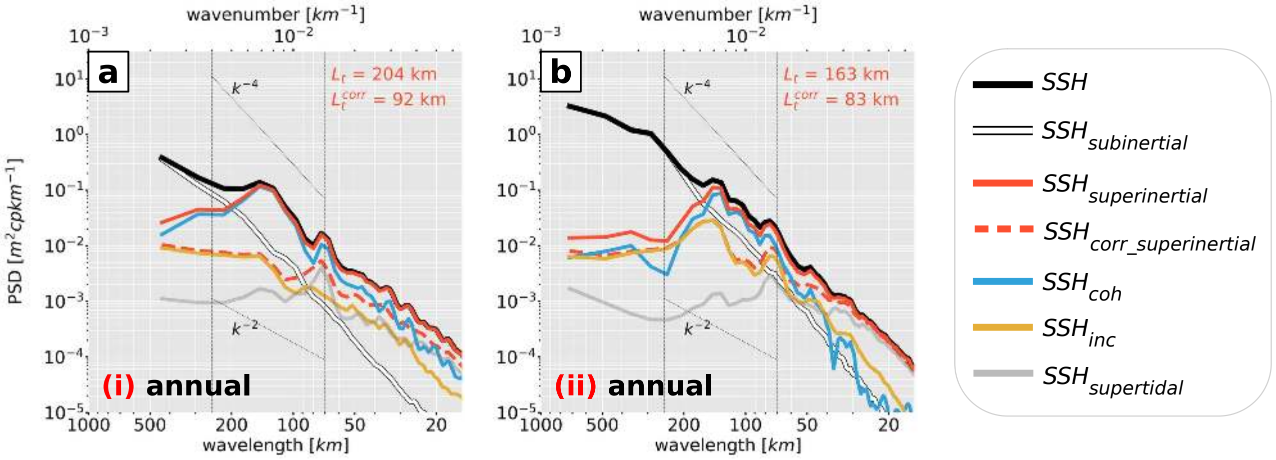

**Figure III.10:** Annually averaged SSH wavenumber spectra for transects **(a)** north and **(b)** south of New Caledonia, denoted (i) and (ii), respectively, in Fig. III.9a. SSH spectra are presented for the altimetry-like SSH (corrected for the barotropic tide, SSH, black) with regard to the different dynamics that are separated in terms of frequency bands: subinertial ($\omega < f$, $\mathrm{SSH}_{\mathrm{subinertial}}$, white) for meso- and submesoscale dynamics, superinertial frequencies ($\omega > f$, $\mathrm{SSH}_{\mathrm{superinertial}}$, solid red) for internal gravity waves decomposed into the coherent ($\mathrm{SSH}_{\mathrm{coh}}$, blue), incoherent ($\mathrm{SSH}_{\mathrm{inc}}$, yellow) internal tide, and supertidal frequencies ($\omega$ > 1/10 h, $\mathrm{SSH}_{\mathrm{supertidal}}$, gray). The altimetry-like SSH corrected for both the barotropic and baroclinic tide and filtered for motions at superinertial frequencies ($\mathrm{SSH}_{\mathrm{corr\_superinertial}}$, dashed red) is also given. The characteristic wavenumber slopes $\mathrm{k}^{-2}$ and $\mathrm{k}^{-4}$ are represented by the dotted black lines encompassing the mesoscale band (70-250 km, vertical dotted black lines). The transition scale $L_{\mathrm{t}}$ (i.e. where $\mathrm{SSH}_{\mathrm{superinertial}} > \mathrm{SSH}_{\mathrm{subinertial}}$) and the transition scale corrected for $\mathrm{SSH}_{\mathrm{coh}}$ ($L_{\mathrm{t}}^{\mathrm{corr}}$, i.e. where $\mathrm{SSH}_{\mathrm{corr\_superinertial}} > \mathrm{SSH}_{\mathrm{subinertial}}$) for the annually averaged SSH spectra are specified by the red colored numbers.

Fig. III.10a). In contrast, for the southern transect, the incoherent internal tide (shown by the the yellow curve in Fig. III.10b) is of greater importance, dominating motions at superinertial frequencies down to 60 km wavelength. Though, motions at supertidal frequencies dominate at wavelenghts below 60 km wavelength (as indicated by the gray curve in Fig. III.10b).

We conclude for both regions that the corrected transition scale ($L_{\mathrm{t}}^{\mathrm{corr}}$) at wavelengths just below 100 km is predominantly governed by the incoherent internal tide, which limits in the annual mean the observability of balanced motions in the mesoscale band (70-250 km). At smaller scales, motions at supertidal frequencies gradually increase in importance. In the following section, we will show that seasonal variations of motions at subinertial and superinertial frequencies have further implications for the transition scale and, hence, for the observability of balanced motions.

#### III.2.4.1 Seasonal dependence

We computed seasonal SSH wavenumber spectra distinguishing between southern hemisphere summer (January-March, JFM) and winter (July-September, JAS) to investigate how the transition scale is affected by seasonal variations of subinertial and superinertial motions north and south of New Caledonia (Fig. III.11).
By definition, the coherent internal-tide signal referenced to the full-model calendar year is the same in both seasons. The seasonality of the transition scale $L_{\mathrm{t}}^{\mathrm{corr}}$ is thus attributed to seasonal variations of subinertial motions, i.e. mesoscale/submesoscale motions, and unbalanced wave motions. Seasonal variations of the mesoscale and submesoscale flow including their underlying mechanism are discussed in detail in Sect. III.4. Here, we just refer to Fig. II.2 which illustrates dominant mesoscale motion during summer months and a highly turbulent flow regional due to arising submesoscale motions in the winter months (see Sect. II.1.1). Further, the seasonality in submesoscale turbulence is more pronounced south of New Caledonia. The pronounced seasonality of subinertial motions south of the New Caledonia has important implications for the transition scale as explained in the following.

Seasonal modulations of the SSH spectra become evident for all scales $<$300 km wavelength (thick black line in Fig. III.11c-d). In summer, it features a more flattened wavenumber slope in the mesoscale to submesoscale range with a characteristic wave slope of $k^{-2}$ (Fig. III.11c) corresponding with superinertial motions (internal wave continuum). In winter, it becomes more continuous being characterized by a wave slope of $k^{-4}$ (Fig. III.11d). This can be attributed to subinertial motions such as mesoscale and submesoscale processes that undergo seasonal variability (shown by the white curves in Fig. III.11c-d). Particularly, submesoscale motions are strongly energized in the winter months (e.g. Callies et al., 2015; Rocha et al., 2016b). This was explicitly shown for New Caledonia in Sérazin et al. (2020), where the authors attributed the increasing importance of mixed layer instabilities and frontogenesis to more available potential energy in the southern hemisphere winter months. Seasonal modulations of SSH spectra can also be linked to unbalanced wave motions which are amplified in summer months, particularly for higher-vertical modes due to increasing stratification (Lahaye et al., 2020).

Superinertial processes dominate subinertial motions in both seasons at scales below 180 km. However, the relative importance of superinertial over subinertial motions is more pronounced in summer months. This can be explained by the seasonality of superinertial and subinertial motions being out of phase, i.e. superinertial motions are enhanced in summer while subinertial motions are suppressed and vice versa in winter. The transition scale ($L_\mathrm{t}$) does not feature strong seasonality between summer and winter (represented by the intersection of the white and solid red curves in Fig. III.11c-d). Though, the transition scale is not well defined in winter, where both subinertial and superinertial signals have similar variance at wavelengths 90-180 km (Fig. III.11d).

Important conclusions are made when correcting for the coherent internal tide. In summer, the transition scale ($L_\mathrm{t}^\mathrm{corr}$) is only slightly reduced from 175 km to 156 km (Fig. III.11c). This is linked to the seasonally enhanced incoherent internal tide which is still contained in the signal featuring equal SSH variance with subinertial signals at wavelengths 90-180 km (shown by the yellow curve in Fig. III.11c). At

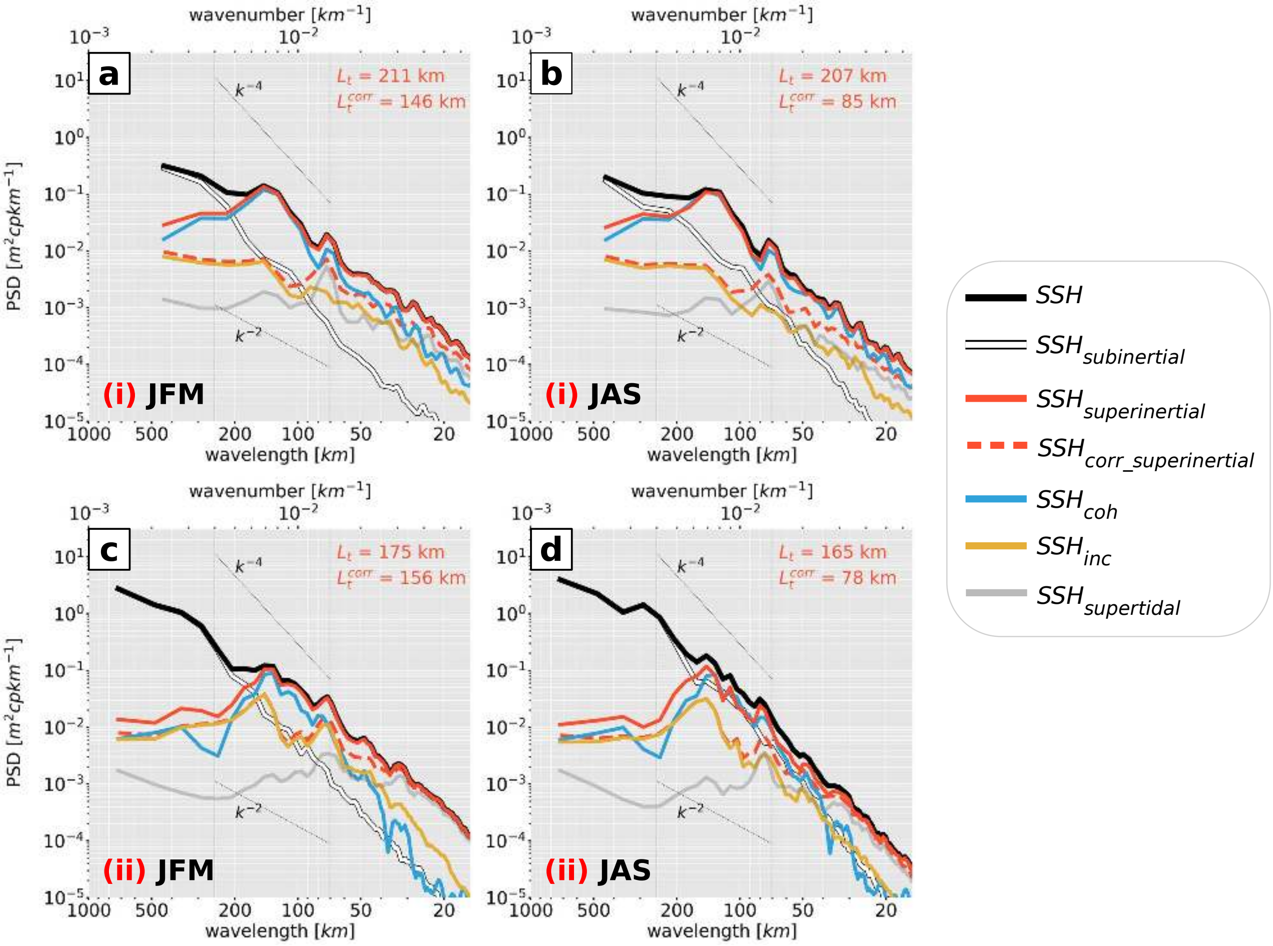

**Figure III.11:** Same as Fig. III.10, but for seasonally averaged SSH wavenumber spectra, i.e. southern hemisphere summer (January-March, JFM) and winter (July-September, JAS) for the **(a)**-**(b)** northern and **(c)**-**(d)** southern transect.

scales below 90 km, the incoherent tide even dominates SSH variance over subinertial motions and is equally important to the coherent tide. In winter, the transition scale is largely reduced from 165 km to 78 km (Fig. III.11d). This is primarily linked to the fact that subinertial motions are energized in the winter while motions at superinertial frequencies lose in relative importance as stated above. We note that a significant contribution of motions at supertidal frequencies is seen for scales smaller than 100 km.

The northern domain differs from the southern domain in that SSH variance of subinertial motions is generally reduced and the seasonal cycle less pronounced (shown by the white curves in Fig. III.11a-b). Motions at superinertial frequencies largely govern over motions at subinertial frequencies throughout the year, dominated by the coherent internal tide. As for the southern transect, the incoherent contribution undergoes a seasonality and increases in summer, but remains weaker than the coherent signal.

Increasing SSH observability of mesoscale and submesoscale motios by correcting for the coherent internal tide signal proves overall to be more efficient since the incoherent internal tide signal is largely reduced in SSH variance compared to the southern transect (seen in Fig. III.11a-b by the intersection of the white and dashed red curves). Specifically, the transition scale is reduced from 211 km to 146 km in summer (Fig. III.11a) and from 207 km to 85 km in winter (Fig. III.11b). Contributions by motions at supertidal frequencies appear to have larger importance in the northern domain compared to the southern domain. In fact, at scales below 146 km and 85 km wavelengths for summer and winter respectively, SSH variance is governed by equal contributions from the incoherent internal tide and motions at supertidal frequencies.

Briefly summarized, the dominance of unbalanced motions in the mesoscale to submesoscale band strongly limits SSH observability of geostrophic dynamics around New Caledonia, especially in summer. In other words, SSH observability of mesoscale dynamics is limited to large eddy scales even after a correction for the coherent tide in numerical simulation output. It is to a large part the incoherent internal-tide and motions at supertidal frequencies at scales <100 km which may eventually determine and challenge SWOT SSH observability of mesoscale and submesoscale dynamics.

### III.2.5 Conclusion

To study mesoscale and submesoscale dynamics using SWOT SSH, a proper disentanglement between balanced and unbalanced motions is required. Internal tide dynamics can be decomposed into a coherent (phase-locked) and incoherent (non phased-locked) component. The coherent tide component is relatively well predictable in time and space and could be corrected using dedicated satellite altimetry products. These satellite altimetry products provided a robust estimate of the coherent tide over a long time series spanning over two decades (Ray and Zaron, 2016; Zhao et al., 2016; Zaron, 2019). The incoherent tide component represents a bigger challenge due to its high unpredictability, and has been shown to account for a large fraction of the total tide signal, i.e. up to 100 % in some regions such as the equatorial Pacific (Zaron, 2017). A better understanding of how tidal incoherence arises, how it expresses in SSH, and finally how it limits SSH observability of balanced motions is indispensable to infer what SWOT will be able to observe in regions with strong tidal activity. Here, we gave first insight into tidal incoherence around New Caledonia using high-resolution regional model output from a full-model calendar year. We investigated potential sources of arising incoherence in both the far-field and near-field. Preliminary results shed light on implications for SSH observability.

Even though the coherent internal tide is dominant around New Caledonia, tidal incoherence may represent an important fraction of the total variance, particularly with increasing distance to the internal-tide generation sites. Our analysis suggests that tidal incoherence arises from mesoscale eddy variability in both the near-field and far-field. In the far-field, it was shown that tidal incoherence occurs when the tidal beam propagates through the eddy field. A simplistic ray tracing method reveals that phase variations accompanied by changing phase and group speeds in propagation direction cause a refraction of the tidal beam with respect to a theoretical ray in the absence of background currents. Tidal beam refraction is more pronounced south of New Caledonia for both mode 1 and mode 2. This corresponds with elevated levels of tidal incoherence due to a more energetic eddy field. Particularly, it is the intensified background currents, i.e. swirl velocities of mesoscale eddies, south of New Caledonia which are more enhanced than north of New Caledonia as suggested by an eddy tracking analysis.

The ray tracing has provided important insight into the fate of internal tide energy propagation in the far-field. We focused our analysis on tidal beam reflection due to background currents of mesoscale eddies. Mesoscale eddies may also be associated with strong stratification anomalies compared to their surrounding, which can impact tidal beam propagation. It remains an open question to what extent stratification anomalies associated with mesoscale eddies can alter ray propagation. Guo et al. (2023) studied the contribution of background currents and stratification changes associated with mesoscale eddies in the South China Sea. Their analysis strongly suggested that stratification changes only play a secondary role. Using ARGO floats, Keppler et al. (2018) reported strong anomalies in temperature and salinity within mesoscale eddies and down to 1000 m depth south of New Caledonia. Further investigations are needed to understand to what extent stratification changes associated with mesoscale eddies can alter the ray propagation around New Caledonia.

We suggest that tidal incoherence can also arise in the near-field, i.e. at the internal tide generation site. Preliminary results showed that barotropic-to-baroclinic conversion may be subject to temporal variations. They are mainly governed by pressure amplitude variations in the hot spot regions north and south of New Caledonia. Along the Hawaiian Ridge, Zilberman et al. (2011) found on the contrary that variations in conversion terms were mainly explained in the perturbation pressure phase, thus, suggesting the influence of remotely generated internal tides. Our results advocate for a greater influence of local changes in stratification, and propose that these pressure amplitude variations are associated with temporally constrained, elevated levels of mesoscale eddy kinetic energy. Specifically, temporally reduced conversion goes hand in hand with decreasing energy flux divergence. This finding comes to the same conclusion as above pointing out that the effect of stratification on tidal incoherence needs more investigation.

The SSH signature of internal tides around New Caledonia was revisited to address implications of tidal incoherence for SWOT SSH observability of mesoscale and submesoscale dynamics. To improve SSH observability of balanced motions, previous efforts have suggested to subtract the coherent internal tide signature from the altimetry-like SSH, derived from decades-long time series collected from conventional satellite altimetry (Zhao et al., 2016; Ray and Zaron, 2016; Ubelmann et al., 2022; Zaron, 2019). This approach is interesting, but limited as it largely depends on the strength of tidal incoherence. We showed for two transects in along-beam direction that SSH variance of motions at superinertial frequencies corrected for the coherent internal tide are governed by the incoherent internal tide and motions at supertidal frequencies. This has implications for the transition scale, which separates the larger scale dominated by balanced geostrophic motions from the smaller scale dominated by unbalanced wave motions. Because of the remaining contributions of the incoherent internal tide and motions at supertidal frequencies, SSH observability can be maximally increased to wavelengths below 100 km in the annual mean. SSH observability may be strongly limited south of New Caledonia where tidal incoherence is increased. Depending on the season and the relative importance of motions at subinertial and superinertial frequencies, we find that SSH observability of balanced motions may vary between 80 and 150 km wavelength.

The results are partly in accordance with the global numerical model analysis in Qiu et al. (2018). When not correcting for the coherent tide, the transition scales around New Caledonia vary in the annual mean from around 150-200 km in the north (compared to 204 km in our study) to around 100-150 km in the south (compared to 163 km in our study). Qiu et al. (2018) reported strong seasonal differences in the transition scales. Particularly, in the summer months around New Caledonia, the transition scale is reduced by 50-100 km toward smaller wavelengths. This is not in agreement with our study, where the transition scale (not corrected for the coherent tide) does not undergo a strong seasonal cycle. When correcting for the coherent tide, Qiu et al. (2018) showed that in the annual mean the transition scale can be reduced by up to 80 km toward smaller wavelengths. This is in good agreement with our findings. A transition scale estimate is also given by an in-situ analysis in Sérazin et al. (2020). The authors find the transition scale at wavelengths as low as 10 km at which divergent motions take over rotational dynamics. However, their analysis is based on velocity structure functions and kinetic energy spectra. Further, it is argued the internal tide signature might vanish in their approach which involves isotropic averaging of structure functions over horizontal bins.

Overall, the remaining signature of incoherent tides raises concerns over the general applicability of the coherent internal tide correction. Alternative approaches have been proposed in the SWOT Science community such as in Le Guillou et al. (2021) and Wang et al. (2022). Using a joint estimation algorithm and a deep-learning approach respectively, the authors are able to simultaneously map and separate balanced motions and internal tides from two-dimensional SSH field. Most importantly, both the coherent and incoherent internal tide field are extracted. Important work was also done by separating balanced motion from internal gravity waves by the allocation of spectral characteristics to their respective dynamics (Savage et al., 2017; Torres et al., 2018, 2019).

In the one-dimensional wavenumber spectra that we computed for two transects in tidal beam propagation direction, the internal tide signature is well captured. This raises the question, though, of how the anisotropic internal tide signature affects SSH spectra along an altimetry track, not orientated along a tidal beam. Take the SWOT swaths during the fast-sampling phase south of New Caledonia as example (see Fig. 12 in Bendinger et al., 2023). Preliminary analyses suggest that the characteristic internal tide signature is not properly sampled in our study region (not shown). The spectral peaks are less evident, and the incoherent internal tide tends to increase in importance. The latter may be partially attributed to the dominance of the incoherent internal tide away from the tidal beam's mean propagation direction. Moreover, the correction for the coherent internal tide increases SSH observability of balanced motions only marginally. It becomes clear that our ability to observe mesoscale and submesoscale dynamics from SWOT SSH observations ultimately depends on the proper correction of both the coherent and incoherent internal tide. We have no doubt, whatsoever, that SWOT data will contribute to and improve the characterization of the internal tide field.

## III.3 Internal tides around New Caledonia: an in-situ approach

### III.3.1 Introduction

The previous results offered a comprehensive description of internal-tide dynamics around New Caledonia through a dedicated regional numerical modeling effort. In this section, we shift our focus to the study of internal tides using in-situ observations from autonomous underwater gliders. While numerical modeling has played a key role in investigating the fine spatial and temporal scales of internal tides, it may not fully capture the fine-scale physics associated with high-frequency motion due to sub-grid scale parameterizations and turbulent closure schemes. Therefore, in-situ observations are indispensable.

Here, we focus on glider observations that provided high-resolution spatio-temporal measurements of hydrography in the upper 1000 m south/southwest of New Caledonia. We attributed this area in Sect. III.1 and Sect. III.2 to intense westward tidal energy propagation and arising incoherence due to eddy-internal tide interactions. The glider observations with their broad spatial extent are highly valuable, not only for the study of internal tides from an in-situ perspective but also for the validation of numerical simulation output, complementing in-situ measurements at fixed locations. Furthermore, they have interesting applications in the context of SWOT-AdAC and SWOT's fast-sampling phase by linking internal-tide dynamics in the ocean interior with the signature in SSH which may help interpret SWOT's SSH observability of balanced and unbalanced motions.

However, in-situ glider measurements represent a challenge for inferring the spatial and temporal scales considered here due to glider's irregular sampling technique. Thus, they require special dedication. In the following, we address the following questions as stated in Sect. I.5:

**C Internal tides inferred from autonomous underwater gliders around New Caledonia**

1) Are glider observations around New Caledonia suitable to infer internal-tide characteristics? How do glider observations compare with regional modeling?

2) Can glider observations serve as an in-situ observation platform to deduce the SSH signature of internal tides?

This work was conducted to a large part during a two-month research visit in fall 2023 in the framework of this thesis at the Applied Physics Laboratory at the University of Washington, Seattle, USA, in active collaboration with Kyla Drushka and Luc Rainville. The results are presented below in form of a journal manuscript, which has been submitted to *Ocean Science* and is currently under review.

**Publication**

**Bendinger, A.**, Cravatte, S., Gourdeau, L., Rainville, L., Vic, C., Sérazin, G., Durand, F. , Marin, F., Fuda, J.-L.: Internal tides vertical structure and steric sea surface height signature south of New Caledonia revealed by glider observations. EGUsphere, 2014, 1-29, https://doi.org/10.5194/egusphere-2024-247, **(submitted to *Ocean Science*)**,

### III.3.2 Internal tides vertical structure and steric sea surface height signature south of New Caledonia revealed by glider observations (submitted to *Ocean Science*)

# Internal tides vertical structure and steric sea surface height signature south of New Caledonia revealed by glider observations

Arne Bendinger[1], Sophie Cravatte[1,2], Lionel Gourdeau[1], Luc Rainville[3], Clément Vic[4], Guillaume Sérazin[4,a], Fabien Durand[1], Frédéric Marin[1], and Jean-Luc Fuda[5]

[1]Université de Toulouse, LEGOS (CNES/CNRS/IRD/UT3), Toulouse, France
[2]IRD, Centre IRD de Nouméa, New Caledonia
[3]Applied Physics Laboratory, University of Washington, Seattle, WA, USA
[4]Laboratoire d'Océanographie Physique et Spatiale, Univ. Brest, CNRS, Ifremer, IRD, IUEM, Brest, France
[5]Aix Marseille Univ., Université de Toulon, CNRS, IRD, MIO UM 110, Marseille, France
[a]now at: Institut de Recherche de l'Ecole Navale (IRENav), EA 3634 - Ecole Navale, 29240, Brest, France

**Correspondence:** Arne Bendinger (arne.bendinger@univ-tlse3.fr)

**Abstract.** In this study, we exploit autonomous underwater glider data to infer internal tide dynamics south of New Caledonia, an internal-tide generation hot spot in the southwestern tropical Pacific. By fitting a sinusoidal function to vertical displacements at each depth using a least-squares method, we simultaneously estimate diurnal and semidiurnal tides. Our analysis reveals regions of enhanced tidal activity, strongly dominated by the semidiurnal tide. To validate our findings, we compare the glider observations to a regional numerical simulation that includes tidal forcing. This comparison assesses the simulation's realism in representing tidal dynamics and evaluates the glider's ability to infer internal tide signals and their signature in sea surface height (SSH). The glider observations and a pseudo glider, simulated using hourly numerical model output with identical sampling, exhibit similar amplitude and phase characteristics along the glider track. Existing discrepancies are primarily explained by tidal incoherence induced by eddy-internal tide interactions. We infer the semidiurnal internal tide signature in steric SSH by the integration of vertical displacements. Within the upper 1000 m, the pseudo glider captures roughly 78 % of the steric SSH total variance explained by the full water column signal. This value increases to over 90 % when projecting the pseudo glider's vertical displacements onto climatological baroclinic modes and extrapolating to full depth. Notably, the steric SSH from glider observations aligns closely with empirical estimates derived from satellite altimetry, highlighting the glider observations' predominating coherent nature.

*Copyright statement.* TEXT

## 1 Introduction

Over the last two decades, in-situ observations (e.g., Park and Watts, 2006; Zilberman et al., 2011; Nash et al., 2012; Vic et al., 2018), satellite altimetry (Ray and Zaron, 2016; Zhao et al., 2016; Zaron, 2019), and numerical modeling (for a review see Arbic et al., 2018; Arbic, 2022) have shed light on internal-tide dynamics at both regional and global scales. Important internal tide generation sites have been identified in regions such as the Hawaiian Islands, the Luzon Strait, the Indonesian Seas, French Polynesia, the southwestern tropical Pacific, Madagascar, the Amazonian shelf break, and the Mid-Atlantic Ridge. At these locations, the barotropic tidal flow interacts with the bathymetry while radiating internal waves at tidal frequency into the stably stratified water column, expressed by vertical displacements of density surfaces (Bell Jr, 1975; Baines, 1982).

Each of the above tools, namely in-situ observations, satellite altimetry, and numerical modeling, possesses its own set of benefits and limitations. In-situ observations such as moorings provide excellent temporal resolution and in most cases a sufficient vertical resolution to resolve the wave's vertical structure. However, these scattered in-situ measurements are only representative at very local scales. Satellite altimetry provides a global view of internal tides, but long time series are needed and the derived signal is mostly representative of low-vertical mode dynamics at large horizontal scales. Numerical modeling overcomes both of these issues by investigating the fine spatial and temporal scales over a large region. Though, high-resolution grid spacing is needed making numerical modeling computationally expensive. Further, these models and the underlying primitive equations may be simplifications of the complex reality that do not fully encapsulate the intricacies of the actual physical system. This concerns sub-grid scale physics such as unresolved dissipative effects which require parameterization through turbulent closure schemes. Generally, any interpretation and conclusion drawn from the above approaches should be taken with thoughtful consideration.

Among the in-situ platforms, gliders have the potential to infer the vertical structure of internal tides, while documenting their spatial variability. Traditionally used to document lower frequency features such as mesoscale and submesoscale features at high spatial resolution (Rudnick, 2016; Testor et al., 2019), they have the potential to complement knowledge obtained from moorings and satellite altimetry. Commonly, gliders are programmed to provide subsurface observations by sampling the upper ocean in a saw-tooth manner. For a maximum depth of 1000 m, a typical glider dive cycle is 6 h during which it travels 6 km horizontally. As they travel autonomously through the ocean over thousands of km and for a duration of the order of months per mission, they can sample a large area. This makes gliders advantageous compared to other in-situ platforms such as moorings, which are confined to fixed locations. However, glider measurements merge spatial and temporal variability and, thus, make it difficult to separate high-frequency signals from low-frequency (but spatially varying) motions such as mesoscale and submesoscale features.

Despite these limitations, glider measurements have been previously successfully exploited to access hydrographic data at fine-scale resolution, and to infer internal-tide dynamics in dedicated areas. Pioneer work using glider data was carried out by Rainville et al. (2013) and Johnston et al. (2013) who estimated amplitude and phase of diurnal and semidiurnal internal tides. Glider data were shown to capture the phase propagation away from the generation site and map the mode-1 energy flux at the Luzon Strait. Johnston and Rudnick (2015) extracted diurnal and semidiurnal internal tides from repeated glider cross-shore transects in the California Current System. They link the internal tide induced mixing with elevated diffusivity estimates. Johnston et al. (2015) revealed standing wave patterns in the Tasman Sea as incident mode-1 internal tides reflected on the continental slope. Moreover, internal tides were extracted from gliders that were employed for vertical profiling, serving as fixed-point time series while maintaining station (Hall et al., 2017, 2019).

This study focuses on internal tides south of New Caledonia, an internal tide generation hot spot in the southwestern tropical Pacific (Fig. 1), recently described and quantified in Bendinger et al. (2023) using numerical modeling. Internal tide generation was found to be closely linked with the north-south stretching ridge system composed of shelf breaks, oceanic ridges, and seamounts which represent a major obstacle for the barotropic tidal flow bending around New Caledonia. In the full-regional domain, a total of 15.27 GW is converted from the barotropic to the baroclinic M2 tide, comparable to well-known sites of enhanced energy conversion (e.g. the Hawaiian Ridge). Barotropic-to-baroclinic energy conversion is associated with the main bathymetric structures, namely Grand Passage, Pines Ridge, Norfolk Ridge, and Loyalty Ridge (see Fig. 1), governed by the semidiurnal M2 tide and strongly dominated by mode 1. Tidal energy propagation is characterized by well-confined tidal beams that diverge away from the generation hot spots north and south of New Caledonia with depth-integrated energy fluxes of up to 30 kW $m^{-1}$ in the annual mean. The modeled internal-tide dynamics have been validated in terms of barotropic-to-baroclinic energy conversion against semianalytical theory. In addition, the surface signature has been validated against satellite altimetry products revealing reasonable amplitude and large-scale (interference) patterns. The above model analysis only concerned the coherent tide, which is the stationary component being constant in amplitude and phase. The departure from tidal coherence is referred to as tidal incoherence, i.e. the temporally varying amplitude and phase within the tidal frequency band. It is characterized by its unpredictability often linked to mesoscale variability and stratification changes both close to the generation site and during tidal energy propagation. Particularly, mesoscale turbulence and background currents were shown to cause a tidal beam refraction associated with changing phase speeds and, consequently, alterations in the propagation of internal tides (Rainville

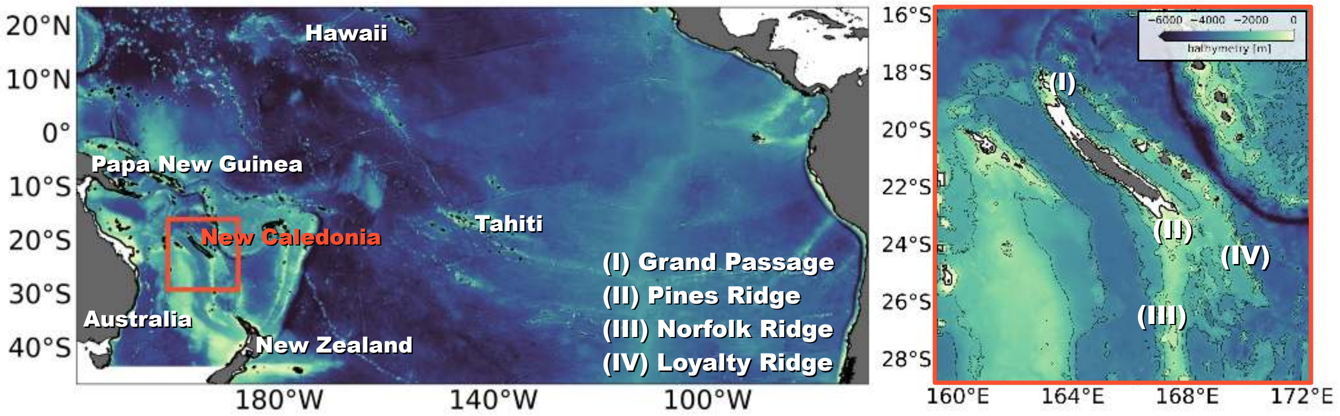

**Figure 1.** New Caledonia is located in the southwestern tropical Pacific, an area of complex bathymetry with continental shelves, shelf breaks, large- and small-scale ridges, and seamounts. It is subject to strong internal tide generation associated with the major bathymetric features, i.e. (I) Grand Passage, (II) Pines Ridge, (III) Norfolk Ridge, and (IV) Loyalty Ridge.

and Pinkel, 2006; Duda et al., 2018; Guo et al., 2023).

From an in-situ perspective, the numerical model results remain to be fully validated. In-situ observations of fine-scale physics in the region are rare. Moored measurements of velocity were used to compare kinetic energy frequency spectra with the numerical model output (Durand et al., 2017; Bendinger et al., 2023). However, the mooring is neither located close to a pronounced internal tide generation site, nor in propagation direction. Insight into fine-scale dynamics around New Caledonia is given by a unique set of glider surveys undertaken in the period from 2011 to 2014 (Durand et al., 2017). One of these glider missions surveyed the region of high internal tide activity south of New Caledonia, which is also a region of high mesoscale eddy activity (Keppler et al., 2018) and submesoscale activity (Sérazin et al., 2020). Disentangling balanced from unbalanced motions (mesoscale and submesoscale features from internal waves) in this area is a challenge of particular interest in the context of the Surface Water Ocean Topography (SWOT) satellite altimetry mission and the SWOT Adopt-A-Crossover (AdAC) initiative (d'Ovidio et al., 2019; Morrow et al., 2019). SWOT will provide high-resolution sea surface height (SSH) measurements along two swaths of 60 km width each resolving wavelengths down to 15 km, which is up to ten times higher resolution than conventional altimetry (Fu et al., 2012; Ballarotta et al., 2019; d'Ovidio et al., 2019; Morrow et al., 2019). The availability of three-dimensional in-situ observations may provide insight into the SSH expression of fine-scale dynamics, with important implications for disentangling SWOT SSH measurements. New Caledonia represents an interesting site for addressing mesoscale and submesoscale SSH observability in a region with strong internal tides. Specifically, the glider data can be very useful in linking the vertical structure of the ocean interior with the ocean surface. Although not suitable for the direct assessment of SWOT, it represents an important in-situ dataset with relevant information about the governing dynamics at play.

This study's objective lies in the exploitation of the glider's spatio-temporal sampling in the upper 1000 m to infer internal-tide dynamics, including their steric SSH signature south of New Caledonia. To assess our findings, we seek a complementary validation of the regional numerical simulation by glider observations and vice-versa. On the one hand, the glider observations will assess the realism of internal tides' simulation in the regional model. On the other hand, the regional model will address the capability of the methodologies applied to the glider observations. Specifically, we address the following questions: How do the observation-based and simulated internal tide fields compare with each other? Can observations and the model be used complementarily to deduce tidal coherence and/or tidal incoherence? To what extent are the glider observations of the upper 1000 m sufficient to deduce the internal tide steric SSH signature?

## 2 Data

### 2.1 Glider observations

This study focuses on autonomous Spray glider observations obtained during a mission from 12 August 2014 to 23 October 2014 within a series of glider surveys around New Caledonia in the framework of the Southwest Pacific Ocean Circulation and Climate Experiment (SPICE, Ganachaud et al., 2014; Durand et al., 2017). The glider surveyed continuously temperature and salinity with respect to pressure in the upper 1000 m as it travelled horizontally and vertically in the water column while sending its GPS location before each descending and after each ascending profile (Fig. 2).

Along the glider's path, a total of 560 (ascending/descending) profiles were analyzed which were acquired over the course of 73 days and a horizontal travel distance of 1150 km. The glider track as a function of days since deployment is shown in Fig. 3. The glider was deployed at the southern edge of the New Caledonia lagoon at 166° E, 22° S before heading south to 26.5° S and heading back north to its initial starting position. The mean duration of a glider profile is 2.9 h (3.4 h for the mean descending profile, 2.4 h for the mean ascending profile). The mean horizontal displacement is 2.1 km (2.4 km for the mean

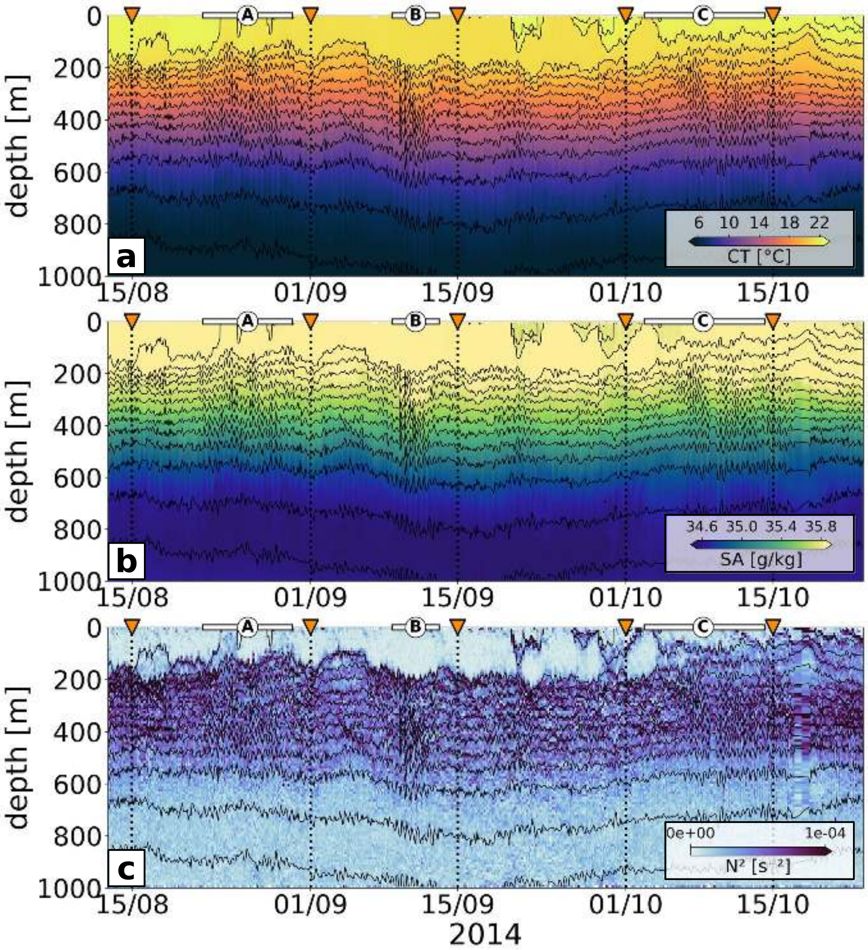

**Figure 2.** Glider observations (a) conservative temperature (CT), (b) absolute salinity (SA), and (c) squared buoyancy frequency ($N^2$) overlaid by potential density contours and gridded in 10 m bins along the vertical axis. The orange triangles (and the dotted vertical lines) mark the glider way points as given in Fig. 3. The white bars represent the sections of potential tidal beam crossing, namely A, B, C (as defined in Fig. 3).

descending profile, 1.7 km for the mean ascending profile). Aborted glider profiles as well as profiles featuring faulty GPS data were discarded from the analysis. The acquired glider time series of temperature and salinity with respect to pressure were divided into descending and ascending profiles by allocating the glider time stamp with the maximum dive depth. The profiles were then vertically gridded and binned in 10 m depth intervals.

## 2.2 Numerical simulation

This study uses numerical output of a model configuration that consists of a host grid (TROPICO12, 1/12°horizontal resolution and 125 vertical levels) and covers the tropical and subtropical Pacific Ocean basin from 142° E-70° W and 46° S-24° N (Fig. 1), as introduced in Bendinger et al. (2023). The oceanic reanalysis GLORYS2V4 prescribes initial conditions for temperature and salinity as well as the forcing with daily currents, temperature, and salinity at the open lateral boundaries. ERA5 produced by the European Centre for Medium-Range Weather Forecasts (ECMWF, Hersbach et al., 2020) provides atmospheric forcing at hourly temporal resolution and a spatial resolution of 1/4°to compute surface fluxes using bulk formulae and the

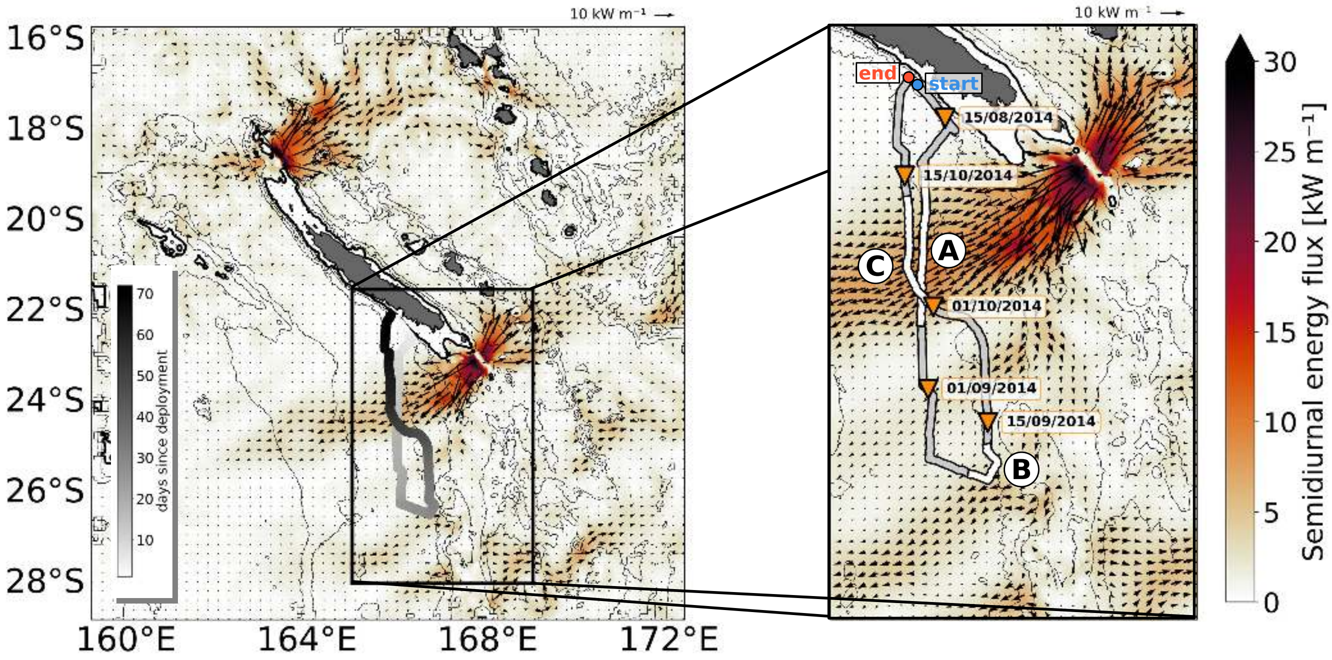

**Figure 3.** CALEDO60 regional model domain showing the depth-integrated coherent semidiurnal energy flux (shading) including flux vectors and the glider track of the glider mission south of New Caledonia as a function of days since deployment. The inset zooms into the study area. For the sake of better visualization and orientation, orange triangles and the associated time stamps mark way points along the glider track (15 August, 1 September, 15 September, 1 October, and 15 October 2014. The highlighted white segments (A, B, C) illustrate potential major crossings of glider track and tidal beam energy propagation. The thin black lines represent the 1000, 2000, and 3000 m depth contours. The thick black line is the 100 m depth contour representative for the New Caledonia lagoon.

model prognostic sea surface temperature. The model is forced by the tidal potential of the five major diurnal (K1, O1) and semidiurnal (M2, S2, N2) tidal constituents. At the open lateral boundaries it is forced by barotropic sea surface height and barotropic currents of the same five tidal constituents taken from the global tide atlas FES2014 (Finite Element Solution 2014, Lyard et al., 2021). A higher-resolution horizontal grid is nested within the host grid in the southwestern tropical Pacific Ocean encompassing New Caledonia (Fig. 3). This nesting grid features 1/60°horizontal resolution or $\sim$1.7 km grid box spacing initialized by an Adaptive Grid Refinement in Fortran (AGRIF, Debreu et al., 2008). AGRIF was explicitly designed for NEMO to set up regional simulations embedded in a pre-defined model configuration. Further, it enables the two-way lateral boundary coupling between the host and the nesting grid during the whole length of the simulation. Bendinger et al. (2023) illustrated the model's eligibility of realistically simulating both background ocean dynamics (i.e. large-scale circulation, kinetic energy spectra) and tidal dynamics. We refer to Bendinger et al. (2023) for a more detailed model description and model assessment.

Here, we focus on the model year 2014 using the hourly regional model output (CALEDO60) of the three-dimensional velocity field, temperature, salinity, pressure. This model output was also subject to a coherent tidal analysis at each grid point providing the tidal harmonics for the diurnal and semidiurnal constituents as well as tidal energetics. The harmonic analysis constraint to a full calendar year relies upon a compromise between high computational expenses and the representative extraction of the coherent tide through a time series long enough to sample a representative variability of the mesoscale turbulent field. The annual mean depth-integrated semidiurnal coherent energy flux for the regional model domain is shown in Fig. 3 suggesting that the glider crossed several times an area of pronounced westward internal tide energy propagation, characterized by narrow tidal beams. The temporal overlap of glider observations and numerical model output allows for a complementary assessment of both data sets.

### 2.3 Geostrophic surface currents

We used altimetry-derived global ocean gridded maps (1/4°) of geostrophic surface currents from absolute dynamic topography, generated and processed by the E.U. Copernicus Marine Environment Monitoring Service (CMEMS). We used the multimission Data Unification and Altimeter Combination System (DUACS) product in delayed time and daily resolution with all satellite missions available at a given time. We extracted geostrophic surface currents for the glider period August-October 2014, which served as input for the ray tracing in Sect. 3.5.

### 2.4 HRET

The internal tide induced SSH signature along the glider track is computed using empirical estimates from the High Resolution Empirical Tide product (HRET version 8.1, Zaron, 2019). This product uses essentially all-exact repeat altimeter mission data during a 25-year long time series of SSH observations (1992-2017, TOPEX/Jason, Geosat, ERS, Envisat). Based on a point-wise harmonic analysis along all available satellite track, and a plane-wave fit in overlapping patches, it provides the coherent amplitude and phase for the major semidiurnal (M2, S2) and diurnal (K1, O1) tides for modes 1-3. Here, we reconstruct the coherent semidiurnal timeseries of SSH in along glider-track direction using the M2 and S2 harmonics for modes 1-2 to compare with the glider derived steric height (Sect. 2.4).

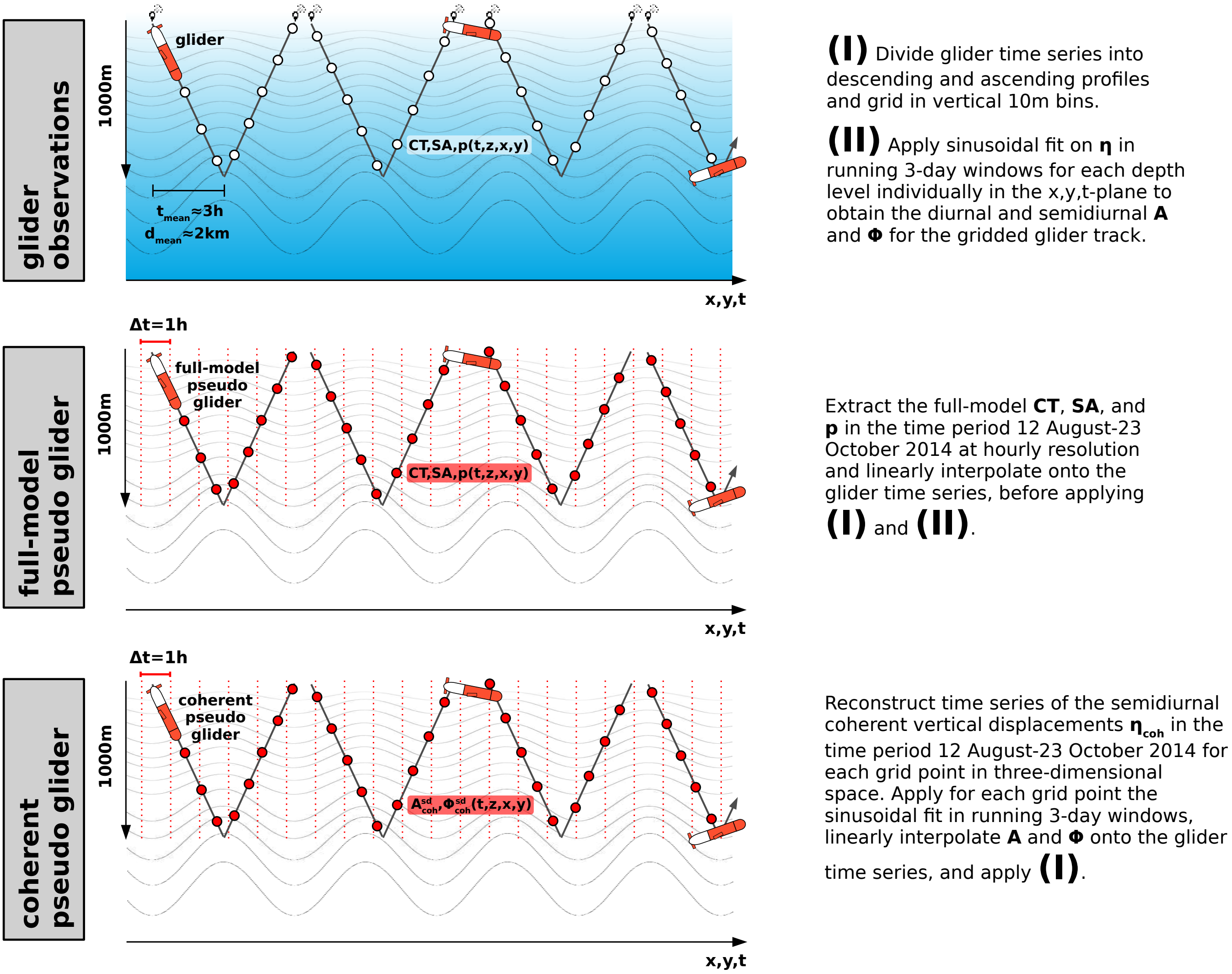

**(I)** Divide glider time series into descending and ascending profiles and grid in vertical 10m bins.

**(II)** Apply sinusoidal fit on **$\eta$** in running 3-day windows for each depth level individually in the x,y,t-plane to obtain the diurnal and semidiurnal **A** and **$\Phi$** for the gridded glider track.

Extract the full-model **CT**, **SA**, and **p** in the time period 12 August-23 October 2014 at hourly resolution and linearly interpolate onto the glider time series, before applying **(I)** and **(II)**.

Reconstruct time series of the semidiurnal coherent vertical displacements **$\eta_{coh}$** in the time period 12 August-23 October 2014 for each grid point in three-dimensional space. Apply for each grid point the sinusoidal fit in running 3-day windows, linearly interpolate **A** and **$\Phi$** onto the glider time series, and apply **(I)**.

**Figure 4.** Schematic for the glider observations (top panel), the full-model pseudo glider (middle panel), and the coherent pseudo glider (bottom panel). Note that the full-model pseudo glider and the coherent pseudo glider sampling are identical to the one in the glider observations, i.e. the sampling considers the horizontal displacement during the glider profile as a function of time. This is achieved by linearly interpolating the model hourly output onto the glider time series.

## 3 Methods

### 3.1 Glider-derived internal tide amplitude and phase in 3-day running windows

The amplitude and phase of internal tides, derived from glider observations with irregular sampling in both space and time, are determined using a well-established methodology from Rainville et al. (2013). This methodology relies on the sinusoidal regression of vertical (isopycnal) displacements in 3-day running windows using a least squares fit. The choice of the 3-day window is ultimately linked to a compromise between 1) a minimum time series length that captures the diurnal period between 18 and 36 h and the semidiurnal period between 10.3 and 14.4 h, 2) an adequate number of tidal cycles within 3 days for the statistical analysis, and 3) a time period during which the internal tide amplitude and phase do not vary significantly during the glider's horizontal displacement. In our case, the corresponding travel distance over 3 days is approximately 50 km. The vertical displacement is computed as follows:

$$\eta = g\frac{\sigma_s - \overline{\sigma}}{\sigma_s \overline{N^2}}, \tag{1}$$

where g is the gravitational acceleration, $\sigma_s$ is the sample density, and $\overline{\sigma}$ and $\overline{N^2}$ are the mean density and mean squared buoyancy frequency relative to the 3-day running window, respectively. Further, a linear trend was subtracted which we attribute to sloping isopycnals of low-frequency motion. Following Rainville et al. (2013), we fit simultaneously the K1 ($\omega_\mathrm{d}$ = $2\pi$/23.9345 $\mathrm{h}^{-1}$) and M2 ($\omega_\mathrm{sd}$ = $2\pi$/12.4206 $\mathrm{h}^{-1}$) internal tide for each depth layer and each 3-day time window, i.e.

$$\eta(t,z) = A_\mathrm{d}(z)e^{(-iw_\mathrm{d}t+\phi_\mathrm{d}(z))} + A_\mathrm{sd}(z)e^{(-iw_\mathrm{sd}t+\phi_\mathrm{sd}(z))}, \tag{2}$$

where $A_\mathrm{d}$ and $A_\mathrm{sd}$ are the diurnal and semidiurnal amplitude, respectively. Equivalently, $\phi_\mathrm{d}$ and $\phi_\mathrm{sd}$ are the diurnal and semidiurnal phases. Here, the phase is relative to the Unix epoch (00:00:00 UTC on 1 January 1970). Note that even though we solve for the peak frequencies of the K1 and M2 tides, the fitted amplitude and phase are representative for the diurnal and semidiurnal frequency band since the 3-day window does not allow for a separation among the diurnal or semidiurnal tidal constituents. The sampling of the glider observations, the underlying methodology to extract the diurnal and semidiurnal tide, and the overall workflow is illustrated and summarized in the schematic in Fig. 4.

The sinusoidal fit for the diurnal and semidiurnal internal tide applied on the glider observations is explicitly shown for a 3-day window in Fig. 5. Explained variability $\gamma$ is here given by the covariance: cov($\eta_\mathrm{d}$,$\eta$)/var($\eta$) for the diurnal fit with the diurnal internal tide induced vertical displacement $\eta_\mathrm{d}$ and cov($\eta_\mathrm{sd}$,$\eta$)/var($\eta$) for the semidiurnal fit with the semidiurnal internal tide induced vertical displacement $\eta_\mathrm{sd}$. In this example, the measured signal is governed by a semidiurnal cycle, well captured by the sinusoidal fit and explaining 77 % of the total variance. The diurnal signal is rather weak in amplitude and barely contributes to the total variance (1 %). The residual signal accounts for 22 %. Overall, the methodology gives us confidence in our ability to accurately reconstruct the amplitude and phase of the internal tide south of New Caledonia.

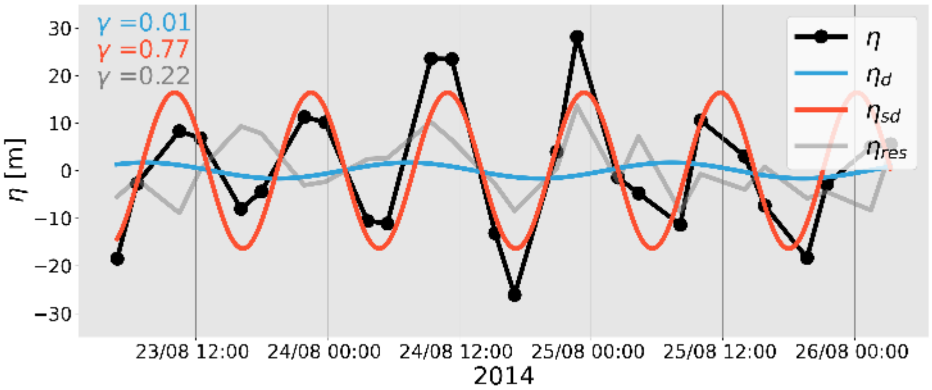

**Figure 5.** Glider observations derived vertical displacements (black, $\eta$) for an exemplary 3-day window at 300 m depth and the sinusoidal fit of the diurnal (blue, $\eta_{\mathrm{d}}$), semidiurnal (red, $\eta_{\mathrm{sd}}$) internal tide, and the residual signal (gray, $\eta_{\mathrm{res}}$). The respective explained variability $\gamma$ is also shown.

### 3.2 Full-model pseudo glider simulation

The temporal overlap of glider observations and numerical simulation output is a great opportunity to compare in-situ observations and the regional simulation. To do so, we simulate what we call a full-model pseudo glider by extracting the model's three-dimensional and hourly output for conservative temperature, salinity, and pressure (see middle panel in Fig. 4). The variables are then interpolated onto the glider track with the same irregular spatio-temporal sampling than the glider observations, followed by the division into descending and ascending profiles and the gridding in vertical 10 m bins. Moreover, diurnal and semidiurnal amplitude and phase are determined just as in the glider observations by applying a sinusoidal fit on vertical displacements in 3-day running windows. In this way, we create pseudo-like observations mimicking the glider mission with the full-model variability.

### 3.3 Coherent pseudo glider simulation

In this study we build upon a harmonic analysis performed on the full-model output for each grid point in the regional model domain as described in Bendinger et al. (2023). Briefly, the objective is to obtain a reference data set from a modeling perspective for the coherent internal tide amplitude and phase along the glider track. We refer to this as the coherent pseudo glider. The methodology is presented in the following and illustrated in the bottom panel in Fig. 4. The coherent internal tide induced amplitude and phase of vertical displacements are deduced from the three-dimensional baroclinic vertical velocity harmonic as follows:

$$\eta_{\mathrm{coh}}(z) = \frac{w_A(z)T}{2\pi}, \tag{3}$$

where $w_A$ is the harmonically fitted amplitude of vertical velocity for each grid point in the domain and $T$ is the respective tidal period. Note that here we only consider the semidiurnal coherent internal tide since it is largely dominant over the diurnal tide as shown further below. The semidiurnal coherent vertical displacements are computed by reconstructing a time series for each semidiurnal tidal constituent (i.e. M2, S2, N2) using $w_A$ and the harmonically fitted phase $w_\Phi$, before summing over the three time series to obtain the semidiurnal time series $\eta^{\mathrm{sd}}_{\mathrm{coh}}$ for each grid point in three-dimensional space. Once reconstructed, we apply the sinusoidal fit in 3-day running windows just as we did for the glider observations, but for each grid point. We obtain the semidiurnal coherent amplitude $A^{\mathrm{sd}}_{\mathrm{coh}}$ and phase $\Phi^{\mathrm{sd}}_{\mathrm{coh}}$ in three-dimensional space at hourly resolution. Finally, we interpolate $A^{\mathrm{sd}}_{\mathrm{coh}}$ and $\Phi^{\mathrm{sd}}_{\mathrm{coh}}$, onto the glider track with the same irregular spatio-temporal sampling than the glider observations, and as above followed by the division into descending and ascending profiles and the gridding in vertical 10 m bins. We computed the semidiurnal coherent amplitude and phase for both the total baroclinic signal (modes 1-9) and mode 1.

### 3.4 Climatological vertical modes

We computed climatological vertical mode profiles for vertical velocity and displacement along the glider track to infer the modal structure of the glider and the pseudo glider vertical displacements (see Sect. 3.6.1). Climatological modes are computed by solving the Sturm-Liouville eigenvalue problem (Gill, 1982):

$$\frac{\partial^2 \Phi_n}{\partial z^2} + \frac{N^2}{c_n^2}\Phi_n = 0, \tag{4}$$

where $\Phi$ is the eigenfunction describing the vertical structure for vertical velocity or displacement subject to the boundary conditions $\Phi(0) = \Phi(-H) = 0$, $n$ is the mode number, and $c_n$ is the separation constant. We solve the eigenvalue problem for climatological profiles of stratification $N$ inferred from climatological profiles of conservative temperature and absolute salinity taken from the CSIRO Atlas of Regional Seas (CARS) for each glider profile location (Ridgway et al., 2002). For this study's purpose, the climatological modes were averaged along the glider track and cut to a representative depth of 3000 m, which is being considered as the full-depth range below.

### 3.5 Ray tracing

A ray tracing method following Rainville and Pinkel (2006) is used to infer the departure from tidal coherence in the glider observations or full-model pseudo glider, associated with the refraction of the tidal beam due to mesoscale background currents, i.e. mesoscale eddies. Specifically, the horizontal propagation of internal gravity modes is investigated considering spatially varying topography, climatological stratification, planetary vorticity, and depth-independent currents. Following this approach, we assume that departure from tidal coherence is primarily due to varying background currents. The choice of depth-independent currents relies on the general assumption that mesoscale eddies are well represented by a barotropic and a mode-1 baroclinic structure with limited vertical shear (Smith and Vallis, 2001). Also, the assumption of considering only depth-independent is validated a posteriori, given the relevance of the qualitative picture of ray trajectories that are obtained.

Bathymetry is taken from ETOPO2v2 (Smith and Sandwell, 1997). Internal gravity wave speeds are predefined and solved by the Sturm-Liouville problem for stratification from the World Ocean Atlas (Locarnini et al., 2018; Zweng et al., 2019). We model semidiurnal ray paths for modes 1-2, initialized at the internal tide generation hot spot south of New Caledonia near Pines Ridge (167.65° E, 23.35° S) and for a given propagation angle (southwestward; 210°). In an iterative procedure, the ray tracing considers for each step size (1 km) bathymetry, climatological buoyancy and planetary vorticity effects, and the background currents. Through the dispersion relation from the Helmholtz equation for internal wave modes assuming a local wave expression, the ray's group and phase velocity are obtained, which are then used to update the ray's position and direction (angle of propagation). To mimick the effects of background currents on the ray's path, a no-currents scenario is also given. The ray tracing is applied on two different velocity products: (1) the depth-averaged currents as derived from the daily-mean three-dimensional velocity field from the regional model output (CALEDO60) and (2) the geostrophic surface currents as derived from CMEMS. For the latter, the depth-independent currents are approximated by multiplying the SSH derived geostrophic surface currents by a factor of 0.5, following Rainville and Pinkel (2006). Note that the ray tracing results of (1) and (2) are rather qualitative. The two data products used in the ray tracing contain different dynamics. Specifically, the gridded two-dimensional fields from CMEMS do not resolve the same spatial and temporal scales as CALEDO60. Thus, the direct comparison of the ray tracing needs to be taken with caution.

### 3.6 Internal tide induced steric height

To our knowledge, glider observations have never been used the SSH signature of fine-scale dynamical structures such as internal tides. In the following, we introduce the methodology to derive the SSH signature, i.e. steric height, of internal tides using glider data limited to the upper 1000 m. Further, the available data in the upper 1000 m is exploited to account for the internal tide steric height signal at depths beyond 1000 m and, thus, for the full-depth range.

#### 3.6.1 Glider and pseudo glider steric height

Following Zhao et al. (2010), we deduce the steric height $h$ of internal tides from surface pressure $p_{\mathrm{surf}}$, i.e. the vertical integral of vertical displacements $\eta$:

$$h(t) = \frac{1}{\rho_0 g} \underbrace{\rho_0 \int\limits_{-H}^{0} N^2(z,t)\eta(z,t)dz,}_{p_{\mathrm{surf}}(t)} \tag{5}$$

where $H$ is the ocean depth. Since the glider observations are limited to the upper 1000 m depth, Equation 5 becomes:

$$h^{\mathrm{1000m}}_{\mathrm{obs}}(t) = \frac{1}{\rho_0 g} \underbrace{\rho_0 \int\limits_{1000m}^{0} N^2(z,t)\eta^{\mathrm{1000m}}_{\mathrm{obs}}(z,t)dz,}_{p^{\mathrm{1000m}}_{\mathrm{surf}}(t)} \tag{6}$$

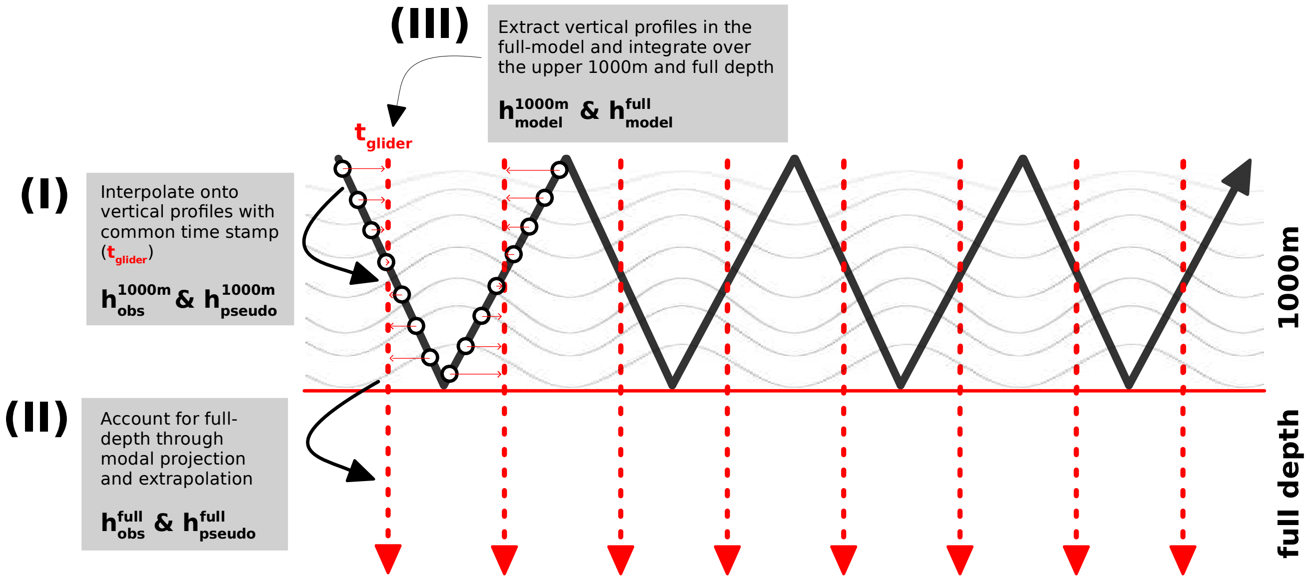

**Figure 6.** Schematic illustrating (I) the linear interpolation of vertical displacements for a given profile onto a common time stamp $t_{\mathrm{glider}}$ prior to the vertical integration to obtain $h^{\mathrm{1000m}}_{\mathrm{obs}}$ and $h^{\mathrm{1000m}}_{\mathrm{pseudo}}$, (II) the modal projection on climatological modes and extrapolation to the full-depth range to obtain $h^{\mathrm{full}}_{\mathrm{obs}}$ and $h^{\mathrm{full}}_{\mathrm{pseudo}}$, and (III) the vertical extraction in the full-model at $t_{\mathrm{glider}}$ to obtain $h^{\mathrm{1000m}}_{\mathrm{model}}$ and $h^{\mathrm{full}}_{\mathrm{model}}$.

where $h^{\mathrm{1000m}}_{\mathrm{obs}}$ is the glider steric height and $\eta^{\mathrm{1000m}}_{\mathrm{obs}}$ are the glider vertical displacements. Since glider measurements for a given profile are not instantaneous and are associated with different time stamps, we interpolated the vertical displacements onto a common time stamp ($t_{\mathrm{glider}}$) that represents the glider's time stamp at mid-depths (see the schematic in Fig. 6). This is achieved by interpolating the reconstructed time series, utilizing amplitude and phase data from the sinusoidal fit, onto the respective $t_{\mathrm{glider}}$ of the profile.

Additionally, we explore steric height inferred by a modal projection of glider vertical displacements on a set of climatological modes followed by an extrapolation to the full-depth range. The objective is to understand to what extent Equation 6 and, thus, the vertical integral limited to glider measurements in the upper 1000 m is a sufficient approximation to account for the surface signature of internal tides. Further, we investigate whether we could infer the surface signature with a better accuracy assuming that internal tides are well represented by the modal structure of modes 1-2.

Using a least-squares fitting method, we project the glider vertical displacements onto a set of climatological modes, as obtained from Sect. 3.4 and limited to the upper 1000 m:

$$\eta^{\mathrm{1000m}}_{\mathrm{obs}}(z,t) = \sum_{n=1}^{2} \widetilde{\eta}^{\mathrm{1000m}}_{n,obs}(t)\Phi^{\mathrm{1000m}}_{n}(z), \tag{7}$$

For each time step, the least-squares solution is then used to extrapolate to the full-depth range using the regression coefficient $\widetilde{\eta}_{n,obs}^{\mathrm{1000m}}$ and the full-depth climatological mode $\Phi_n^{\mathrm{full}}$ to obtain the full-depth glider vertical displacements $\eta_{\mathrm{obs}}^{\mathrm{full}}$. In this study the glider vertical displacements are projected using a maximum of two modes (two-mode approximation). The projection on the first mode only is referred to as first-mode approximation. The associated steric height for the full-depth range was computed equivalent to above:

$$h_{\mathrm{obs}}^{\mathrm{full}}(t) = \frac{1}{\rho_0 g} \underbrace{\rho_0 \int_{-H}^{0} N^2(z)\eta_{\mathrm{obs}}^{\mathrm{full}}(z,t)dz}_{p_{\mathrm{surf}}^{\mathrm{full}}(t)}. \tag{8}$$

where $h_{\mathrm{obs}}^{\mathrm{full}}$ is referred to as the full-depth glider steric height. Similarly, we compute pseudo glider steric height $h_{\mathrm{pseudo}}^{\mathrm{1000m}}$ and the full-depth pseudo glider steric height $h_{\mathrm{pseudo}}^{\mathrm{full}}$ as deduced from $\eta_{\mathrm{pseudo}}^{\mathrm{1000m}}$ and $\eta_{\mathrm{pseudo}}^{\mathrm{full}}$, respectively.

### 3.6.2 Full-model steric height

To have a ground truth for the internal tide surface signature for the full-depth range, we computed steric height from the regional model output as follows:

$$h_{\mathrm{model}}^{\mathrm{full}} = \int_{-H}^{\eta_0} \delta(z)\rho_0 dz, \tag{9}$$

where $\rho_0$=1035 kg m$^{-3}$ is the reference density, $\eta_0$ is the free surface displacement and $\delta$ is the specific volume anomaly. The latter is computed as:

$$\delta(z) = \frac{1}{\rho(\mathrm{CT},\mathrm{SA},z)} - \frac{1}{\rho(\mathrm{CT}_{\mathrm{ref}},\mathrm{SA}_{\mathrm{ref}},z)} \tag{10}$$

with $\mathrm{CT}_{\mathrm{ref}}$ and $\mathrm{SA}_{\mathrm{ref}}$ the reference conservative temperature ($0^\circ\ C$) and the reference absolute salinity (Standard Ocean Reference Salinity, 35.16504 g/kg). Steric anomaly was computed for each grid point from vertical profiles of conservative temperature and absolute salinity. The steric SSH is then obtained through vertical integration before being bandpassed in the semidiurnal frequency band and interpolated onto the time stamps representative for the glider profiles along the glider track ($t_{\mathrm{glider}}$ in Fig. 6). The full-depth steric height $h_{\mathrm{model}}^{\mathrm{full}}$ is compared with the full-depth pseudo glider steric height $h_{\mathrm{pseudo}}^{\mathrm{full}}$. In addition, we also computed the steric height contribution in the upper 1000 m, i.e.

$$h_{\mathrm{model}}^{\mathrm{1000m}} = \int_{1000m}^{\eta_0} \delta(z)\rho_0 dz, \tag{11}$$

which serves for the comparison with the pseudo glider steric height $h_{\mathrm{pseudo}}^{\mathrm{1000m}}$.

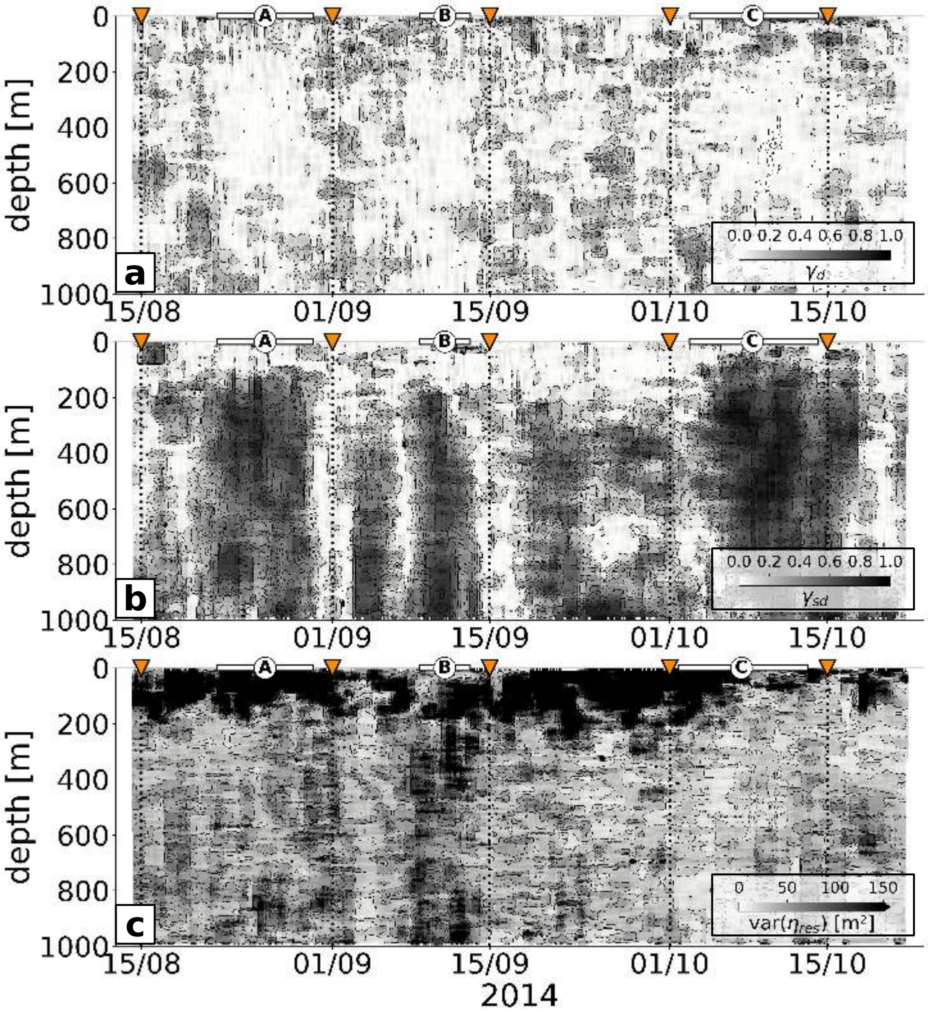

**Figure 7.** Explained variance by the (a) diurnal ($\gamma_\mathrm{d} = \mathrm{cov}(\eta_\mathrm{d}, \eta)/\mathrm{var}(\eta)$) and (b) semidiurnal ($\gamma_{sd} = \mathrm{cov}(\eta_\mathrm{sd}, \eta)/\mathrm{var}(\eta)$) internal tide as given by the sinusoidal fit applied on the glider observations. (c) Variance of the residual signal $\mathrm{var}(\eta_\mathrm{res})$.

## 4 Results

In the following, we first explore the glider observations, the underlying dominance and spatio-temporal variability of the semidiurnal internal tide before comparing it with the model. The pseudo glider simulation is then used to link the ocean interior with the ocean surface by investigating the extent to which the upper 1000 m vertical displacements are sufficient to determine the steric height signal of internal tides.

### 4.1 Semidiurnal internal tide dominance

The simultaneous fit of vertical displacements $\eta$ for the diurnal and semidiurnal tide for the upper 1000 m along the whole glider section, expressed by the explained variance of the total signal, is presented in Fig. 7. The field is overwhelmingly dominated by the semidiurnal tide, along the entirety of the section and throughout the water column from 100-200 m below the surface down to 1000 m depth. Locally, the semidiurnal fit explains up to 80 % of the total variance (Fig. 7b). The diurnal tide is of rather patchy nature and explains less than 10 % of the whole signal most of the time (Fig. 7a). The residual signal stands out as it features high variance near the surface in the upper 100-200 m while diurnal and semidiurnal signals are weak. This corresponds with expectations, i.e. vertical displacements of low-mode baroclinic tides are zero at the surface and weak in the upper layers. Further, the mixed layer near the surface represents a complex flow regime with a broad variety of dynamics, i.e. internal tide induced vertical displacements are no longer the dominant signal. Considering that the fit is performed over a period of 3 days and a horizontal distance of 50 km, the residual may be linked to surface-intensified submesoscale dynamics. In the following, we will only focus on the semidiurnal internal tide since it represents the dominant signal in the region. This is also in agreement with Bendinger et al. (2023), which attributed 96 % of the barotropic-to baroclinic energy conversion in their regional model domain to the semidiurnal tide (M2, S2, N2).

### 4.2 Spatio-temporal variability of semidiurnal internal tide: in-situ observations vs. numerical model

The spatio-temporal variability of the semidiurnal internal tide is investigated in the following (Fig. 8). The glider observations reveal strong spatio-temporal variability during the $>$2 months glider survey as shown by the semidiurnal amplitude (Fig. 8a) and phase (Fig. 8e). Along the glider track, there are distinct patterns of enhanced semidiurnal tide amplitude ($>$20 m) corresponding to large fractions of explained variability (see Fig. 7b).

Based on the modeling results, these patterns are localized to the most distinct tidal beams (labeled as A, B, and C). At these locations, semidiurnal tidal energy propagates westward, which can be traced back to the formation and/or superposition of tidal beams to the south/southeast of New Caledonia (Fig. 3). The pronounced southwestward propagating tidal beam is crossed twice: on the way south in late August (A), and when heading back north in early to mid-October (C) towards the coast of New Caledonia. A third distinct tidal beam worth mentioning is encountered when the glider changes its heading direction from southward to northward (B). Another double crossing of tidal beams (but with weaker amplitudes) is observed in early September and from mid-to-end of September, also visible in the depth-integrated semidiurnal energy flux (Fig. 3).

Glider observations and the full-model pseudo glider show an overall similarity in the spatio-temporal variability. Specifically, this applies to the location, the magnitude, and the vertical structure/extent of the tidal beams (Fig. 8a,e for the glider observations and Fig. 8b,f for the full-model pseudo glider).

Differences between the observations and the full-model pseudo glider are most evident mid-August and early October. During these periods, we find strong tidal signatures in the full-model pseudo glider expressed by elevated amplitudes of isopycnal displacements. This is also apparent from the fitted phase. Given that both glider observations and the full-model pseudo glider feature identical sampling, variations linked to the spring-neap tide cycle are not valid hypotheses. Discrepancies may arise due to inaccuracies in simulating the precise beam locations or in deficiencies in representing the model's vertical mode structure. Another contributing factor is tidal incoherence, which can arise from eddy-internal tide interactions, i.e. temporally varying

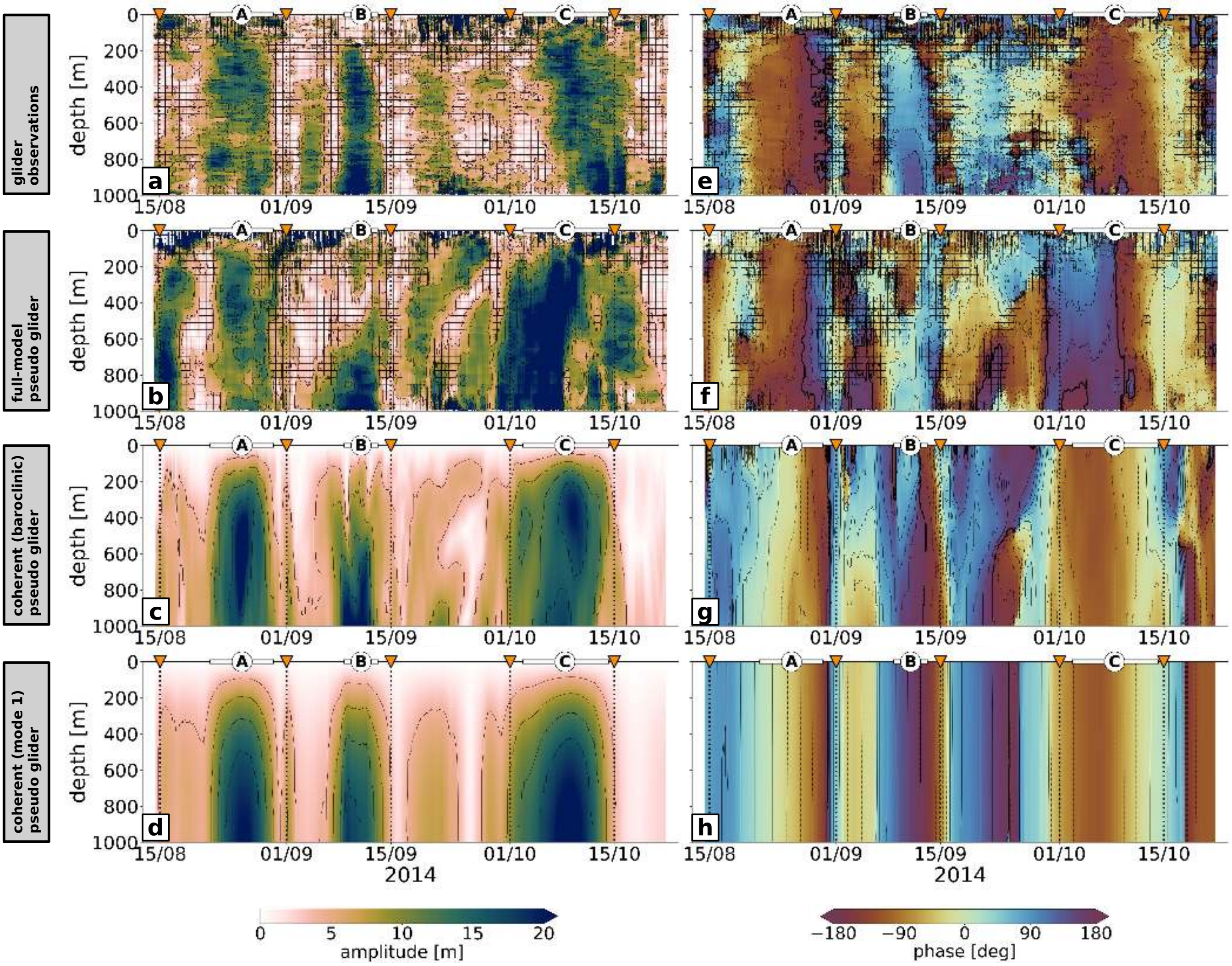

**Figure 8.** Semidiurnal amplitude for (a) glider observations, (b) the full-model pseudo glider, and (c) the coherent pseudo glider. (d) Same than (c) but for vertical mode 1. (e-f) Same than (a-d) but for the semidiurnal phase. Hatches in (a-b) and (e-f) represent areas where the residual signal explains more than twice the variance of the semidiurnal fit.

background currents. Mesoscale and submesoscale features are by nature stochastic. Particularly, mesoscale and submesoscale eddies are not expected to be found at similar location and time in reality and the numerical simulation. The semidiurnal internal tide as derived from glider observations and the full-model pseudo glider appears to a large extent of coherent nature when taking the coherent pseudo glider as a reference data set (Fig. 8c,g). The tidal signatures mid-August and early October in the full-model pseudo glider pose a clear exception. In the subsequent section, we explore whether discrepancies in the mesoscale background field offer insights into differences observed in the sampled semidiurnal internal tide field.

### 4.3 Tidal incoherence inferred from pseudo glider simulation

To infer the impact of mesoscale eddies on the tidal beam's refraction and corresponding incoherence, we apply a simplified ray tracing following Rainville and Pinkel (2006), see Sect. 3.5. We initiate a semidiurnal ray just west of the Pines Ridge, which is known as a hot spot of internal tide generation (Bendinger et al., 2023). The theoretical ray paths for modes 1-2 are shown for two different snapshots on 13 August 2014 (Fig. 9) and 3 October 2014 (Fig. 10). The background velocity field is clearly different between glider observations and the full-model pseudo glider for both snapshots. The no-currents scenario is by definition the same since it relies on the same climatological stratification, bathymetry, and planetary vorticity. The semidiurnal ray

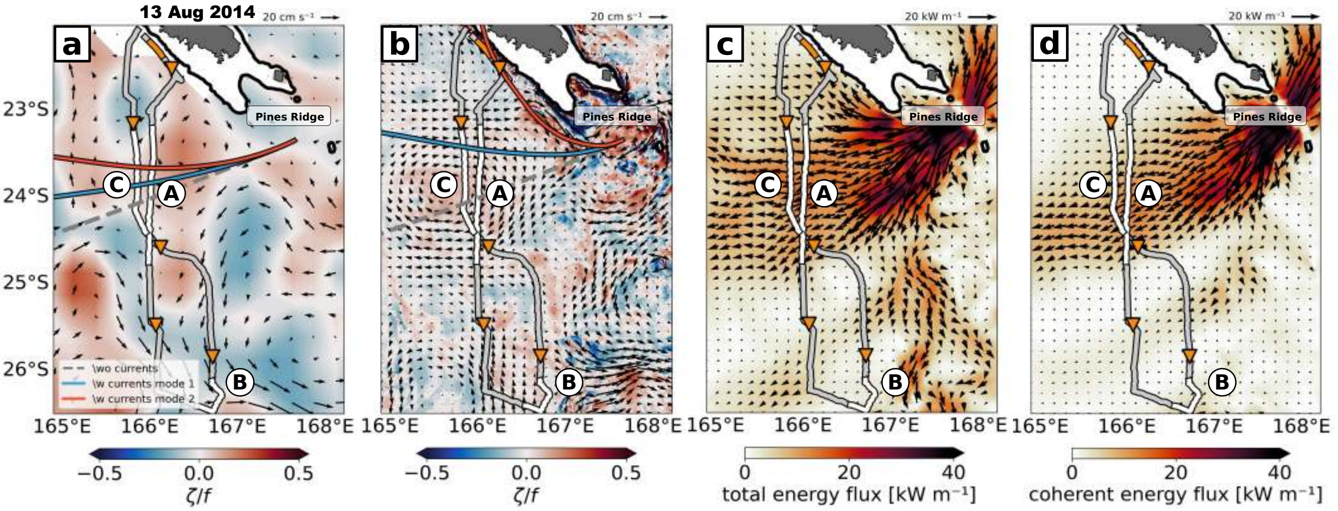

**Figure 9.** Zoom into the glider study site showing (a) the geostrophic surface currents (vectors) as obtained from satellite altimetry (CMEMS) with the underlying relative vorticity normalized by $f$ (shading) for a daily-mean snapshot on 13 August 2014. (b) Same as (a) but showing the depth-averaged currents as obtained from CALEDO60. Also shown is the modeled (c) total semidiurnal energy flux, and (d) coherent semidiurnal energy flux for a daily-mean snapshot on 13 August 2014. The ray-tracing results in (a) and (b) show the theoretical ray path of a semidiurnal tidal beam for mode 1 (blue), mode 2 (red) that initiate from the generation site south of New Caledonia close to the Pines Ridge. The no-current scenario is also given (dashed gray). The orange triangles are as in Fig. 3. The glider position and the distance covered on 13 August 2014 are shown by highlighted orange bar along the glider track. The thick black line is the 100 m depth contour representative for the New Caledonian lagoon.

propagates southwestward corresponding to the well-confined propagation direction of the coherent tidal beam. Including the background currents introduces differing ray paths between glider observations and the full-model pseudo glider, as explored next.

On 13 August 2014, the mesoscale eddy field as given by satellite altimetry derived geostrophic surface currents has only little impact on the semidiurnal ray path, though it is slightly refracted northward. Mode 2 is more affected than mode 1 (Fig. 9a). This contrasts with the numerical simulation, which is characterized by a mesoscale cyclone close to the New Caledonia coast and the Pines Ridge, and which quickly refracts the semidiurnal ray northward (Fig. 9b). This aligns with the modeled semidiurnal energy flux along the western New Caledonia coast (Fig. 9c) and corresponds with the full-model pseudo glider sampling at the start of the section in mid-August (see Fig. 8b,f).

On 3 October 2014, the ray tracing provides a similar picture (Fig. 10). Even though a mesoscale anticyclone governs the background velocity field in the satellite altimetry observations, the tidal beam orientation is barely affected (Fig. 10a). Further, it is refracted equatorward, away from the glider sampling and therefore not captured by the glider observations early October (see Fig. 8a,e). This is opposed to the numerical simulation in which a predominant anticyclone is located just off the New Caledonia coast and the Pines Ridge (Fig. 10b). In propagation direction, the semidiurnal rays are increasingly refracted southward (poleward) with increasing distance to the initialization region as they pass through the mesoscale eddy. Again, mode 2 is more affected than mode 1. Particularly, the theoretical beam is refracted toward the full-model pseudo glider sampling

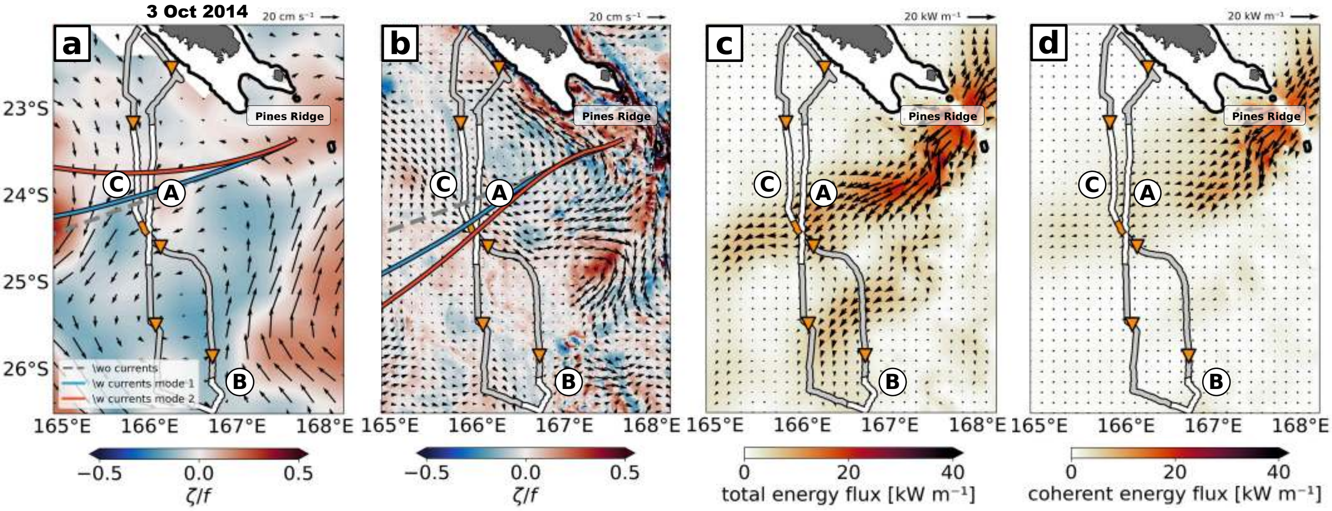

**Figure 10.** Same as Fig. 9, but for a daily-mean snapshot on 3 October 2014. Note that the semidiurnal energy flux underlies spring-neap tide variability, which explains the differences in the modeled coherent energy flux for different snapshots. The difference between the total and coherent energy flux can be associated with tidal incoherence.

**Table 1.** Explained variability of $h^{\mathrm{1000m}}_{\mathrm{model}}$, $h^{\mathrm{1000m}}_{\mathrm{pseudo}}$, $h^{\mathrm{full}}_{\mathrm{model}}$ using a first-mode approximation ($\Sigma^{1}_{n=1}$) and a two-mode approximation ($\Sigma^{2}_{n=1}$), referenced to $h^{\mathrm{full}}_{\mathrm{model}}$.

| | $h^{\mathrm{1000m}}_{\mathrm{model}}$ | $h^{\mathrm{1000m}}_{\mathrm{pseudo}}$ | $h^{\mathrm{full}}_{\mathrm{pseudo}}\Sigma^{1}_{n=1}$ | $h^{\mathrm{full}}_{\mathrm{pseudo}}\Sigma^{2}_{n=1}$ |
|---|---|---|---|---|
| $\gamma$ (cov(...,$h^{\mathrm{full}}_{\mathrm{model}}$)/var($h^{\mathrm{full}}_{\mathrm{model}}$)) | 0.91 | 0.78 | 0.85 | 0.93 |

location, providing a possible explanation for the premature detection of the tidal beam early October (see Fig. 8b,f), which in the no-currents scenario is predicted at later stage $O(1\ \mathrm{d})$ along the glider track.

From an in-situ perspective, the glider observations have provided first insight into the spatio-temporal variability of the internal tide south of New Caledonia. Largely dominated by the semidiurnal tide, and especially mode 1, the glider observations also highlight the realism of internal tides in the regional numerical simulation in the upper 1000 m. We conclude that major discrepancies between glider observations and the full-depth pseudo glider are not associated with deficiencies in the glider sampling or the model's realism of simulating internal tides, but rather tidal incoherence. Here, we showed that tidal incoherence is largely depending on the background eddy field. In the following, we attempt to derive how the vertical structure of the semidiurnal internal tide in the upper 1000 m expresses in the steric SSH signature.

### 4.4 To what extent can we use gliders to account for internal tide induced steric height?

The ability of the glider to retrieve the steric SSH signature of the semidiurnal tide is investigated using the regional numerical simulation only. We first use the full-model pseudo glider simulation to evaluate the limitations due to the depth extent of the glider measurements. We compare (1) steric height inferred from the semidiurnal vertical displacements within the upper 1000 m only with, ($h^{\mathrm{1000m}}_{\mathrm{pseudo}}$) with (2) steric heigth inferred from the semidiurnal vertical displacements in the upper 1000 m extrapolated to full-depth using projections on climatological modes 1-2 ($h^{\mathrm{full}}_{\mathrm{pseudo}}$). To evaluate the errors in steric SSH reconstruction arising from the irregular glider sampling, we finally use the full-model steric SSH, which is free of any glider-like sampling. We remind the reader, that the full-model steric SSH was initially computed from vertical profiles of specific volume anomaly, integrated over the water column, bandpassed in the semidiurnal frequency band, and interpolated onto the glider's profile location and time stamp at mid-depth. It can be regarded as ground truth for steric SSH within the upper 1000 m ($h^{\mathrm{1000m}}_{\mathrm{model}}$), and the full-depth range ($h^{\mathrm{full}}_{\mathrm{model}}$). They are respectively confronted with $h^{\mathrm{1000m}}_{\mathrm{pseudo}}$ and $h^{\mathrm{full}}_{\mathrm{pseudo}}$ to assess the glider's ability to deduce steric SSH (see Sect. 3.6).

We first analyze $h^{\mathrm{full}}_{\mathrm{model}}$ along the glider track (Fig. 11a). The semidiurnal internal tide expresses in steric height with magnitudes of up to 5 cm. It is primarily associated with the locations that have been identified as segments of elevated tidal activity (A, B, C in Fig. 3 and Fig. 8). The overwhelming majority of the semidiurnal steric SSH, i.e. 91 % ($h^{\mathrm{1000m}}_{\mathrm{model}}$), is attributed to the contribution of internal tide vertical displacements in the upper 1000 m (Fig. 11a and Table 1).

The pseudo glider steric height ($h^{\mathrm{1000m}}_{\mathrm{pseudo}}$) follows the overall pattern of $h^{\mathrm{1000m}}_{\mathrm{model}}$ (Fig. 11a). However, it only accounts for 78 % of explained variance when referenced to $h^{\mathrm{full}}_{\mathrm{model}}$ (Table 1). This is, by construction, only due to the irregular glider sampling.

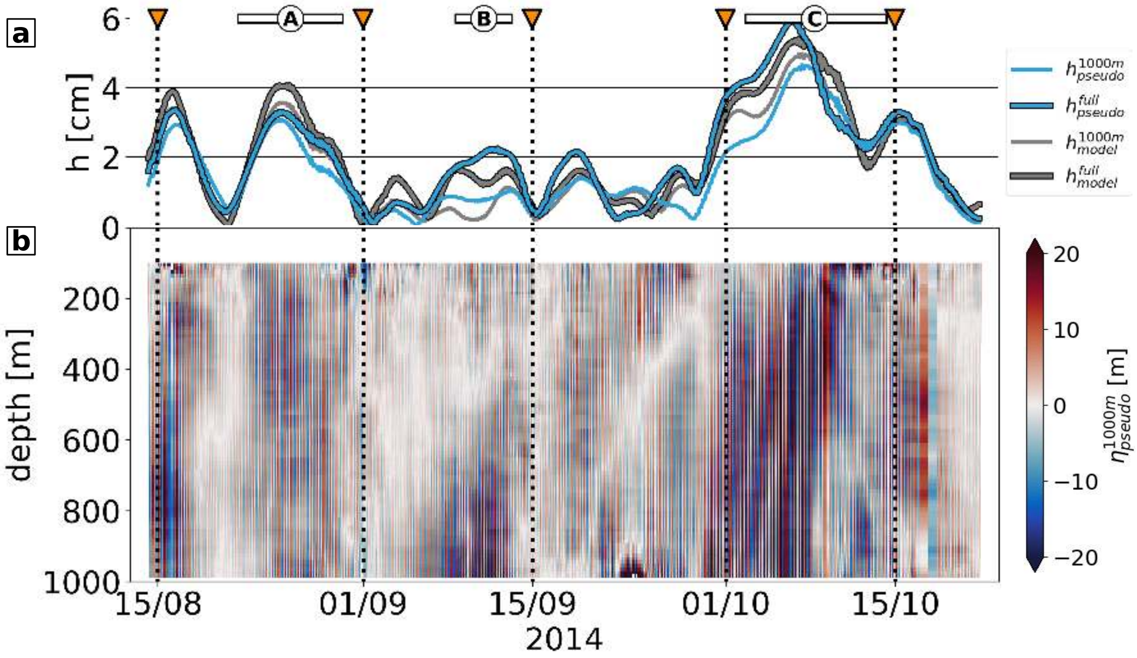

**Figure 11.** (a) Semidiurnal amplitude for the pseudo glider steric height $h^{\mathrm{1000m}}_{\mathrm{pseudo}}$ (blue), the full-depth pseudo glider steric height $h^{\mathrm{full}}_{\mathrm{pseudo}}$ (blue with black outlines), and the full-model steric height $h^{\mathrm{1000m}}_{\mathrm{model}}$ for the upper 1000 m (gray) and $h^{\mathrm{full}}_{\mathrm{model}}$ for the full-depth range (gray with black outlines. Here, we use a two-mode approximation to calculate $h^{\mathrm{full}}_{\mathrm{pseudo}}$. (b) Pseudo glider vertical displacements $\eta^{\mathrm{1000m}}_{pseudo}$ which are ultimately used to compute $h^{\mathrm{1000m}}_{\mathrm{pseudo}}$ and $h^{\mathrm{full}}_{\mathrm{pseudo}}$.

Projecting the pseudo-glider vertical displacements onto climatological modes and extrapolating to the full-depth range can partly account for missing variance due to the glider sampling limited to the upper 1000 m. Using a two-mode approximation, we are able to increase the explained variance from 78 % ($h^{\mathrm{1000m}}_{\mathrm{pseudo}}$) to 93 % ($h^{\mathrm{full}}_{\mathrm{pseudo}}\Sigma^{2}_{n=1}$, Table 1). From a qualitative perspective, this is also apparent in Fig. 11a, where $h^{\mathrm{full}}_{\mathrm{pseudo}}$ provides an overall improvement and compares better with $h^{\mathrm{full}}_{\mathrm{model}}$. Projecting on the two lowest modes gives the best result. Though, projecting on the first mode only increases the variance from 78 % to 85 % ($h^{\mathrm{full}}_{\mathrm{pseudo}}\Sigma^{1}_{n=1}$,Table 1).

### 4.5 How do the glider measurements compare with satellite altimetry?

Using a two-mode approximation, the methodology described in Sect. 3.6.1 and applied to the full-model pseudo glider in the previous section is now applied to the glider observations. The full-depth glider steric height $h^{\mathrm{full}}_{\mathrm{obs}}$ is compared to the empirical SSH estimates from HRET (see Sect. 2.4) to evaluate the spatio-temporal variability of the semidiurnal internal tide from a satellite altimetry point of view (Fig. 12). Note that in contrast to the glider observations, HRET represents exclusively the coherent tide. Within this context, we utilize HRET to reconstruct the semidiurnal signals composed of the M2 and S2 tides, for modes 1-2, prior to interpolating the resulting time series to align with the time stamps along the glider's track.

The overall spatio-temporal variability of the full-depth glider steric height corresponds well with HRET (Fig. 12a and Fig. 12c). Particularly, the spatio-temporal signals in the segments denoted as A and C are well captured, even though reduced in amplitude (maximum 2 cm in HRET compared to maximum 4 cm in the glider observations). Good agreement is also seen for the signature mid-to-end September. Contrarily, the distinct signal, denoted as B, which exhibits a surface signature of almost

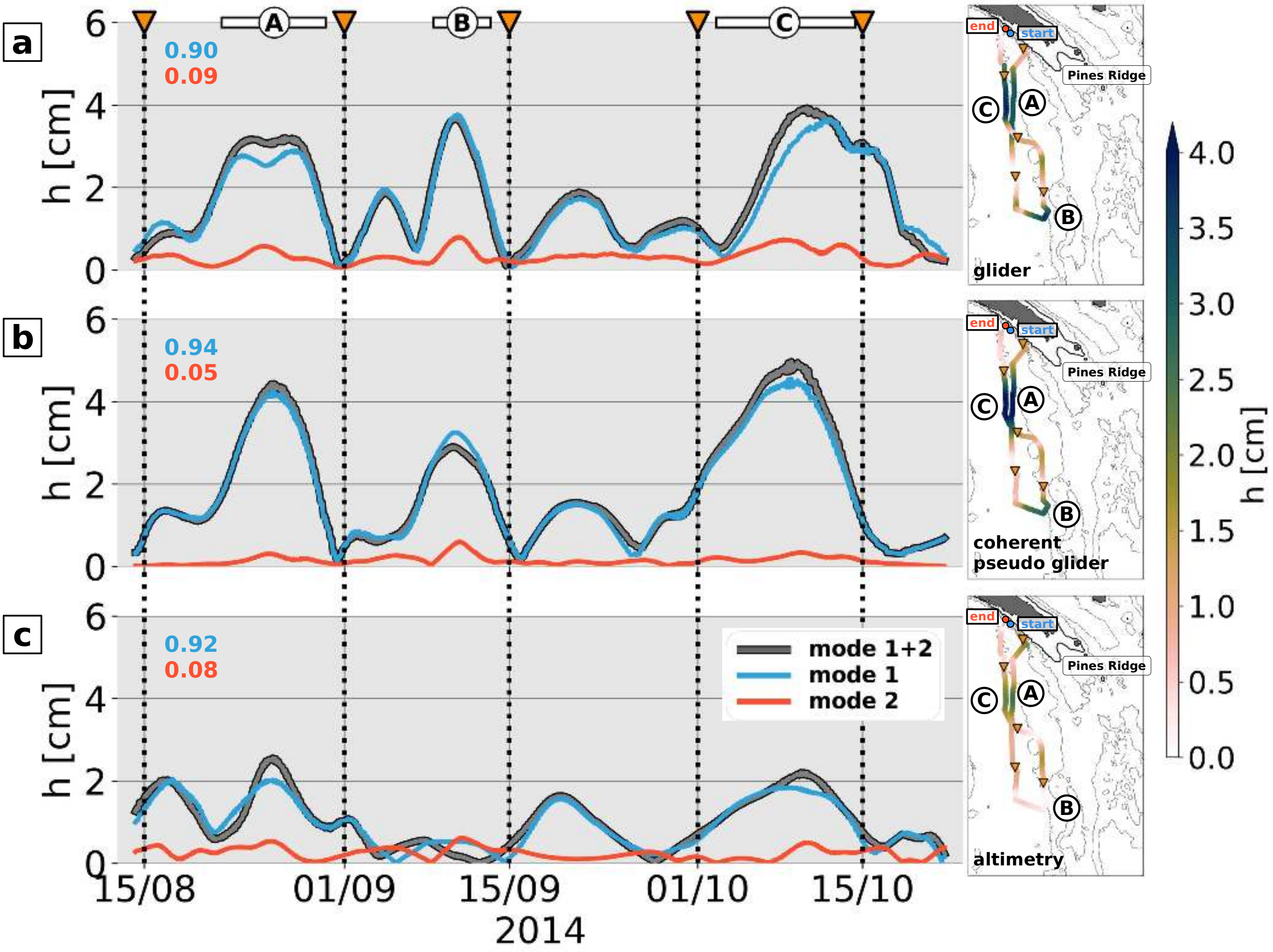

**Figure 12.** Semidiurnal amplitude in along glider-track direction of (a) the full-depth glider steric height using a two-mode approximation $(h^{\text{full}}_{\text{obs}}\Sigma^{2}_{n=1})$, (b) the full-depth coherent pseudo glider steric height $h^{\text{full}}_{\text{coh}}$, and (c) HRET SSH for the baroclinic tide (gray with black outlines), mode 1 (blue), and mode 2 (red). The modal contribution of modes 1-2 are given in the upper left corners. The right panels of (a)-(c) show the baroclinic amplitude in along glider-track direction on a spatial map.

4 cm in the glider observations is entirely absent in HRET.

Here, we build upon the full-depth steric height signal of the semidiurnal coherent internal tide, which sheds light on the coherent tide along the glider track (Fig. 12b). It corresponds with the full-depth glider steric height (Fig. 12a), suggestive for prevailing tidal coherence in the glider observations. Specifically, the tidal signature at B is also present indicating at this location a potential misrepresentation of the coherent tide in HRET. This is not necessarily surprising considering that the glider sampling can access finer spatial scales. In contrast, the correct representation of the internal tide field in HRET is largely depending on the available satellite tracks for a given area that are subject to a point-wise harmonic analysis, followed by a plane-wave fit in overlapping patches. Moreover, fine-scale features may be smoothed out due to the mapping technique applied in HRET Zaron (2019).

Despite apparent deviations in the spatio-temporal variability, it is noteworthy that the modal structures, specifically modes 1-2, match closely among in-situ observations, numerical modeling, and altimetry. Among all the products, mode 1 predominates the signal accounting for $>$90 % of the baroclinic variance.

## 5 Summary and Discussion

In-situ observations from autonomous glider data have been previously exploited to infer internal-tide dynamics while providing important information on the spatial variability of high-frequency motion at fine spatial scales. Recent numerical modeling results have identified New Caledonia as a significant hot spot for internal tide generation, characterized by the westward propagation of tidal energy within well-defined tidal beams (Bendinger et al., 2023).

In this study, we inferred internal tides from a glider survey carried out in the area south of New Caledonia in the southwestern tropical Pacific over the course of $>$2 months. Spatio-temporal variability of the diurnal and semidiurnal internal tide is deduced by fitting a sinusoidal function on vertical isopycnal displacements using a least-squares method in 3-day running windows, from the surface down to 1000 m depth. The glider observations suggest a pronounced dominance of the semidiurnal tide, which can explain locally up to 80 % of the total variance of the vertical displacements. This semidiurnal dominance is in agreement with the model results in Bendinger et al. (2023). Further, our analysis reveals distinct segments of elevated tidal activity expressed by semidiurnal isopycnal displacements exceeding 20 m.

Glider observations are combined with four-dimensional regional model output. This approach serves a dual purpose. First, glider observations assess the realism of internal-tide dynamics in the numerical simulation. Second, the four-dimensional regional model outputs are used to assess the glider's capability within the upper 1000 m to infer internal tides and to retrieve their associated SSH signature. To do so, we modelled the trajectory and sampling of a pseudo glider using the hourly output of the regional model linearly interpolated onto the glider time series with identical spatio-temporal sampling.

The observed spatio-temporal variability of the semidiurnal internal tide closely matches with the results of the pseudo glider demonstrating an overall similarity in location, magnitude, and vertical structure of the tidal signatures. The previously performed tidal analysis in Bendinger et al. (2023) suggests that these signatures sampled by both the glider and pseudo glider are associated with westward propagation of semidiurnal tidal energy, which can be traced back to the internal tide generation south/southeast of New Caledonia.

We attribute the major discrepancies between glider observations and the full-model pseudo glider to tidal incoherence induced by eddy-internal tide interactions. This is supported by a simplified ray tracing analysis which tracks the propagation of a semidiurnal ray for a given initialization region and propagation angle. In propagation direction, the semidiurnal ray may be refracted associated with variations in phase velocity induced by the background currents of mesoscale eddies affecting the tidal ray orientation. Specifically, the theoretical pathway of the refracted tidal beam intersects with the glider track, coinciding with the location and time stamp where and when departure from tidal coherence is expected in the pseudo glider.

Using glider observations alone, a single glider mission is not sufficient to distinguish between tidal coherence and incoherence. Surely, repeated glider sections would provide additional information on the coherent and incoherent variance while allowing for a model validation with more confidence. Whatsoever, we note that the complementary analysis of in-situ observations and numerical modeling can be used as a potential approach to infer where tidal incoherence may occur in glider observations. Though, this approach is limited to regions with available high-resolution model output including tidal forcing, which overlaps in space and time with glider data.

Through the vertical integration of vertical displacements, we established a connection between the semidiurnal internal tide's signature in the upper 1000 m and its expression in SSH. In the semidiurnal frequency band, the upper 1000 m in the pseudo glider simulation accounts for 78 % of the full-depth steric height variance. To encompass the entire depth range of the semidiurnal tide, extending beyond 1000m, we projected the pseudo glider's vertical displacements onto a set of climatological modes before extrapolating vertically. Utilizing a two-mode approximation, we increased the explained variance from 78 % to 93 % percent. When projecting on the first mode only, the explained variance increased to 85 %. Steric height, derived from the glider observations, shows good agreement with empirical SSH estimates from satellite altimetry, indicating the prevalence of tidal coherence during the glider mission. We point out that the methodology accounting for the full-depth range needs validation, especially in regions where high modes play a more significant role.

Linking interior dynamics of fine-scale physics with the expression in SSH has important implications for SWOT, as SWOT's SSH measurements encompass both balanced and unbalanced motions. In-situ observations play a crucial role in disentangling the physical processes in the three-dimensional water column. We have demonstrated that gliders can serve as an effective in-situ platform for extracting the SSH signature of internal tides, particularly in the area south of New Caledonia. This region became the focus of a dedicated in-situ field campaign in boreal spring 2023, conducted within the framework of the SWOT AdAC consortium. The primary objective of this campaign was to comprehensively survey fine-scale physics, including internal tides, along two SWOT swaths during the fast-sampling phase. In an area of increased tidal activity, the SWOT observability of mesoscale and submesoscale dynamics may suffer from the dominance of unbalanced motion. For obvious reasons, the analyzed glider in this study cannot be used for the direct validation of SWOT.

Preliminary analyses using conventional satellite altimetry products have revealed the presence of multiple mesoscale eddies and frontal zones in along glider-track direction. Future work will focus on the residual signal seen in Fig. 7c and the investigation whether the glider observations corrected for the diurnal and semidiurnal tide can indeed be attributed to mesoscale and submesoscale dynamics (e.g. eddies and front), as suggested by satellite altimetry.

*Code and data availability.* This study has been conducted using EU Copernicus Marine Service Information CMEMS (https://doi.org/10.48670/moi-00148). Climatological hydrography data were obtained from CARS (http://www.marine.csiro.au/~dunn/cars2009/). The tidal analysis was performed using the COMODO-SIROCCO tools, which are developed and maintained by the SIROCCO national service (CNRS/INSU). SIROCCO is funded by INSU and Observatoire Midi-Pyrénées/Université Paul Sabatier and receives project support from CNES, SHOM, IFREMER, and ANR (https://sirocco.obs-mip.fr/other-tools/prepost-processing/comodo-tools/). The publicly available HRET products from Edward Zaron (Zaron, 2019) were downloaded from https://ingria.ceoas.oregonstate.edu/~zarone/downloads.html. The numerical model configuration (CALEDO60) used in this study is introduced and described in detail in Bendinger et al. (2023). The data to reproduce the figures can be found in Bendinger (2023a) with the associated scripts in Bendinger (2023b). The ray tracing algorithm is described in full detail in Sect. 3b in Rainville and Pinkel (2006).

*Author contributions.* AB performed the analysis and drafted the manuscript under the supervision of LG and SC. LR and CV provided the ray tracing algorithm and contributed to its analysis. GS contributed by providing preliminary code on the extraction of internal tides using glider observations. FD, FM, and J-LF were involved in the preparation of the spray glider deployments, the data collection and data postprocessing. All co-authors reviewed the manuscript and contributed to the writing and final editing.

*Competing interests.* The authors declare that they have no conflict of interest.

*Acknowledgements.* This research has been supported by the Université Toulouse III - Paul Sabatier (grant from the Ministère de l'Enseignement supérieur de la Recherche et de l'Innovation, MESRI) carried out within the PhD program of AB at the Faculty of Science and Engineering and the Doctoral School of Geosciences, Astrophysics, Space and Environmental Sciences (SDU2E). Sophie Cravatte, Lionel Gourdeau, Fabien Durand, Frédéric Marin are funded by the Institut de Recherche pour le Développement (IRD); Luc Rainville is supported by NASA (award number 80NSSC20K1132); Clément Vic is funded by the Institut français de recherche pour l'exploitation de la mer (IFREMER); Guillaume Sérazin and Jean-Luc Fuda are funded by CNRS. This study has been partially supported through the grant EUR TESS N°ANR-18-EURE-0018 in the framework of the Programme des Investissements d'Avenir. This work is a contribution to the joint CNES-NASA project SWOT in the Tropics and is supported by the French TOSCA (la Terre, l'Océan, les Surfaces Continentales, l'Atmosphère) program and the French national program LEFE (Les Enveloppes Fluides et l'Environnement). We would like to thank the IMAGO team who were deeply involved in the preparation of the first spray glider deployments around New Caledonia from 2010 to 2013. We also thank Kyla Drushka for her invitation to host AB at the Applied Physics Laboratory in Seattle, USA, her time and fruitful discussions which significantly contributed to this study.

## References

Arbic, B. K.: Incorporating tides and internal gravity waves within global ocean general circulation models: A review, Progress in Oceanography, 206, 102 824, https://doi.org/10.1016/j.pocean.2022.102824, 2022.

Arbic, B. K., Alford, M. H., Ansong, J. K., Buijsman, M. C., Ciotti, R. B., Farrar, J. T., Hallberg, R. W., Henze, C. E., Hill, C. N., Luecke, C. A., et al.: Primer on global internal tide and internal gravity wave continuum modeling in HYCOM and MITgcm, New frontiers in operational oceanography, pp. 307–392, https://doi.org/10.17125/gov2018.ch13, 2018.

Baines, P. G.: On internal tide generation models, Deep Sea Research Part A. Oceanographic Research Papers, 29, 307–338, https://doi.org/10.1016/0198-0149(82)90098-X, 1982.

Ballarotta, M., Ubelmann, C., Pujol, M.-I., Taburet, G., Fournier, F., Legeais, J.-F., Faugère, Y., Delepoulle, A., Chelton, D., Dibarboure, G., et al.: On the resolutions of ocean altimetry maps, Ocean Science, 15, 1091–1109, https://doi.org/10.5194/os-15-1091-2019, 2019.

Bell Jr, T.: Topographically generated internal waves in the open ocean, Journal of Geophysical Research, 80, 320–327, https://doi.org/10.1029/JC080i003p00320, 1975.

Bendinger, A.: To what extent can we use glider observations to infer internal tides and their steric sea surface height signature south of New Caledonia? [Data set], Zenodo, https://doi.org/10.5281/zenodo.10174169, 2023a.

Bendinger, A.: To what extent can we use glider observations to infer internal tides and their steric sea surface height signature south of New Caledonia? [Software], Zenodo, https://doi.org/10.5281/zenodo.10174311, 2023b.

Bendinger, A., Cravatte, S., Gourdeau, L., Brodeau, L., Albert, A., Tchilibou, M., Lyard, F., and Vic, C.: Regional modeling of internal-tide dynamics around New Caledonia – Part 1: Coherent internal-tide characteristics and sea surface height signature, Ocean Science, 19, 1315–1338, https://doi.org/10.5194/os-19-1315-2023, 2023.

Debreu, L., Vouland, C., and Blayo, E.: AGRIF: Adaptive grid refinement in Fortran, Computers & Geosciences, 34, 8–13, https://doi.org/10.1016/j.cageo.2007.01.009, 2008.

Duda, T. F., Lin, Y.-T., Buijsman, M., and Newhall, A. E.: Internal tidal modal ray refraction and energy ducting in baroclinic Gulf Stream currents, Journal of Physical Oceanography, 48, 1969–1993, https://doi.org/10.1175/JPO-D-18-0031.1, 2018.

Durand, F., Marin, F., Fuda, J.-L., and Terre, T.: The east caledonian current: a case example for the intercomparison between altika and in situ measurements in a boundary current, Marine Geodesy, 40, 1–22, https://doi.org/10.1080/01490419.2016.1258375, 2017.

d'Ovidio, F., Pascual, A., Wang, J., Doglioli, A. M., Jing, Z., Moreau, S., Grégori, G., Swart, S., Speich, S., Cyr, F., et al.: Frontiers in fine-scale in situ studies: Opportunities during the SWOT fast sampling phase, Frontiers in Marine Science, 6, 168, https://doi.org/10.3389/fmars.2019.00168, 2019.

Fu, L.-L., Alsdorf, D., Morrow, R., Rodriguez, E., and Mognard, N.: SWOT: the Surface Water and Ocean Topography Mission: wide-swath altimetric elevation on Earth, Tech. rep., Pasadena, CA: Jet Propulsion Laboratory, National Aeronautics and Space …, http://hdl.handle.net/2014/41996, 2012.

Ganachaud, A., Cravatte, S., Melet, A., Schiller, A., Holbrook, N., Sloyan, B., Widlansky, M., Bowen, M., Verron, J., Wiles, P., et al.: The S outhwest P acific O cean circulation and climate experiment (SPICE), Journal of Geophysical Research: Oceans, 119, 7660–7686, https://doi.org/10.1002/2013JC009678, 2014.

Gill, A. E.: Atmosphere-ocean dynamics, vol. 30, Academic press, 1982.

Guo, Z., Wang, S., Cao, A., Xie, J., Song, J., and Guo, X.: Refraction of the M2 internal tides by mesoscale eddies in the South China Sea, Deep Sea Research Part I: Oceanographic Research Papers, 192, 103 946, https://doi.org/10.1016/j.dsr.2022.103946, 2023.

Hall, R. A., Aslam, T., and Huvenne, V. A.: Partly standing internal tides in a dendritic submarine canyon observed by an ocean glider, Deep Sea Research Part I: Oceanographic Research Papers, 126, 73–84, https://doi.org/10.1016/j.dsr.2017.05.015, 2017.

Hall, R. A., Berx, B., and Damerell, G. M.: Internal tide energy flux over a ridge measured by a co-located ocean glider and moored acoustic Doppler current profiler, Ocean Science, 15, 1439–1453, https://doi.org/doi.org/10.5194/os-15-1439-2019, 2019.

Hersbach, H., Bell, B., Berrisford, P., Hirahara, S., Horányi, A., Muñoz-Sabater, J., Nicolas, J., Peubey, C., Radu, R., Schepers, D., et al.: The ERA5 global reanalysis, Quarterly Journal of the Royal Meteorological Society, 146, 1999–2049, https://doi.org/10.1002/qj.3803, 2020.

Johnston, T. S. and Rudnick, D. L.: Trapped diurnal internal tides, propagating semidiurnal internal tides, and mixing estimates in the California Current System from sustained glider observations, 2006–2012, Deep Sea Research Part II: Topical Studies in Oceanography, 112, 61–78, https://doi.org/10.1016/j.dsr2.2014.03.009, 2015.

Johnston, T. S., Rudnick, D. L., Alford, M. H., Pickering, A., and Simmons, H. L.: Internal tidal energy fluxes in the South China Sea from density and velocity measurements by gliders, Journal of Geophysical Research: Oceans, 118, 3939–3949, https://doi.org/10.1002/jgrc.20311, 2013.

Johnston, T. S., Rudnick, D. L., and Kelly, S. M.: Standing internal tides in the Tasman Sea observed by gliders, Journal of Physical Oceanography, 45, 2715–2737, https://doi.org/10.1175/JPO-D-15-0038.1, 2015.

Keppler, L., Cravatte, S., Chaigneau, A., Pegliasco, C., Gourdeau, L., and Singh, A.: Observed characteristics and vertical structure of mesoscale eddies in the southwest tropical Pacific, Journal of Geophysical Research: Oceans, 123, 2731–2756, https://doi.org/10.1002/2017JC013712, 2018.

Locarnini, M., Mishonov, A., Baranova, O., Boyer, T., Zweng, M., Garcia, H., Seidov, D., Weathers, K., Paver, C., and Smolyar, I.: World ocean atlas 2018, volume 1: Temperature, NOAA Atlas NESDIS 81, p. 52pp, https://archimer.ifremer.fr/doc/00651/76338/, 2018.

Lyard, F. H., Allain, D. J., Cancet, M., Carrère, L., and Picot, N.: FES2014 global ocean tide atlas: design and performance, Ocean Science, 17, 615–649, https://doi.org/10.5194/os-17-615-2021, 2021.

Morrow, R., Fu, L.-L., Ardhuin, F., Benkiran, M., Chapron, B., Cosme, E., d'Ovidio, F., Farrar, J. T., Gille, S. T., Lapeyre, G., et al.: Global observations of fine-scale ocean surface topography with the Surface Water and Ocean Topography (SWOT) mission, Frontiers in Marine Science, 6, 232, https://doi.org/10.3389/fmars.2019.00232, 2019.

Nash, J. D., Kelly, S. M., Shroyer, E. L., Moum, J. N., and Duda, T. F.: The unpredictable nature of internal tides on continental shelves, Journal of Physical Oceanography, 42, 1981–2000, https://doi.org/10.1175/JPO-D-12-028.1, 2012.

Park, J.-H. and Watts, D. R.: Internal tides in the southwestern Japan/East Sea, Journal of Physical Oceanography, 36, 22–34, https://doi.org/10.1175/JPO2846.1, 2006.

Rainville, L. and Pinkel, R.: Propagation of low-mode internal waves through the ocean, Journal of Physical Oceanography, 36, 1220–1236, https://doi.org/10.1175/JPO2889.1, 2006.

Rainville, L., Lee, C. M., Rudnick, D. L., and Yang, K.-C.: Propagation of internal tides generated near Luzon Strait: Observations from autonomous gliders, Journal of Geophysical Research: Oceans, 118, 4125–4138, https://doi.org/10.1002/jgrc.20293, 2013.

Ray, R. D. and Zaron, E. D.: M2 internal tides and their observed wavenumber spectra from satellite altimetry, Journal of Physical Oceanography, 46, 3–22, https://doi.org/10.1175/JPO-D-15-0065.1, 2016.

Ridgway, K., Dunn, J., and Wilkin, J.: Ocean interpolation by four-dimensional weighted least squares—Application to the waters around Australasia, Journal of atmospheric and oceanic technology, 19, 1357–1375, https://doi.org/10.1175/1520-0426(2002)019<1357:OIBFDW>2.0.CO;2, 2002.

Rudnick, D. L.: Ocean research enabled by underwater gliders, Annual review of marine science, 8, 519–541, https://doi.org/10.1146/annurev-marine-122414-033913, 2016.

Sérazin, G., Marin, F., Gourdeau, L., Cravatte, S., Morrow, R., and Dabat, M.-L.: Scale-dependent analysis of in situ observations in the mesoscale to submesoscale range around New Caledonia, Ocean Science, 16, 907–925, https://doi.org/10.5194/os-16-907-2020, 2020.

Smith, K. S. and Vallis, G. K.: The scales and equilibration of midocean eddies: Freely evolving flow, Journal of Physical Oceanography, 31, 554–571, https://doi.org/10.1175/1520-0485(2001)031<0554:TSAEOM>2.0.CO;2, 2001.

Testor, P., De Young, B., Rudnick, D. L., Glenn, S., Hayes, D., Lee, C. M., Pattiaratchi, C., Hill, K., Heslop, E., Turpin, V., et al.: OceanGliders: a component of the integrated GOOS, Frontiers in Marine Science, 6, 422, https://doi.org/10.3389/fmars.2019.00422, 2019.

Vic, C., Garabato, A. C. N., Green, J. M., Spingys, C., Forryan, A., Zhao, Z., and Sharples, J.: The lifecycle of semidiurnal internal tides over the northern Mid-Atlantic Ridge, Journal of Physical Oceanography, 48, 61–80, https://doi.org/10.1175/JPO-D-17-0121.1, 2018.

Zaron, E. D.: Baroclinic tidal sea level from exact-repeat mission altimetry, Journal of Physical Oceanography, 49, 193–210, https://doi.org/10.1175/JPO-D-18-0127.1, 2019.

Zhao, Z., Alford, M. H., MacKinnon, J. A., and Pinkel, R.: Long-range propagation of the semidiurnal internal tide from the Hawaiian Ridge, Journal of Physical Oceanography, 40, 713–736, https://doi.org/10.1175/2009JPO4207.1, 2010.

Zhao, Z., Alford, M. H., Girton, J. B., Rainville, L., and Simmons, H. L.: Global observations of open-ocean mode-1 M2 internal tides, Journal of Physical Oceanography, 46, 1657–1684, https://doi.org/10.1175/JPO-D-15-0105.1, 2016.

Zilberman, N., Merrifield, M., Carter, G., Luther, D., Levine, M., and Boyd, T. J.: Incoherent nature of M 2 internal tides at the Hawaiian Ridge, Journal of physical oceanography, 41, 2021–2036, https://doi.org/10.1175/JPO-D-10-05009.1, 2011.

Zweng, M., Seidov, D., Boyer, T., Locarnini, M., Garcia, H., Mishonov, A., Baranova, O., Weathers, K., Paver, C., Smolyar, I., et al.: World ocean atlas 2018, volume 2: Salinity, NOAA Atlas NESDIS 82, p. 50pp, https://archimer.ifremer.fr/doc/00651/76339/, 2019.

### III.3.3 Conclusion

In-situ glider observations provided important insight into internal-tide dynamics south of New Caledonia. We showed that glider observations are not only suitable as an in-situ platform to capture high-frequency motion at small horizontal and vertical scales, but also they prove useful in validating regional model output.

In both in-situ observations and regional model output, the semidiurnal tide is strongly dominant and governed by low-vertical mode-1 dynamics. Enhanced tidal signals show an overall similarity in the location, magnitude, and vertical structure, associated with the westward propagating tidal beam initiated at the internal tide generation hot spot south of New Caledonia. Discrepancies between in-situ observations and regional model output are primarily linked with the stochastic nature of the mesoscale eddy field which causes phase variations along the glider track.

While our analysis is based on a single glider mission, it gives us confidence in the regional model's representation of internal-tide dynamics. Certainly, further glider observations are essential to enhance the statistical significance of these findings.

This study's primary contribution lies in linking the vertical structure of internal tides to overall SSH variability. Our method proves to be highly suitable when compared to SSH estimates from conventional satellite altimetry products. Notably, glider data offer distinct advantages over conventional satellite altimetry by providing access to smaller spatial scales and insights into the total internal tide field, including both coherent and incoherent components. This methodology holds promise for applications within the SWOT-AdAC framework and associated in-situ field campaigns, aiming to capture the vertical structure of fine-scale physics and understand its expression in SWOT SSH data.

## III.4 Impact of internal tides on cross-scale energy exchanges

### III.4.1 Introduction

In Sect. III.2, we have discussed the role of mesoscale activity on the propagation of internal tides and tidal incoherence. It remains to be investigated what role internal tides have on mesoscale to submesoscale features and on the modulation of energy pathways across spatial scales. This was initially addressed in the beginning of this manuscript driven by the question on how the oceanic energy budget is closed and climate equilibrium achieved (see Sect. I.1). Among the potential ways to address this question, the focus here is limited on the energy transfer among different spatial scales modulated by internal tides. To do that, we use the twin numerical simulation around New Caledonia, one with tidal forcing and the other without (see Sect. II.1).

The analysis focuses on a square-shaped domain southwest of New Caledonia, characterized by a significant energy flux of internal tides of 10-20 kW $m^{-1}$ into an intense mesoscale and submesoscale regime with eddy kinetic energy signatures >400 $cm^2$ $s^{-2}$ (see Fig. III.12a). It's worth emphasizing that this area drastically differs from the region north of New Caledonia, i.e. equatorward, where a strong internal tide energy flux is also present but within a more linear dynamical regime. Therefore, it is essential to recognize that the conclusions drawn from this analysis may not necessarily apply to the entire regional domain surrounding New Caledonia. The disparities observed between these different regions will be addressed in future work.

Initial insights into the role of internal tides on mesoscales were provided by the time series of mesoscale eddy kinetic energy, spatially averaged for the full-regional CALEDO60 domain for both the simulation with and without tides (Fig. III.12b).

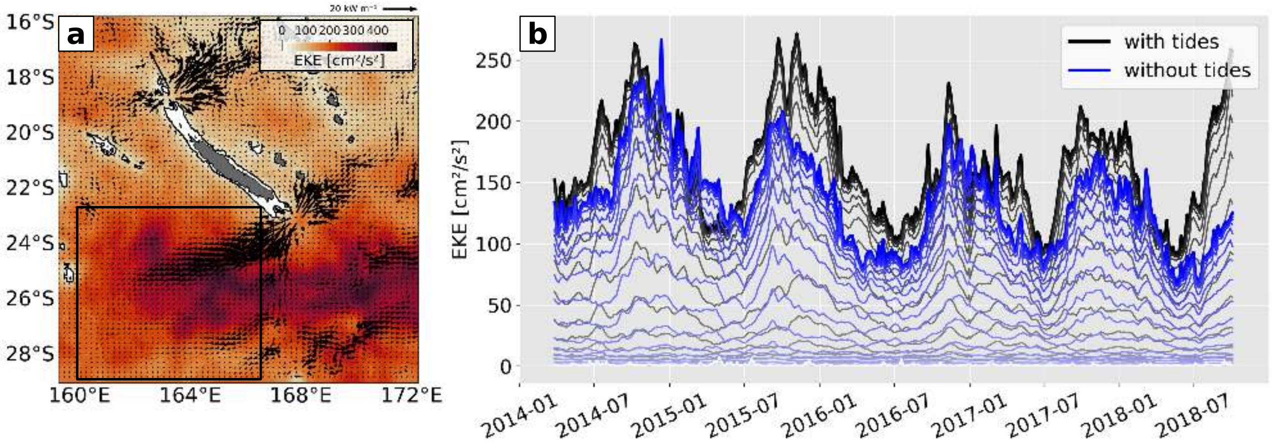

**Figure III.12: (a)** Surface mesoscale eddy kinetic energy (shading) overlaid by the depth-integrated semidiurnal coherent internal tide energy flux vectors (vectors). Eddy kinetic energy was computed from 5-day mean horizontal velocities, binned on a regular two-dimensional 1/4° grid before applying a highpass-filter with a cut-off frequency of 180 days. The black represents the square-shaped domain, as described in Sect. II.5 for which seasonal kinetic energy and spectral energy fluxes were calculated. **(b)** Domain-averaged time series of mesoscale eddy kinetic energy (model years 2014-2018) for selected depth levels from the surface to the bottom for the simulation with (black) and without tides (blue). The thick lines represent surface eddy kinetic energy. The increasing transparency of the thin lines indicates increasing depth.

Mesoscale eddy kinetic energy clearly exhibits a seasonal cycle and is enhanced in the simulation with tides, particularly during the southern hemisphere summer months. Due to time constraints, these preliminary results could not be explored in full detail. However, as a first step, some effort has been made to investigate the impact of tides on kinetic energy and energy flux spectra and their seasonal modulations.

This work was conducted to a large part during a two-month research visit in spring 2022 in the framework of this thesis at the Department of Earth and Environmental Sciences at the University of Michigan, Ann Arbor, USA, in active collaboration with Brian Arbic. The results provide interesting insights into how cross-scale energy fluxes can be significantly affected in regions with pronounced tidal activity. Though, we note that this work should be considered as preliminary as it is subject to undergoing/future work. In essence, this chapter aims to provide an overview of the current findings. Additionally, it highlights the promising opportunities that emerge alongside the comprehensive description of internal tide dynamics around New Caledonia obtained during this thesis, with the goal of advancing our understanding of nonlinear scale-interaction and energy exchanges. We will address the following questions, as stated in Sect. I.5:

**D** **Impact of internal tides on cross-scale energy exchanges**

**1)** Do internal tides affect cross-scale energy exchanges by modifying kinetic energy fluxes?

**2)** Do internal tides affect the length scale at which the inverse energy cascade transitions into the forward energy cascade?

We first give insight into seasonal variations of the mesoscale and submesoscale circulation before presenting the seasonally varying dominant scales of motion and the imprint of tidal motion by studying kinetic energy spectra. Using spectral energy flux calculations, we then highlight the seasonal importance of internal tides in promoting an energy transfer toward smaller scales.

### III.4.2 Mesoscale/submesoscale seasonality

We start by describing the seasonality of mesoscale/submesoscale features, the associated mechanisms, and the way how internal tides modify this seasonality. We specifically focus on the southern hemisphere summer (January-March, JFM) and winter (July-September, JAS) months. Snapshots of surface relative vorticity for summer (JFM) and winter (JAS) are shown for the square-shaped domain southwest of New Caledonia for both simulations with and without tides (Fig. III.13). We first analyze the simulation without tides before looking at the simulation with tides.

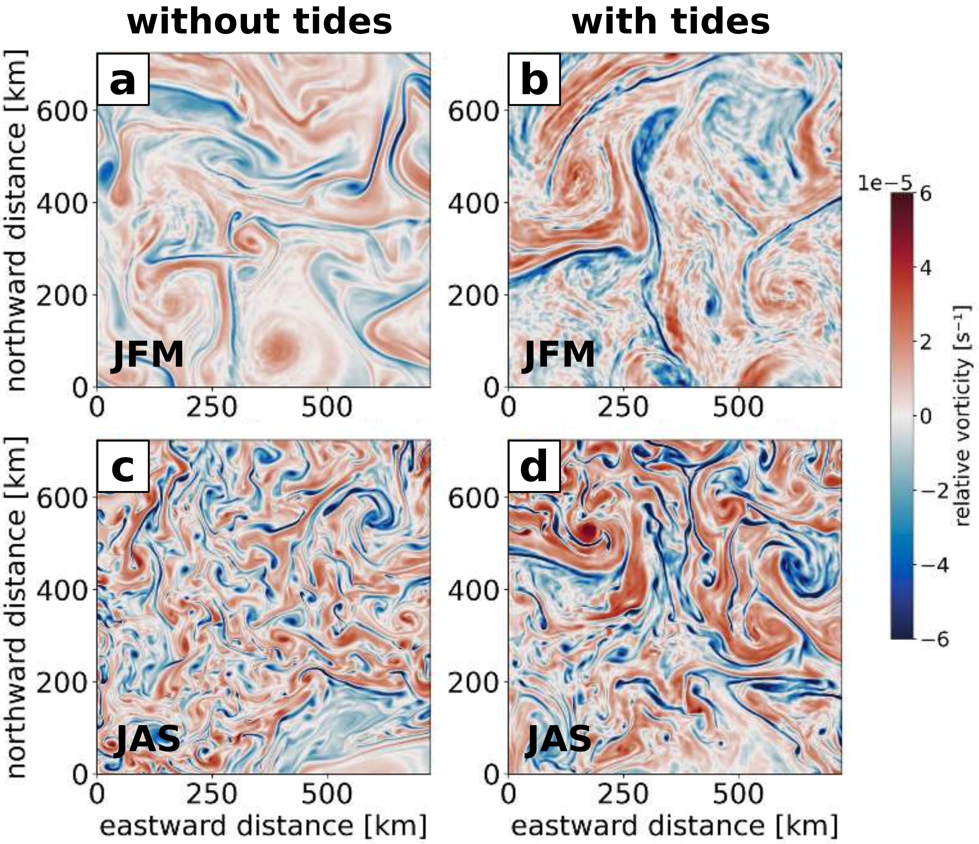

**Figure III.13:** Representative snapshots of summer (JFM) and winter (JAS) surface relative vorticity for a square-shaped domain southwest of New Caledonia, i.e. **(a)** summer without tides, **(b)** summer with tides, **(c)** winter without tides, **(d)** winter with tides.

Seasonal differences in the horizontal flow field highlight a dominant mesoscale regime in summer and a more active submesoscale field in winter, during which the scales of motion significantly reduce, accompanied by increasing turbulence (Fig. III.13a,c). Seasonality in submesoscale motion is often associated with mixed layer instabilities due to increasing available potential energy when the mixed layer deepens (see Sect. I.1.2.2). Here, the mixed layer depth is determined by the depth at which the density increases by 0.03 kg $m^{-3}$ from the surface, using a reference depth of 10 m. The monthly-mean mixed layer depth is shown for the simulation without tides (model year 2014) and a climatology (de Boyer Montégut et al., 2007) in Fig. III.14a. First, CALEDO60 and the climatology exhibit good agreement. Second, mixed layer depth peaks in the winter months when submesoscale activity is fully developed,

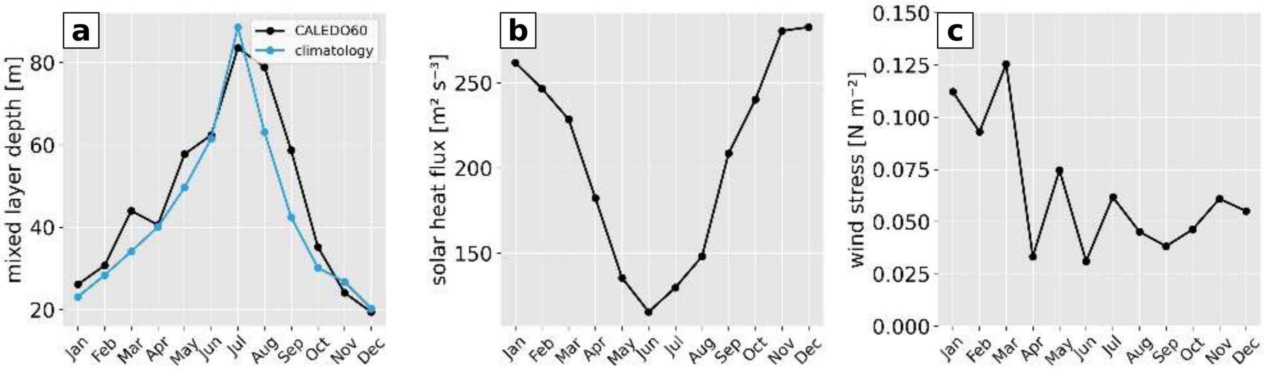

**Figure III.14:** Seasonal cycle (model year 2014) of **(a)** mixed layer depth (black: CALEDO60 without tides, blue: climatology), **(b)** solar heat flux, and **(c)** wind stress, spatially averaged for the square-shaped domain southwest of New Caledonia (Fig. II.8).

suggesting mixed layer instabilities as a potential mechanism. The deepening of the mixed layer in winter appears to be more related to a minimum atmospheric heat forcing than to a strengthening of the wind stress, as it is the case for mid-latitude dynamics (Fig. III.14b). In this tropical area, wind stress forcing seems to play a minor role in driving mixed layer depth, as it increases in summer months when the mixed layer depth is shallow (Fig. III.14c).

As introduced in Sect. II.4, several diagnostics exists which help quantifying submesoscale motion. Here, we consider surface relative vorticity $\zeta$, horizontal divergence $\delta$, the lateral buoyancy gradient $|\nabla_h b|$, and frontogenesis $F$. All these indicators follow a seasonal cycle and peak in the winter months (Fig. III.15). Elevated variability of relative vorticity $\zeta$ indicates the emergence of submesoscale coherent vortices accompanied by large $Ro$ due to increasing importance of fluid inertia (Fig. III.15a). They may arise from mixed layer instabilities and/or frontogenesis. Frontogenesis $F$ along-side horizontal divergence $\delta$, and the lateral buoyancy gradient $|\nabla_h b|$ is primarily indicative of frontal dynamics (Fig. III.15b-d).

Typically, frontogenesis itself does not feature temporal variations since it is induced by the mesoscale strain field, which does not undergo a strong seasonal cycle (Callies et al., 2015). However, it can be favored through mixed layer instabilities and the induced strain by mixed layer submesoscale eddies. In turn, frontogenesis facilitated by mixed layer stabilities may enhance the seasonal cycle at mesoscales through the absorption of submesoscale mixed layer eddies by the mesoscale eddy field (Schubert et al., 2020). Here, the mesoscale eddy field is most energetic in spring to summer months. This seasonal cycle is reported to arise from baroclinic instabilities of the vertically aligned SEC(/SCJ)-STCC current system (see Sect. I.4.1, Qiu and Chen, 2004). The associated shear is maximum in the summer months, followed by a 3-month lag of peaking eddy kinetic energy (Fig. I.34). We note that the role of frontogenesis in the seasonal cycle of mesoscale eddy kinetic energy needs further investigations.

The impact of the internal tide field on the mesoscale and submesoscale fields is qualitatively illustrated in Fig. III.13b,d. During the summer months when the mesoscale

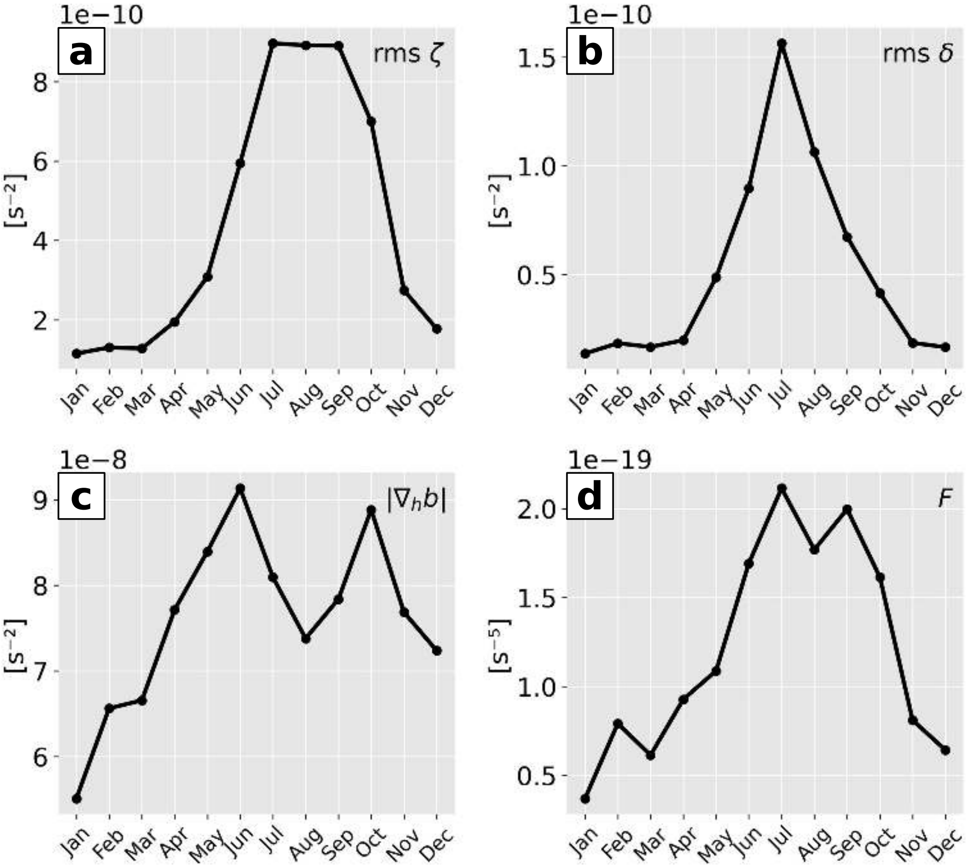

**Figure III.15:** Seasonal cycle (model year 2014) of monthly **(a)** relative vorticity $\zeta$ and **(b)** horizontal divergence variance $\delta$ (root-mean-square variability), spatially averaged for the square-shaped domain southwest of New Caledonia (Fig. II.8). **(c)**-**(d)** same as **(a)**-**(b)**, but representing the seasonal cycle of monthly mean values of the lateral buoyancy gradient $|\nabla_h b|$ and frontogenesis $F$, respectively.

regime dominates, the simulation with tides exhibits more energetic structures and finer scales. Conversely, in the winter months when the submesoscale regime prevails, the simulation with tides displays a mixture of mesoscale and submesoscale structures. We did not have the time to push forward this analysis by looking at the different submesoscale quantities as for the simulation without tides. Nevertheless, at this stage, it is evident that the internal tide field has a clear impact on mesoscale activity, resulting in a global effect of enhancing energetics and minimizing seasonal contrasts. However, the quantification of this impact remains to be explored.

Here, the main message is that southwest of New Caledonia submesoscale turbulence undergoes strong seasonality peaking in the southern hemisphere winter months, likely driven by mixed layer instabilities and frontogenesis. The comparison of the simulation with and without tides illustrates the impact of the internal tide field in reducing the seasonal contrast. Next, we will look into kinetic energy spectra to shed light on how energy is redistributed and transferred among different spatial scales. We refer to Sect. II.5 for a more detailed description of the theory and methodology.

### III.4.3 Seasonal kinetic energy spectra

Power spectral density of horizontal kinetic energy (see Sect. II.5.1) is shown as a function of depth for summer (JFM) and winter (JAS) for the square-shaped domain southwest of New Caledonia for both simulations with and without tides in Fig. III.16. For both simulations, kinetic energy is most energetic in the mesoscale band (70-250 km) and features little to no seasonal variations. Further, there is little depth dependence.

Spectral variance decreases towards smaller wavelengths, where seasonal variations and a surface intensification are evident. The energy spectra are specifically shown for depths 20 m, 200 m, and 400 m to better illustrate the seasonal variations and the differences between the simulation with and without tides in Fig. III.17. The main findings are given below.

In the simulation without tides, seasonal variations are clearly evident at all wavelengths <150 km at 20 m (Fig. III.17a) and 200 m depth (Fig. III.17b) with more energy during the winter months. They are most pronounced near the surface and vanish at 400 m depth (Fig. III.17). This corresponds with surface-intensified submesoscale motions being more energetic in the winter months. In the simulation with tides, seasonal variations at wavelengths <150 km are also apparent, even if they are less important and confined to the near-surface layer (Fig. III.17a). While energy levels in the winter months between the two simulations are comparable, the discrepancies are particularly evident during the summer months with more energy in the simulation with tides when the eddy kinetic energy is at its lowest level.

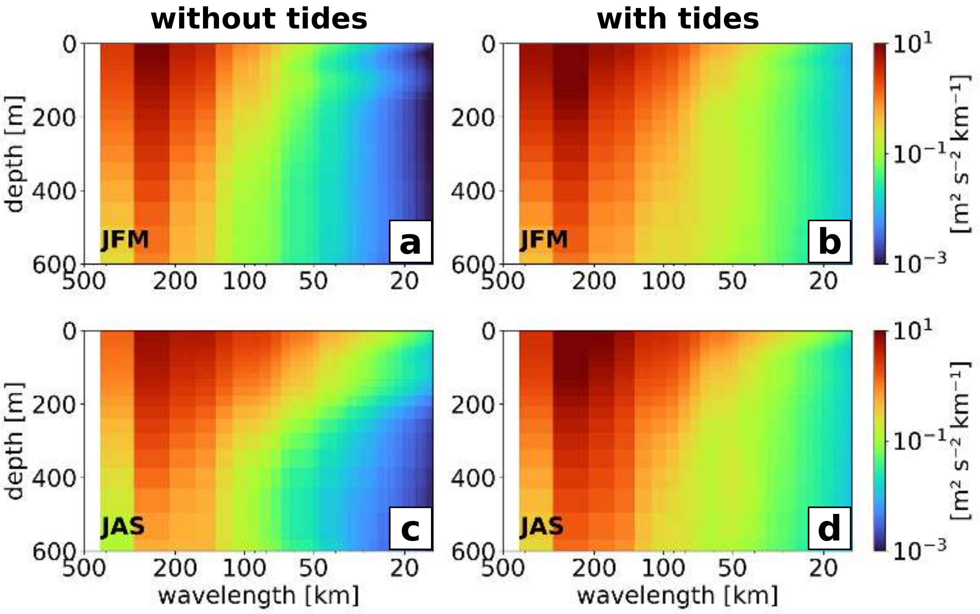

**Figure III.16:** Power spectral density of horizontal kinetic energy as a function of depth for summer (JFM) and winter months (JAS), i.e. **(a)** summer without tides, **(b)** summer with tides, **(c)** winter without tides, **(d)** winter with tides. The spectra are cut off at 15 km wavelength for visualization reasons. Further, this wavelength represents the minimum length scale that can be resolved by the model.

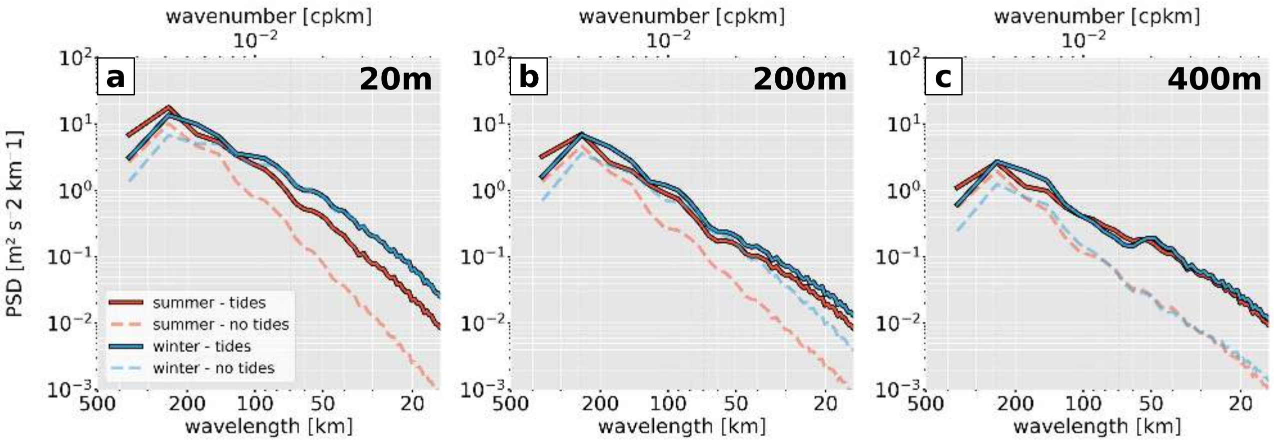

**Figure III.17:** Horizontal kinetic energy spectra at **(a)** 20 m, **(b)** 200 m, and **(c)** 400 m depth for summer with tides (red solid), summer without tides (red dashed), winter with tides (blue solid), and winter without tides (blue dashed). The spectra are cut off at 15 km wavelength for visualization reasons. Further, this wavelength represents the minimum length scale that can be resolved by the model.

At greater depth (400 m), seasonal variations are no more visible, but the simulation with tides is more energetic across all spatial scales (Fig. III.17c) highlighting the importance of energetic unbalanced motions such as internal tides at fine scales. Interestingly, compared to the simulation without tides the simulation with tides contains more energy at large mesoscales (>200 km), regardless of the depth being considered.

This suggests that internal tides play a crucial role in raising energy levels both at the mesoscale and submesoscale. Near the surface, this effect is only apparent in the summer months, when submesoscale energy levels are reduced. In the winter months, wavelengths <100 km are largely dominated by submesoscale processes, e.g. mixed layer instabilities and frontogenesis (Fig. III.17a). In depths where submesoscale motions diminish, internal tides raise energy levels in both seasons across all scales to 15 km wavelengths and below (Fig. III.17c).

### III.4.4 Seasonal spectral energy fluxes

To address the question regarding the impact of internal tides on energy pathways, we have computed spectral kinetic energy fluxes, presented as a function of depth for summer (January-March, JFM) and winter (July-September, JAS) for both simulations with and without tides (Fig. III.18). Briefly, positive values indicate a forward energy cascade, signifying energy transfer from larger to smaller scales. Conversely, negative values represent an inverse energy cascade, indicating energy transfer from smaller to larger scales. The transition from the inverse to the forward cascade is marked by a zero flux.

In the simulation without tides, we find that both the inverse and forward energy cascades are notably strong during the winter months and relatively weaker during the summer months. The signal is more pronounced near the surface but extends to depths below 200 m for the inverse cascade. In contrast, in the simulation with tides, the inverse cascade during the winter months appears less prominent and does not

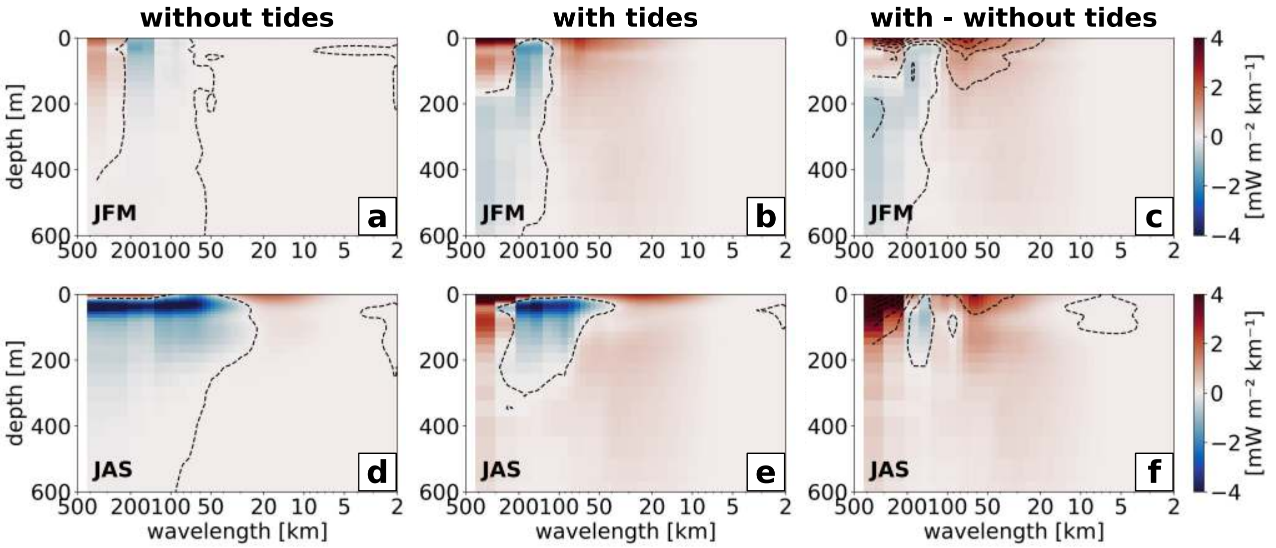

**Figure III.18:** Power spectral density of horizontal kinetic energy as a function of depth for summer (JFM) and winter months (JAS), i.e. **(a)** summer without tides, **(b)** summer with tides, **(c)** difference between **(b)** and**(a)** and **(d)** winter without tides, **(e)** winter with tides, **(f)** difference between **(e)** and**(d)**. Positive values indicate a forward cascade, negative values an inverse cascade.

extend as deeply. However, during the summer months, we now find a strong forward cascade, particularly within the upper 200 m of the water column. Similarly to the kinetic energy spectra, the spectral energy fluxes are specifically shown for depths 20 m, 200 m, and 400 m to better illustrate the seasonal variations and the difference between the simulation with and without tides (Fig. III.19).

Spectral kinetic fluxes quickly vanish with increasing depth. In the simulation with tides, even though strongly reduced in amplitude compared to the near surface, a forward cascade is present at depth independently of the season. This suggests that internal tides are an important energy source at mid-depths and in the deeper ocean to provide a route to energy dissipation via the forward cascade away from the surface and lateral boundaries.

The most notable discovery is that the inclusion of tidal forcing leads to a significant forward cascade near the surface during the summer months for wavelengths around and below 100 km (Fig. III.19a), whereas when tidal forcing is omitted, the forward cascade is almost non-existent. This is in good agreement with the findings in Ajayi (2020) which also reported a strong forward cascade in summer in the simulation with tides. The length scale that separates the forward and inverse cascade is well above 100 km wavelength.

In the winter months, the forward cascade is assumed to be governed by submesoscale processes that dominate over unbalanced wave motion during that time of the year. Tidal forcing seems to play a secondary role as the forward cascade is only slightly increased in amplitude. Though, tidal forcing shifts the transition scale between the inverse and forward cascade towards larger wavelengths from 30 km to 50 km. Further, the inverse cascade is reduced in amplitude.

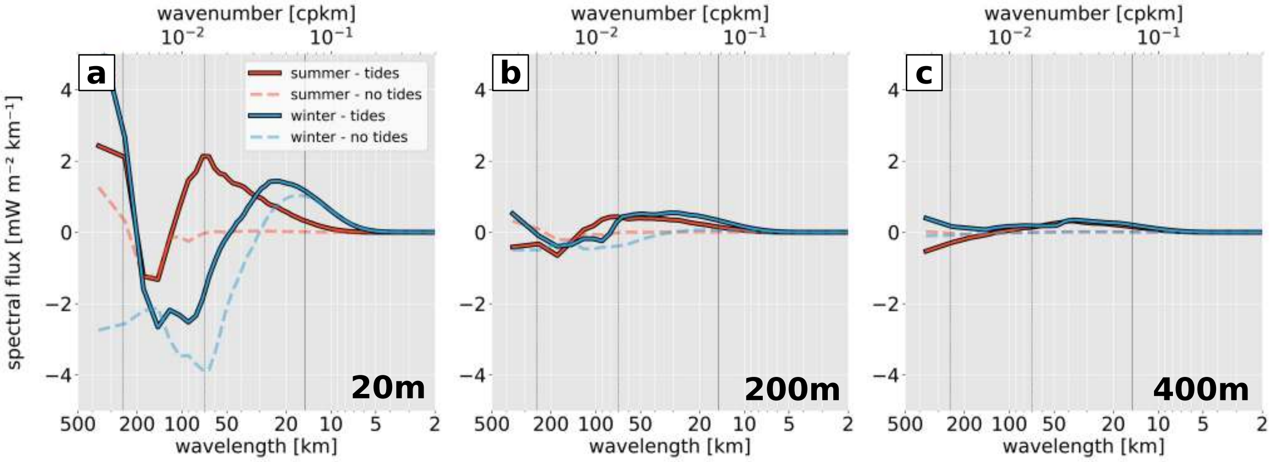

**Figure III.19:** Spectral kinetic energy fluxes at **(a)** 20 m, **(b)** 200 m, and **(c)** 400 m depth for summer with tides (red solid), summer without tides (red dashed), winter with tides (blue solid), and winter without tides (blue dashed). Positive values indicate a forward cascade, negative values an inverse cascade.

### III.4.5 Conclusion

We showed that kinetic energy spectra and spectral energy flux undergo strong temporal variations, attributed to internal tides and submesoscale processes which are seasonally out of phase. These preliminary results can be briefly summarized as follows.

- In summer months, internal tides induce a strong forward energy cascade at scales around and below 100 km wavelength and near the surface. The forward cascade is supposedly driven by tidal forcing alone as submesoscale motion is largely suppressed during this season and for the region southwest of New Caledonia.
- Contrarily, in the winter months the forward cascade is primarily driven by submesoscale motions induced by increased mixed layer instabilities and surface-intensified frontogenesis. However, tidal forcing shifts the transition scale, i.e. the length scale at which the inverse cascade transitions into a forward cascade towards larger wavelengths from 30 km to 50 km. Tidal forcing, thus, limits the inverse cascade.

These are interesting results showing that high-frequency motions such as internal tides can provide a route to energy dissipation by reversing the inverse energy cascade into a forward energy cascade. The findings are in partial agreement with Ajayi (2020) which also revealed a pronounced forward cascade during summer months when tides are included. Our results diverge from Ajayi (2020) in that, in the simulation with tides, the transition scale shifts towards larger wavelengths in the winter months. In Ajayi (2020), the transition scale is unaffected by the inclusion of tides.

There are several open questions that concern the actual physical processes that break the geostrophically constrained flow and facilitate the energy transfer to smaller scales at wavelengths around and below 100 km and a pathway toward energy dissipation. Thomas and Daniel (2021) suggested two-way wave-balance energy exchanges that

result in dissipation of geostrophic balanced energy. The extent to which waves extract energy from the balanced flow depends though on the wave field's energy level. In this context, the study region around New Caledonia represents a unique opportunity as internal tides are very energetic and interactions with the mesoscale background circulation persist throughout the year.
We made use of the spectral approach to compute cross-scale energy exchanges. This approach is associated with relatively low computational costs, but it comes with disadvantages closely linked to the two-dimensional Fourier transformation as discussed by Schubert et al. (2020): 1) It assumes that turbulence is isotropic and homogeneous. 2) A fixed value is assigned at the small-scale end, i.e. zero flux at the smallest investigated scale. 3) It is often associated with high noise levels. An alternative approach exist in the so-called coarse-graining approach. The basic concept of coarse-graining involves the application of a low-pass filter on a horizontal field by applying a convolution with a circular top-hat kernel to filter out scales smaller than a specified diameter $L$, allowing for the analysis of energy flux between specific scale ranges. Typically, this is done for a range of length scales. Coarse-graining is not associated with the disadvantages listed for the spectral approach above. Though, the coarse-graining approach is computationally more expensive, i.e. computational expenses scale with $L^2$ (Schubert et al., 2020). Nonetheless, it may provide insightful around New Caledonia as, in contrast to the spectral approach, it can be applied to the whole domain, i.e. every grid point. Islands and or shallow bathymetry can be treated as cells with zero velocity.

The above preliminary results are subject to future work which involves the explicit separation of the horizontal field into the rotational and divergent flow using the Helmholtz decomposition method. Further, to make the results statistically more significant, we seek longer time series. Here, we focused on seasonal spectra based on and limited to a single full-model calendar year, similar to the remaining analyses during this thesis. Future efforts will take into account the multi-year simulation (model years 2014-2018).

# Conclusion and Perspectives

## Conclusion

The objective of this thesis was to address internal tides and their interactions with the mesoscale and submesoscale circulation around New Caledonia, motivated by understanding how such events will express in SSH of the SWOT satellite mission. This thesis is to large extent based on a tailored high-resolution regional numerical modeling effort, but observations from autonomous underwater gliders play an important role to get insight from an in-situ perspective. As a crucial initial step, a comprehensive description of the internal-tide dynamics around New Caledonia was required. This task deserves attention by itself given the growing interest within the oceanographic community in internal tides and their role for vertical mixing processes with implications for the global oceanic energy budget and marine ecosystems.

We gave a detailed overview of internal tide generation, dissipation, and tidal energy propagation before shifting the focus on SWOT's SSH observability of both mesoscale

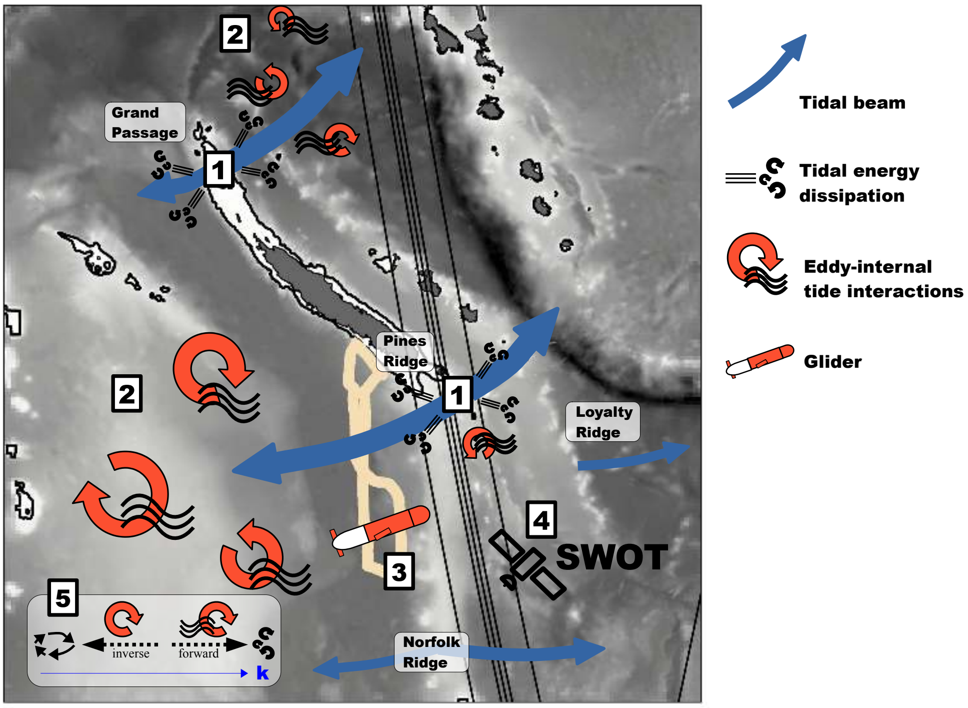

**Figure 5:** Summarizing schematic of the main thesis results. **[1]** The major internal tide generation hot spots are located north and south of New Caledonia associated with both strong energy dissipation in the near-field and pronounced tidal energy propagation in narrow beams. **[2]** In the far field, internal tides interact with the mesoscale eddy field leading to tidal incoherence. **[3]** SSH variance of unbalanced motions (internal tides) dominates over balanced motions (mesoscale to submesoscale) with important implications for the observability of mesoscale and submesoscale dynamics in an area with strong tidal activity such as New Caledonia. **[4]** Important insight on internal-tide dynamics is given from an in-situ perspective by autonomous underwater gliders which is in good agreement with the model results and satellite altimetry. **[5]** Internal tides may play a crucial role in providing a route to energy dissipation by extracting energy from the geostrophically balanced flow, i.e. reversing the inverse cascade to a forward cascade (thin blue arrow indicates direction of increasing wavenumber).

and submesoscale geostrophic dynamics (balanced) and ageostrophic dynamics (unbalanced) from submesoscale motions and internal gravity waves. We then inferred internal-tide dynamics from a unique data set of glider observations, which also served as an important tool to assess regional numerical simulation output. Finally, we gave preliminary insight into the impact of internal tides around New Caledonia on cross-scale energy exchanges. The main findings of this thesis are summarized in the schematic in Fig. 5 and listed below by referring individually to each research question labeled A, B, C, and D as stated in Sect. I.5.

## A Coherent internal-tide dynamics and sea surface height signature around New Caledonia

**1) What regions and bathymetric structures are subject to strong internal- tide generation around New Caledonia?**

Internal tide generation is largely dominated by the semidiurnal M2 tide, explaining more than 80 % of the total barotropic-to-baroclinic tidal energy conversion. Hot spots of internal tide generation are closely linked with the complex bathymetry associated with continental slopes, shelf breaks, ridges, and seamounts around New Caledonia. Internal tide generation is pronounced near Grand Passage (2.17 GW) to the north and near Pines Ridge (3.92 GW) to the south of New Caledonia (see **[1]** in Fig. 5). Together, these two regions account for roughly 40 % of tidal energy conversion in the regional model domain. An important conclusion is that the bulk of baroclinic energy is generated in shallow waters around 500 m depth and on critical to supercritical slopes - regions of internal tide generation which are typically not well captured by linear semi-analytical models.

**2) In what regions do we expect elevated tidal energy dissipation? What fraction of locally generated tidal energy is dissipated in the near-field?**

Tidal energy dissipation is found throughout the domain. However, it is strongest near the generation sites and across the shelf break. In tidal energy propagation direction, dissipation is enhanced along the barrier reef and at bathymetric obstacles such as seamounts. We found elevated ratios between local tidal energy dissipation and generation of up to 50 %, implying that internal tides are a source of near-field vertical mixing (see **[1]** in Fig. 5). The underlying mechanisms remain to be investigated in detail. Though, wave-topography interactions and scattering to higher modes are believed to play major role in the high dissipation rates. Tidal energy dissipation was only estimated from the coherent tide analysis. It must be assumed that a non-negligible fraction of the coherent dissipation is not associated with true dissipation but with a loss of coherence or an energy transfer to the incoherent tide.

**3) Is the internal tide dominated by low- or high-vertical mode dynamics?**

New Caledonia represents a hot spot of mode-1 internal tide generation explaining 75 % of the energy conversion in the regional domain and locally up to 85 %. This is in agreement with semi-analytical theory as low-mode tidal dynamics are favored at tall and steep slopes, and in shallow depths. Low-mode tidal energy propagates away from the generation sites with baroclinic energy fluxes of up to 30 kW $m^{-1}$ in well-defined, narrow beams toward the open ocean (see **[1]** in Fig. 5). The Loyalty Ridge poses an exception as modes $>1$ slightly increase in importance.

**4) How do internal tides express in SSH variance and at what wavelengths? How do SSH variance and wavelengths compare with balanced motion?**
The internal tide has a strong signature in SSH that may reach amplitudes >6 cm for mode 1 and 1-2 cm for mode 2 close to the internal tide generation sites. Away from the generation site, the internal tide SSH features multiple interference patterns with tidal waves emanating from multiple sources. In specific regions, the internal tide exhibits wavelengths similar to those of balanced motion, with peaks occurring at approximately 160 km for mode 1 and 80 km for mode 2, respectively. Further, internal tide motion dominates SSH variance over balanced motion for scales smaller than 200 km, implying that SWOT SSH observability of balanced motions may be challenging around New Caledonia. We defined SSH observability of balanced motion for wavelengths where SSH variance of subinertial processes is higher than superinertial processes. A correction for the coherent internal tide was suggested to improve the SSH observability of balanced motion, which shifts the length scale between subinertial and superinertial motion, i.e the transition scale, to smaller wavelengths. Our analysis showed that this simple approach can increase SSH observability of balanced motion from 200 km to below 100 km.

## B Tidal incoherence and implications for sea surface height observability around New Caledonia

**1) What regions are expected to feature increased levels of tidal incoherence around New Caledonia and what is its fraction to the total tidal variance?**
We have shown that tidal incoherence for the semidiurnal energy flux features large spatial variations around New Caledonia and is generally of higher importance south/southwest of New Caledonia. As the internal tide tide propagates toward the open ocean, it becomes increasingly incoherent and may account for up to 25 % of the total variance within 200 km distance to the generation site. In far-field at >500 km distance, the incoherent tide tends to be the dominant component. Though, the total internal tide becomes significantly weaker at distances >800 km ($\sim$1 kW $m^{-1}$).

**2) What are sources of tidal incoherence around New Caledonia both close to the generation site and toward the open ocean?**
Mesoscale eddy variability is suggested to be the main source for tidal incoherence around New Caledonia (see **[2]** in Fig. 5). In the far-field, mesoscale currents cause a refraction of the tidal beam accompanied by changing group and phase speeds as found by a ray tracing method that tracks the horizontal propagation of a tidal ray in the presence of depth-independent background currents. Generally, tidal incoherence was found to express by increasing phase variability as the tidal beam propagates through the mesoscale eddy field. Mesoscale eddy variability may also play a role in the near-field by inducing temporal variations of the barotropic-to-baroclinic conversion term. In contrast to the far-field, tidal incoherence in the near-field is suggested

to be primarily driven by mesoscale-eddy induced stratification changes.

**3) How does tidal incoherence manifest in SSH? How much does it contribute to SSH variance? What are potential implications for SSH observability of balanced motion?**
The incoherent internal tide has an overall widespread signature in SSH around New Caledonia with maximum amplitudes of 2 cm. Despite the reduced amplitude in comparison to the coherent internal tide, it represents a non-negligible fraction in SSH variance that may dominate over balanced motions at wavelengths $<$100 km depending on the region and season. At scales below 100 km, it is the incoherent tide in addition to motions at near-inertial and supertidal frequencies that limit SWOT's SSH observability of mesoscale and submesoscale motions. The key takeaway is that in regions with both strong tidal activity and mesoscale eddy variability, a comprehensive understanding of the incoherent tide and its manifestation in SSH becomes crucial for the success of interpreting future SWOT measurements (see **[3]** in Fig. 5).

## C Internal tides inferred from autonomous underwater gliders around New Caledonia

**1) Are glider observations around New Caledonia suitable to infer internal-tide characteristics? How do glider observations compare with regional modeling?**
Glider observations were successfully exploited to infer internal-tide dynamics by fitting a sinusoidal function on internal-tide induced vertical isopycnal displacements (see **[4]** in Fig. 5). In a dedicated area south of New Caledonia, the glider observations revealed elevated tidal activity expressed by vertical displacements exceeding 20 m. The semidiurnal tide is largely dominant explaining locally up to 80 % of the total variance of the vertical displacements.

Internal-tide characteristics inferred from the glider observations are in good agreement with regional modeling output demonstrating the realism of internal-tide dynamics in the numerical simulation. Specifically, glider observations and the regional model feature large similarities in location, magnitude, and vertical structure of the tidal signatures. Both data sets reveal the westward propagation of semidiurnal tidal energy, which can be traced back to the internal tide generation south of New Caledonia near Pines Ridge, and which appears to be governed by the coherent tide (see **[4]** in Fig. 5). Discrepancies between glider observations and the regional model are attributed to tidal incoherence due to eddy-internal tide interactions and are, thus, due to the stochastic nature of mesoscale and submesoscale features rather than a deficiency in the regional model's representation of internal-tide dynamics.

**3) Can glider observations serve as an in-situ observation platform to deduce the SSH signature of internal tides?**
The irregular glider sampling with depth measurements as a function of time and horizontal distance limited to the upper 1000 m represents a challenge to link interior dynamics to their SSH signature. We showed that glider observations of the upper 1000 m can capture a large fraction (78 %) of the internal tide steric SSH signature. We achieve even better results when accounting for the full-depth range (93 %) ob-

tained through a dedicated methodology that projects glider vertical displacements onto climatological vertical modes. Good agreement also exists between the steric SSH signature between glider observations and empirical estimates from satellite altimetry. It's worth noting that satellite altimetry, while unable to resolve the fine spatial scales captured by the glider sampling, still shows consistency with our observations. Given the large distances that gliders travel during a mission, they provide information with a broad spatial extent, which can complement in-situ measurements at fixed locations. We therefore suggest that glider observations can make an important contribution to our understanding of how internal tides manifest in steric SSH from an in-situ perspective.

## D Impact of internal tides on cross-scale energy exchanges

**1) Do internal tides affect cross-scale energy exchanges by modifying kinetic energy fluxes?**

Preliminary results suggest that tidal forcing can modulate cross-scale energy exchanges as revealed by spectral kinetic energy fluxes calculation for a region south of New Caledonia characterized by pronounced tidal activity and eddy-internal tide interactions (see **[5]** in Fig. 5). Internal tides are shown to promote the energy transfer toward smaller scales via the forward energy cascade, though, underlying strong seasonal variations. While in winter months, the forward energy cascade is primarily driven by submesoscale motion with only little contribution from internal tides, internal tides induced a strong forward cascade in summer months at scales around and below 100 km wavelength. The forward cascade is supposedly driven by tidal forcing alone as submesoscale motion is largely suppressed in summer time.

**2) Do internal tides affect the length scale at which the inverse energy cascade transitions into the forward energy cascade?**

We have shown for the region around New Caledonia that the inclusion of tidal forcing does indeed affect the transition scale between the inverse and forward cascade. Though, the changing transition scale is seasonally confined to winter months when mesoscale and submesoscale turbulence is enhanced. Specifically, internal tides shifted the transition scale toward larger wavelengths from 30 km to 50 km while reversing the inverse cascade to a forward cascade.

# Perspectives

This work provides several routes for future work which can be supported by three primary components: (1) the regional numerical modeling effort that has been initiated during this thesis, (2) the utilization of SWOT SSH measurements, and (3) the SWOTALIS in-situ experiment conducted in the framework of SWOT-AdAC during SWOT's fast sampling phase (1-day repeat cycle). The latter represents a huge observational effort in an area of complex bathymetry and strong internal tide generation, dissipation, and tidal energy propagation. It is presented in the following in more detail as it plays a key role in the future perspectives below.

Shortly introduced in Sect. I.3.3, the SWOTALIS in-situ experiment was carried out aboard RV Antéa in three separated legs from March to April 2023 beneath two SWOT swaths south of New Caledonia - an area of complex bathmetry and intense internal tide generation (Fig. 6). Leg 1 was dedicated to the deployment of three oceanographic moorings, fully equipped with acoustic current meters as well as temperature, salinity, and pressure sensors in the hot spots of internal tide generation, dissipation, and in tidal energy propagation direction beneath the SWOT swaths and on the nadir track. Leg 2 was dedicated to the alternating acquisition of CTD (Conductivity-Temperature-Depth) and VMP (Vertical Microstructure Profiler) data at fixed stations of up to 48 h length at the mooring deployment locations and in addition away from the generation site and on the slope of New Caledonia barrier reef. Leg 3 was dedicated to repeatedly conducted zonal sections of hydrography of the upper water column using underway CTD (uCTD) measurements in addition to SSH measurements as obtained from a GPS blanket beneath the SWOT swaths. An additional campaign is planned for November 2023 to recover the moorings (leg 4). Preliminary results of repeated CTD profiles show a clear signature of the semidiurnal internal tide with peak-to-peak amplitudes of more than 100 m (Fig. 6c). The acquired data sets provide plenty of opportunities to deepen our understanding of internal-tide dynamics south of New Caledonia and SWOT SSH observability. This concerns particularly

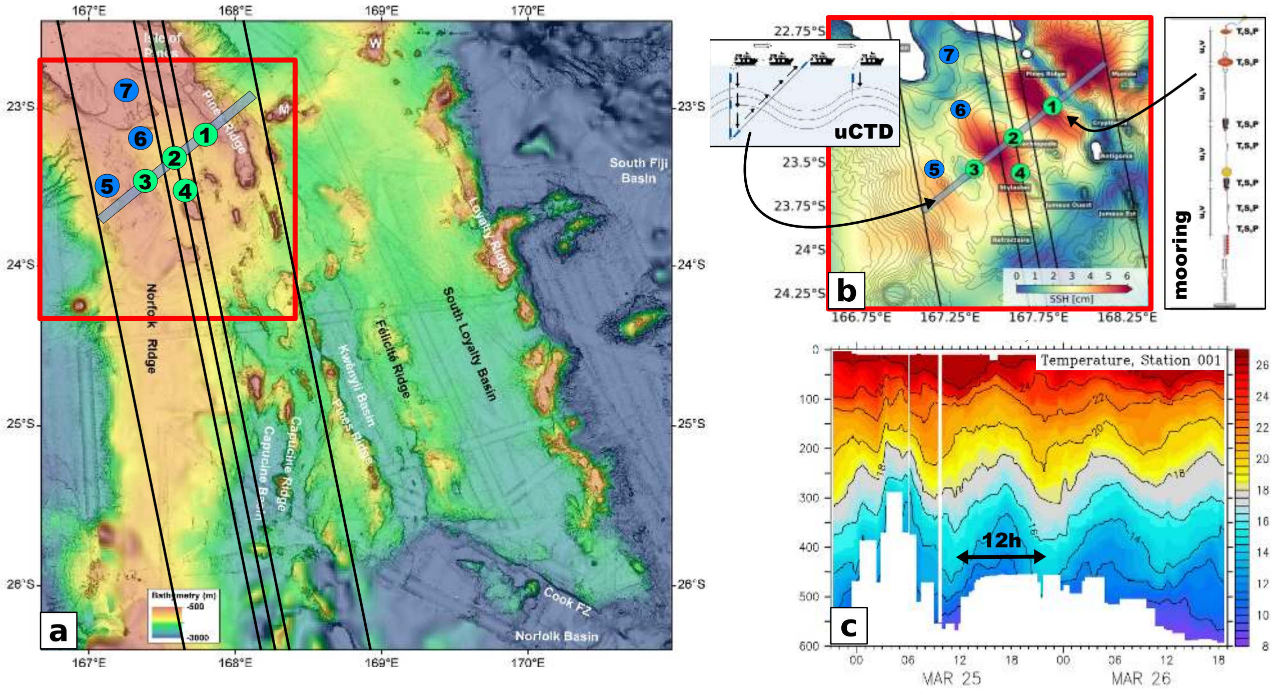

**Figure 6:** **(a)** Bathymetry map south of New Caledonia showing the complex bathymetry with small- and large-scale ridges and basins, and seamounts (Credits: M. Patriat, Ifremer). The red square demonstrates the SWOTALIS study site in the area of predominant internal tide generation, dissipation, and tidal energy propagation. Green circles represent the mooring deploymenet locations and fixed stations of CTD and VMP measurements. Blue circles represent fixed stations of CTD and VMP measurements only. The blue line represents the transect of repeated underway CTD measurements. **(b)** Same as **(a)** but showing a zoom for the SWOTALIS study site overlaid by the coherent M2 SSH amplitude. The underway CTD measuring technique and an exemplary mooring configuration equipped with current meters (u,v) as well as temperature, salinity, and pressure sensors (T,S,P) are also shown. **(c)** Preliminary results from repeated CTD profiles at a fixed location reveal pronounced semidiurnal internal tides with peak-to-peak amplitudes of more than 100 m.

the contribution of internal tides to vertical mixing processes and energy dissipation as well as a detailed investigation of the underlying mechanisms such as wave-wave and wave-topography interactions.

Perspectives presented below are motivated to advance our understanding in several key points: 1) internal tides, including their dissipation and interactions with mesoscale and submesoscale dynamics, 2) the utilization of SWOT SSH observations as a unique data set for studying fine-scale ocean dynamics, and 3) the establishment of a foundation for future studies aimed at optimizing the use of SWOT SSH observations and fine-scale modeling to promote sustainable practices.

## Internal tides and mesoscale and submesoscale interactions

### Dissipation

First insight into elevated dissipation rates around New Caledonia was given by this thesis. Energy dissipation rates in this thesis were found highly enhanced compared to other prominent internal tide generation sites such as the Luzon Strait or the Hawaiian Ridge. Yet, it is unclear to what extent the reported dissipation estimates are robust. Factors such as the model's horizontal and vertical grid spacing or the implemented turbulent closure scheme to parameterize dissipative effects (and many more) can influence the overall realism of modeled internal-tide dynamics. In this context, the SWOTALIS in-situ experiment is a promising approach to validate the numerical model output and overall the model's realism of tidal energy dissipation. During leg 2, various CTD and VMP profiles were acquired throughout the domain at fixed stations (see Fig. 6a-b), which allow to estimate dissipation rates over several tidal cycles from in-situ observations.

Energy dissipation as inferred in this thesis are not necessarily associated with true energy dissipation, but a significant fraction may represent the energy transfer or energy scattering to the incoherent tide, induced for example by the refraction of a tidal beam as it propagates through the mesoscale eddy field. It is suggested that eddies may facilitate the energy transfer from low to high modes and subsequently lead to energy dissipation (Dunphy and Lamb, 2014). As this thesis is being concluded, a newly published study (Wang and Legg, 2023) demonstrates that indeed, strong baroclinic eddies are capable of trapping low-mode internal tides and effectively transfer energy to higher-vertical modes, resulting in internal tide dissipation within the eddies. Estimating the fraction of dissipation associated with such processes using regional numerical model output is underway.

Eddy-internal tide interactions are very complex due to their non-linear nature. Further effort is needed to quantify energy dissipation on various scales. Advancing our understanding of tidal energy dissipation is essential for improving parameterization schemes in coarse-resolution ocean general circulation and climate models, especially when tidal motion is not explicitly resolved. Current parameterizations heavily rely on semi-analytical theory, which have limitations, particularly in regions characterized by shallow and complex bathymetry, as exemplified by New Caledonia. Further work is required encompassing regional numerical modeling efforts, in-situ observations, and high-resolution satellite altimetry to understand the life cycle of internal tides and their contribution to energy dissipation.

### Impact of internal tides on the energy cascade

This thesis contributed by studying the impact of internal tides on cross-scale energy exchanges, such as an enhanced forward or a reduced inverse energy cascade depending on the season. This field of research is of high relevance but it is in its early stages. The twin model configuration, with and without tides, developed during this thesis has only just begun to tap into its full potential. Further work will be needed to identify spatial variations in cross-scale energy exchanges, particularly in the dynamically very different flow regime north and south of New Caledonia. This is planned by replacing the spectral approach used in this manuscript by the more dedicated coarse-graining approach, which is argued in the scientific community to be more robust in estimating the energy transfer across a given length scale. Further, and in contrast to the spectral approach, it can be applied to every grid point in the domain. In a recent theoretical study by Shakespeare (2023), it was shown that when internal tide energy interacts with mesoscale eddies, it splits into two parts. One part transfers to eddy kinetic energy, and the remaining part undergoes irreversible turbulent mixing. Understanding how the energy transfer between the different energy reservoirs and the energetic balance are sensitive to internal tides is ongoing work.

### Internal tides and interannual variability

An important aspect disregarded in this work is the interannual variability of the governing dynamics at play which will be given insight by the available full-model 5-year time series. This thesis is almost entirely based on a single full-model calendar year (model year 2014). However, this raises the question of how large-scale, low-frequency variations in circulation, affecting both stratification and eddy activity, influence the significance of internal tides with the background dynamics.

## SWOT SSH observations

### Disentangling balanced and unbalanced motion

The disentangling of balanced and unbalanced motions in SWOT SSH measurements represents a major challenge in the upcoming years. Here, the goal here lies in the in-situ reconstruction of SSH and the validation with SWOT during the SWOTALIS cruise, explicitly designed to observe the vertical structure of fine-scale physics and their spatio-temporal variability. This will help interpret SWOT SSH measurements in the presence of pronounced internal tides and elevated levels of mesoscale eddy variability. In the same way, the two-dimensional SWOT SSH measurements along and across the SWOT swaths will help interpret the in-situ measurements from SWOTALIS.

### SWOT SSH inversion

The shift from the 1-day orbit of the fast sampling phase to the 21-day scientific orbit raises the question of how to take into account high frequency motions such as internal tides. This requires the development of mapping algorithms to combine SWOT SSH with SSH from conventional (nadir-pointing) satellite altimetry but also others satellite mission such as MODIS providing pictures of sea surface temperature, chlorophyll, etc. The future satellite mission ODYSEA (in competition at NASA) aims to directly measure surface currents from space. Combined with SWOT SSH observations, this may lead to a better disentanglement of ageostrophic motions. Huge efforts are being made by the SWOT Science community to address these challenges, such as in the Modeling, Inversion, and Data Assimilation (MIDAS) group at the Institut des Géosciences de l'Environnement in Grenoble, France. This group's interest lies in the development of data inversion techniques that are able to separate between balanced and unbalanced motions (Le Guillou et al., 2021). In this context, collaborations must be enhanced with the SWOTALIS in-situ experiment, which is expected to help validate the developed methodologies.

## Environmental impacts of internal tides

### Marine heat waves

New Caledonia is afflicted by reoccurring marine heat waves. An recent example is the marine heat wave in 2016, which affected two-thirds of the New Caledonia coral reefs and expressed by temporary coral bleaching events (Payri et al., 2019). It is well acknowledged that sea surface temperatures are affected by internal tides. In fact, the heat budget can be significantly modified due to vertical mixing processes induced by internal tides (Wyatt et al., 2020, 2023). This has important implications for shallow and coastal areas such as coral reefs (Payri et al., 2019). It is even considered that internal tides and their associated upwelling of colder waters are an important component in partly counteracting the increasingly progressive coral bleach of coral reefs due to climate change induced rising sea surface temperatures, by acting as a thermal buffer (Green et al., 2019; Storlazzi et al., 2020). The twin model configuration developed in this thesis should provide important insight into the role of internal tides on the possible mitigation of marine heat waves.

### Marine ecosystems

Apart from coastal temperatures, vertical mixing processes associated with internal tides also have direct implications for the New Caledonia marine ecosystem, biological productivity, biodiversity, and overall ecological processes. Understanding the impact of internal tides on the ecosystem up to trophic levels is of large socio-economic interest for the island's conservation management of marine protected areas as well as the associated maintenance of the food web dynamics and food security related to commercial fishing. The ScInObs (Science, Innovation and Observatories of seamounts) has been recently initiated to understand the tidally-driven mixing on temperature, tracer fields, and biogeochemical properties. Led by the French Research Institute for Exploitation of the Sea (IFREMER) and in collaboration with the Japan

Agency for Marine–Earth Science and Technology (JAMSTEC), this initiative focuses inter alia on the Stylaster seamount south of New Caledonia which represents a tidal energy dissipation and biodiversity hot spot.

### Next steps and future research directions

To conclude, it's important to note that I will not be leading these initiatives on my own. The goal was rather to show the potential route for future work for which this thesis could serve as a base. Over the next two years, my primary focus will be on finalizing the work that could not be completed during this thesis. This concerns the study of tidal incoherence around New Caledonia with a special focus on the temporal variations of tidal energy dissipation. The results are planned to be published as part of a companion paper with the published results in Bendinger et al. (2023), specifically *Bendinger et al. (in preparation for submission): Regional modeling of internal-tide dynamics around New Caledonia - Part 2. Tidal incoherence and implications for sea surface height observability*. This is followed by the finalization of the work done on internal tides and their role on modulating cross-scale energy exchanges.
The SWOTALIS in-situ experiment will play a major role in the CNES-funded post-doctoral position that I received for a full 2-year period starting in spring 2024 at LOPS (Laboratoire d'Océanographie Physique et Spatial) in the Ocean Scale Interaction Team in collaboration with Clément Vic. In this postdoctoral position, the objective is to infer fine-scale dynamics and internal tide propagation/attenuation beneath the SWOT swaths and at the nadir track. I personally attended leg 2 of the SWOTALIS cruise, and I am convinced that together with the numerical model output and SWOT SSH data we will deepen our understanding of the enhanced dissipation rates and vertical mixing processes south of New Caledonia.

# Conclusion et Perspectives

## Conclusion

L'objectif de cette thèse était l'étude des marées internes et de leurs interactions avec la dynamique tourbillonnaire autour de la Nouvelle-Calédonie. La motivation est double. D'une part il s'agit d'appréhender le rôle de la marée interne dans les transferts d'énergie vers les échelles dissipatives, d'autre part il s'agit d'appréhender l'observabilité de ces processus en termes de niveau de la mer en lien notamment avec la mission SWOT. Cette thèse est en grande partie basée sur un effort de modélisation numérique régionale à haute résolution, mais également sur une analyse d'observation in-situ.

La première étape a été de décrire, à partir d'une simulation numérique régionale, le plus complétement possible et pour la première fois, la dynamique des marées internes autour de la Nouvelle-Calédonie en considérant à la fois leur génération, leur propagation et leur dissipation. Une seconde étape s'est concentrée sur l'observabilité SSH

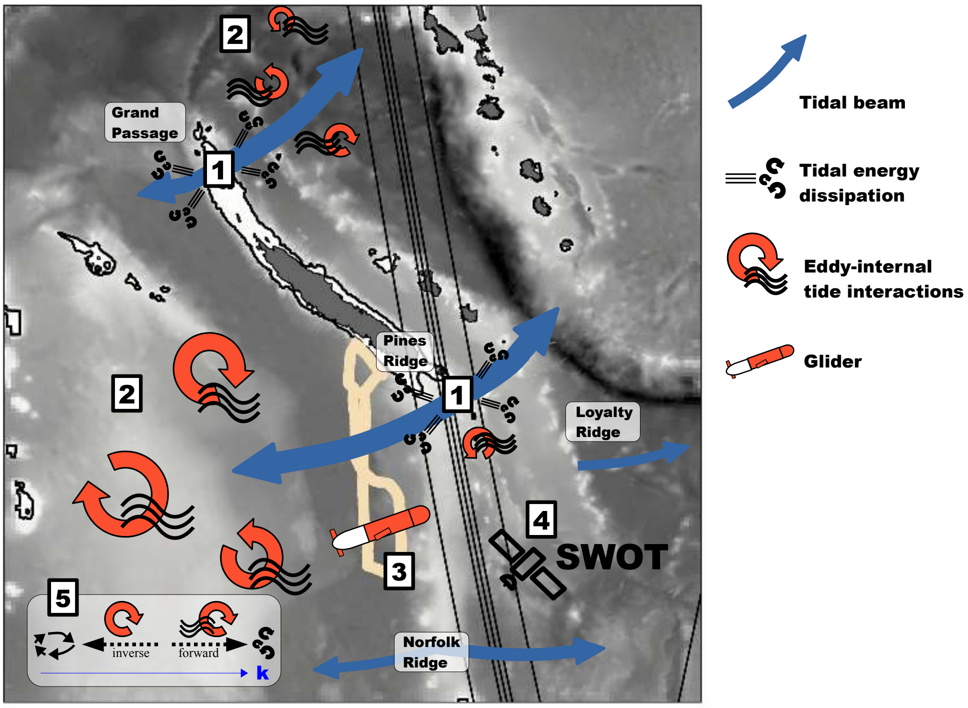

**Figure 7:** Schéma récapitulatif des principaux résultats de la thèse. **[1]** Les principales zones de génération de marée interne sont situés au nord et au sud de la Nouvelle-Calédonie et sont associés à une forte dissipation d'énergie dans le champ proche et à une propagation prononcée de l'énergie de marée dans des faisceaux étroits. **[2]** Dans le champ lointain, les marées internes interagissent avec le champ de tourbillons à mésoéchelle, ce qui entraîne une incohérence des marées. **[3]** La variance SSH des mouvements déséquilibrés (marées internes) domine sur les mouvements équilibrés (mésoéchelle à sous-mésoéchelle) avec des implications importantes pour l'observabilité de la dynamique mésoéchelle et sous-mésoéchelle dans une zone à forte activité de marée telle que la Nouvelle-Calédonie. **[4]** Un aperçu important de la dynamique des marées internes est donné d'un point de vue in-situ par des planeurs sous-marins autonomes, qui est en bon accord avec les résultats du modèle et l'altimétrie par satellite. **[5]** Les marées internes peuvent jouer un rôle crucial dans la dissipation de l'énergie en extrayant l'énergie du flux géostrophiquement équilibré, c'est-à-dire en inversant la cascade inverse en une cascade avant (la flèche bleue fine indique la direction de l'augmentation du nombre d'ondes).

de SWOT à partir d'analyses spectrales en distinguant les dynamiques géostrophiques méso-échelle et sous méso-échelle et les dynamiques agéostrophiques avec notamment la signature des marées internes. Une troisième étape s'est intéressée au traitement des observations in-situ fonction de leur spécificité d'échantillonnage pour restituer la signature de la marée interne et sa signature en surface. Cette analyse in-situ a permis d'évaluer positivement la simulation numérique régionale. Une quatrième étape a été une étude préliminaire de l'impact des marées internes sur les cascades d'énergie.

Les principaux résultats de cette thèse sont résumés dans le schéma de la Fig. 7 et énumérés ci-dessous en se référant individuellement à chaque question de recherche étiquetée A, B, C, et D comme indiqué dans la Sect. I.5.

## A Dynamique cohérente des marées internes et signature de la hauteur de la surface de la mer autour de la Nouvelle-Calédonie

**1) Quelles sont les régions de forte génération de marée interne? A quelles structures bathymétriques correspondent elles?**
La génération de marée interne est largement dominée par la marée semi-diurne M2 expliquant plus de 80 % de la conversion totale de l'énergie de marée barotrope à barocline. Les zones de forte génération sont étroitement liées à la bathymétrie complexe autour de la Nouvelle-Calédonie associée aux pentes continentales, à la présence de plateaux, de rifts et de monts sous-marins. La génération de marée interne est importante au nord de la Nouvelle Calédonie près du Grand Passage (2.17 GW) et au sud près de l'île des Pins (3.92 GW) (voir **[1]** dans la Fig. 7). Ensemble, ces deux régions représentent environ 40 % de la conversion de l'énergie barotrope-barocline estimée sur l'ensemble du domaine simulé. Un résultat important concerne la typologie des zones de génération avec la marée barocline générée préférentiellement dans les eaux peu profondes autour de 500 m de profondeur et sur les pentes critiques à supercritiques - des régions de génération de marée interne qui ne sont généralement pas bien prises en compte par les modèles semi-analytiques linéaires.

**2) Quelles sont les régions où la dissipation de la marée interne est importante? Quelle fraction de l'énergie de marée générée est dissipée localement?**
L'énergie de marée interne se dissipe sur l'ensemble du domaine. Cependant, la dissipation est plus forte près des sites de génération pouvant atteindre 50 % de l'énergie barocline générée. Les marées internes apparaissent donc comme une source de mélange importante dans les zones de génération (voir **[1]** dans la Fig. 7). Sinon, en dehors des zones de génération l'énergie de marée va se dissiper préférentiellement le long de la barrière de corail et au niveau des obstacles bathymétriques tels que les monts sous-marins. Les mécanismes sous-jacents doivent encore être étudiés en détail. Les interactions entre les ondes internes et la topographie avec une diffusion de l'énergie vers les modes verticaux élevés pourrait expliquer le taux de dissipation élevé. La dissipation de l'énergie de la marée barocline, estimée ici à partir de la marée cohérente, peut également être surévaluée si une fraction de cette dissipation intègre une part de l'énergie de la marée incohérente.

### 3) Quels modes verticaux dominant pour la marée interne autour de la Nouvelle Calédonie?

Le premier mode barocline est largement dominant puisqu'il explique 75 % de l'énergie de marée barocline générée sur l'ensemble du domaine et jusqu'à 85 % localement. Ceci est en accord avec la théorie semi-analytique qui favorise les premiers modes pour des marées baroclines générées sur des pentes raides et des faibles profondeurs. Seule la dorsale des Loyauté constitue une exception puisque les modes >1 ont une contribution non négligeable. L'énergie de marée barocline des premiers modes se propage loin des sites de génération avec des flux d'énergie barocline allant jusqu'à 30 kW m-1 concentrés dans des faisceaux étroits (voir **[1]** dans la Fig. 7).

### 4) Quelles caractéristiques pour la signature en SSH des marées internes? Comment se distinguent-elles de la signature en SSH de la dynamique méso sous méso-échelle?

La marée interne a une forte signature en SSH qui peut atteindre des amplitudes >6 cm pour le mode 1 et 1-2 cm pour le mode 2 près des sites de génération. Loin de ceux-ci, les structures de SSH expriment les multiples interférences des ondes de marée émanant des différentes sources de génération. Dans certains endroits, la marée interne présente des longueurs d'onde de l'ordre de 160 km pour le mode 1 et de 80 km pour le mode 2 similaires à celles de la dynamique méso-échelle. Pour les échelles inférieures à 200 km, la variance en SSH de la marée interne domine celle de la dynamique turbulente ce qui implique que l'observabilité de la SSH SWOT pour la dynamique méso et sous méso-échelle peut être difficile autour de la Nouvelle-Calédonie. Cette observabilité est définie par les longueurs d'onde où la variance en SSH des processus subinertiels est plus élevée que celle des processus superinertiels. Corriger le signal en SSH de la marée interne cohérente améliore l'observabilité SSH de la dynamique turbulente en déplaçant l'échelle de transition vers les plus courtes longueurs d'onde. Dans notre région, cette approche simple améliore l'observabilité en SSH de la dynamique turbulente de 200 km à moins de 100 km de longueur d'onde.

## B Incohérence des marées et implications pour l'observabilité de la hauteur de la surface de la mer autour de la Nouvelle-Calédonie.

### 1) Quelles régions pour la marée incohérente? Quel part de l'énergie de la marée interne correspond à sa composante incohérente?

Le flux d'énergie correspondant à la marée incohérente varie considérablement selon les zones de propagation de la marée interne. Elle est généralement plus importante au sud/sud-ouest de la Nouvelle-Calédonie comparée aux régions plus au nord. Au fur et à mesure que la marée interne se propage vers le large, elle devient de plus en plus incohérente et peut représenter jusqu'à 25 % de la variance totale à une distance de 200 km de la zone de génération; elle devient la composante dominante au-delà de 500 km mais le flux d'énergie est alors relativement faible ($\sim$1 kW m$^{-1}$ à une distance $>$800 km).

### 2) Quelles sont les sources d'incohérence de la marée interne?

Les tourbillons méso-échelle seraient la principale source d'incohérence de la marée autour de la Nouvelle-Calédonie (voir **[2]** dans la Fig. 7). Lors de la propagation de la marée interne, la circulation mésoéchelle provoque une réfraction du faisceau de marée accompagnée d'un changement des vitesses de groupe et de phase. En général, l'incohérence de la marée s'exprime par un changement de phase qui croit au fur et à mesure que le faisceau de marée se propage dans le champ de tourbillons. Les tourbillons peuvent également influencer la génération des ondes internes en induisant des variations temporelles du terme de convergence barotrope-barocline. induites principalement par les changements de stratification induits par les tourbillons.

**3) Quelle signature en SSH de la marée incohérente? Quelles sont les implications potentielles pour l'observabilité en SSH de la dynamique turbulente?**
La marée interne incohérente a une signature en SSH visible sur l'ensemble du domaine avec des amplitudes maximales de 2 cm. Malgré son amplitude relativement faible comparée à la marée interne cohérente, elle peut représenter une fraction non négligeable de la variance en SSH en certains endroits. Aux longueurs d'onde inférieures à 100 km, La marée incohérente est la principale source limitant l'observabilité de la dynamique turbulente. Cette notion d'observabilité est bien sur dépendante du régime turbulent (meso, sous mésoéchelle) qui varie en fonction des régions et des saisons. Dans les régions de forte activité d'ondes internes dominé par une dynamique méso-échelle, comme c'est le cas dans la partie sud de la Nouvelle Calédonie en été austral, la compréhension des interactions entre marée interne et tourbillons sera cruciale pour interpréter la SSH SWOT (voir **[3]** dans la Fig. 7).

## C Marées internes déduites de planeurs sous-marins autonomes autour de la Nouvelle-Calédonie.

**1) Comment extraire des informations sur la marée interne autour de la Nouvelle-Calédonie à partir d'observations de planeurs sous-marin? Comment ces informations in-situ corroborent les résultats de la simulation numérique?**
En ajustant une fonction sinusoïdale sur les déplacements verticaux isopycnaux induits par les marées internes les observations des planeurs sous-marin ont permis de renseigner avec succès les marées internes (voir **[4]** dans la Fig. 7). Les missions de planeurs sous-marin qui ont eu lieu au sud de la Nouvelle-Calédonie révèlent une forte activité de marée interne exprimée par des déplacements verticaux supérieurs à 20 m. La marée semi-diurne est largement dominante, expliquant localement jusqu'à 80 % de la variance totale des déplacements verticaux. Ces caractéristiques, en bon accord avec les résultats de la modélisation régionale, valident le réalisme de la simulation à décrire la dynamique de la marée interne. Plus précisément, observations et modèle convergent sur la localisation, l'amplitude et les structures verticales associées à la marée interne. Ils permettent de conforter la propagation vers l'ouest de l'énergie de marée interne cohérente générée au sud de la Nouvelle Calédonie au niveau de l'île des pins (voir **[4]** dans la Fig. 7). Les différences entre les observations et la simulation sont attribuées à la nature stochastique des interactions marée interne/tourbillons qui induisent une composante de marée interne incohérente différentes selon les sources d'information.

**2) Les planeurs sous-marins peuvent-ils servir de plate-forme d'observation in-situ pour déduire la signature de la SSH des marées internes?**
L'échantillonnage irrégulier des planeurs sous-marins limité aux premiers 1000 m de l'océan avec des mesures de profondeur fonction du temps et de la distance horizontale représente un défi pour relier l'observation interne de la marée interne à sa signature en SSH. Dans notre région, 78 % de la signature en SSH des marées internes correspond aux premiers 1000 m sous la surface. En utilisant une méthode de projection sur des modes verticaux climatologiques afin d'étendre les observations jusqu'au fond celles-ci sont capables de représenter 93 % de la signature en SSH. Il existe également un bon accord entre la signature en SSH observée par les planeurs sous-marins et les estimations altimétriques malgré l'incapacité de l'altimétrie à résoudre les échelles spatiales fines capturées par l'échantillonnage des planeurs. Ainsi, les planeurs sous-marins en parcourant de grande distance au cours d'une mission sont capables de fournir des informations spatiales en SSH à même de compléter celles obtenues à des stations fixes particulièrement adaptées pour décrire la variabilité temporelle des marées internes.

## D Impact des marées internes sur les échanges d'énergie entre les échelles.

**1) Comment les marées internes affectent les cascades d'énergie?**
Il s'agit ici de résultats préliminaires à partir de spectres de flux d'énergie calculés à partir des simulations numériques avec et sans forçage de la marée dans une région au sud de la Nouvelle-Calédonie caractérisée par une activité de forte marée interne en interaction avec la circulation méso-échelle (voir **[5]** dans la Fig. 7). Les différences spectrales entre les simulations suggèrent que le forçage par les marées module les transferts d'énergie. Les marées internes favorisent le transfert d'énergie vers les courtes longueurs d'onde via la cascade directe d'énergie, mais leur impact varie selon les saisons. En hiver austral, la marée interne a un rôle négligeable sur la cascade directe d'énergie qui est principalement associée à la dynamique sous méso-échelle alors qu'en été austral, dominé par une dynamique méso-échelle, la marée interne est à l'origine d'une forte cascade directe d'énergie pour les longueurs d'onde inférieures à 100 km.

**2) Comment les marées internes modifient les longueurs d'onde relatives aux cascades directe et inverse?**
Les spectres de flux d'énergie utilisés en 1) montrent que l'échelle de transition entre la cascade inverse et la cascade directe est affecté par l'inclusion de la marée dans la simulation. Cela est surtout vrai lors de l'hiver austral où la turbulence sous méso-échelle est bien développée. La marée interne déplace l'échelle de transition vers les plus grandes longueurs d'onde (de 30 à 50 km) avec pour l'effet de réduire la cascade inverse d'énergie bien prononcée à cette saison.

# Perspectives

Les perspectives de ces travaux reposent sur trois composantes principales: (1) la modélisation numérique régionale initiée au cours de cette thèse, (2) l'utilisation des mesures de SSH SWOT, (3) la campagne à la mer SWOTALIS menée dans le cadre de SWOT-AdAC pendant la phase de CalVal SWOT caractérisée par une orbite répétitive à un jour. SWOTALIS représente un énorme effort d'observation dans une zone de bathymétrie complexe et de forte génération de marée interne, de dissipation et de propagation de l'énergie de marée. Elle a été brièvement introduite dans la Sect. I.3.3, elle est présentée plus en détail ci-après.

SWOTALIS s'est tenu à bord du RV Antéa lors de trois legs entre mars et avril 2023 sous une fauchée SWOT au sud de la Nouvelle-Calédonie - une zone de bathymétrie complexe et de forte génération de marée interne (Fig. 8). Le leg 1 visait à déployer trois mouillages entièrement équipés de courantomètres acoustiques ainsi que de capteurs de température, de salinité et de pression. Deux mouillages sont situés sous la fauchée SWOT dans les zones de génération de la marée interne et le troisième situé entre les deux précédents sous le nadir de SWOT. Le leg 2 visait à échantillonner des stations fixes pendant en alternant des données CTD (conductivité-température-profondeur) et des mesures de turbulence à l'aide d'un VMP (Vertical Microstructure

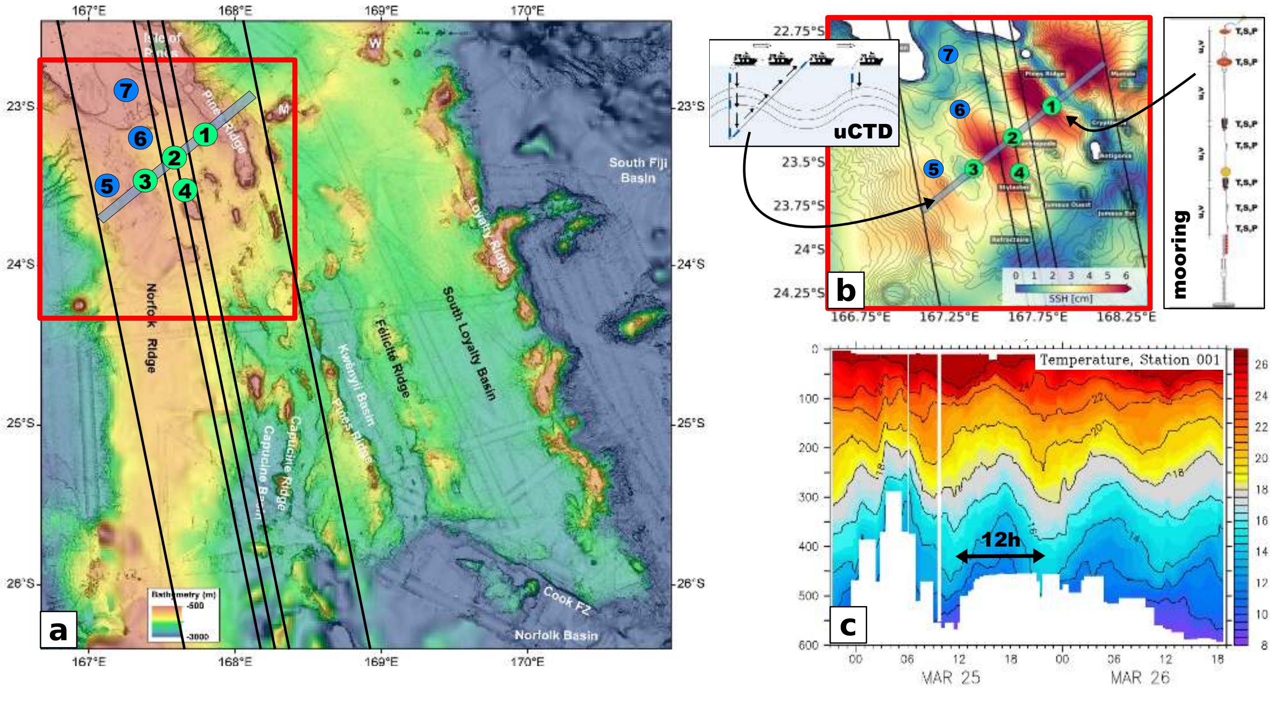

**Figure 8:** **(a)** Carte de bathymétrie au sud de la Nouvelle-Calédonie montrant la bathymétrie complexe avec des crêtes et des bassins à petite et grande échelle, et des monts sous-marins (Crédits : M. Patriat, Ifremer). Le carré rouge représente le site d'étude SWOTALIS dans la zone de génération et de dissipation de la marée interne et de propagation de l'énergie de la marée. Les cercles verts représentent les emplacements de déploiement des mouillages et les stations fixes de mesures CTD et VMP. Les cercles bleus représentent les stations fixes des mesures CTD et VMP uniquement. La ligne bleue représente le transect des mesures CTD répétées en cours de route. **(b)** Identique à **(a)** mais avec un zoom sur le site d'étude SWOTALIS superposé à l'amplitude cohérente M2 de la SSH. La technique de mesure CTD en cours et une configuration d'amarrage exemplaire équipée de courantomètres (u,v) ainsi que de capteurs de température, de salinité et de pression (T,S,P) sont également représentées. **(c)** Les résultats préliminaires des profils CTD répétés à un emplacement fixe révèlent des marées internes semidiurnes prononcées avec des amplitudes de crête à crête de plus de 100 m.

Profiler). 7 stations fixes ont été effectuées à la fois au niveau des trois mouillages et dans le flux d'énergie de la marée interne ainsi que dans les régions de forte dissipation au niveau de la barrière récifale. Le leg 3 a consisté à répéter une section sous la fauchée SWOT dans l'alignement des trois mouillages. Il s'agit de combiner à la fois des mesures hydrographiques sur les premiers 600 m obtenues en continu à partir d'un EcoCTD et d'un treuil rapidcast et des mesures SSH obtenues en tirant une nappe GNSS. Le leg 4 est programmé en novembre 2023 afin de récupérer les mouillages.

Les résultats préliminaires montrent une signature claire de la marée interne semi-diurne avec des déplacement d'isopycnes de plus de 100 m (Fig. 8). Les données acquises vont permettre d'approfondir notre compréhension de la dynamique des marées internes au sud de la Nouvelle-Calédonie notamment en ce qui concerne la contribution des marées internes pour le mélange vertical, les mécanismes de dissipation de l'énergie comme les interactions onde/onde ou onde/topographie et leur signature en SSH.

Les perspectives présentées ci-dessous sont motivées par la volonté de faire progresser notre compréhension des marées internes avec un focus sur les mécanismes de dissipation et leurs interactions avec la dynamique méso-échelle et sous méso-échelle et de valoriser au mieux les données SSH SWOT avec à terme l'utilisation de méthodes d'inversion pour documenter les fines échelles océaniques (dynamique turbulente/ondes internes) à la surface mais aussi en profondeur.

## Marées internes et leurs interactions avec la méso-échelle et sous méso-échelle

### Dissipation

Cette thèse a mis en avant des taux de dissipation élevés autour de la Nouvelle-Calédonie supérieures à ceux estimés dans d'autres sites importants de marée interne tels que le détroit de Luzon ou Hawaï. Ces taux de dissipation estimés au travers du modèle sont sensibles à des facteurs tels que les discrétisations horizontale et verticale, le schéma de fermeture turbulente mis en œuvre pour paramétrer les effets dissipatifs, etc. qui peuvent influencer le réalisme global de la dynamique de la marée interne modélisée. Aussi, la dissipation d'énergie estimée dans cette thèse fait référence à la marée interne cohérente et une partie de cette dissipation peut intégrer une fraction significative d'énergie traduisant un transfert de la marée cohérente vers la marée incohérente. Dans ce contexte, la campagne en mer SWOTALIS va permettre d'évaluer le réalisme de la dissipation d'énergie de marée interne dans le modèle. En effet, les profils CTD et VMP acquis aux stations fixes lors du leg 2 (voir Fig. 8a-b) vont permettre de calculer des taux de dissipation sur plusieurs cycles de marée à partir d'observations in-situ.

Il sera également important d'évaluer le rôle des tourbillons dans la dissipation d'énergie de marée interne. En effet, les tourbillons en facilitant le transfert d'énergie des premiers modes baroclines vers les modes élevés peuvent participer à dissiper cette énergie (Dunphy and Lamb, 2014). Une étude théorique récemment publiée

(Wang and Legg, 2023) démontre que les forts tourbillons baroclines sont capables de piéger l'énergie des premiers modes baroclines de la marée interne et de la transférer aux modes baroclines élevés, ce qui entraîne une dissipation de la marée interne au sein des tourbillons. Les interactions entre les tourbillons et les marées internes sont très complexes en raison de leur nature non linéaire. L'estimation de la fraction de dissipation associée à de tels processus à l'aide de modèles numériques régionaux demandent de nouvelles études.

Une meilleure compréhension de la dissipation de l'énergie des marées est essentielle pour améliorer les paramétrisations utilisées dans les modèles de circulation générale des océans et de climat à basse résolution qui ne résolvent pas explicitement la marée. Les paramétrisations actuelles s'appuient sur les modèles semi-analytique qui représentent mal les régions caractérisées par une bathymétrie peu profonde et complexe, comme c'est le cas en Nouvelle-Calédonie. Des travaux supplémentaires sont nécessaires, englobant la modélisation numérique régionale, les observations in-situ et l'altimétrie satellitaire à haute résolution pour comprendre le cycle de vie des marées internes et leur contribution à la dissipation de l'énergie.

### Impact des marées internes sur la cascade d'énergie

Dans une étude théorique récente, Shakespeare (2023) a montré que lorsque l'énergie de la marée interne interagit avec les tourbillons à mésoéchelle, elle se divise en deux parties. Une partie est transférée à l'énergie cinétique du tourbillon, et la partie restante subit un mélange turbulent irréversible. Dans la dernière partie de cette thèse, une étude préliminaire à montrer l'impact des marées internes sur les cascades d'énergie directe et inverse qui varie selon les saisons et le régime turbulent associé. Cette étude demande à être poursuivie en exploitant le potentiel des simulations avec et sans marée développées au cours de la thèse. Il s'agit d'étendre l'étude actuelle concentrée au sud de la Calédonie aux autres régions où l'activité de marée interne est forte, notamment au nord de la Calédonie. L'approche des transferts d'énergie entre différentes échelles par les spectres de flux d'énergie pourra être compléter par celle du " coarse-graining " qui a l'avantage de considérer chaque point de grille du domaine indépendamment.

### Marées internes et variabilité interannuelle

Les résultats de cette thèse se basent essentiellement sur l'année 2014 de la simulation. On peut se poser la question de savoir comment les variations basse fréquence de la circulation, affectant à la fois la stratification et l'activité tourbillonnaire, influencent la description des marées internes faites ici. Or, les simulations dont on dispose couvrent la période 2014-2018. Examiner la robustesse de nos résultats au regard de cette longue série interannuelle reste à faire.

## Valorisation de la SSH SWOT

### Quelle signature de la dynamique turbulente et des ondes internes dans la SSH SWOT

Déconvoluer la signature en SSH entre mouvements turbulents et ondes internes représente un défi majeur pour SWOT. La campagne SWOTALIS a été pensée afin d'observer les marées internes et leurs interactions avec la méso et sous méso-échelle et d'avoir de façon concomitante leurs signatures en SSH. La confrontation de la SSH SWOT avec celle observée permettra d'interpréter la mesure SWOT. De la même manière, les mesures bidimensionnelles de la SSH SWOT aideront à interpréter les structures dynamiques observées durant SWOTALIS.

### Inversion de la SSH SWOT

Le passage de l'orbite à un jour lors de la phase de cal/val de SWOT à l'orbite scientifique de 21 jours soulève la question de la décorrélation temporelle des mouvements haute fréquence tels que les marées internes entre deux passages du satellite. Afin de tirer pleinement bénéfice de ces nouvelles données, il apparait important de les combiner à l'ensemble des autres observations spatiales existantes que ce soit celles des satellites altimétriques conventionnels mais aussi celles des images à haute résolution de la température de surface de la mer, de la chlorophylle, etc. A noter l'élaboration de nouvelles missions satellitaires telles que ODYSEA qui visent à mesurer directement les courants de surface depuis l'espace. Combinées aux observations SSH de SWOT, ces mesures pourraient permettre de mieux distinguer les circulations géostrophiques et agéostrophiques.

Des efforts considérables sont déployés par la communauté scientifique de SWOT pour relever ces défis, notamment par le groupe MIDAS (Modélisation, Inversion et Assimilation des Données) de l'Institut des Géosciences de l'Environnement de Grenoble, en France. Ce groupe s'intéresse au développement de techniques d'inversion de données capables de distinguer les mouvements géostrophiques des ondes internes (Le Guillou et al., 2021). L'application de telles méthodes dans notre région permettrait de bénéficier du jeu de données SWOTALIS pour aider à valider les méthodologies développées.

## Influence des marées internes sur l'écosystème

### Les vagues de chaleur marine

La Nouvelle-Calédonie est touchée par des vagues de chaleur marine récurrentes. Un exemple récent est la vague de chaleur marine de 2016, qui a affecté les deux tiers des récifs coralliens de Nouvelle-Calédonie, se traduisant par des épisodes de blanchiment temporaire des coraux (Payri et al., 2019). Les marées internes en raison des processus de mélange vertical qu'elles induisent affectent la température de surface de la mer (Wyatt et al., 2020, 2023). Cela a des implications importantes dans les zones peu profondes et côtières telles que les récifs coralliens (Payri et al., 2019). Les marées internes et les remontées d'eaux froides associées, en agissant comme un tampon thermique, sont supposées être un élément important pour contrer en partie le blanchiment des récifs coralliens dû à la hausse des températures de surface de la mer induite par le changement climatique (Green et al., 2019; Storlazzi et al., 2020). La configuration des simulations avec et sans marée développées dans cette thèse devrait fournir des informations importantes sur le rôle des marées internes dans l'atténuation possible des vagues de chaleur marines.

### Les écosystèmes marins

Les processus de mélange vertical associés aux marées internes sont supposés avoir des implications directes sur l'écosystème marin de Nouvelle-Calédonie. Comprendre l'impact des marées internes sur cette écosystème est d'un grand intérêt pour la gestion de la conservation des zones marines protégées de l'île, ainsi que pour aider au maintien de la dynamique du réseau trophique et en point de mire la sécurité alimentaire liée à la pêche commerciale. C'est dans cette logique que le projet ScInObs (Science, Innovation et Observatoires des monts sous-marins) a été récemment lancé par l'Institut français de recherche pour l'exploitation de la mer (IFREMER) en collaboration avec l'Agence japonaise pour les sciences et technologies marines et terrestres (JAMSTEC) pour comprendre les effets du mélange induit par les marées sur la température, les champs de traceurs et les propriétés biogéochimiques au niveau des monts sous-marins présents au sud de la Nouvelle-Calédonie.

## Prochaines étapes et orientations futures de mes recherches

Les perspectives énoncées plus haut éclairent des voies potentielles de travaux futurs pour lesquels cette thèse pourrait servir de base. Evidemment, ces perspectives dépassent le cadre de mes activités. Au cours des deux prochaines années, je me concentrerai principalement sur la finalisation des travaux qui n'ont pas pu être achevés au cours de cette thèse. Il s'agit de l'étude de l'incohérence des marées internes autour de la Nouvelle-Calédonie, avec un accent particulier sur les variations temporelles de la dissipation de l'énergie des marées. Les résultats devraient être publiés comme part 2 de l'article sur la marée cohérente (Bendinger et al., 2023): Regional modeling of internal-tide dynamics around New Caledonia - Part 2. Tidal incoherence and implications for sea surface height observability. Un autre travail en cours de finalisation concernera l'analyse conjointe des simulations avec et sans marée afin de quantifier les processus en jeu expliquant les effets de la marée sur les transferts d'énergie.

J'ai obtenu un post doc CNES qui commencera au printemps 2024 pour deux années. J'intégrerai le LOPS (Laboratoire d'Océanographie Physique et Spatial) et l'équipe Ocean Scale Interaction avec Clément Vic comme principal collaborateur. Je vais m'investir dans l'analyse de la campagne SWOTALIS, l'objectif est de décrire la dissipation et les processus de mélange verticale observés sous la fauchée SWOT en lien avec la marée interne et le régime sous mésoéchelle.

# Bibliography

, 2005. Direct evidence of an oceanic inverse kinetic energy cascade from satellite altimetry, author=Scott, Robert B and Wang, Faming. Journal of Physical Oceanography 35, 1650–1666. doi:10.1175/JPO2771.1.

Ajayi, A., 2020. Cross-scale interactions and turbulent cascades in the North Atlantic Ocean. Ph.D. thesis. Université Grenoble Alpes.

Alford, M.H., 2020. Revisiting near-inertial wind work: Slab models, relative stress, and mixed layer deepening. Journal of Physical Oceanography 50, 3141–3156. doi:10.1175/JPO-D-20-0105.1.

Alford, M.H., MacKinnon, J.A., Zhao, Z., Pinkel, R., Klymak, J., Peacock, T., 2007. Internal waves across the Pacific. Geophysical Research Letters 34. doi:10.1029/2007GL031566.

Amores, A., Jordà, G., Arsouze, T., Le Sommer, J., 2018. Up to what extent can we characterize ocean eddies using present-day gridded altimetric products? Journal of Geophysical Research: Oceans 123, 7220–7236. doi:10.1029/2018JC014140.

Ansong, J.K., Arbic, B.K., Alford, M.H., Buijsman, M.C., Shriver, J.F., Zhao, Z., Richman, J.G., Simmons, H.L., Timko, P.G., Wallcraft, A.J., et al., 2017. Semidiurnal internal tide energy fluxes and their variability in a Global Ocean Model and moored observations. Journal of Geophysical Research: Oceans 122, 1882–1900. doi:10.1002/2016JC012184.

Arbic, B.K., 2022. Incorporating tides and internal gravity waves within global ocean general circulation models: A review. Progress in Oceanography 206, 102824. doi:https://doi.org/10.1016/j.pocean.2022.102824.

Arbic, B.K., Alford, M.H., Ansong, J.K., Buijsman, M.C., Ciotti, R.B., Farrar, J.T., Hallberg, R.W., Henze, C.E., Hill, C.N., Luecke, C.A., et al., 2018. Primer on global internal tide and internal gravity wave continuum modeling in HYCOM and MITgcm. New frontiers in operational oceanography , 307–392URL: http://purl.flvc.org/fsu/fd/FSU_libsubv1_scholarship_submission_1536242074_55feafcc, doi:10.17125/gov2018.ch13.

Arbic, B.K., Garner, S.T., Hallberg, R.W., Simmons, H.L., 2004. The accuracy of surface elevations in forward global barotropic and baroclinic tide models. Deep Sea Research Part II: Topical Studies in Oceanography 51, 3069–3101. doi:10.1016/j.dsr2.2004.09.014.

Arbic, B.K., Richman, J.G., Shriver, J.F., Timko, P.G., Metzger, E.J., Wallcraft, A.J., 2012. Global modeling of internal tides: Within an eddying ocean general circulation model. Oceanography 25, 20–29. doi:10.5670/oceanog.2012.38.

Arbic, B.K., Wallcraft, A.J., Metzger, E.J., 2010. Concurrent simulation of the eddying general circulation and tides in a global ocean model. Ocean Modelling 32, 175–187. doi:10.1016/j.ocemod.2010.01.007.

Baines, P.G., 1982. On internal tide generation models. Deep Sea Research Part A. Oceanographic Research Papers 29, 307–338. doi:10.1016/0198-0149(82)90098-X.

Ballarotta, M., Ubelmann, C., Pujol, M.I., Taburet, G., Fournier, F., Legeais, J.F., Faugère, Y., Delepoulle, A., Chelton, D., Dibarboure, G., et al., 2019. On the resolutions of ocean altimetry maps. Ocean Science 15, 1091–1109. doi:10.5194/os-15-1091-2019.

Bell Jr, T., 1975. Topographically generated internal waves in the open ocean. Journal of Geophysical Research 80, 320–327. doi:10.1029/JC080i003p00320.

Bendinger, A., Cravatte, S., Gourdeau, L., Brodeau, L., Albert, A., Tchilibou, M., Lyard, F., Vic, C., 2023. Regional modeling of internal-tide dynamics around New Caledonia – Part 1: Coherent internal-tide characteristics and sea surface height signature. Ocean Science 19, 1315–1338. URL: https://os.copernicus.org/articles/19/1315/2023/, doi:10.5194/os-19-1315-2023.

Boccaletti, G., Ferrari, R., Fox-Kemper, B., 2007. Mixed layer instabilities and restratification. Journal of Physical Oceanography 37, 2228–2250. doi:10.1175/JPO3101.1.

Boyd, T.J., Levine, M.D., Gard, S.R., Waldorf, W., 2002. Mooring observations from the Hawaiian ridge: November 2000-January 2002: a component of the Hawaii Ocean Mixing Experiment (HOME) Survey Program URL: https://ir.library.oregonstate.edu/concern/technical_reports/bv73c164v.

de Boyer Montégut, C., Mignot, J., Lazar, A., Cravatte, S., 2007. Control of salinity on the mixed layer depth in the world ocean: 1. General description. Journal of Geophysical Research: Oceans 112. doi:10.1029/2006JC003953.

Buijsman, M.C., Arbic, B.K., Richman, J.G., Shriver, J.F., Wallcraft, A.J., Zamudio, L., 2017. Semidiurnal internal tide incoherence in the equatorial Pacific. Journal of Geophysical Research: Oceans 122, 5286–5305. doi:10.1002/2016JC012590.

Cairns, J.L., Williams, G.O., 1976. Internal wave observations from a midwater float, 2. Journal of Geophysical Research 81, 1943–1950. doi:10.1029/JC081i012p01943.

Callies, J., Ferrari, R., Klymak, J.M., Gula, J., 2015. Seasonality in submesoscale turbulence. Nature communications 6, 6862. doi:10.1038/ncomms7862.

Callies, J., Flierl, G., Ferrari, R., Fox-Kemper, B., 2016. The role of mixed-layer instabilities in submesoscale turbulence. Journal of Fluid Mechanics 788, 5–41. doi:10.1017/jfm.2015.700.

Capet, X., McWilliams, J.C., Molemaker, M.J., Shchepetkin, A., 2008. Mesoscale to submesoscale transition in the California Current System. Part II: Frontal processes. Journal of Physical Oceanography 38, 44–64. doi:10.1175/2007JPO3672.1.

Carrere, L., Arbic, B.K., Dushaw, B., Egbert, G., Erofeeva, S., Lyard, F., Ray, R.D., Ubelmann, C., Zaron, E., Zhao, Z., et al., 2021. Accuracy assessment of global internal-tide models using satellite altimetry. Ocean Science 17, 147–180. doi:`10.5194/os-17-147-2021`.

Carter, G.S., Fringer, O.B., Zaron, E.D., 2012. Regional models of internal tides. Oceanography 25, 56–65. URL: `https://www.jstor.org/stable/24861344`.

Carter, G.S., Merrifield, M., Becker, J.M., Katsumata, K., Gregg, M., Luther, D., Levine, M., Boyd, T.J., Firing, Y., 2008. Energetics of M 2 barotropic-to-baroclinic tidal conversion at the Hawaiian Islands. Journal of Physical Oceanography 38, 2205–2223. doi:`10.1175/2008JPO3860.1`.

Chelton, D.B., Schlax, M.G., Samelson, R.M., 2011. Global observations of nonlinear mesoscale eddies. Progress in oceanography 91, 167–216. doi:`10.1016/j.pocean.2011.01.002`.

Chereskin, T.K., Rocha, C.B., Gille, S.T., Menemenlis, D., Passaro, M., 2019. Characterizing the transition from balanced to unbalanced motions in the southern California Current. Journal of Geophysical Research: Oceans 124, 2088–2109. doi:`10.1029/2018JC014583`.

Couvelard, X., Marchesiello, P., Gourdeau, L., Lefèvre, J., 2008. Barotropic zonal jets induced by islands in the southwest Pacific. Journal of Physical Oceanography 38, 2185–2204. doi:`10.1175/2008JPO3903.1`.

Cravatte, S., Kestenare, E., Eldin, G., Ganachaud, A., Lefèvre, J., Marin, F., Menkes, C., Aucan, J., 2015. Regional circulation around New Caledonia from two decades of observations. Journal of Marine Systems 148, 249–271. doi:`10.1016/j.jmarsys.2015.03.004`.

Cummins, P.F., Oey, L.Y., 1997. Simulation of barotropic and baroclinic tides off northern British Columbia. Journal of Physical oceanography 27, 762–781. doi:`10.1175/1520-0485(1997)027<0762:SOBABT>2.0.CO;2`.

Cushman-Roisin, B., Beckers, J.M., 2011. Introduction to geophysical fluid dynamics: physical and numerical aspects. Academic press.

D'Asaro, E.A., 1985. The energy flux from the wind to near-inertial motions in the surface mixed layer. Journal of Physical Oceanography 15, 1043–1059. doi:`10.1175/1520-0485(1985)015<1043:TEFFTW>2.0.CO;2`.

D'Asaro, E.A., Eriksen, C.C., Levine, M.D., Niiler, P., Van Meurs, P., et al., 1995. Upper-ocean inertial currents forced by a strong storm. Part I: Data and comparisons with linear theory. Journal of Physical Oceanography 25, 2909–2936. doi:`10.1175/1520-0485(1995)025<2909:UOICFB>2.0.CO;2`.

Debreu, L., Vouland, C., Blayo, E., 2008. AGRIF: Adaptive grid refinement in Fortran. Computers & Geosciences 34, 8–13. doi:`10.1016/j.cageo.2007.01.009`.

Doty, M.S., Oguri, M., 1956. The island mass effect. ICES Journal of Marine Science 22, 33–37. doi:`10.1093/icesjms/22.1.33`.

Duda, T.F., Lin, Y.T., Buijsman, M., Newhall, A.E., 2018. Internal tidal modal ray refraction and energy ducting in baroclinic Gulf Stream currents. Journal of Physical Oceanography 48, 1969–1993. doi:10.1175/JPO-D-18-0031.1.

Dunphy, M., Lamb, K.G., 2014. Focusing and vertical mode scattering of the first mode internal tide by mesoscale eddy interaction. Journal of Geophysical Research: Oceans 119, 523–536. doi:10.1002/2013JC009293.

Dunphy, M., Ponte, A.L., Klein, P., Le Gentil, S., 2017. Low-mode internal tide propagation in a turbulent eddy field. Journal of Physical Oceanography 47, 649–665. doi:10.1175/JPO-D-16-0099.1.

Durand, F., Marin, F., Fuda, J.L., Terre, T., 2017. The east caledonian current: a case example for the intercomparison between altika and in situ measurements in a boundary current. Marine Geodesy 40, 1–22. doi:10.1080/01490419.2016.1258375.

Dushaw, B.D., Howe, B.M., Cornuelle, B.D., Worcester, P.F., Luther, D.S., 1995. Barotropic and baroclinic tides in the central North Pacific Ocean determined from long-range reciprocal acoustic transmissions. Journal of Physical Oceanography 25, 631–647. doi:10.1175/1520-0485(1995)025<0631:BABTIT>2.0.CO;2.

d'Ovidio, F., Pascual, A., Wang, J., Doglioli, A.M., Jing, Z., Moreau, S., Grégori, G., Swart, S., Speich, S., Cyr, F., et al., 2019. Frontiers in fine-scale in situ studies: Opportunities during the swot fast sampling phase. Frontiers in Marine Science 6, 168. doi:10.3389/fmars.2019.00168.

Early, J.J., Samelson, R., Chelton, D.B., 2011. The evolution and propagation of quasigeostrophic ocean eddies. Journal of Physical Oceanography 41, 1535–1555. doi:10.1175/2011JPO4601.1.

Egbert, G.D., Ray, R.D., 2001. Estimates of M2 tidal energy dissipation from TOPEX/Poseidon altimeter data. Journal of Geophysical Research: Oceans 106, 22475–22502. doi:10.1029/2000JC000699.

Falahat, S., Nycander, J., Roquet, F., Zarroug, M., 2014. Global calculation of tidal energy conversion into vertical normal modes. Journal of Physical Oceanography 44, 3225–3244. doi:10.1175/JPO-D-14-0002.1.

Ferrari, R., Rudnick, D.L., 2000. Thermohaline variability in the upper ocean. Journal of Geophysical Research: Oceans 105, 16857–16883. doi:10.1029/2000JC900057.

Ferrari, R., Wunsch, C., 2009. Ocean circulation kinetic energy: Reservoirs, sources, and sinks. Annual Review of Fluid Mechanics 41, 253–282. doi:10.1146/annurev.fluid.40.111406.102139.

Fjørtoft, R., Gaudin, J.M., Pourthie, N., Lion, C., Mallet, A., Souyris, J.C., Ruiz, C., Koudogbo, F., Duro, J., Ordoqui, P., et al., 2010. KaRIn-the Ka-band radar interferometer on SWOT: Measurement principle, processing and data specificities, in: 2010 IEEE International Geoscience and Remote Sensing Symposium, IEEE. pp. 4823–4826. doi:10.1109/IGARSS.2010.5650601.

Fu, L.L., Alsdorf, D., Morrow, R., Rodriguez, E., Mognard, N., 2012. SWOT: the Surface Water and Ocean Topography Mission: wide-swath altimetric elevation on Earth. Technical Report. Pasadena, CA: Jet Propulsion Laboratory, National Aeronautics and Space . . . . URL: `http://hdl.handle.net/2014/41996`.

Fu, L.L., Ferrari, R., 2008. Observing oceanic submesoscale processes from space. Eos, Transactions American Geophysical Union 89, 488–488. doi:`10.1029/2008EO480003`.

Fu, L.L., Ubelmann, C., 2014. On the transition from profile altimeter to swath altimeter for observing global ocean surface topography. Journal of Atmospheric and Oceanic Technology 31, 560–568. doi:`10.1175/JTECH-D-13-00109.1`.

Furuichi, N., Hibiya, T., Niwa, Y., 2008. Model-predicted distribution of wind-induced internal wave energy in the world's oceans. Journal of Geophysical Research: Oceans 113. doi:`10.1029/2008JC004768`.

Ganachaud, A., Cravatte, S., Melet, A., Schiller, A., Holbrook, N., Sloyan, B., Widlansky, M., Bowen, M., Verron, J., Wiles, P., et al., 2014. The Southwest Pacific Ocean circulation and climate experiment (SPICE). Journal of Geophysical Research: Oceans 119, 7660–7686. doi:`10.1002/2013JC009678`.

Ganachaud, A., Kessler, W., Wijffels, S., Ridgway, K., Cai, W., Holbrook, N., Bowen, M., Sutton, P., Qiu, B., Timmerman, A., et al., 2007. Southwest Pacific Ocean Circulation and Climate Experiment (SPICE): Part I. Scientific background 111.

Ganachaud, A., Kessler, W., Wijffels, S., Ridgway, K., Cai, W., Holbrook, N., Bowen, M., Sutton, P., Qiu, B., Timmerman, A., et al., 2008. Southwest Pacific Ocean Circulation and Climate Experiment (SPICE): Part II. Implemention Plan 133.

Ganachaud, A., Vega, A., Rodier, M., Dupouy, C., Maes, C., Marchesiello, P., Eldin, G., Ridgway, K., Le Borgne, R., 2010. Observed impact of upwelling events on water properties and biological activity off the southwest coast of New Caledonia. Marine Pollution Bulletin 61, 449–464. doi:`10.1016/j.marpolbul.2010.06.042`.

Gardes, L., Tessier, E., Allain, V., Alloncle, N., Baudat-Franceschi, J., Butaud, J., Collot, J., Etaix-Bonnin, R., Hubert, A., Jourdan, H., et al., 2014. Analyse stratégique de l'Espace maritime de la Nouvelle-Calédonie–vers une gestion intégrée. Nouméa: Agence des aires marines protégées doi:`10.13140/RG.2.1.2888.0803`.

Garrett, C., Kunze, E., 2007. Internal tide generation in the deep ocean. Annu. Rev. Fluid Mech. 39, 57–87. doi:`10.1146/annurev.fluid.39.050905.110227`.

Garrett, C., Munk, W., 1975. Space-time scales of internal waves: A progress report. Journal of Geophysical Research 80, 291–297. doi:`10.1029/JC080i003p00291`.

Garrett, C., Munk, W., 1979. Internal waves in the ocean. Annual review of fluid mechanics 11, 339–369. doi:`10.1146/annurev.fl.11.010179.002011`.

Gasparin, F., Ganachaud, A., Maes, C., 2011. A western boundary current east of New Caledonia: Observed characteristics. Deep Sea Research Part I: Oceanographic Research Papers 58, 956–969. doi:`10.1016/j.dsr.2011.05.007`.

GEBCO, B., 2019. The GEBCO_2019 Grid–a Continuous Terrain Model of the Global Oceans and Land, BODC [data set].

Gill, A.E., 1982. Atmosphere-ocean dynamics. volume 30. Academic press.

Gourdeau, L., Kessler, W.S., Davis, R.E., Sherman, J., Maes, C., Kestenare, E., 2008. Zonal jets entering the Coral Sea. Journal of Physical Oceanography 38, 715–725. doi:10.1175/2007JPO3780.1.

Green, R.H., Lowe, R.J., Buckley, M.L., Foster, T., Gilmour, J.P., 2019. Physical mechanisms influencing localized patterns of temperature variability and coral bleaching within a system of reef atolls. Coral Reefs 38, 759–771. doi:10.1007/s00338-019-01771-2.

Guo, Z., Wang, S., Cao, A., Xie, J., Song, J., Guo, X., 2023. Refraction of the M2 internal tides by mesoscale eddies in the South China Sea. Deep Sea Research Part I: Oceanographic Research Papers 192, 103946. doi:10.1016/j.dsr.2022.103946.

Haine, T.W., Marshall, J., 1998. Gravitational, symmetric, and baroclinic instability of the ocean mixed layer. Journal of physical oceanography 28, 634–658. doi:10.1175/1520-0485(1998)028<0634:GSABIO>2.0.CO;2.

Hendershott, M.C., 1981. Long waves and ocean tides. Evolution of physical oceanography .

Hersbach, H., Bell, B., Berrisford, P., Hirahara, S., Horányi, A., Muñoz-Sabater, J., Nicolas, J., Peubey, C., Radu, R., Schepers, D., et al., 2020. The ERA5 global reanalysis. Quarterly Journal of the Royal Meteorological Society 146, 1999–2049. doi:10.1002/qj.3803.

Holloway, P.E., 1996. A numerical model of internal tides with application to the Australian North West Shelf. Journal of Physical Oceanography 26, 21–37. doi:10.1175/1520-0485(1996)026<0021:ANMOIT>2.0.CO;2.

Hristova, H.G., Kessler, W.S., McWilliams, J.C., Molemaker, M.J., 2014. Mesoscale variability and its seasonality in the Solomon and Coral Seas. Journal of Geophysical Research: Oceans 119, 4669–4687. doi:10.1002/2013JC009741.

Jan, S., Chen, C.T.A., 2009. Potential biogeochemical effects from vigorous internal tides generated in Luzon Strait: a case study at the southernmost coast of Taiwan. Journal of Geophysical Research: Oceans 114. doi:10.1029/2008JC004887.

Jeffreys, H., 1921. VIII. Tidal friction in shallow seas. Philosophical transactions of the royal society of London. Series a, containing papers of a mathematical or physical character 221, 239–264. doi:doi.org/10.1098/rsta.1921.0008.

Jeon, C.H., Buijsman, M.C., Wallcraft, A.J., Shriver, J.F., Arbic, B.K., Richman, J.G., Hogan, P.J., 2019. Improving surface tidal accuracy through two-way nesting in a global ocean model. Ocean Modelling 137, 98–113. doi:https://doi.org/10.1016/j.ocemod.2019.03.007.

Jiang, J., Lu, Y., Perrie, W., 2005. Estimating the energy flux from the wind to ocean inertial motions: The sensitivity to surface wind fields. Geophysical research letters 32. doi:`10.1029/2005GL023289`.

Jithin, A., Francis, P., Unnikrishnan, A., Ramakrishna, S., 2019. Modeling of internal tides in the western Bay of Bengal: Characteristics and energetics. Journal of Geophysical Research: Oceans 124, 8720–8746. doi:`10.1029/2019JC015319`.

Johnston, T.S., Rudnick, D.L., 2015. Trapped diurnal internal tides, propagating semidiurnal internal tides, and mixing estimates in the California Current System from sustained glider observations, 2006–2012. Deep Sea Research Part II: Topical Studies in Oceanography 112, 61–78. doi:`10.1016/j.dsr2.2014.03.009`.

Johnston, T.S., Rudnick, D.L., Alford, M.H., Pickering, A., Simmons, H.L., 2013. Internal tidal energy fluxes in the South China Sea from density and velocity measurements by gliders. Journal of Geophysical Research: Oceans 118, 3939–3949. doi:`10.1002/jgrc.20311`.

Johnston, T.S., Rudnick, D.L., Kelly, S.M., 2015. Standing internal tides in the Tasman Sea observed by gliders. Journal of Physical Oceanography 45, 2715–2737. doi:`10.1175/JPO-D-15-0038.1`.

Kang, S., Foreman, M., Crawford, W., Cherniawsky, J., 2000. Numerical modeling of internal tide generation along the Hawaiian Ridge. Journal of Physical Oceanography 30, 1083–1098. doi:`10.1175/1520-0485(2000)030<1083:NMOITG>2.0.CO;2`.

Kelly, S., Jones, N., Nash, J., Waterhouse, A., 2013. The geography of semidiurnal mode-1 internal-tide energy loss. Geophysical Research Letters 40, 4689–4693. doi:`10.1002/grl.50872`.

Kelly, S.M., Lermusiaux, P.F., 2016. Internal-tide interactions with the Gulf Stream and Middle Atlantic Bight shelfbreak front. Journal of Geophysical Research: Oceans 121, 6271–6294. doi:`10.1002/2016JC011639`.

Keppler, L., Cravatte, S., Chaigneau, A., Pegliasco, C., Gourdeau, L., Singh, A., 2018. Observed characteristics and vertical structure of mesoscale eddies in the southwest tropical Pacific. Journal of Geophysical Research: Oceans 123, 2731–2756. doi:`10.1002/2017JC013712`.

Kerry, C.G., Powell, B.S., Carter, G.S., 2014. The impact of subtidal circulation on internal tide generation and propagation in the Philippine Sea. Journal of Physical Oceanography 44, 1386–1405. doi:`10.1175/JPO-D-13-0142.1`.

Kerry, C.G., Powell, B.S., Carter, G.S., 2016. Quantifying the incoherent M 2 internal tide in the Philippine Sea. Journal of Physical Oceanography 46, 2483–2491. doi:`10.1175/JPO-D-16-0023.1`.

Kessler, W.S., Cravatte, S., 2013. Mean circulation of the Coral Sea. Journal of Geophysical Research: Oceans 118, 6385–6410. doi:`10.1002/2013JC009117`.

Klein, P., Lapeyre, G., 2009. The oceanic vertical pump induced by mesoscale and submesoscale turbulence. Annual review of marine science 1, 351–375. doi:10.1146/annurev.marine.010908.163704.

Klein, P., Lapeyre, G., Siegelman, L., Qiu, B., Fu, L.L., Torres, H., Su, Z., Menemenlis, D., Le Gentil, S., 2019. Ocean-scale interactions from space. Earth and Space Science 6, 795–817. doi:10.1029/2018EA000492.

Klymak, J.M., Moum, J.N., Nash, J.D., Kunze, E., Girton, J.B., Carter, G.S., Lee, C.M., Sanford, T.B., Gregg, M.C., 2006. An estimate of tidal energy lost to turbulence at the Hawaiian Ridge. Journal of Physical Oceanography 36, 1148–1164. doi:doi.org/10.1175/JPO2885.1.

Kundu, P.K., Cohen, I.M., Dowling, D.R., 2015. Fluid mechanics. Academic press.

Kunze, E., 2017a. Internal-wave-driven mixing: Global geography and budgets. Journal of Physical Oceanography 47, 1325–1345. doi:10.1175/JPO-D-16-0141.1.

Kunze, E., 2017b. The internal-wave-driven meridional overturning circulation. Journal of Physical Oceanography 47, 2673–2689. doi:10.1175/JPO-D-16-0141.1.

Lahaye, N., Gula, J., Roullet, G., 2020. Internal Tide Cycle and Topographic Scattering Over the North Mid-Atlantic Ridge. Journal of Geophysical Research: Oceans 125, e2020JC016376. doi:10.1029/2020JC016376.

Lapeyre, G., Klein, P., Hua, B.L., 2006. Oceanic restratification forced by surface frontogenesis. Journal of Physical Oceanography 36, 1577–1590. doi:10.1175/JPO2923.1.

Laurent, L.S., Garrett, C., 2002. The role of internal tides in mixing the deep ocean. Journal of physical oceanography 32, 2882–2899. doi:10.1175/1520-0485(2002)032<2882:TROITI>2.0.CO;2.

Laurent, L.S., Stringer, S., Garrett, C., Perrault-Joncas, D., 2003. The generation of internal tides at abrupt topography. Deep Sea Research Part I: Oceanographic Research Papers 50, 987–1003. doi:10.1016/S0967-0637(03)00096-7.

de Lavergne, C., Falahat, S., Madec, G., Roquet, F., Nycander, J., Vic, C., 2019. Toward global maps of internal tide energy sinks. Ocean Modelling 137, 52–75. doi:10.1016/j.ocemod.2019.03.010.

de Lavergne, C., Vic, C., Madec, G., Roquet, F., Waterhouse, A.F., Whalen, C., Cuypers, Y., Bouruet-Aubertot, P., Ferron, B., Hibiya, T., 2020. A parameterization of local and remote tidal mixing. Journal of Advances in Modeling Earth Systems 12, e2020MS002065. doi:10.1029/2020MS002065.

Laxenaire, R., Speich, S., Blanke, B., Chaigneau, A., Pegliasco, C., Stegner, A., 2018. Anticyclonic eddies connecting the western boundaries of Indian and Atlantic Oceans. Journal of Geophysical Research: Oceans 123, 7651–7677. doi:10.1029/2018JC014270.

Le Guillou, F., Lahaye, N., Ubelmann, C., Metref, S., Cosme, E., Ponte, A., Le Sommer, J., Blayo, E., Vidard, A., 2021. Joint estimation of balanced motions and internal tides from future wide-swath altimetry. Journal of Advances in Modeling Earth Systems 13, e2021MS002613. doi:`10.1029/2021MS002613`.

Le Traon, P.Y., Klein, P., Hua, B.L., Dibarboure, G., 2008. Do altimeter wavenumber spectra agree with the interior or surface quasigeostrophic theory? Journal of Physical Oceanography 38, 1137–1142. doi:`10.1175/2007JPO3806.1`.

Le Vu, B., Stegner, A., Arsouze, T., 2018. Angular Momentum Eddy Detection and tracking Algorithm (AMEDA) and its application to coastal eddy formation. Journal of Atmospheric and Oceanic Technology 35, 739–762. doi:`10.1175/JTECH-D-17-0010.1`.

Lee, C.M., Sanford, T.B., Kunze, E., Nash, J.D., Merrifield, M.A., Holloway, P.E., 2006. Internal tides and turbulence along the 3000-m isobath of the Hawaiian Ridge. Journal of Physical Oceanography 36, 1165–1183. doi:`doi.org/10.1175/JPO2886.1`.

Leichter, J.J., Stewart, H.L., Miller, S.L., 2003. Episodic nutrient transport to Florida coral reefs. Limnology and Oceanography 48, 1394–1407. doi:`10.4319/lo.2003.48.4.1394`.

Lévy, M., Iovino, D., Resplandy, L., Klein, P., Madec, G., Tréguier, A.M., Masson, S., Takahashi, K., 2012. Large-scale impacts of submesoscale dynamics on phytoplankton: Local and remote effects. Ocean Modelling 43, 77–93. doi:`10.1016/j.ocemod.2011.12.003`.

Liu, X., Levine, N.M., 2016. Enhancement of phytoplankton chlorophyll by submesoscale frontal dynamics in the North Pacific Subtropical Gyre. Geophysical Research Letters 43, 1651–1659. doi:`10.1002/2015GL066996`.

Löb, J., Köhler, J., Mertens, C., Walter, M., Li, Z., von Storch, J.S., Zhao, Z., Rhein, M., 2020. Observations of the low-mode internal tide and its interaction with mesoscale flow south of the Azores. Journal of Geophysical Research: Oceans 125, e2019JC015879. doi:`10.1029/2019JC015879`.

Locarnini, M., Mishonov, A., Baranova, O., Boyer, T., Zweng, M., Garcia, H., Seidov, D., Weathers, K., Paver, C., Smolyar, I., 2018. World ocean atlas 2018, volume 1: Temperature. NOAA Atlas NESDIS 81 , 52ppURL: `https://archimer.ifremer.fr/doc/00651/76338/`.

Lueck, R.G., Mudge, T.D., 1997. Topographically induced mixing around a shallow seamount. Science 276, 1831–1833. doi:`10.1126/science.276.5320.18`.

Luecke, C.A., Arbic, B.K., Richman, J.G., Shriver, J.F., Alford, M.H., Ansong, J.K., Bassette, S.L., Buijsman, M.C., Menemenlis, D., Scott, R.B., et al., 2020. Statistical comparisons of temperature variance and kinetic energy in global ocean models and observations: Results from mesoscale to internal wave frequencies. Journal of Geophysical Research: Oceans 125, e2019JC015306. doi:`10.1029/2019JC015306`.

Lyard, F.H., Allain, D.J., Cancet, M., Carrère, L., Picot, N., 2021. FES2014 global ocean tide atlas: design and performance. Ocean Science 17, 615–649. doi:10.5194/os-17-615-2021.

Madec, G., Team, N.S., . NEMO ocean engine. Number 27 in Scientific Notes of Climate Modelling Center, Zenodo. doi:10.5281/zenodo.1464816. backup Publisher: Institut Pierre-Simon Laplace (IPSL) ISSN: 1288-1619.

Mazloff, M.R., Cornuelle, B., Gille, S.T., Wang, J., 2020. The importance of remote forcing for regional modeling of internal waves. Journal of Geophysical Research: Oceans 125, e2019JC015623. doi:10.1029/2019JC015623.

McWilliams, J.C., 2016. Submesoscale currents in the ocean. Proceedings of the Royal Society A: Mathematical, Physical and Engineering Sciences 472, 20160117. doi:10.1098/rspa.2016.0117.

McWilliams, J.C., Gula, J., Molemaker, M.J., Renault, L., Shchepetkin, A.F., 2015. Filament frontogenesis by boundary layer turbulence. Journal of Physical Oceanography 45, 1988–2005. doi:10.1175/JPO-D-14-0211.1.

Melet, A., Hallberg, R., Legg, S., Nikurashin, M., 2014. Sensitivity of the ocean state to lee wave–driven mixing. Journal of physical oceanography 44, 900–921. doi:10.1175/JPO-D-13-072.1.

Melet, A., Hallberg, R., Legg, S., Polzin, K., 2013. Sensitivity of the ocean state to the vertical distribution of internal-tide-driven mixing. Journal of Physical Oceanography 43, 602–615. doi:10.1175/JPO-D-12-055.1.

Melet, A., Legg, S., Hallberg, R., 2016. Climatic impacts of parameterized local and remote tidal mixing. Journal of Climate 29, 3473–3500. doi:10.1175/JCLI-D-15-0153.1.

Menkès, C.E., Allain, V., Rodier, M., Gallois, F., Lebourges-Dhaussy, A., Hunt, B.P., Smeti, H., Pagano, M., Josse, E., Daroux, A., et al., 2015. Seasonal oceanography from physics to micronekton in the south-west Pacific. Deep Sea Research Part II: Topical Studies in Oceanography 113, 125–144. doi:10.1016/j.dsr2.2014.10.026.

Mensa, J.A., Garraffo, Z., Griffa, A., Özgökmen, T.M., Haza, A., Veneziani, M., 2013. Seasonality of the submesoscale dynamics in the Gulf Stream region. Ocean Dynamics 63, 923–941. doi:10.1007/s10236-013-0633-1.

Merrifield, M.A., Holloway, P.E., 2002. Model estimates of M2 internal tide energetics at the Hawaiian Ridge. Journal of Geophysical Research: Oceans 107, 5–1. doi:10.1029/2001JC000996.

Merrifield, M.A., Holloway, P.E., Johnston, T.S., 2001. The generation of internal tides at the Hawaiian Ridge. Geophysical Research Letters 28, 559–562. doi:10.1029/2000GL011749.

Messié, M., Petrenko, A., Doglioli, A.M., Martinez, E., Alvain, S., 2022. Basin-scale biogeochemical and ecological impacts of islands in the tropical Pacific Ocean. Nature Geoscience 15, 469–474. doi:10.1038/s41561-022-00957-8.

Morrow, R., Fu, L.L., Ardhuin, F., Benkiran, M., Chapron, B., Cosme, E., d'Ovidio, F., Farrar, J.T., Gille, S.T., Lapeyre, G., et al., 2019. Global observations of fine-scale ocean surface topography with the surface water and ocean topography (SWOT) mission. Frontiers in Marine Science 6, 232. doi:10.3389/fmars.2019.00232.

Morrow, R., Fu, L.L., Rio, M.H., Ray, R., Prandi, P., Le Traon, P.Y., Benveniste, J., 2023. Ocean circulation from space. Surveys in Geophysics , 1–44.

Mowbray, D., Rarity, B., 1967. A theoretical and experimental investigation of the phase configuration of internal waves of small amplitude in a density stratified liquid. Journal of Fluid Mechanics 28, 1–16. doi:10.1017/S0022112067001867.

Muacho, S., Da Silva, J., Brotas, V., Oliveira, P., 2013. Effect of internal waves on near-surface chlorophyll concentration and primary production in the Nazaré Canyon (west of the Iberian Peninsula). Deep Sea Research Part I: Oceanographic Research Papers 81, 89–96. doi:10.1016/j.dsr.2013.07.012.

Müller, M., Arbic, B.K., Richman, J.G., Shriver, J.F., Kunze, E.L., Scott, R.B., Wallcraft, A.J., Zamudio, L., 2015. Toward an internal gravity wave spectrum in global ocean models. Geophysical Research Letters 42, 3474–3481. doi:10.1002/2015GL063365.

Müller, M., Cherniawsky, J., Foreman, M., von Storch, J.S., 2012. Global M2 internal tide and its seasonal variability from high resolution ocean circulation and tide modeling. Geophysical Research Letters 39. doi:10.1029/2012GL053320.

Munk, W., Armi, L., Fischer, K., Zachariasen, F., 2000. Spirals on the sea. Proceedings of the Royal Society of London. Series A: Mathematical, Physical and Engineering Sciences 456, 1217–1280.

Munk, W., Wunsch, C., 1998. Abyssal recipes II: Energetics of tidal and wind mixing. Deep Sea Research Part I: Oceanographic Research Papers 45, 1977–2010. doi:10.1016/S0967-0637(98)00070-3.

Munk, W.H., 1966. Abyssal recipes, in: Deep sea research and oceanographic abstracts, Elsevier. pp. 707–730. doi:10.1016/0011-7471(66)90602-4.

Nash, J.D., Kelly, S.M., Shroyer, E.L., Moum, J.N., Duda, T.F., 2012. The unpredictable nature of internal tides on continental shelves. Journal of Physical Oceanography 42, 1981–2000. doi:10.1175/JPO-D-12-028.1.

Nelson, A., Arbic, B., Menemenlis, D., Peltier, W., Alford, M., Grisouard, N., Klymak, J., 2020. Improved internal wave spectral continuum in a regional ocean model. Journal of Geophysical Research: Oceans 125, e2019JC015974. doi:10.1029/2019JC015974.

Nelson, A.D., Arbic, B.K., Zaron, E.D., Savage, A.C., Richman, J.G., Buijsman, M.C., Shriver, J.F., 2019. Toward realistic nonstationarity of semidiurnal baroclinic tides in a hydrodynamic model. Journal of Geophysical Research: Oceans 124, 6632–6642. doi:10.1029/2018JC014737.

Nikurashin, M., Ferrari, R., 2011. Global energy conversion rate from geostrophic flows into internal lee waves in the deep ocean. Geophysical Research Letters 38. doi:`10.1029/2011GL046576`.

Niwa, Y., Hibiya, T., 2001. Numerical study of the spatial distribution of the M2 internal tide in the Pacific Ocean. Journal of Geophysical Research: Oceans 106, 22441–22449. doi:`10.1029/2000JC000770`.

Nycander, J., 2005. Generation of internal waves in the deep ocean by tides. Journal of Geophysical Research: Oceans 110. doi:`10.1029/2004JC002487`.

Ou, H.W., 1984. Geostrophic adjustment: A mechanism for frontogenesis. Journal of Physical Oceanography 14, 994–1000. doi:`10.1175/1520-0485(1984)014<0994:GAAMFF>2.0.CO;2`.

Park, J.H., Watts, D.R., 2006. Internal tides in the southwestern Japan/East Sea. Journal of Physical Oceanography 36, 22–34. doi:`10.1175/JPO2846.1`.

Payri, C.E., Allain, V., Aucan, J., David, C., David, V., Dutheil, C., Loubersac, L., Menkes, C., Pelletier, B., Pestana, G., et al., 2019. New Caledonia, in: World Seas: An Environmental Evaluation. Elsevier, pp. 593–618. doi:`10.1016/B978-0-08-100853-9.00035-X`.

Payri, C.E., de Forges, B.R., 2006. Compendium of marine species from New Caledonia. IRD (Institut de recherche pour le développement).

Pétrélis, F., Smith, S.L., Young, W., 2006. Tidal conversion at a submarine ridge. Journal of Physical Oceanography 36, 1053–1071. doi:`10.1175/JPO2879.1`.

Pickering, A., Alford, M., Nash, J., Rainville, L., Buijsman, M., Ko, D.S., Lim, B., 2015. Structure and variability of internal tides in Luzon Strait. Journal of Physical Oceanography 45, 1574–1594. doi:`10.1175/JPO-D-14-0250.1`.

Polzin, K., Toole, J., Ledwell, J., Schmitt, R., 1997. Spatial variability of turbulent mixing in the abyssal ocean. Science 276, 93–96. doi:`10.1126/science.276.5309.93`.

Ponte, A.L., Klein, P., 2015. Incoherent signature of internal tides on sea level in idealized numerical simulations. Geophysical Research Letters 42, 1520–1526. doi:`10.1002/2014GL062583`.

Ponte, A.L., Klein, P., Dunphy, M., Le Gentil, S., 2017. Low-mode internal tides and balanced dynamics disentanglement in altimetric observations: Synergy with surface density observations. Journal of Geophysical Research: Oceans 122, 2143–2155. doi:`10.1002/2016JC012214`.

Pujol, M.I., Faugère, Y., Taburet, G., Dupuy, S., Pelloquin, C., Ablain, M., Picot, N., 2016. DUACS DT2014: the new multi-mission altimeter data set reprocessed over 20 years. Ocean Science 12, 1067–1090. doi:`10.5194/os-12-1067-2016`.

Qiu, B., Chen, S., 2004. Seasonal modulations in the eddy field of the South Pacific Ocean. Journal of Physical Oceanography 34, 1515–1527. doi:`10.1175/1520-0485(2004)034<1515:SMITEF>2.0.CO;2`.

Qiu, B., Chen, S., Kessler, W.S., 2009. Source of the 70-day mesoscale eddy variability in the Coral Sea and the North Fiji Basin. Journal of Physical Oceanography 39, 404–420. doi:10.1175/2008JPO3988.1.

Qiu, B., Chen, S., Klein, P., Sasaki, H., Sasai, Y., 2014. Seasonal mesoscale and submesoscale eddy variability along the North Pacific Subtropical Countercurrent. Journal of Physical Oceanography 44, 3079–3098. doi:10.1175/JPO-D-14-0071.1.

Qiu, B., Chen, S., Klein, P., Wang, J., Torres, H., Fu, L.L., Menemenlis, D., 2018. Seasonality in transition scale from balanced to unbalanced motions in the world ocean. Journal of Physical Oceanography 48, 591–605. doi:10.1175/JPO-D-17-0169.1.

Qiu, B., Scott, R.B., Chen, S., 2008. Length scales of eddy generation and nonlinear evolution of the seasonally modulated South Pacific Subtropical Countercurrent. Journal of Physical Oceanography 38, 1515–1528. doi:10.1175/2007JPO3856.1.

Qu, T., Lindstrom, E.J., 2002. A climatological interpretation of the circulation in the western South Pacific. Journal of Physical Oceanography 32, 2492–2508. doi:10.1175/1520-0485(2002)032<2492:ACIOTC>2.0.CO;2.

Rainville, L., Lee, C.M., Rudnick, D.L., Yang, K.C., 2013. Propagation of internal tides generated near Luzon Strait: Observations from autonomous gliders. Journal of Geophysical Research: Oceans 118, 4125–4138. doi:10.1002/jgrc.20293.

Rainville, L., Pinkel, R., 2006. Propagation of low-mode internal waves through the ocean. Journal of Physical Oceanography 36, 1220–1236. doi:10.1175/JPO2889.1.

Rattray, M.J., 1969. Generation of the long internal waves at the continental slope. Deep-Sea Res. 16, 179–195.

Ray, R.D., Cartwright, D.E., 2001. Estimates of internal tide energy fluxes from Topex/Poseidon altimetry: Central North Pacific. Geophysical Research Letters 28, 1259–1262. doi:10.1029/2000GL012447.

Ray, R.D., Zaron, E.D., 2011. Non-stationary internal tides observed with satellite altimetry. Geophysical Research Letters 38. doi:10.1029/2011GL048617.

Ray, R.D., Zaron, E.D., 2016. M2 internal tides and their observed wavenumber spectra from satellite altimetry. Journal of Physical Oceanography 46, 3–22. doi:10.1175/JPO-D-15-0065.1.

Renault, L., Molemaker, M.J., McWilliams, J.C., Shchepetkin, A.F., Lemarié, F., Chelton, D., Illig, S., Hall, A., 2016. Modulation of wind work by oceanic current interaction with the atmosphere. Journal of Physical Oceanography 46, 1685–1704. doi:10.1175/JPO-D-15-0232.1.

Rimac, A., von Storch, J.S., Eden, C., Haak, H., 2013. The influence of high-resolution wind stress field on the power input to near-inertial motions in the ocean. Geophysical Research Letters 40, 4882–4886. doi:10.1002/grl.50929.

Rocha, C.B., Chereskin, T.K., Gille, S.T., Menemenlis, D., 2016a. Mesoscale to submesoscale wavenumber spectra in Drake Passage. Journal of Physical Oceanography 46, 601–620. doi:`10.1175/JPO-D-15-0087.1`.

Rocha, C.B., Gille, S.T., Chereskin, T.K., Menemenlis, D., 2016b. Seasonality of submesoscale dynamics in the Kuroshio Extension. Geophysical Research Letters 43, 11–304. doi:`10.1002/2016GL071349`.

Roger, J., Pelletier, B., Duphil, M., Lefèvre, J., Aucan, J., Lebellegard, P., Thomas, B., Bachelier, C., Varillon, D., 2021. The Mw 7.5 Tadine (Maré, Loyalty Is.) earthquake and related tsunami of December 5, 2018: implications for tsunami hazard assessment in New Caledonia. Natural Hazards and Earth System Sciences, Discussions, https://doi. org/10.5194/nhess-2021-58 doi:`10.5194/nhess-2021-58`.

Rudnick, D.L., Boyd, T.J., Brainard, R.E., Carter, G.S., Egbert, G.D., Gregg, M.C., Holloway, P.E., Klymak, J.M., Kunze, E., Lee, C.M., et al., 2003. From tides to mixing along the Hawaiian Ridge. science 301, 355–357. doi:`10.1126/science.1085837`.

Sandström, J.W., 1908. Dynamische Versuche mit Meerwasser.

Sasaki, H., Klein, P., Qiu, B., Sasai, Y., 2014. Impact of oceanic-scale interactions on the seasonal modulation of ocean dynamics by the atmosphere. Nature communications 5, 5636. doi:`10.1038/ncomms6636`.

Savage, A.C., Arbic, B.K., Alford, M.H., Ansong, J.K., Farrar, J.T., Menemenlis, D., O'Rourke, A.K., Richman, J.G., Shriver, J.F., Voet, G., et al., 2017. Spectral decomposition of internal gravity wave sea surface height in global models. Journal of Geophysical Research: Oceans 122, 7803–7821. doi:`10.1002/2017JC013009`.

Schubert, R., Gula, J., Greatbatch, R.J., Baschek, B., Biastoch, A., 2020. The submesoscale kinetic energy cascade: Mesoscale absorption of submesoscale mixed layer eddies and frontal downscale fluxes. Journal of Physical Oceanography 50, 2573–2589. doi:`10.1175/JPO-D-19-0311.1`.

Scott, R.B., Arbic, B.K., 2007. Spectral energy fluxes in geostrophic turbulence: Implications for ocean energetics. Journal of physical oceanography 37, 673–688. doi:`10.1175/JPO3027.1`.

Sérazin, G., Marin, F., Gourdeau, L., Cravatte, S., Morrow, R., Dabat, M.L., 2020. Scale-dependent analysis of in situ observations in the mesoscale to submesoscale range around New Caledonia. Ocean Science 16, 907–925. doi:`10.5194/os-16-907-2020`.

Shakespeare, C.J., 2023. Eddy acceleration and decay driven by internal tides. Journal of Physical Oceanography doi:`10.1175/JPO-D-23-0127.1`.

Shriver, J., Arbic, B.K., Richman, J., Ray, R., Metzger, E., Wallcraft, A., Timko, P., 2012. An evaluation of the barotropic and internal tides in a high-resolution global ocean circulation model. Journal of Geophysical Research: Oceans 117. doi:`10.1029/2012JC008170`.

Simmons, H.L., Hallberg, R.W., Arbic, B.K., 2004. Internal wave generation in a global baroclinic tide model. Deep Sea Research Part II: Topical Studies in Oceanography 51, 3043–3068. doi:10.1016/j.dsr2.2004.09.015.

Siyanbola, O.Q., Buijsman, M.C., Delpech, A., Renault, L., Barkan, R., Shriver, J.F., Arbic, B.K., McWilliams, J.C., 2023. Remote internal wave forcing of regional ocean simulations near the US West Coast. Ocean Modelling 181, 102154. doi:10.1016/j.ocemod.2022.102154.

Smith, S.G.L., Young, W., 2002. Conversion of the barotropic tide. Journal of Physical Oceanography 32, 1554–1566. doi:10.1175/1520-0485(2002)032<1554:COTBT>2.0.CO;2.

Smith, W.H., Sandwell, D.T., 1997. Global sea floor topography from satellite altimetry and ship depth soundings. Science 277, 1956–1962. doi:10.1126/science.277.5334.1956.

Srinivasan, K., McWilliams, J.C., Renault, L., Hristova, H.G., Molemaker, J., Kessler, W.S., 2017. Topographic and mixed layer submesoscale currents in the near-surface southwestern tropical Pacific. Journal of Physical Oceanography 47, 1221–1242. doi:10.1175/JPO-D-16-0216.1.

St. Laurent, L., Simmons, H., Jayne, S., 2002. Estimating tidally driven mixing in the deep ocean. Geophysical research letters 29, 21–1. doi:10.1029/2002GL015633.

Stammer, D., 1997. Global characteristics of ocean variability estimated from regional TOPEX/POSEIDON altimeter measurements. Journal of Physical Oceanography 27, 1743–1769. doi:10.1175/1520-0485(1997)027<1743:GCOOVE>2.0.CO;2.

Storer, B.A., Buzzicotti, M., Khatri, H., Griffies, S.M., Aluie, H., 2022. Global energy spectrum of the general oceanic circulation. Nature communications 13, 5314. doi:10.1038/s41467-022-33031-3.

Storlazzi, C.D., Cheriton, O.M., Van Hooidonk, R., Zhao, Z., Brainard, R., 2020. Internal tides can provide thermal refugia that will buffer some coral reefs from future global warming. Scientific reports 10, 13435. doi:10.1038/s41598-020-70372-9.

Tandon, A., Garrett, C., 1995. Geostrophic adjustment and restratification of a mixed layer with horizontal gradients above a stratified layer. Journal of physical oceanography 25, 2229–2241. doi:10.1175/1520-0485(1995)025<2229:GAAROA>2.0.CO;2.

Taylor, G.I., 1920. I. Tidal friction in the Irish Sea. Philosophical Transactions of the Royal Society of London. Series A, Containing Papers of a Mathematical or Physical Character 220, 1–33. doi:doi.org/10.1098/rsta.1920.0001.

Tchilibou, M., Gourdeau, L., Lyard, F., Morrow, R., Koch Larrouy, A., Allain, D., Djath, B., 2020. Internal tides in the Solomon Sea in contrasted ENSO conditions. Ocean Science 16, 615–635. doi:10.5194/os-16-615-2020.

Tchilibou, M., Koch-Larrouy, A., Barbot, S., Lyard, F., Morel, Y., Jouanno, J., Morrow, R., 2022. Internal tides off the Amazon shelf during two contrasted seasons: interactions with background circulation and SSH imprints. Ocean Science 18, 1591–1618. doi:10.5194/os-18-1591-2022.

Thakur, R., Arbic, B.K., Menemenlis, D., Momeni, K., Pan, Y., Peltier, W.R., Skitka, J., Alford, M.H., Ma, Y., 2022. Impact of vertical mixing parameterizations on internal gravity wave spectra in regional ocean models. Geophysical Research Letters 49, e2022GL099614. doi:10.1029/2022GL099614.

Thomas, J., Daniel, D., 2021. Forward flux and enhanced dissipation of geostrophic balanced energy. Journal of Fluid Mechanics 911, A60. doi:10.1017/jfm.2020.1026.

Thomas, L.N., Tandon, A., Mahadevan, A., 2008. Submesoscale processes and dynamics. Ocean modeling in an Eddying Regime 177, 17–38. doi:10.1029/177GM04.

Torres, H., Klein, P., Siegelman, L., Qiu, B., Chen, S., Ubelmann, C., Wang, J., Menemenlis, D., Fu, L.L., 2019. Diagnosing ocean-wave-turbulence interactions from space. Geophysical Research Letters 46, 8933–8942. doi:10.1029/2019GL083675.

Torres, H.S., Klein, P., Menemenlis, D., Qiu, B., Su, Z., Wang, J., Chen, S., Fu, L.L., 2018. Partitioning ocean motions into balanced motions and internal gravity waves: A modeling study in anticipation of future space missions. Journal of Geophysical Research: Oceans 123, 8084–8105. doi:10.1029/2018JC014438.

Ubelmann, C., Carrere, L., Durand, C., Dibarboure, G., Faugère, Y., Ballarotta, M., Briol, F., Lyard, F., 2022. Simultaneous estimation of ocean mesoscale and coherent internal tide sea surface height signatures from the global altimetry record. Ocean Science 18, 469–481. doi:10.5194/os-18-469-2022.

Vallis, G.K., 2017. Atmospheric and oceanic fluid dynamics. Cambridge University Press.

Vergara, O., Morrow, R., Pujol, I., Dibarboure, G., Ubelmann, C., 2019. Revised global wave number spectra from recent altimeter observations. Journal of Geophysical Research: Oceans 124, 3523–3537. doi:10.1029/2018JC014844.

Vergara, O., Morrow, R., Pujol, M.I., Dibarboure, G., Ubelmann, C., 2023. Global submesoscale diagnosis using along-track satellite altimetry. Ocean Science 19, 363–379. doi:10.5194/os-19-363-2023.

Vic, C., Garabato, A.C.N., Green, J.M., Spingys, C., Forryan, A., Zhao, Z., Sharples, J., 2018. The lifecycle of semidiurnal internal tides over the northern Mid-Atlantic Ridge. Journal of Physical Oceanography 48, 61–80. doi:10.1175/JPO-D-17-0121.1.

Vic, C., Naveira Garabato, A.C., Green, J.M., Waterhouse, A.F., Zhao, Z., Melet, A., de Lavergne, C., Buijsman, M.C., Stephenson, G.R., 2019. Deep-ocean mixing driven by small-scale internal tides. Nature communications 10, 2099. doi:`10.1038/s41467-019-10149-5`.

Wang, H., Grisouard, N., Salehipour, H., Nuz, A., Poon, M., Ponte, A.L., 2022. A deep learning approach to extract internal tides scattered by geostrophic turbulence. Geophysical Research Letters 49, e2022GL099400. doi:`10.1029/2022GL099400`.

Wang, Y., Legg, S., 2023. Enhanced Dissipation of Internal Tides in a Mesoscale Baroclinic Eddy. Journal of Physical Oceanography 53, 2293–2316. doi:`10.1175/JPO-D-23-0045.1`.

Wang, Y.H., Dai, C.F., Chen, Y.Y., 2007. Physical and ecological processes of internal waves on an isolated reef ecosystem in the South China Sea. Geophysical Research Letters 34. doi:`10.1029/2007GL030658`.

Waterhouse, A.F., MacKinnon, J.A., Nash, J.D., Alford, M.H., Kunze, E., Simmons, H.L., Polzin, K.L., Laurent, L.C.S., Sun, O.M., Pinkel, R., et al., 2014. Global patterns of diapycnal mixing from measurements of the turbulent dissipation rate. Journal of Physical Oceanography 44, 1854–1872. doi:`10.1175/JPO-D-13-0104.1`.

Whalen, C.B., De Lavergne, C., Naveira Garabato, A.C., Klymak, J.M., MacKinnon, J.A., Sheen, K.L., 2020. Internal wave-driven mixing: Governing processes and consequences for climate. Nature Reviews Earth & Environment 1, 606–621. doi:`https://doi.org/10.1038/s43017-020-0097-z`.

Wolanski, E., Colin, P., Naithani, J., Deleersnijder, E., Golbuu, Y., 2004. Large amplitude, leaky, island-generated, internal waves around Palau, Micronesia. Estuarine, Coastal and Shelf Science 60, 705–716. doi:`10.1016/j.ecss.2004.03.009`.

Wolanski, E., Pickard, G., 1985. Long-term observations of currents on the central Great Barrier Reef continental shelf. Coral Reefs 4, 47–57.

Wunsch, C., Ferrari, R., 2004. Vertical mixing, energy, and the general circulation of the oceans. Annu. Rev. Fluid Mech. 36, 281–314. doi:`10.1146/annurev.fluid.36.050802.122121`.

Wyatt, A.S., Leichter, J.J., Toth, L.T., Miyajima, T., Aronson, R.B., Nagata, T., 2020. Heat accumulation on coral reefs mitigated by internal waves. Nature Geoscience 13, 28–34. doi:`10.1038/s41561-019-0486-4`.

Wyatt, A.S., Leichter, J.J., Washburn, L., Kui, L., Edmunds, P.J., Burgess, S.C., 2023. Hidden heatwaves and severe coral bleaching linked to mesoscale eddies and thermocline dynamics. Nature Communications 14, 25. doi:`10.1038/s41467-022-35550-5`.

Xu, Y., Fu, L.L., 2011. Global variability of the wavenumber spectrum of oceanic mesoscale turbulence. Journal of physical oceanography 41, 802–809. doi:`10.1175/2010JPO4558.1`.

Xu, Y., Fu, L.L., 2012. The effects of altimeter instrument noise on the estimation of the wavenumber spectrum of sea surface height. Journal of Physical Oceanography 42, 2229–2233. doi:`10.1175/JPO-D-12-0106.1`.

Zaron, E.D., 2017. Mapping the nonstationary internal tide with satellite altimetry. Journal of Geophysical Research: Oceans 122, 539–554. doi:10.1002/2016JC012487.

Zaron, E.D., 2019. Baroclinic tidal sea level from exact-repeat mission altimetry. Journal of Physical Oceanography 49, 193–210. doi:10.1175/JPO-D-18-0127.1.

Zaron, E.D., Ray, R.D., 2017. Using an altimeter-derived internal tide model to remove tides from in situ data. Geophysical Research Letters 44, 4241–4245. doi:10.1002/2017GL072950.

Zhao, Z., Alford, M.H., Girton, J.B., Rainville, L., Simmons, H.L., 2016. Global observations of open-ocean mode-1 M 2 internal tides. Journal of Physical Oceanography 46, 1657–1684. doi:10.1175/JPO-D-15-0105.1.

Zhao, Z., Alford, M.H., MacKinnon, J.A., Pinkel, R., 2010. Long-range propagation of the semidiurnal internal tide from the Hawaiian Ridge. Journal of Physical Oceanography 40, 713–736. doi:10.1175/2009JPO4207.1.

Zilberman, N., Becker, J., Merrifield, M., Carter, G., 2009. Model estimates of M2 internal tide generation over Mid-Atlantic Ridge topography. Journal of Physical Oceanography 39, 2635–2651. doi:10.1175/2008JPO4136.1.

Zilberman, N., Merrifield, M., Carter, G., Luther, D., Levine, M., Boyd, T.J., 2011. Incoherent nature of M2 internal tides at the Hawaiian Ridge. Journal of physical oceanography 41, 2021–2036. doi:10.1175/JPO-D-10-05009.1.

Zweng, M., Seidov, D., Boyer, T., Locarnini, M., Garcia, H., Mishonov, A., Baranova, O., Weathers, K., Paver, C., Smolyar, I., et al., 2019. World ocean atlas 2018, volume 2: Salinity. NOAA Atlas NESDIS 82 , 50ppURL: https://archimer.ifremer.fr/doc/00651/76339/.

# List of Figures

# List of Tables